Structure and properties of tunable Pickering emulsions

Benjamin Christopher Munro

A thesis presented in partial fulfilment
of the requirements for the degree of

Doctor of Philosophy
in
Chemistry

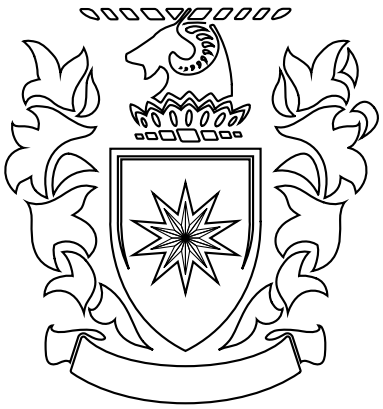

Massey University
Manawatū, New Zealand

2019

Abstract

The ability to design soft-materials with targeted rheological properties is a vital part of the modern world. One type of soft-materials that are important across a range of industries from food and consumer goods, to paints and oil products are emulsions. Generally speaking, emulsions are mixtures of oil and water, with a stabiliser which controls the interactions between the droplets. Pickering emulsions are a subset of emulsions which utilise a solid nanoparticle stabiliser to increase droplet stability. Pickering emulsions are becoming increasingly attractive due to the wide, and varied, range of stabilisers available, along with the remarkable stability that these systems can have.

Recently a number of workers have demonstrated the ability to tune the interactions between high volume fraction emulsions (with modifications prior to emulsification), resulting in the changes to the bulk strength of the emulsion systems and the droplet size distribution. Additionally, some unique yielding behaviour has been uncovered in certain situations, presenting an area which can be further investigated.

The work presented in this thesis has developed low volume fraction emulsion systems with interactions between the droplets that were tuned post-emulsification. This was carried out through two distinct processes, modification of the Debye length with the addition of salt, and modification of the surface charge of the Pickering emulsifier by changing the pH of the aqueous phase. The results of this have demonstrated low volume percentage emulsions with interactions ranging from highly attractive through to repulsive between the droplets while maintaining a consistent droplet size. These new systems have demonstrated interesting rheological properties, with the attractive systems demonstrating significantly higher strength than anticipated. In certain cases these low volume percentage emulsion systems were demonstrated to show multi-stage yielding behaviour, something that has previously only been seen for higher volume fraction systems. In addition to these properties, this work is thought to present the first case of a titania stabilised Pickering emulsion system with tunable interactions, demonstrating a new material for future development.

Acknowledgments

While this has been my work, I would not have been able to complete it without a vast amount of help from a range of people over the course of the past years.

First, my supervisors Dr. Catherine Whitby, and Prof. Simon Hall. Thank you both for your support over the past few years. Catherine, your expertise in Pickering emulsions has been vitally important over the course of this work, in addition to this, your availability, and willingness to help when needed has been a huge support. Simon, thank you for coming up with challenging questions throughout our meetings over the past few years, and for the funding for this PhD project.

The experiments carried out throughout this thesis would not have been possible without the training and guidance provided by a range of people, including:

- The team at the Manawatu Microscopy and Imaging Centre, Matthew, Niki, Jordan, and Pani – Thank you all for your expertise and helpfulness whenever I turned up with some abnormal looking emulsions.
- Dr. Allan Raudsepp – Thank you for your rheology knowledge and help in getting me up and running with our rheometer.
- Chris Hall and lab members at the Massey Institute of Food Science and Technology – Thank you for willingness to let us use your rheometer, and zeta sizer, often for long periods of time, and also for your help in training me to use these machines.

The (Institute/School) of Fundamental Sciences administration and technical staff, thank you for putting up with my still ongoing requests for help and stupid questions.

Thanks are also due for past and present lab group members for all of the useful talks we have shared over the years, many of which have been over a beer or three.

It would be amiss of me to not thank my family and friends for the help not only over the past few years, but also much further back. Thanks are needed for my children Scarlett and Delilah. I hope that you both have enjoyed the adventures that we have been on, and hopefully there will be many more to come.

Finally, Rebecca. Your support has been the most important factor in helping me complete this work. You have put up with an enormous amount over the course of this PhD, from the pressures of being a mother, to the nights alone while I was working, you are still here and still supporting me, thank you.

Contents

List of Figures

List of Tables

1 Introduction

1.1. Background

Emulsions are vitally important in a wide range of biological processes, industries, and products including pharmaceuticals, paints, oil processing, and foods. Emulsions consist of mixtures of two liquid phases that are substantially immiscible, where one phase is dispersed as discrete droplets throughout the other liquid phase. These mixtures are unstable with respect to the droplet size, and require the inclusion of a stabiliser at the interface between the two liquids. There are two general types of stabilisers that can be utilised for this, surfactant emulsifiers, and Pickering emulsifiers. Surfactant emulsifiers typically consist of molecular species with both hydrophilic and lipophilic functionalities. Pickering emulsifiers consist of solid nanoparticles of a material discrete from the two liquid phases of the emulsion. Pickering emulsions were originally described in the early 1900s, however the field did not receive significant attention among researchers until the 1990s[1]. Pickering emulsions have become of greater interest recently due to their remarkable stability and wide array of potential "food-safe" stabilisers [1–7]. The stability of Pickering emulsions predominately arises from the mechanical barrier that the solid nanoparticles create on the surface of the emulsion droplets, as well as network formation between additional nanoparticles in the continuous phase. Altering the interactions between the nanoparticles in Pickering emulsions provides a pathway to change the bulk properties of the material. The effects of particle shape, size, and surface charge on the microstructure and rheology of Pickering emulsions have been studied [8–10]. These studies took the approach of forming emulsions in the presence of particles of different surface charge (or shape). This approach complicates the relationship between the particle interactions and emulsion microstructure as the size of emulsion droplets stabilised by the particles, as well as the extent of droplet aggregation varied with the particle charge (and shape).The work pre-

[1] A Google Scholar search for "Pickering Emulsions" citations between 1900 and 1990 finds about 50 results, while the same search between 1991 and 2019 finds over 10,000.

sented in this thesis focused on altering the interactions (and hence aggregation) between the nanoparticle-coated droplets after emulsification. These alterations have demonstrated significant changes to the rheological properties, such as the yielding and flow behaviour of the emulsion systems.

Rheology is one technique that can be used to understand the structures present in emulsion systems, and has been used throughout the work presented here. Rheology allows insight into the flow behaviours (the viscosity and stress response of a material to the application under shear), and elasticity of a material (the ability of a material to resist deformation under stress, and to return to the original shape after the stress is removed) [11]. Bulk rheology measurements will demonstrate an increase in the magnitude of the data when there is significant structure present in the emulsion. In addition, some researchers have noticed complex, multi-step yielding behaviour of colloidal materials which has been associated with attractive interactions between the particles generating structures with more than on characteristic length scale [8–10, 12–15]. Changes in the rheology and yielding behaviour of a number of Pickering emulsions will be considered in this thesis, with an overall goal of increasing the understanding of the structural changes that can occur in these materials as a result of changes in the interactions between the nanoparticle stabilisers present in the emulsion systems.

1.2. Aims

The research reported in this thesis aimed to create emulsions with micro-structures ranging from well dispersed (repulsive) to flocculated (attractive) through the modification of two different aspects of the surface chemistry of particle stabilisers (surface charge, and Debye length); i.e. the use of 'tuneable' Pickering emulsifiers. Visual identification of the microstructures of each emulsion was carried out using microscopy techniques. Rheological changes resulting from the changes in the microstructure across the range of emulsions were investigated. This allows insight into the effect that the microstructure of an emulsion system can have on the bulk physical properties.

1.3. Chapter outline

This chapter expands on the aims of the present research by outlining the history of Pickering emulsion study and rheology that led to the development of the research questions addressed in this thesis. It also sets the background for the experiments and results

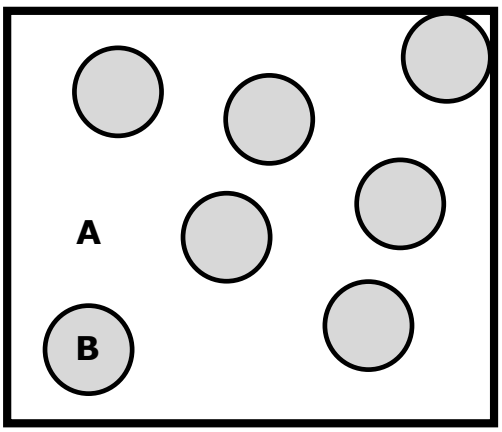

Fig. 1.1 The general structure of colloidal materials showing the discontinuous phases dispersed throughout the continuous phase of the material. (A) Continuous phase (white). (B) Discontinuous phase (grey).

that will be reported through this work. The study of colloidal and, more specifically, emulsion systems will be discussed with considerations to the preparation of emulsions, the factors affecting emulsion stability, the different types of stabilisers that can be used to prepare emulsions, and some of the key properties of emulsions. The key experimental technique used for the work reported in this thesis is rheology. The history, different types of rheometers, and a range of routinely used experiments will be outlined. One of key feature that will be shown throughout this work is the difference between emulsions with altered interdroplet interactions. The changes in the rheology of these materials demonstrated in previous works will be discussed, with an outline of the areas of work that still require further investigation. Finally, the scope of this thesis and a brief outline of each chapter is included as a guide to this work.

1.4. Colloids

Colloidal dispersions, at the most general description, are multi-phase systems where one of the phases is dispersed throughout the other phase. Each of the phases can be either solid, liquids, or gases, with the general material type for the colloid being dependent on the specific combination [16, 17]. It is important to recognise the distinction between colloidal systems and molecularly-solubilised materials. In a colloidal system, there are at least two distinct phases (Fig. 1.1). In a molecularly-solubilised system, the solute is dissolved into the continuous phase, resulting in only a single phase. This leads to a difference in the systems where the dispersed phase in a colloid is much greater in size (nano to micrometer scale), compared to that of a molecular system (Ångstrom scale).

The research area of colloids is one that has expanded greatly since it was first named over one hundred and fifty years ago, with well over one million articles found in a Google Scholar search for "colloids" [18]. Despite the first recognition of colloids in 1861, colloidal materials had been artificially prepared and studied much earlier, with the production and inclusion of gold nanoparticles in glasses made in the 4th century [19]. As the area of colloids developed, further investigations into these materials demonstrated that the stability of aqueous colloidal suspensions were strongly dependent on the ionic strength of the continuous phase, indicating the ability to tune the interactions between for example, gold nanoparticles [20]. Calculations that model the interaction energy between colloidal systems such as these were independently developed by two groups during the 1940s, resulting in the Derjaguin, Landau, Verwey, and Overbeek (DLVO) theory [21, 22]. This model will be discussed further in Section 1.4.1.3. Further developments to this model have been added over the years, each accounting for previously unrepresented phenomena such as hydration forces [23, 24].

These examples of colloidal materials have focused on solid-in-liquid colloids, sols, ignoring the wide range of other colloidal materials that have been studied. As mentioned earlier, colloidal materials are multiphase systems, where the dispersed phase is of sufficiently small size. As such, there are a number of different material types that can be prepared. The range of materials that can be prepared as binary mixtures of two phases are outlined in Table 1.1. Each of these material types have common, well known examples which are present in modern life, ranging from solid and liquid aerosols like smoke and fog, to soap foams, cheese, and milk representing foams, gels, and emulsions. Each of these materials demonstrate properties that are different and altered from those for the individual component phases.

1.4.1. Emulsions

One of the colloidal types listed in Table 1.1 are emulsions. Emulsions are a colloid formed when two (generally) immiscible liquids are mixed forming a series of disrupted liquid droplets of one liquid spread throughout the other continuous liquid phase. These dispersions of two liquid phases are unstable, and the dispersed liquid droplets progressively come together due to van der Waals' forces resulting in bulk separation of the two liquid phases, particularly when they have different bulk densities. To combat this instability, emulsifiers are added to help stabilise the emulsion. There are a range of different general emulsions, with the key difference being the size of the dispersed droplets present in the

Table 1.1. Specific combinations of phases in colloidal systems and the resultant materials.

Continuous phase	Dispersed phase	Material type
Solid	Solid	Solid sol
Solid	Liquid	Gel
Solid	Gas	Solid foam
Liquid	Solid	Sol (suspension)
Liquid	Liquid	Emulsion
Liquid	Gas	Foam
Gas	Solid	Solid aerosol
Gas	Liquid	Liquid aerosol
Gas	Gas	N/A (Molecular mixture)

emulsion material. Macro-emulsions are the most common type of emulsions, and have droplets that are 1 µm to 100 µm in diameter [25]. Due to the size of macro-emulsion droplets, the emulsion material will appear opaque and generally white (provided the emulsion materials do not contain coloured components or dyes). This opaqueness and colouration is due to the scattering of the light passing through the material. The emulsions prepared and studied in this work are all macro-emulsions. Nano-emulsions are at the other end of the size scale with droplet diameters of 20 nm to 500 nm [25]. These are relatively uncommon currently outside of research settings; however they display significant promise for future applications. The smaller droplet size of these emulsions yields altered optical properties. Nano-emulsions will often tend towards being transparent. This is due to the droplet sizes being smaller than the wavelength of visible light, resulting in very little scattering.

Emulsions are a vitally important part of modern-life, with many industrial uses for these materials. One area in which emulsions are heavily used is food products. There are a number of food products that are either biologically-produced or artificially manufactured emulsions, which exhibit a range of properties. Some examples of biologically-produced emulsions are dairy products. Dairy products are a hugely important example of emulsions, which have a range of physical properties from soft-solid materials such as butter and cheese, to foams like whipped cream, or liquid cream and milk. The physical properties of each of these materials are determined by changes to the microstructure of these materials that originate from an emulsion.

In addition to the popularity of emulsions as food products, these materials have also

been used in a range of industrial uses such as insecticides, oil recovery, paints, and drilling fluids [26–29]. These materials are utilised in each of these cases for their unique ability to contain both lipophilic and aqueous components, giving the materials exploitable properties.

1.4.1.1. Emulsification

Emulsification is the process that involves the mixing of at least two liquid phases and results in the formation of an emulsion. As emulsions are generally comprised of immiscible liquids, this mixing is a thermodynamically unstable process, and requires the input of energy to form an emulsion. The energy input into the system results in the discontinuous phase breaking down into smaller droplets. The formation of these smaller droplets is in constant opposition to the merging of droplets which, if unopposed, will lead to complete phase separation. To reduce this complete phase separation, emulsifiers are used to stabilise the emulsion systems. A range of the common types of emulsifiers will be discussed in the next section (Section 1.4.1.2). The energy required to form these droplets can be added through a number of different methods. Some of the more common methods that relate to the work carried out in this thesis are are demonstrated below. Other methods have been detailed in previous works [30]:

- High-speed homogenisers (Fig. 1.2)

  High-speed homogenisers are simple, yet effective method for the preparation of coarse emulsion materials. A high-speed homogeniser utilises a rapidly spinning inner rotor in combination with a fixed stator to impart a shear force on to the liquid materials. The rotation of the rotor draws liquid into the centre, before it is passed centrifugally through the gaps in the homogeniser in a turbulent manner and then returned to the bulk liquid. High-speed homogenisers are one of the more routinely utilised methods for the formation of an emulsion due to their relatively simple design, simplicity of use, and ability to be scaled to process a range of volumes. One possible downside of a high-speed homogeniser is accessible droplet sizes. The droplet size is limited by the energy input by the rotor, and can be varied through alterations to the rotor speed (with practical upper limits), geometry, homogenisation time, and the viscosities of the liquids [11, 31].

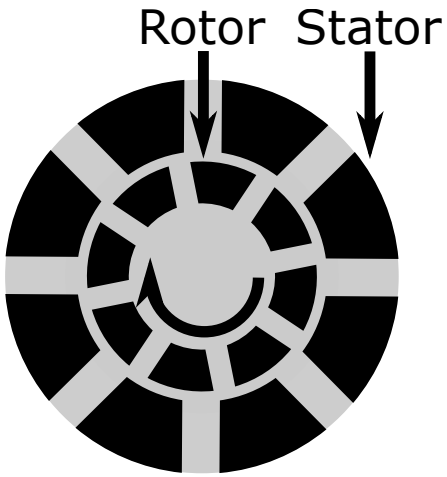

Fig. 1.2 Schematic diagram outlining the general structure of a high-speed rotor-stator homogeniser. The inner rotor spins resulting in the shearing of the liquids between the rotor and the stator.

- High-pressure homogenisers (Fig.1.3)

  High-pressure homogenisers are a method utilised to form emulsions with small emulsion droplets by passing a coarse (large droplet size [32]) emulsion through a small valve opening at high pressure as shown in the diagram of Fig. 1.3. This results in the coarse emulsion droplets impacting the valve piston and impact ring, splitting into smaller droplets as the material passes through the orifice. High-pressure homogenisers can form emulsions with very fine droplet sizes, however issues can be had with emulsions containing solid particulate materials, and the droplet size distribution can often be variable [33].

- Ultrasonic homogenisers (Fig. 1.4)

  Ultrasonic homogenisers act to break down emulsion droplets through high frequency vibrations as is outlined in Fig. 1.4. These vibrations result in cavitation occurring throughout the emulsion material, imparting a significant amount of energy onto the liquid, resulting in cavitation, turbulent flow, and high shear [34]. As there is no flow induced in the sample, the area affected by the shear is small. This limited shear area is one of the downsides of an ultrasonic homogeniser, which limits its use to small laboratory volume samples.

Each of these methods works by breaking up the dispersed phase liquid into smaller droplets forming an emulsion. The disruptive forces produced by the homogenisers drive the breakdown of these droplets. In constant opposition to this disruptive force are the

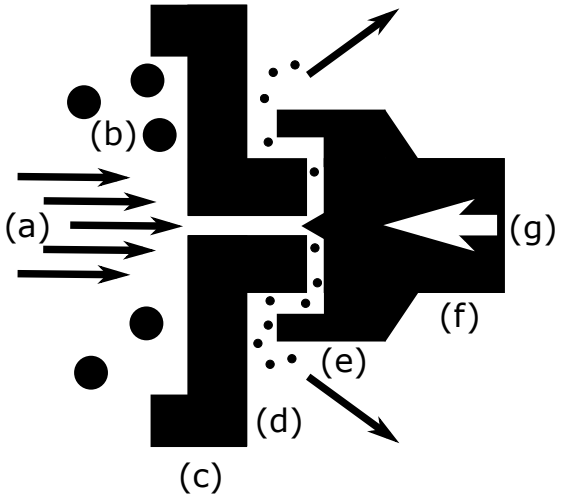

Fig. 1.3 Schematic diagram outlining the general structure of a high-pressure homogeniser. (a) High-pressure flow of a coarse emulsion. (b) Coarse emulsion before high-pressure homogenisation. (c) Entry valve. (d) Ejected fine emulsion droplets at low pressure. (e) Impact ring. (f) Valve piston. (g) High pressure.

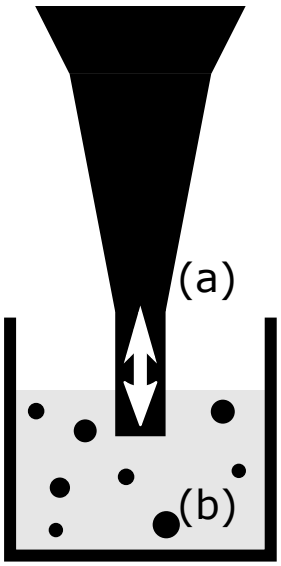

Fig. 1.4 Schematic diagram outlining the general structure of an ultrasonic homogeniser. (a) Ultrasonic probe with high frequency vibrating tip. (b) Homogenised emulsion.

interfacial forces, which drive the emulsion droplets to reduce the interfacial surface area. Left unchecked, the interfacial forces will lead to complete phase separation. This interfacial force is known as the Laplace pressure (ΔP_L) given by Equation 1.1 [35, 36]:

$$\Delta P_L = \frac{2\gamma}{a} \tag{1.1}$$

in which, γ is the surface tension between the two liquid phases, and a is the droplet radius. From this, it is clear that an increase in the droplet size reduces the pressure gradient between the two phases. The inverse of this, where the pressure is high at small a results in a large pressure gradient, driving the droplets towards coalescence.

This small selection of some of the more common homogenisation techniques gives an account of how emulsions can be formed in a laboratory setting, while outlining some of the differences between each of these techniques. The choice of method depends largely on the desired properties of the final emulsion, and the choices of the users, with each method having certain advantages and disadvantages. The tools used for the formation of emulsions throughout this work were high-speed rotor-stator homogenisers due to limitations with the other homogenisation techniques demonstrated above.

1.4.1.2. Emulsion types

As discussed in Section 1.4.1, emulsions are dispersions of one liquid phase within another liquid. Each of these liquids can be broadly categorised as either "water" or "oil". While the majority of emulsions encountered in the everyday world are oil-in-water emulsions, where there are oil droplets dispersed in a bulk water phase, other combinations of oil and water phases are possible. The range of single emulsions possible include oil-in-water (o/w) [37], water-in-oil (w/o) [38], water-in-water (w/w) [39], and oil-in-oil (o/o) [40]. Each of these combinations require specific combinations of oil phase, water phase, and emulsifiers, with the selection of these determining the type of emulsion prepared.

In addition to these "simple" emulsions where there are two liquid components, multiple emulsions can be formed. Multiple emulsions are emulsions that contain liquid droplets nested inside other droplets of an emulsion [41]. Multiple emulsions can be comprised of different combinations of either oil or water phases, with examples of water-in-oil-in-water (w/o/w) [42], oil-in-water-in-oil (o/w/o) [43], oil-in-oil-in-oil (o/o/o) [44], and water-in-water-in-water (w/w/w) [45] all appearing in the literature. The emulsions investigated in this work are all "simple" oil-in-water (o/w) emulsions.

1.4.1.3. Emulsion stability

Emulsions are unstable. Due to thermodynamics an emulsion system, given sufficient time, will breakdown and phase separate. External forces such as electrostatic, solvation, and gravitational forces influence this thermodynamic instability. That being said, it is possible to generate emulsions that are stable over finite time scales, due to kinetic stabilisation of the droplet interfaces. This kinetic stabilisation is carried out by emulsifiers, and aids in reducing possible contact between the two emulsion droplets. Limiting the contact between emulsion droplets reduces droplet coalescence, slowing the emulsions breakdown.

Droplets in an emulsion at rest have a number of forces acting upon them that will result in changes to the material over time. One of the main forces that will act on an emulsion is gravity. In an emulsion, gravity will drive the separation of component liquids by density, with the less dense liquid rising to the top of the emulsion. Another two of the forces that act on emulsion droplets are the attractive van der Waals force, and the repulsive electrostatic force. These forces may be significant between any two materials on the colloidal scale, and the summation will give a net interaction between the materials. The sum of these forces will result in the attraction or repulsion of pairwise interactions between the droplets present in the emulsion materials. There are a number of other forces that occur between droplets in an emulsion, such as depletion, and hydration forces, however these will not be considered in this thesis [23, 24, 46–48].

The breakdown processes that occur in emulsions can be broadly classified into four categories; flocculation [49], creaming/sedimentation [50, 51], coalescence [52–54], and Ostwald ripening [11, 55, 56] (Fig. 1.5). Each of these, along with some of the forces that give rise to these phenomena, and results are discussed here:

- Altering interactions

  Of the forces acting on emulsions, the attractive van der Waals, and repulsive electrostatic forces are the most directly related to the work presented here. These two forces occur between any two objects, and are affected by a number of factors. The repulsive interaction between two charged objects arises from the overlapping interactions of charges at the object surfaces. The materials that are used in this work are assumed to be spherical for ease of the calculations, as such the equations provided are for spherical objects.

  The repulsive interaction energy, $\phi_R(D)$, between two charged spheres is first shown in Equation 1.2 [23, 24, 48, 57],

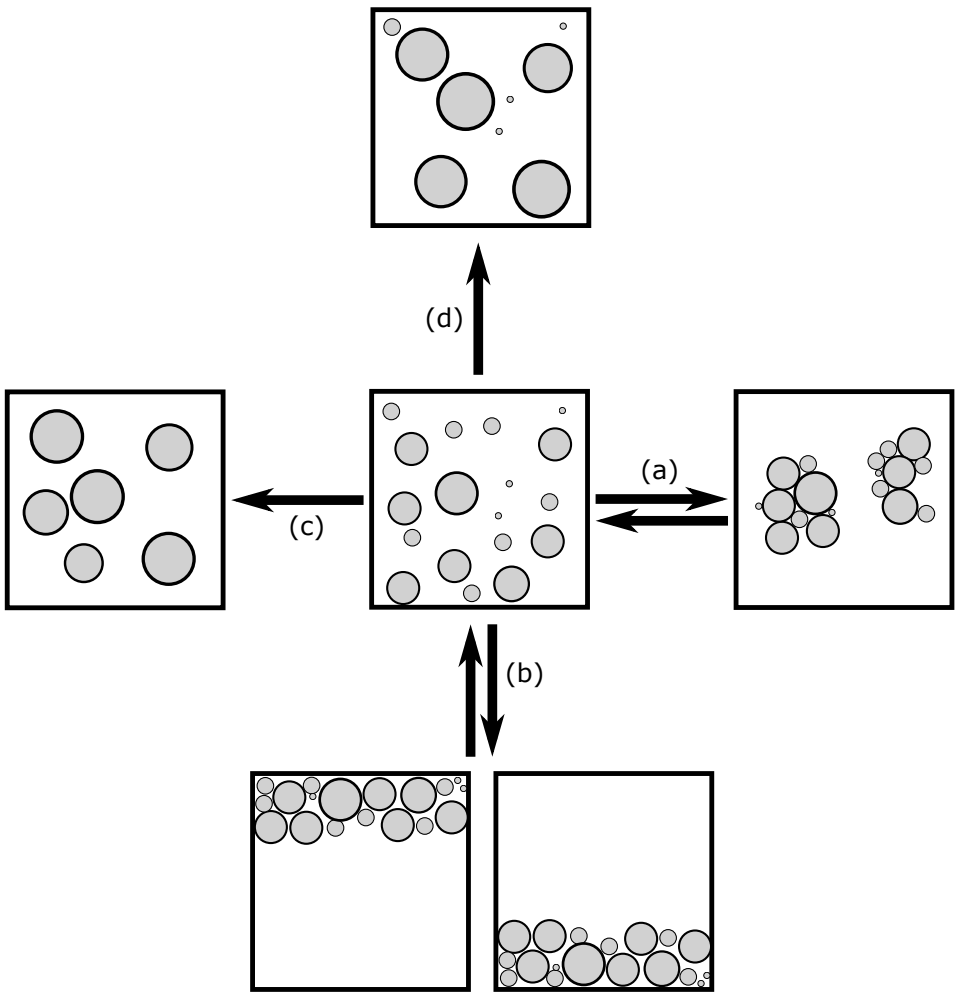

Fig. 1.5 The breakdown processes in emulsions. (a) Reversible flocculation. (b) Reversible creaming or sedimentation. (c) Coalescence. (d) Ostwald ripening.

$$\phi_R(D) = \frac{32\pi\varepsilon\varepsilon_0 a k_B^2 T^2 \gamma^2}{e^2 z^2} \exp(-\kappa D) \tag{1.2}$$

in which a wide range of variables and constants are demonstrated to alter the repulsive interaction energy. This includes ϵ, ϵ_0, and a which are the relative dielectric constant of the solvent, the dielectric constant of a vacuum, and the particle radius respectively. k_B, T, e, and z are the Boltzmann constant, absolute temperature, charge of an electron, and charge of the symmetrical co-electrolyte species, while D is the closest separation distance between the two spheres (the separation between centers of mass is $D+2a$). γ and κ are described in Equations 1.3 and 1.4 respectively.

$$\gamma = \frac{\exp(\frac{ze\varphi_d}{2k_B T}) - 1}{\exp(\frac{ze\varphi_d}{2k_B T}) + 1} \tag{1.3}$$

Equation 1.3 includes a term that accounts for the charge of the spheres (the potential energy at the Stern layer, the layer at which counterions are tightly bound which is outlined in Fig. 1.10), φ_d, which in this work is the measured zeta potential [57].

Equation 1.4 calculates the inverse Debye length for a particle suspended in a liquid with a monovalent salt concentration of c (in $\mathrm{mol\,L^{-1}}$), with R as the gas constant, and F as the Faraday constant. The Debye length is a measure of how far into a solution the electrostatic effect of a material will propagate.

$$\kappa^{-1} = \sqrt{\frac{\epsilon\epsilon_0 RT}{2 \times 10^3 F^2 c}} \tag{1.4}$$

These equations demonstrate how the charges on the surface of a pair of spherical objects can contribute the repulsive interaction energy between them. In addition to these repulsive interactions, pairs of spherical objects can also experience attractive van der Waals interactions. An attractive interaction occurs between two objects due to induced electrical interactions between two objects, and is very sensitive to the interaction distance. This attractive interaction, $\phi_A(D)$, is shown in Equation 1.5 [58],

$$\phi_A(D) = -\frac{H}{3}\left[\frac{a^2}{D(4a+D)} + \frac{a^2}{(2a+D)^2} + \frac{1}{2}\ln\left(1 - \frac{4a^2}{(2a+D)^2}\right)\right] \tag{1.5}$$

and is demonstrated to be heavily influenced by the separation distance between the two spheres, D, while also considering the Hamaker constant for the given materials, H. With both the attractive and repulsive forces between a pair of objects, it is relatively straightforward to determine the total interaction energy, $\phi_T(D)$, from the sum of these as provided in Equation 1.6,

$$\phi_T(D) = \phi_R(D) + \phi_A(D) \tag{1.6}$$

These interactions between the particles in a colloidal system or emulsion can give indications of the separation distance (at the secondary minimum of $\phi_T(D)$ provided the thermal energy of the system is low enough) of object pairs, and as such, allows predictions around the flocculation of a material to be made.

- Flocculation

  If the repulsive interactions between the droplets of an emulsion are limited, the droplets will be attracted together. If the energy barrier to coalescence is limited, then this attraction between the emulsion droplets results in the formation of aggregates of droplets, without immediately causing the droplets to change in size [49, 50, 59]. Droplets that have flocculated and formed aggregates or flocs are commonly able to separate from the floc with simple mixing, reverting to individual droplets. The properties and strength of the flocs formed are dependent on the droplet fraction and the attractive energy between droplets. If the droplet fraction is increased, the number of flocs or number of droplets in each floc will be larger, resulting in an increase in the structure present in the emulsion. In addition to this, increasing the attractive energy between the oil droplets will result in flocs, which are less likely to shed droplets, and will add more elasticity to an emulsions bulk structure. Flocculation will generally result in increases to the rate of creaming/sedimentation due to the size of the flocs increasing.

- Creaming/sedimentation

  As mentioned above, gravity is one of the forces that, unsurprisingly, acts on the components of an emulsion. When an emulsion is prepared with liquids that are not density matched, the more dense liquid will move downward, while the less dense liquid rises. This process is known as creaming if the droplets rise or sedimentation if the droplets fall. The typical example of this is less dense oil droplets

rising to the top of an oil-in-water emulsion. The rate of creaming is determined by a number of factors including the continuous phase viscosity, the difference in densities of the liquids, and any network formed between the emulsion droplets [60–62]. Creaming/sedimentation is a reversible process, with light mixing or agitation often re-suspending the droplets [51]. The creaming/sedimentation of an emulsion can be a detrimental process, due to the droplets coming into close contact, which can often allow the droplet liquids to contact, eventually resulting in complete phase separation.

- Coalescence

  Coalescence is the first irreversible emulsion destabilisation process discussed here. Coalescence is the combination of two droplets to form a single larger droplet, and occurs after creaming or flocculation due to the close contact of the droplets if the energy barrier preventing droplet merging is less than the thermal energy of the system. Coalescence is not a reversible process without the re-homogenisation of the material. When the droplets come into close contact the shape of the droplets may become distorted, leaving a flat contact zone between the drops [63]. Separating this contact zone of the two droplets is a thin liquid film of the continuous phase. If the attractive forces between the two droplets are dominant at the specific separation distance, the film will drain and the droplets will merge [11]. The inclusion of emulsifiers at the droplet surface will reduce the effect of coalescence by adding a steric barrier between the droplets. In the case of Pickering emulsions, the focus of this work, the energy barrier is physical in nature (Section 1.4.1.5). The rate of coalescence is dependent on a number of factors including the droplet size, the emulsifier loading, and the volume fraction of the system [64, 65].

- Ostwald ripening

  Ostwald ripening is an interesting process that can alter the size distribution of droplets in an emulsion, while leading to breakdown of the emulsion. Ostwald ripening involves the transfer of molecules from small droplets into larger droplets without direct contact between the two drops [56]. This occurs through diffusion of the generally sparingly soluble discontinuous phase molecules through the continuous phase between droplets due to the partial solubility of the discontinuous

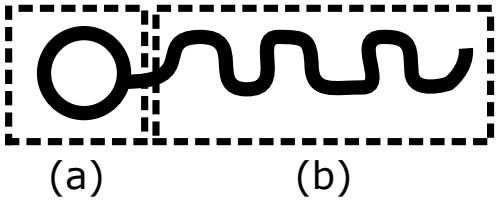

Fig. 1.6 General structure of a surfactant molecule. (a) Hydrophilic head group. (b) Hydrophobic tail. Diagram is not drawn to scale.

phase. The diffusion of these molecules is a result of the differences in curvature of the droplets, with the highly curved small droplets being less energetically favourable when compared to the less curved larger droplets [56]. Ostwald ripening is an irreversible destructive process for emulsions, and will result in the full breakdown of the material given sufficient time.

- Complete phase separation

  Emulsions by definition are phase separated as the two liquid phases are not solvated in each other. However, the term phase separation is often used in emulsion science to describe the breakdown of the emulsion droplet structure, which is also known as complete phase separation. Complete phase separation is the result of destructive processes that have been discussed. Complete phase separation occurs when all emulsion droplets have combined, leaving the two component liquids separated by a single continuous interface. References to phase separation throughout this thesis are referring to complete phase separation.

1.4.1.4. Surfactant stabilised systems

Surfactants have long been used to stabilise emulsions as emulsifiers due to their amphipathic structure. The structure of these molecules have a hydrophilic head group, while the tail of the surfactant is hydrophobic, as illustrated by a general structure in Fig. 1.6. This structure results in the surfactant being preferentially adsorbed onto the interface of the droplets of liquid in an emulsion as demonstrated in Fig. 1.7. This adsorbed layer of surfactants adds a barrier between the emulsion droplets, while also lowering the surface tension of the interface, reducing the coalescence occurring in an emulsion system.

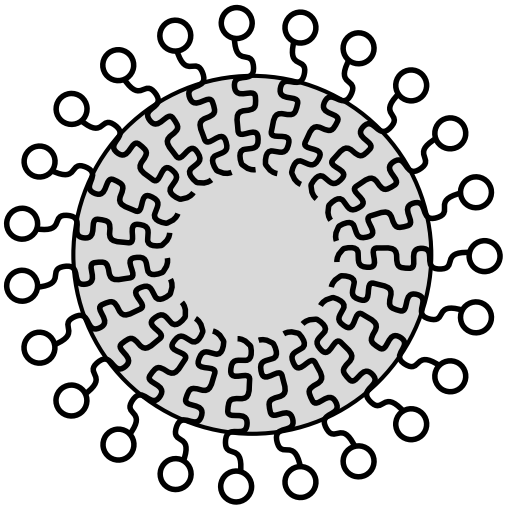

Fig. 1.7 General structure of an emulsion droplet coated with a surface layer of surfactant molecules. The grey circle represents an oil droplet, with the surfactant molecules surrounding the droplet. Diagram is not drawn to scale.

There are a number of different types of surfactants that can stabilise emulsions:

- Anionic: Negatively charged head group.
- Cationic: Positively charged head group.
- Non-ionic: Uncharged head group.
- Zwitterionic: Both positively and negatively charged head group.

The type of emulsion prepared depends not only on the volume percentages of each liquid phase, but also on the chosen type of emulsifier, and as such, care must often be taken when preparing surfactant stabilised emulsions.

1.4.1.5. Pickering stabilised systems

The stabilisation of emulsions is not only possible with surfactant molecules, but also with finely divided solid particles; these are termed Pickering emulsions. Pickering emulsions were first discussed in the literature over 100 years ago by Ramsden and Pickering, where they noticed solid particles coating liquid–liquid interfaces [66, 67]. Despite this long history, research into Pickering emulsions only received substantial attention in the late 1900s, with a vast number of different Pickering emulsifiers now being displayed from inorganic powders such as silica [52, 68–70], titania [71–73], and magnetic iron oxide [74], through to more complex man-made solids such as carbon nanotubes [75, 76], or metal-organic-frameworks [77]. In addition to these, a range of natural food-safe solids such as

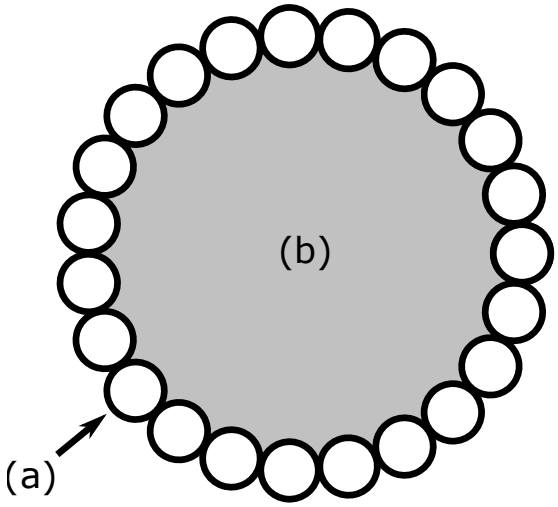

Fig. 1.8 General structure of a Pickering stabilised emulsion droplet. (a) Finely divided solid particles located at the droplet interface. (b) Discontinuous phase of the emulsion. Diagram is not drawn to scale.

soy and whey proteins [1–3], or starches [6, 7] have also been demonstrated to assist with the formation of Pickering emulsions [78].

The stabilisation of emulsion systems with Pickering emulsifiers is due to the irreversible adsorption of the solid particles to the interface between the liquids (Fig. 1.8) [78, 79]. For the particles to adsorb to the interface, they must be partially wettable by both component liquids, allowing the particles to sit between the two liquids. When adsorbed to the interface, the free energy of the interface is reduced due to the partial wettability of the particles and the minimisation of the total exposed liquid interfacial surface area, resulting in the trapping of the particles at this interface. The reduction in energy (ΔE) of the interface is given by Equation 1.7 [80, 81],

$$\Delta E = \pi a^2 \gamma_{ow} (1 +/- |\cos\theta_c|)^2 \tag{1.7}$$

where a is the radius of the particle, γ_{ow} is the interfacial tension, and θ_c is the contact angle of the particle with one of the liquids (conventionally the aqueous phase). When the contact angle is lower than 90° the equation employs a $-|\cos\theta_c|$ term, while the form is $+|\cos\theta_c|$ when the contact angles greater than 90°. The energy required to remove a 0.5 µm particle located at an interface ($\theta_c = 90°$) with an interfacial tension of $\approx$50 mN m^{-1} has been found to be $\approx 10 \times 10^6\, k_B T$, a significant barrier to overcome before a particle can be freed [81, 82].

The wettability of the particles is demonstrated through the contact angle of the solid particles and the liquid-liquid interfaces present in Pickering emulsions, as shown in Fig.

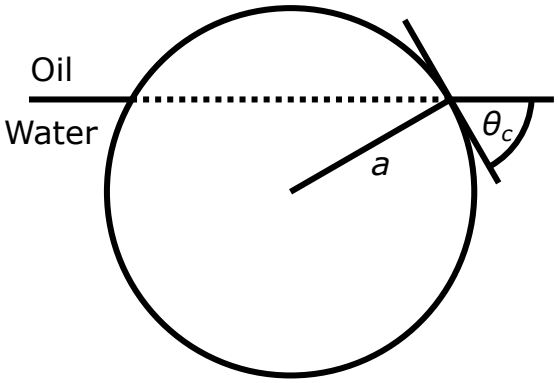

Fig. 1.9 Demonstration of the contact angle (θ_c) of a solid particle with radius a at an oil-water interface.

1.9. Contact angles for these colloidal particles are measured with respect to the aqueous phase, and as such are low when the particle is hydrophilic and preferentially wet by the aqueous phase, or large when the particle is hydrophobic and wet preferentially by the oil phase. The contact angle that is measured for a given particle and set of liquids will determine the type of emulsion that is formed. When the contact angle is less than 90°, the emulsion formed will typically be an oil-in-water emulsion. In contrast to this, when the contact angle is greater than 90°, the emulsion will typically be a water-in-oil emulsion [73, 83, 84]. This results in the particles locating predominantly in the continuous phase of the emulsion, on the outside curvature of the droplet, reducing steric interactions between the particles [85].

Another feature of the particles that can aid in the stabilisation of Pickering emulsions is the extent of flocculation of the nanoparticles. In order to effectively stabilise a Pickering emulsion the particles should be slightly flocculating. This slight flocculation is an indication that the electrostatic repulsive energy between the particles is limited, and that the particles will be able to close pack at the liquid-liquid interface [69].

In contrast to surfactant stabilised systems, where the surfactant molecules lower the interfacial tension, the effect that Pickering emulsifiers have is a more complicated topic. In specific cases the effective interfacial tension has been demonstrated to decrease at low particle loading. However, increasing the particle concentration results in an increase to the surface tension due to the capillary forces between the particles at high concentration [86]. Other workers concluded that the interfacial tension is not appreciably altered by the inclusion of solid particles at the interface [87].

As Pickering emulsifiers are by definition solid, the way in which they stabilise an emulsion system is through providing a physical barrier. When there are sufficient Pickering

emulsifiers added to a system, the surfaces of the droplets will be fully coated with solid material. This solid material limits the contact between neighbouring droplets of the discontinuous phase, and decreases the rate at which the thin film formed between the droplets can drain [88].

Along with the physical barrier afforded by the Pickering stabilisers, in some cases there can be an excess of particles throughout the continuous phase. This typically occurs of emulsions stabilised by fumed silica or clay particles. This excess of particles in some cases have been demonstrated to form either bridges between droplets, or a gel network throughout the continuous phase [89]. Each of these processes have effects on the structure of the emulsion material, including increasing the stability of the emulsion. Ganley and van Duijneveldt [90] investigated the rheological properties of a Pickering emulsion system with an excess of Pickering stabiliser across a range of salt concentrations. In this work they altered the rheological properties of hexadecane-in-water emulsions stabilised by montmorillonite particles by adding salts to the aqueous phase of the emulsion. This addition of salt was demonstrated to alter the strength of the gel network formed by the excess of Pickering stabiliser, and as such change the rheological properties of the emulsion. They found that the emulsion droplets in this system also interacted with the gel network formed, increasing the strength of the emulsion as the droplet concentration is increased. Ganley and van Duijneveldt highlighted the similarity between this behaviour and that of protein stabilised gels.

A previous study by Dickinson [91] compared the interactions between protein stabilised emulsion droplets and the gel networks that can be formed in the aqueous phase. In this work, Dickinson demonstrated that the protein stabilised emulsions can be either active, or inactive fillers in the gel network. An active filler was demonstrated to increase the strength of the emulsion as the droplet volume percentage is increased, compared to an inactive filler which decreases the strength of the emulsion with increases in the droplet volume percentage.

In addition to stabilising drops by forming a protective shell around the drops and by forming a gel-like network in the continuous phase, the solid particles used often carry a surface charge. Coating an emulsion droplet with these charged nanoparticles will result in a net charge on the emulsion drop. This leads to an electrostatic repulsion between neighbouring droplets, in a way similar to that of ionic surfactants [89].

As the surface charge of Pickering emulsifiers can often have significant impacts on the stability and structure of the emulsions they form, understanding the charging behaviour is

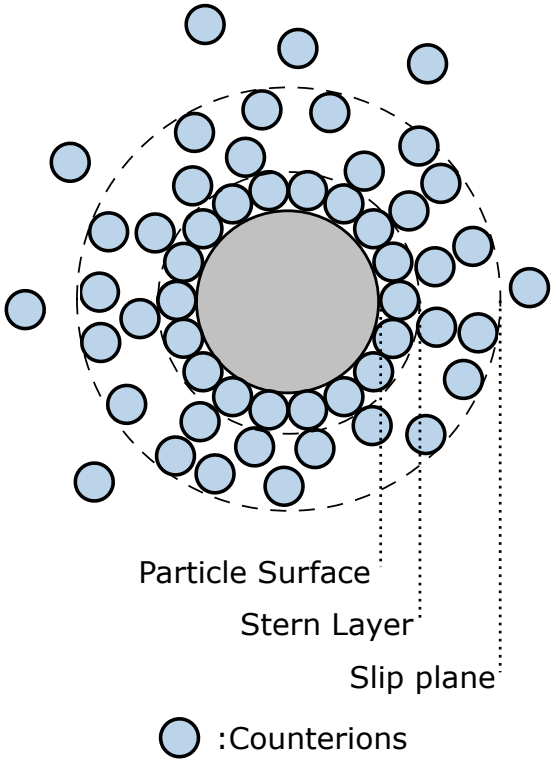

Fig. 1.10 A schematic example of the distribution of counterions surrounding a charged object. Grey circle is an object with a charged surface. Blue circles represent the corresponding counterions surrounding the object. The separation between the particle surface and the Stern layer is typically on the order of the ionic radii, while the slip plane separation is determined through the Debye length for the solution.

important. When a charged particle is in an aqueous environment, the local concentration of counterions will increase due to the electrostatic attraction, as shown in Fig. 1.10. The layer of counterions immediately surrounding the particle are known as the Stern layer. As the distance from the particle is increased, the counterions become less strongly attracted, and will slip away from the particle as it moves through the containing aqueous phase. The boundary that this begins at is the slip plane, and is the point at which the zeta potential is measured [92]. The zeta potential is a useful tool for understanding charging behaviour and stability of colloids. An increase in the magnitude of the zeta potential of dispersed particles in a colloid demonstrates an increase in the electrostatic repulsion between neighbouring colloidal particles, leading to a more stable system. The zeta potential of colloidal dispersions can be investigated by measuring the particle velocity with light scattering while an electric field is applied across the dispersion.

As the zeta potential of a particle is not measured at the particle surface, but rather at the slip plane, it is very sensitive to the addition of salt. Increasing the salt concentration of a particle dispersion will result in an increase in the concentration of counterions located

within the slip plane of the particle. This reduces the apparent zeta potential of the particle (Equation 1.4) [93].

1.4.1.6. Characteristic properties of emulsions

Emulsions demonstrate some interesting properties due to their unique composition and structure. One of these properties is the colouration of emulsions. An emulsion prepared with both transparent oil and water solutions will generally appear as an opaque white material. This colouration is due to the scattering of light by the emulsion droplets. While this effect is seen in a wide range of emulsions, it is not the case for all systems. If the emulsion droplets are less than ≈100 nm, the material will begin to become transparent. This is due to the droplets being smaller than the wavelength of visible light, limiting the multiple scattering that occurs. Light scattering will still occur from Rayleigh scattering in these systems [94].

Many of the properties of an emulsion system are related to the size of the droplets present in the system. It can be seen then that having knowledge of the size of these droplets is an important factor for understanding a given emulsion system. There are a range of methods that can be used to measure the size of colloidal particles such as the drops of an emulsion, including a number of microscopy techniques, dynamic light scattering, and laser diffraction [95, 96].

In addition to these properties, emulsion systems often have a significant structure formed between the droplets. This structure can result in an emulsion system that displays more solid-like viscoelastic behaviours [97]. Pickering emulsions also demonstrate this increased behaviour due to both the emulsion droplets present, and the excess stabiliser forming a network throughout the system [91, 98]. These network structures are best investigated through rheological techniques, and allow comparisons between the extent of network formation to be made, something that will be carried out in this work.

1.5. A brief history of rheology

Since the initial coining of the term "Rheology" by Forel over one hundred years ago, rheology has developed into a wide and varied field [99]. Broadly speaking, rheology is the study of deformation and flow of materials, with the name deriving from the Greek words "rheo" (to flow), and "logos" (science). The development of tools for understanding soft-materials has been a steady and ongoing process, with early interest largely surrounding understanding viscous fluids. Simple viscosimeters have been in use since the 1830s,

and were used to develop theories about the viscosity of fluid materials [100]. Significant developments with regards to understanding the flow curves and the yield stresses of materials were made in the early 1900s, with Bingham, Herschel, and Bulkley presenting models for understanding the yield stress of materials [101, 102]. The 1940s bought about the understanding that both solids and liquids can be described as viscoelastic in their behaviour, a significant step forward for research into soft-materials [103]. Sales of the first commercial rotational and oscillatory rheometers began in the 1950s, allowing easier access to understanding the viscoelastic properties of materials, with significant incremental developments to capabilities of rotational rheometers since then. Throughout the history of viscosimeters and rheometers, the properties of a wide range of material types, including emulsions, have been investigated in a number of different situations. The work presented here primarily looks to investigate the rheological properties of a range of emulsion systems, further demonstrating the use of rheology as a tool for understanding a materials properties and microstructure.

1.5.1. Definition of terms

There are a number of key terms that will be used to discuss the rheological properties of materials throughout this work. A number of these terms are defined here, along with associated relationships.

- Shear stress (τ)

  In a mechanical sense, stress is a fundamental quantity that is defined as an applied force divided by the area of its application. There are two main types of stress that can be applied to an object, a normal stress (where the applied force is perpendicular to the object it is acting on), and shear stress (where the force is applied parallel to the object). All stresses that are discussed in this work are shear stresses. The shear stress applied to a material is defined in Equation 1.8,

  $$\tau = \frac{F}{A} \tag{1.8}$$

  where τ is the shear stress in $\mathrm{N\,m^{-2}}$, F is the applied shear force in N, and A is the area that the shear is applied to in $\mathrm{m^2}$

- Shear strain (γ)

  The shear strain of a material is the result of a deformation or stretching of the material. When a shear is applied to a material, the material will be deformed in

one dimension, the ratio of this deformation and the height of the material is the shear strain. This is defined by Equation 1.9,

$$\gamma = \frac{\Delta x}{h} \tag{1.9}$$

where γ is the dimensionless shear strain, Δx is the deformation distance in m, and h is the separation distance between the shear boundaries in m.

- Shear rate ($\dot{\gamma}$)

  When a shear strain is applied over time the rate of movement is known as the shear rate, and is defined by Equation 1.10,

$$\dot{\gamma} = \frac{v}{h} \tag{1.10}$$

  in which $\dot{\gamma}$ is shear rate in s^{-1}, v is the velocity of the boundaries in $m\,s^{-1}$, and h is the separation distance of the two boundaries in m.

- Viscosity (η)

  The viscosity of a fluid material defines how resistant to flow said material is. The viscosity of a system is an intrinsic property caused by the internal frictional forces between the molecules (or microscopic components) which are moving at different rates throughout the system. The discussion of viscosity in this work is in reference to the shear viscosity, as defined by Equation 1.11,

$$\eta = \frac{\tau}{\dot{\gamma}} \tag{1.11}$$

  in which η is the shear viscosity of the material in Pa s, τ is the shear stress in Pa, and $\dot{\gamma}$ the corresponding shear rate in s^{-1}.

1.5.2. Rheometer types

Over the course of this history of rheology, a range of different types of rheometers have been utilised. In general, each type of rheometer allows the investigation into specific properties of a given material type. Some of the different types of rheometers available are discussed here:

- Viscosimeter

  Viscosimeters are a simple type of rheometer that allow the viscosity of liquid materials to be measured. There are two methods of function that a viscosimeter can have, the first involves a stationary liquid having a moving object pass through it, and the second has a moving liquid pass through a stationary object. As viscosimeters do not allow a varied flow rate, the data obtained from these is somewhat limited, with viscosity of the material being the primary measurement [104].

- Capillary viscosimeter

  The capillary viscosimeter investigates the flow of a liquid or soft-solid material through a pipe or capillary [105]. This viscosimeter functions by pushing the material through a capillary with known dimensions at a varied pressure in order to determine the flow profile of the material. Due to the simple design requirements of these tools, microfluidic variants have been developed, allowing the use of small volumes of liquid [106, 107].

- Rotational

  Rotational rheometers are perhaps the most versatile type of rheometer available, with applications ranging from solid materials all the way through to low viscosity liquids. Rotational rheometers were first commercially available in the 1950s, and have become routinely used since then. These rotational rheometers have the ability to not only evaluate the viscosity response of materials, but also the viscoelastic properties, allowing insight into the network structures present [103]. There are two control methods with rotational rheometers, controlled strain rate, and controlled shear stress. Each of these will be briefly discussed below.

  Rotational rheometers are the most commonly used rheology tools today, and is the tool that is used throughout the work presented here.

- Controlled shear stress

  Controlled shear stress rheometers apply a specific torque to the rheometer head, while the displacement or strain is measured. As torque is applied to the rheometer head, the measured material will apply a counter torque, reducing the resultant deflection that is measured by the rheometer. This resistant torque is corrected for by the instrument, allowing highly sensitive torque measurements.

- Controlled shear rate

  Controlled shear rate rheometers work through the application of a set shear rate, with the motor of the rheometer applying a given torque to reach this shear rate. As this shear rate is applied, the instrument measures the resultant position of the rheometer head, with a feedback loop adjusting the applied shear rate to compensate for the resistance of the material. This results in a "start-up" time, where the initial shear rate at the rheometer head may not be the desired value.

While both controlled shear stress and controlled shear rate rheometers are separate instruments that can target specific properties, modern electronic feedback devices have allowed the development of hybrid rheometers that are able to offer both stress and shear rate control with relative accuracy [108]. The rheometer used for the measurements carried out the work presented here is a hybrid design tool.

1.5.3. Geometry types

Modern rheometers allow the geometry that is in contact with the sample to be altered, allowing measurement of the properties of a range of materials. Some of the more common geometry types are briefly discussed below, with specific indications of the types of materials that are best measured by each.

- Parallel plates

  Of the geometries discussed here, the parallel plate geometry is the most simple. Consisting of two round parallel plates, this geometry is operated by rotating the top plate while the bottom plate is stationary (Fig. 1.11a). The gap height between the two plates can theoretically be set to any value, however it is recommended that the gap be set to about 10 times the diameter of the primary particles in the measured sample. The use of excessively large gap heights can lead to issues with inhomogeneous flow in certain situations [103].

  As the gap height is constant across the parallel plate geometry radius (R) while the circumferential velocity increases with the radius, the shear stress and shear rate experienced across the geometry are not constant [103]. This is a considerable disadvantage of parallel plate geometries, and must be accounted for by the instrument for appropriate measurements to take place. The shear stress ($\tau_{(r)}$) for a parallel plate geometry at a distance from the radial center, r, is given by Equation 1.12,

$$\tau_{(r)} = \frac{(2M)}{(\pi r^3)} = C_{ss}M \tag{1.12}$$

where M is the torque applied by the rheometer, and C_{ss} is the conversion factor that is determined by the distance from the radial center of the geometry. As mentioned previously, with a parallel plate geometry the shear rate experiences across the radius of the geometry is not uniform. This is due to the increase in circumferential velocity as distance from the radial center increases. The shear rate ($\dot{\gamma}_{(r)}$) at a distance from the radial center, r, can be found via Equation 1.13,

$$\dot{\gamma}_{(r)} = \frac{2\pi nr}{60h} = C_{sr}n \tag{1.13}$$

with n as the rotational speed, h as the gap height, and C_{sr} as a conversion factor dependent on both the gap height and distance from the radial center of the geometry.

There are two different methods for reporting the shear rate and shear stress; the maximum shear stress ($\tau_{(R)}$) and shear rate $\dot{\gamma}_{(R)}$ experienced (i.e. the outer edge of the geometry, or the geometry radius R), or the mean shear stress and shear rate. The mean shear stress τ_m and shear rate $\dot{\gamma}_m$ is shown by Equations 1.14 and 1.15.

$$\tau_m = \frac{2}{3}\tau_{(R)} \tag{1.14}$$

$$\dot{\gamma}_m = \frac{2}{3}\dot{\gamma}_{(R)} \tag{1.15}$$

The values reported by the rheometer are single values for both the shear stress and shear rate. The rheometer that is used throughout the work presented here reports the maximum values for both shear stress ($\tau_{(R)}$) and shear rate ($\dot{\gamma}_{(R)}$) as the measured or applied shear stress and shear rate values.

Despite these drawbacks the ease of use, and customisable gap height make parallel plate geometries a useful tool. Parallel plate geometries are employable for measurement of materials ranging from medium viscosity liquids to soft-solids such as gels. With low viscosity materials, the sample may flow out of the geometry, leading to gross errors in the measurements.

- Cone and plate

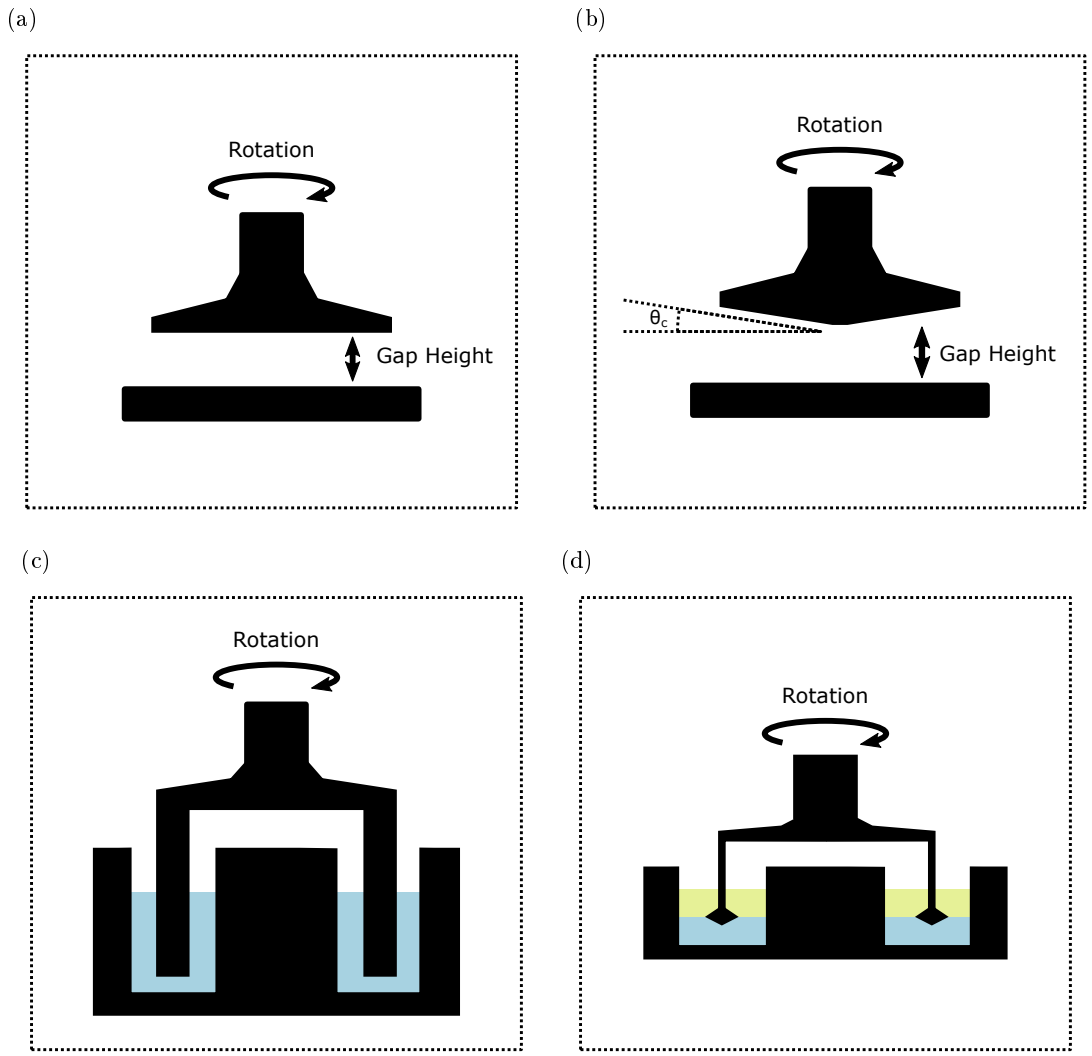

Fig. 1.11 2-D diagram demonstrating the general structure of a range of rheometer geometries. (a) Parallel plate. (b) Cone and plate. (c) Double-gap concentric cylinder. (d) Interfacial rheology setup.

A cone and plate geometry consists of a flat bottom plate with a low angle cone (or truncated cone) as the top plate (Fig. 1.11b). This results in the gap height increasing further from the centre of the geometry. This change removes the disadvantage of the parallel plate geometry, as the shear stress and rate across the geometry is constant [103]. The specific angle of the cone is related to the radius in order to correct for the inhomogeneous shear rate, and is commonly between 0.5° to 4° for 8 mm to 60 mm diameter cones. Cone and plate geometries can be used to measure similar materials to that of parallel plates, and suffer from the same potential issues related to sample run off with low viscosity materials.

- Concentric cylinders

  Concentric cylinder, or double-gap geometries differ greatly from the parallel plate and cone and plate geometries in their structure, with a large stationary cup into which the upper rotor is lowered. In the case of a double-gap geometry, the upper rotor is an inverted cup, while the lower stationary cup has a filled cylinder located in the middle with the sample in a small gap surrounding this (Fig. 1.11c). The double-gap measuring system results in a large contact surface between the rotor and the sample, leading to a much larger torque being required to drive the system [103]. This large surface area results in accurate measurements being possible on low-viscosity liquids that otherwise may not be possible, even on modern rheometers [109]. In order to compensate for the non-uniform shear across the sample, the gap between the two cylinders is kept as small as possible, resulting in a near-uniform shear field.

- Interfacial rheology

  The previous geometries discussed allow the bulk rheological properties of materials to be characterised. Interfacial rheology instead is concerned with the rheological properties of the interfaces between gas and liquid, or two liquids [110, 111]. To achieve this, an interfacial rheology setup is required, which uses a tool positioned carefully at the interface of the two materials (Fig. 1.11d). The measurements obtained from these interfacial measurements are not immediately comparable to the bulk rheological properties of a material, and must be treated as a separate property.

In the work reported in this thesis, the primary geometry used was a parallel plate. This was due to the ease of use, and controllable gap height. A double walled concentric cylinder

set-up was used to verify some low viscosity materials. However, the data for these are not presented.

1.5.4. Experiment types

1.5.4.1. Rotational rheology measurements

Rotational rheology measurements allow insight into the flow behaviours of a material across a range of shear rates. A rotational measurement involves the application of shear to a material while the resultant shear stress is measured. This is carried out by sequentially stepping through a range of shear rates and measuring the resultant stress at each. The flow behaviour of material provides insights into the structures present in the measured system.

Depending on the structure present in the measured system, there is a range of typical behaviours that the stress response can be demonstrated. The most simplistic behaviour is that demonstrated by a Newtonian fluid. A Newtonian fluid will display a linear stress response to an increase in the applied shear rate, demonstrating that there is no change in the microscopic structure of the fluid. Common examples of Newtonian fluids include molecular liquids and gases. As the stress response of Newtonian fluids does not change with variations in the shear rate, the viscosity of these fluids is also constant.

Non-Newtonian fluids do not display this linear response, instead the shear stress varies in a non-linear manner. There are two Non-Newtonian fluids that will be discussed in the work presented here, shear-thinning, and shear-thickening. As the name suggests, shear-thickening fluids increase in viscosity as a shear is applied. Shear-thickening fluids result from a "locking together" of the structural components of the material, resulting in an typical increase in the measured shear stress. Shear-thickening is likely to be apparent in colloidal systems with high particle concentrations or at high shear rates [112].

The viscosity of shear-thinning materials decreases as the applied shear rate is increased. This decrease is due to the disruption of structure, leading to a lowered measured viscosity [113, 114]. This behaviour is demonstrated as a flattening of the shear stress response while the shear rate is increased. Many soft-materials and fluids display shear-thinning behaviour, including most emulsions.

From the rotational rheology data there are a number of key parameters that can be used to characterise the material. These include the low shear (ideally zero shear) viscosity, and the yield stress:

- Low shear viscosity

  A number of models have been proposed to predict the low shear (zero shear) viscosity of colloidal suspensions [115–121]. The first of this selection of models proposed was the Einstein model. Initially published in 1906, this model gives a prediction of the viscosity (η_r) of a low volume fraction ($\leq$2 vol. %) dispersion of non-interacting hard spheres. The Einstein model is detailed in Equation 1.16.

$$\eta_r = \eta_c(1 + 2.5\phi) \tag{1.16}$$

  In which η_c is the viscosity of the continuous phase, and ϕ is the volume fraction of the dispersed phase.

  Since the proposal of the Einstein model, several groups of workers have made improvements. One such example of this is the Batchelor model [117–119]. Batchelor noted that while the Einstein model was sufficient with exceptionally low volume fraction dispersions, as the volume fraction was increased the model progressively could not account for observed behaviours. Outside of very dilute cases, the effect of Brownian motion (the effect where small particles are observed to migrate at random throughout a liquid due to energetic collisions with molecules in the system) [122] and hydrodynamic interactions become significant, and as such must be accounted for. This model is described by Equation 1.17.

$$\eta_r = \eta_c(1 + 2.5\phi + 6.2\phi^2) \tag{1.17}$$

  The Krieger-Dougherty model is a more complex model used for prediction of viscosity. This is a semi-empirical improvement on the Einstein model, which fits a curve asymptotically between both the intrinsic viscosity of the materials, and the maximum packing volume of random spheres ($\phi_p = 0.64$ [123]). This model is described by Equation 1.18.

$$\eta_r = \eta_c \left(1 - \frac{\phi}{\phi_p}\right)^{-2.5\phi_p} \tag{1.18}$$

- Yield stress

  The yield stress of a material is an often-debated concept, and many researchers have debated the value of each method for measuring the value (and indeed if the value exists at all) [124–131]. The static yield stress is the stress required to initiate flow of a material. This is a result of the internal forces of the material leading to structure, that must be disrupted before the material can flow. The dynamic yield stress can also be measured by decreasing the applied stress from a state in which the material is flowing, into an elastic solid-like state. There are often differences between the static and dynamic yield stresses measured for the system, a result of the structural changes that occur within the materials [132, 133]. Discussions of the yield stress throughout this work will be in reference to the static yield stress unless otherwise noted. The concept of the yield stress as it applies to Pickering emulsions will be discussed in more detail in Chapter 3.

  Throughout this work there are two relationships used to calculate a yield stress from the flow curves; the Bingham, and the Herschel-Bulkley equations. In the early 1900s, Bingham named concentrated materials that show rigidity at rest as "plastic materials" [102]. They noted that these plastic materials demonstrate a "yield value", which could be quantified from a flow curve through the fitting of a linear model, now known as the Bingham Model as described by Equation 1.19.

$$\tau = \tau_0 + k\dot{\gamma} \tag{1.19}$$

  Where τ is the measured shear stress, $\dot{\gamma}$ is the applied shear rate, k is the Bingham flow coefficient, and τ_0 is the yield stress. As this is a linear model, it is straightforward to fit to sections of a flow curve.

  Herschel and Bulkley made an improvement on the linear Bingham model, with the addition of an exponential factor known as the Herschel-Bulkley index (n) [101]. The Herschel-Bulkley model is described by Equation 1.20.

$$\tau = \tau_0 + k\dot{\gamma}^n \tag{1.20}$$

1.5.4.2. Oscillatory rheology experiments

The viscoelastic properties of a material can be probed through the application of an oscillatory strain, while the resulting stress is measured [103]. When the strain is applied in a sinusoidal manner, it is expected that the measured stress will be sinusoidal, but phase

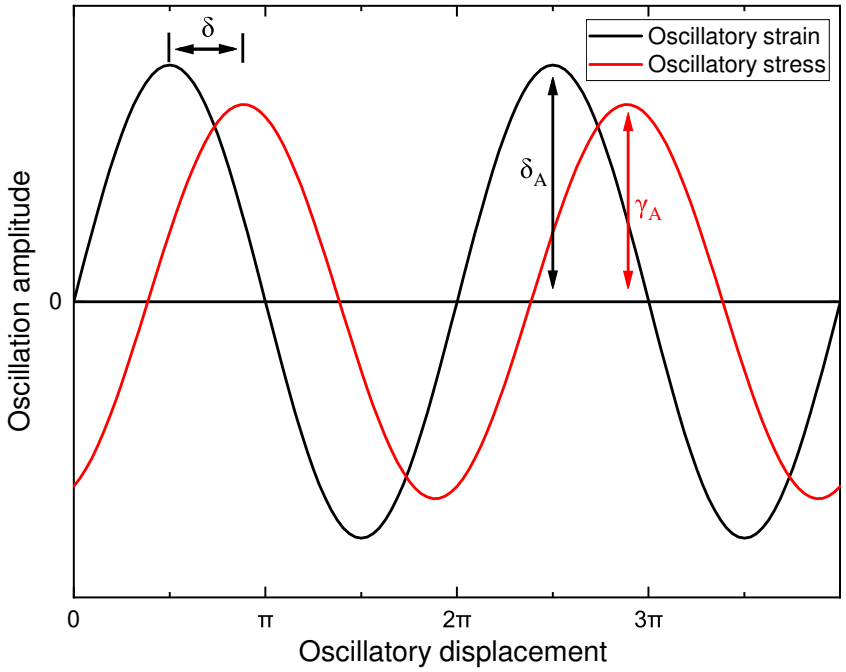

Fig. 1.12 Plot demonstrating the application of a sinusoidal strain and the resulting stress response of a viscoelastic material.

shifted to some degree. An example of this is demonstrated in Fig. 1.12, where the applied strain is shown to be phase shifted by δ.

When an oscillatory strain is applied to an ideal elastic material Hooke's law will apply, as give by Equation 1.21.

$$\tau_{(t)} = G^* \gamma_{(t)} \tag{1.21}$$

With $\tau_{(t)}$ being the time dependent stress, $\gamma_{(t)}$ the time dependent strain, and G^* the complex shear modulus. This demonstrates that with an ideal elastic material the applied strain is directly proportional to the measured stress, and that the phase shift between these two will therefore be 0 [103].

The other extreme case of material properties is a perfectly viscous fluid. When an oscillating strain is applied to an ideal viscous fluid the measured stress response will be perfectly out of phase ($\delta = \frac{\pi}{2}$) [134].

The emulsion materials investigated in this work are neither ideal elastic nor ideal viscous materials, and instead exhibit viscoelastic behaviour. Viscoelastic materials demonstrate both viscous and elastic properties simultaneously, leading to a stress response to an oscillating strain that has a phase shift between $\delta = 0$ and $\delta = \frac{\pi}{2}$. The complex shear modulus,

G^*, describes the stress to strain ratio in these viscoelastic cases, following Equation 1.22.

$$G^* = \frac{\tau_{(t)}}{\gamma_{(t)}} \tag{1.22}$$

With viscoelastic materials it is useful to separate the elastic and viscous components of G^* in order to gain more information about the material. The elastic component of G^* is the elastic storage modulus, G', and is a measure of the elastic energy stored by the material under load [103, 134]. This energy is returnable after the loading is removed, as it does not directly result in the breaking of any elastic structure present in a viscoelastic system. This elastic storage modulus is defined in Equation 1.23.

$$G' = G^* cos\ \delta \tag{1.23}$$

Which when combined with Equation 1.22 yields Equation 1.24.

$$G' = \frac{\tau_{(t)}}{\gamma_{(t)}} cos\ \delta \tag{1.24}$$

The viscous component of G^* is the viscous loss modulus, G'', which demonstrates the energy lost to viscous deformation of the material [103, 134]. The viscous loss modulus is defined in Equations 1.25 and 1.26.

$$G'' = G^* sin\ \delta \tag{1.25}$$

$$G'' = \frac{\tau_{(t)}}{\gamma_{(t)}} sin\ \delta \tag{1.26}$$

The ratio of G' and G'' define the bulk properties of material. When $G' > G''$ the material will predominately display solid-like characteristics, while when $G' < G''$ the properties of the material will be liquid-like. The ratio of G' and G'' are often found to vary with the applied strain and strain rate, with an example demonstrated in Fig. 1.13.

In addition to demonstrating a standard profile of G' and G'' response, Figure 1.13 outlines a number of key points in the data. The first of these is the linear viscoelastic region. This region is an area in which the G' and G'' are relatively unchanging with an increase in the applied strain, indicating that the material is behaving in an elastic manner and is storing the energy from the applied oscillations. The magnitude of G' and G'' throughout this region demonstrate the strength of the material, and can be utilised to compare materials. The second key point in this curve is the inflection point of G'. This

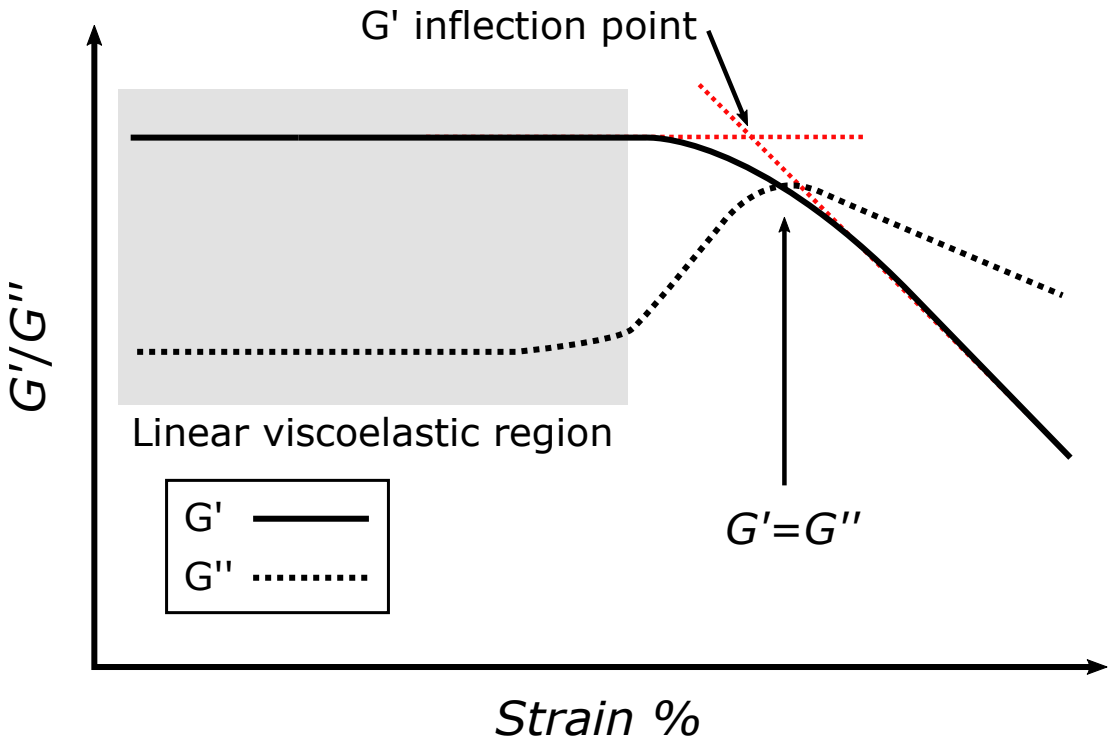

Fig. 1.13 Example of the G' and G'' response to an increase in the applied strain for a viscoelastic material. Key points include the linear viscoelastic region highlighted in light grey, the G' inflection point, and the intersection of G' and G''.

is the point at which the G' begins to decrease, indicating that the material is starting to viscously dissipate the applied energy instead of storing it elastically. This is one of the measures of the yield stress, and will be discussed in more depth in Chapter 3. The final key point, the intersection of G' and G'', is another measure of the yield stress, and is the point at which the viscous loss modulus becomes the dominate feature of the data. This again will be discussed in more detail in Chapter 3.

1.5.4.3. Creep and creep recovery rheology experiments

Creep and creep recovery experiments can be an accurate, although time consuming, method for measuring the yield stress of a viscoelastic material [135]. A creep experiment involves monitoring the strain of the sample while a given stress is applied for a time period before releasing the stress for the recovery phase. The resultant strain profile demonstrates the elastic or viscous nature of the material. The yield stress of a material can be measured by repeating the creep and creep recovery experiments over a range of applied stresses. Comparing the strain profiles of each repeated measurement allows the stress at which the material changes from liquid-like to solid-like behaviour. An example of the the typical strain response for a solid-like elastic material, and a liquid-like viscous

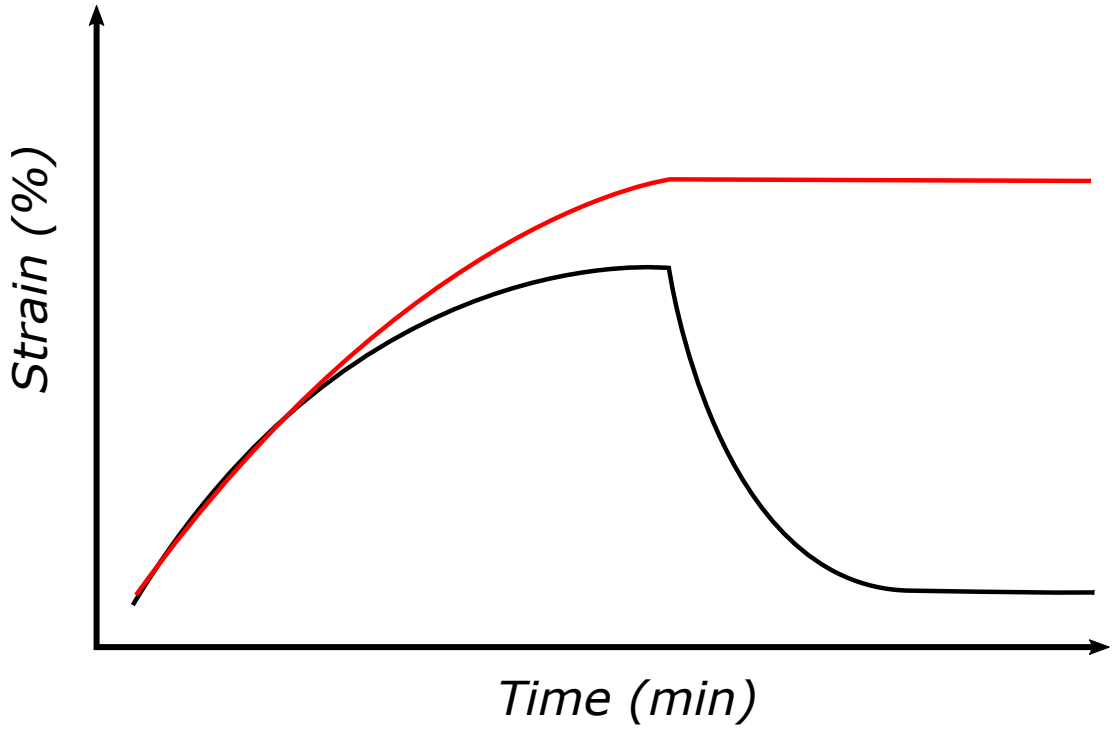

Fig. 1.14 Example strain response of a creep and creep recovery rheology experiment at a stress below (black) and above (red) the yield stress of the material.

material are demonstrated in Fig. 1.14. If the applied stress is below the yield stress of the material, the measured strain will increase to an equilibrium value (given sufficient time) during the creep phase. As the applied stress is removed in the creep recovery phase the measured strain decreases towards an equilibrium value as the elastic solid-like material recovers back to its original state. When the applied stress is above the yield stress over the material the measured stress will continue to increase during the creep phase. As the applied stress is removed in the creep recovery phase, the strain will not return to the original state due to the energy from the applied stress being viscously dissipated.

In order to measure the yield stress of a material utilising creep and creep recovery experiments requires the step-wise repetition of the experiment with slight changes to the applied stress. Stepping through a range of applied stresses allows the point at which the material transitions from solid-like to liquid-like behaviour to be identified. This is often a time and sample consuming exercise due to the number of individual experiments required to be carried out in order to accurately measure a yield stress. Theoretically, it would be expected that the strain responses would increase with an increase in the applied stress. Practically this is not always observed to occur, with repeats of an applied stress showing a difference in the measured strains.

1.5.5. Emulsion rheology

One of the most interesting qualities that emulsions possess is the difference in flow and deformation behaviour displayed when compared to that of their constituent materials. Additionally, in use many of the emulsions are exposed to a range of shear regimes throughout their life cycle, and as such understanding their rheological responses is an important task for their design and manufacture. A range of the rheological properties that emulsions can demonstrate have been studied previously, and a number of key features and concepts have arisen.

A review of the rheology of emulsions in the early 1990s by Barnes [97] recognised that there were three basic parameters that may be utilised to determine the rheological response of an emulsion:

1. The composition and viscosity of the continuous phase.
2. The droplet properties including the size, viscosity, concentration, and deformability.
3. Any interactions between the emulsion droplets.

Throughout that review, Barnes outlined how each of these parameters altered the rheology of the emulsions. Each of these three effects will be utilised in this work to alter the bulk rheological properties of a range of emulsion materials.

Later in the 1990s a number of other reviews of the rheology of emulsions were published, with each highlighting a specific area of research [136–138]. One area that Lequeux [136] covered was concentrated emulsion systems, where the droplets are compressed into solid-like materials. That work outlined the existence of droplet networks within an emulsion system, with discussions around how these complex systems display yield stress and non-linear viscoelastic properties. These workers pointed to previous studies that had investigated the break-down of the complex jammed-droplet networks as flow is induced in a non-homogeneous manner across the emulsion sample, while also identifying an area that could be better understood. These break-down processes are a phenomena that is still of interest today, and is an area that was investigated in this work.

The rheology of emulsions with flocculated droplets was discussed in detail by Dickinson [137]. A number of different methods that can induce flocculation were covered in this review, including depletion interactions, electrostatic interactions between protein coated droplets, and cross-linked or bridged droplets. Dickinson discussed the origins of each of these flocculation processes, and briefly covered the rheological properties of each process. It was noted that the rheology of each of these flocculated droplet systems were different,

with cross-linked droplets displaying gel-like behaviour with their almost "unbreakable" bonds between the droplets. Depletion interactions were described as reversible weak gels, that could easily be disrupted by shear or dilution. Protein coated droplets proved to be one of the more varied emulsion systems, with the rheological strength of the systems being controllable through additions to the continuous phase of the system. This control of droplet network and rheological properties is a key target for this thesis, and will be demonstrated in Chapters 4 and 5.

The creation and use of monodisperse emulsions at a range of volume percentages was covered in depth by Mason [138]. Of relevance to the work presented in this thesis was the rheology of dilute emulsion systems. It was noted that these dilute emulsion systems with attractive interactions between the droplets are able to display interesting flow behaviour despite sparse concentration of droplets in the emulsion systems. In general, the emulsions presented in this thesis have low droplet concentrations (20 vol. % to 50 vol. %), and will be utilised to understand the attractive networks that can be formed between emulsion droplets.

More recently Derkach [139] and Pal [140] independently presented reviews covering the rheology of emulsions ranging from dilute cases, through to highly concentrated systems. These reviews each covered a wide array of the rheological properties of emulsions. Derkach presented a wide range of works carried out on concentrated emulsions in which viscoelastic properties are displayed [139]. Concentrated emulsions systems are defined as a system where the droplet volume fraction exceeds that of random close packing for spheres. This results in systems where the emulsion droplets become deformed and pack together into a network throughout the material. Due to this close packing, there is significant elastic potential in the droplet interfaces, which have been shown to display an interesting range of viscoelastic properties. These viscoelastic properties have been measured through the use of oscillatory rheology. The use of these techniques allows the disruption of the elastic network to be understood and quantified. Understanding these disruption effects is an important characterisation method for emulsion systems, and can allow better control over these important soft-materials.

One area of particular interest in the review presented by Pal was a summary of the rheology carried out on the effect of excess additives [140]. This summary discussed the process that can occur with emulsion additives, such as surfactants, polymers, and colloidal particles. It was noted that these additives can effect the rheology of the system in two ways; by altering the rheology of the continuous phase, or by inducing flocculation between

the oil droplets. The effect of excess colloidal particles were shown to depend on the size of the colloidal particles added. When the particles were significantly larger than the emulsion droplets, no flocculation was demonstrated to occur. However, the viscosity of the continuous phase was altered by this addition. When the added particles were significantly smaller than the droplets (for example Pickering emulsifiers), the excess of particles have been shown to develop a network throughout the continuous phase, greatly altering the rheology of the emulsion. This is of particular interest to the work carried out in this thesis, and will be expanded upon throughout this work.

1.5.6. Pickering emulsion rheology

As briefly covered in the review presented by Pal [140], the inclusion of excess Pickering stabilisers can have a significant effect on the rheology of the bulk emulsion. The buildup of a network of these excess particles is covered in a review of Pickering emulsions by Chevalier and Bolzinger [89], in which the formation, stability, and rheology of the Pickering emulsions are discussed. In this review Chevalier and Bolzinger [89] touch on the electrostatic interactions between Pickering emulsion droplets, and how the addition of salt can alter these interactions. It was noted that the addition of electrolytes weakens the electrostatic repulsion between the silica particles that have commonly been used to stabilise Pickering emulsions. The weakening of the repulsive interactions leads to the formation of aggregates, and an increase in the viscosity and elastic strength of an emulsion system. This increase in elasticity results in the transformation of these emulsions from fluid-like materials, to materials that display solid-like behaviour with a measurable yield stress. Control of the interactions between the droplets of a Pickering emulsion presents a unique opportunity to design and create emulsion products with both desired rheological, and stability properties, and is an area that was investigated throughout the work presented in this thesis.

1.5.7. Rheology of emulsions with tuneable interactions

Rheology is a useful tool for understanding the structures that are present within an emulsion system. This has been demonstrated through the extensive work carried out on the rheology of emulsion systems [97, 138, 139]. Recently, a number of groups have begun to investigate emulsions with altered interactions between the droplets [8–10, 141, 142]. These groups have investigated a range of both Pickering and surfactant stabilised emulsions at high volume percentages where the interactions between the emulsion droplets were altered

from attractive to repulsive.

Becu et al. [141] investigated the rheology and ultrasonic velocimetry of a range of sodium dodecyl sulphate (SDS) stabilised high volume percent emulsions. The interactions between the emulsions were altered through altering the concentration of SDS micelles in the continuous phase, altering the depletion forces between the emulsion droplets. Increasing the concentration of SDS increases the depletion forces, and yields a net attractive force between the oil droplets. Becu et al. investigated the rheology of each of these emulsions and increased strength of the attractive emulsion. This was shown by the increase in the measured yield stress of the attractive emulsion system. Interestingly, the attractive emulsion demonstrated inhomogeneous flow, possibly indicating a non-standard yielding behaviour. While this behaviour does demonstrate novel yielding behaviour, these systems are high volume percentage, with close packing between the emulsion droplets, leading to an increase in the interactions between the emulsion droplets.

Datta et al. [142] investigated two different high volume percentage emulsion systems (SDS stabilised and nonionic polymer stabilised) with attractive and repulsive interactions between the oil droplets in each emulsion system. With each of these emulsion systems, the bulk oscillatory rheology was investigated and differences resulting from the changes in inter-droplet interactions were shown. The differences between the attractive and repulsive emulsions were best demonstrated by the G' and G'' response to alterations in the applied strain. At high volume percentages (above random close packing), the repulsive emulsions demonstrate a single peak in the variation of G'' with γ. This is attributed to a single-step yielding event due to the disruption of the droplet cages surrounding each droplet. When the volume percentage of these repulsive emulsions decreases below the random close packing percentage, the distinctive yielding event is not seen, showing the lack of cohesive network between the repulsive emulsion droplets. Comparing these repulsive emulsions with the attractive systems presented by Datta et al., some clear differences are found. Below the random close packing percentage, the attractive emulsions system show single broad yielding events, indicating a network formed between the emulsion droplets at low strain percentages. Above the random close packing percentage, the attractive emulsion systems demonstrated two distinct yield events. These two yielding events were described as being due to two different processes, a network break-up (similar to that in the lower volume percentage attractive emulsions), and a droplet cage breaking event. This work demonstrates that multiple yield events can occur in emulsion systems.

In addition to these two surfactant stabilised emulsion systems, recent work with Pick-

ering emulsion systems has investigated the alterations of inter-particle interactions. A study by Katepalli et al. [8] has investigated both spherical and fumed silica nanoparticle coated emulsion droplets at 50 vol. %, with the interactions between the Pickering emulsions droplets being altered through the addition of NaCl to the silica dispersion prior to emulsion formation. The average drop sizes of the attractive emulsions stabilised by fumed silica was $22 \pm 16\,\mu m$ while the average drop size of the repulsive emulsion was $27 \pm 18\,\mu m$. Katepalli's work primarily utilised oscillatory rheology to make comparisons between their attractive and repulsive emulsion systems. The G' and G'' response to alterations in the applied strain of the attractive and repulsive fumed silica emulsion systems were demonstrated to be markedly different, with the repulsive fumed silica emulsion demonstrating a linear viscoelastic region which was roughly one order of magnitude lower than that of the attractive system. In addition to the difference in magnitude, the yielding profile of each system was demonstrated to be distinct. The attractive fumed silica emulsion system demonstrated a single very broad yielding event, suggesting there were multiple yielding processes occurring at very similar strain percentages. It is proposed here that the multiple processes are likely to be similar to those seen in the results presented by Datta et al. [142], where there is a network breaking, followed by separate droplet cage-breaking events. The response of G' and G'' to a varied strain for the repulsive fumed silica emulsion system investigated by Katepalli appears to decrease with two distinct inflection points, similar to the results seen by Datta et. al. albeit in a much less distinct manner. This result with the repulsive emulsion system indicates that a residual network structure between the fumed silica coated droplets remains, despite the low salt concentration.

Each of these studies by the previous workers has demonstrated how rheology can be used to understand the structure present in emulsion systems. The distinct events that appear in the rheological data have been attributed to significant structural changes that occur when the interactions between the emulsion droplets are altered. The work presented in this thesis aims to add to our understanding of the influence of inter-particle interactions on the rheology of Pickering emulsions and, in particular, their yielding behaviour. Lower volume percentage emulsions were studied to investigate the interactions between the flocculated drop microstructures and the gel networks that can be formed by particles. Two types of particle stabilisers were studies, a fumed silica which forms networks in the continuous phase, and a titania which does not.

1.6. Research questions

Given the background information presented in this chapter, there were three main research areas which would be investigated throughout the work in this thesis.

1. How does the yielding behaviour of Pickering emulsions vary with measurement technique? Are any differences between measurement techniques maintained across a wide range of oil volume percentage? Is there a "best" technique to measure the yield stress in Pickering emulsions?

2. Are the rheological properties in low volume percentage silica-stabilised Pickering emulsions controllable by altering the Debye length through screening of the surface charge of the silica nanoparticles?

3. Are any changes in the rheological properties exclusive to Pickering emulsions which have oil droplets that interact with networks formed by excess stabiliser? Or can these properties be observed in Pickering emulsions with oil droplets which do not interact with an excess particle network? Can interactions between the droplets of such an emulsion be controlled through alterations to the surface charge of nanoparticles?

1.7. Scope of thesis

The previous studies summarised in this chapter have outlined the range of properties that Pickering emulsions have, as well as some of the techniques that can be used to prepare and study them. It was noted in Section 1.5.7 that it is possible to tune the interactions between emulsions with both surfactant, and Pickering stabilisers, changing the bulk properties of these systems. The work presented in this thesis sets out the development of sets of stable oil-in-water Pickering emulsions which, with alterations to the aqueous phase, demonstrate a range of bulk physical properties. These physical properties were characterised using rheological and microscopic techniques, which allows the droplet and particle network structures present in these emulsions to be understood.

1.8. Thesis layout

This work is presented in six chapters which cover:

- This chapter (Chapter 1) identifies the aims for this work and outlines the literature surrounding Pickering emulsions and the use of rheology to study such systems, while

also defining the scope of this thesis.

- Chapter 2 outlines the experimental techniques undertaken throughout this work including the standard experimental parameters for the techniques used.

- Chapter 3 addresses the first research question. It compares the interpretation of the results from different methods of measuring the yield stress silica particle-stabilised emulsions.

- Chapter 4 further explores the multiple yielding phenomena seen in certain situations of Chapter 3. This was carried out by systematically varying the amount of salt in the aqueous phase, screening the interactions (reducing the Debye length) between a set of silica nanoparticle stabilised Pickering emulsions.

- Chapter 5 reports the results from the first study of the role of interparticle interactions on the rheology of titania-stabilised emulsions. The titania particles were ellipsoidal in shape and did not appear to form a network of interlocked particles in the continuous phase. The interactions between the titania particles were manipulated through changes to the pH of the aqueous phase, resulting in changes in the surface charging behaviour of the particles.

- Chapter 6 summarises the key results and conclusions presented throughout this work, as well as making some comparisons between the results found across each previous chapter, before finally outlining some areas in which this research could be continued into the future.

2 | Experimental Methods

2.1. Preparation of materials

The oils used in the preparation of each emulsion in this work were isopropyl myristate (>99 %, Sigma Aldrich, St. Louis, USA.) and dodecane (>99 %, Sigma Aldrich, St. Louis, Missouri, USA.). They were both passed through neutral alumina columns (neutral activated aluminium oxide, Sigma Aldrich, St. Louis, Missouri, USA.) to remove polar impurities [40]. The oils used in this thesis are presumed to be inert, uncharged, and indifferent to the aqueous phases used.

The aqueous phase used in each emulsion was prepared from Milli-Q water (Barnstead™ Nanopure™, Thermo Fisher Scientific, Waltham, Massachusetts, USA), the ionic strength or pH which was altered with either NaCl (AR grade, Fisher Scientific, Hampton, USA), or NaCl and NaOH (AR grade, Fisher Scientific, Hampton, New Hampshire, USA) depending on the experiment being carried out. NaCl and NaOH were prepared as stock solutions, and then diluted at the point of preparation for each emulsion. NaCl was assumed to be an inert and indifferent electrolyte.

The emulsions reported for Chapters 3 and 4 were prepared using silica nanoparticles as the stabiliser. The silica used in these chapters was a synthetic hydrophilic amorphous fumed silica, (HDK® N20) with a primary particle size of 5 nm to 50 nm, and aggregate sizes of 100 nm to 500 nm (Wacker Chemie AG, Munich, Germany). In Chapter 3 the silica was used directly as received. For Chapter 4, the silica was heated in an oven ($T \approx 150\,^{\circ}\mathrm{C}$) for at least overnight. In Chapter 5 the stabiliser employed was a synthetic titanium dioxide nanoparticle with a coating of aluminium oxide and simethicone (2.5 wt. %) (Eusolex® T-2000, Merck, Kenilworth, New Jersey, USA.). The titania nanoparticles were ellipsoidal with a primary particle size of 20 nm × 100 nm. This titania was deployed by preparing a stock dispersion (1 wt. %) in a NaCl solution ($10^{-4}\,\mathrm{mol\,L^{-1}}$), which was then diluted to the final concentrations at the point of emulsion preparation. The titania nanoparticles were imaged using both transmission electron microscopy (TEM), and scanning electron

microscopy (SEM). These methods were both carried out by drying small droplets of suspensions of the nanoparticles onto the appropriate stubs before imaging. TEM and SEM imaging was carried out at the Manawatu Microscopy Imaging Centre by Niki Minards using a FEI Tecnai G2 Biotwin Transmission Electron Microscope (TEM), and FEI Quanta 200 Environmental Scanning Electron Microscope (SEM).

Two fluorescent dyes were used for confocal microscopy. Nile Red (Sigma Aldrich, St. Louis, Missouri, USA.) was used as an oleophilic dye in the oil phase of the emulsions, while Nile Blue (Sigma Aldrich, St. Louis, Missouri, USA.) was used as a charged hydrophilic dye to stain the stabilisers used in each emulsion. The dyes were deployed from pre-prepared stock solutions (dye in the appropriate oil, or aqueous mixtures $\approx 9 \times 10^{-4}$ M).

2.2. Measurement of zeta potential

The zeta potential is the electric potential of a nanoparticle at the slip plane, and can be used to measure and predict the interactions between colloidal particles. In this work, the nanoparticles that were used to stabilise the emulsions were fumed silica (Chapters 3 and 4) and titania (Chapter 5). Each of these nanoparticulate materials have interactions with neighbouring nanoparticles, which can be modified through changes to the aqueous continuous phase that the particles are dispersed in. In order to relate the changes in the interactions to changes in the aqueous phase, such as ionic concentration or pH, the zeta potential of these materials was quantified. The zeta potential is not a directly measurable property of a colloidal material. Instead, the electrophoretic mobility (U_E) of the colloidal particles are measured, which is the converted to the zeta potential (ζ) through the Henry equation (Equation 2.1 [143]),

$$U_E = \frac{2\epsilon\zeta f(\kappa a)}{3\eta} \tag{2.1}$$

where ϵ is the dielectric constant, η is the zero-shear viscosity of the continuous phase, $f(\kappa a)$ is the Henry function which is comprised of κ, the Debye length, a, the particle radius, and is shown in Equation 2.2 [143],

$$f(\kappa a) = 1 + \frac{1}{16}(\kappa a)^2 - \frac{5}{48}(\kappa a)^3 - \frac{1}{8}(\kappa a)^4 \times \left[\frac{1}{12}(1-\kappa a) - \left(1 - \frac{1}{12}(\kappa a)^2\right) e^{\kappa a} E_1(\kappa a)\right] \tag{2.2}$$

with $E_1(\kappa a)$ as the exponential integral of order one.

The electrophoretic mobility of the colloid is measured through the application of a oscillating electric field, with the corresponding velocity of the colloidal particles measured by laser Doppler velocimetry (LDV) [144].

Zeta potential measurements carried out in this work using a Malvern Zetasizer Nano ZS90 instrument (Malvern Instruments Ltd., Malvern, Worcestershire, UK). This instrument employs a combination of LDV and phase angle analysis light scattering (M3-PALS) techniques to give the surface charge of colloidal particles. Zeta potential measurements carried out in this work were always performed on nanoparticle dispersions alone rather than in the final emulsion mixtures. The measurements were made using approximately 1 mL of dispersion which was injected into a folded capillary cell (DTS1070, Malvern Instruments Ltd., Malvern, Worcestershire, UK.) equipped with a gold-plated beryllium/copper electrode. Any residual air bubbles were removed before the measurements. Measurements were carried out at 25 °C with at least three results measured per single loaded sample, each comprised of up to 100 measurements. This measurement was repeated multiple times for each dispersion, and the results of these are presented as a mean and standard deviation as described in each chapter.

2.3. Preparation of emulsions

Emulsions prepared for this work were prepared in the order described in each chapter, but in general, involved the addition of the stabiliser to a 50 mL centrifuge vial before the aqueous and oil phases were added. Once the appropriate volumes of materials were added, the sample was homogenised with either a Miccra D-9 high-speed homogeniser (Chapter 4) (Miccra GmbH, Heitersheim, Germany), or a Fisher Scientific PowerGen 125 high-speed homogeniser (Chapters 3 and 5) (Fisher Scientific International, Hampton, USA.) for two minutes. The Miccra D-9 high-speed homogeniser rotor was operated at 39 000 min^{-1}, while the Fisher Scientific PowerGen 125 high-speed homogeniser rotor was set at 30 000 min^{-1}. During the homogenisation of the samples, the homogeniser head was moved within the 50 mL centrifuge tube to incorporate all of the material present in the mixture. This method was used to prepare all stock emulsions. This method was assumed to result in the nanoparticles being located in the aqueous continuous phase and at the interface between the oil and aqueous phases, but not in the oil phase.

Once the stock emulsions were prepared, the samples were then diluted to their final oil volume percentage with the appropriate stock aqueous solutions to afford the final

compositions. In Chapters 3 and 4 the aqueous solutions used were prepared for a range of NaCl concentrations, while the dilutions carried out for Chapter 5 comprised of NaCl and the appropriate amount of NaOH to give the final sample with appropriate pH.

2.4. Light microscopy of emulsions

All light microscopy images presented in this work were captured on a Zeiss Axiophot Microscope (Carl Zeiss AG, Oberkochen, Germany) using a range of objectives to demonstrate different structural features present in the emulsions. Samples were diluted to between ≈1.25 vol. % and ≈2.5 vol. % before being placed on a welled microscope plate and covered with a cover slip.

2.5. Confocal microscopy of emulsions

Confocal microscopy is an important microscopy technique, which allows the capture of images which exclude light from other focal planes, leading to an image with much greater resolution and clarity than what can be obtained with wide-field microscopy techniques [145]. Confocal microscopy utilises two pinhole apertures located at the light source and the detector. This approach eliminates out of focus light from reaching the detector. This allows much greater image clarity, primarily in the plane perpendicular to the light direction, with a trade-off of image intensity.

All confocal microscopy images presented in this work were captured on a Leica SP5 DM6000B Scanning Confocal Microscope with a 63× oil immersion objective ($f/1.4$ aperture HCX PL APO lambda blue) and a 3× digital zoom (images captured as 1024×1024 pixel images). This required the use of fluorescent dyes, which allows the visualisation of the oil and aqueous phase separately. The dyes that were used in this work were Nile Red for the staining of the oil phase, and Nile Blue for the staining of the charged particles in the aqueous phase. A 514 nm laser excites the Nile Red dye, while the emission was captured between 450 nm to 587 nm. As the chemical environment of the aqueous phase of each type of emulsion will be different, the excitation and emission of the Nile Blue dyes will differ between emulsions. The particular excitation and emission wavelengths for the Nile Blue dye is detailed in each chapter. The excitation and emission profiles for both Nile Red and Nile Blue have both been previously reported by others [146, 147].

2.6. Cryo-SEM of emulsions

Scanning electron microscopy (SEM) is a microscopy technique that utilises a focused electron beam, which is scanned across the surface of a material. This beam of electrons will interact with the surface of the material, and produces a signal that can be measured to yield information about the material, producing an image [148].

Due to the need to impinge a beam of electrons at the surface to produce an image, the capture of standard SEM images requires a high vacuum, so that gaseous atoms are eliminated from the beam path of the electrons. This high vacuum environment makes the measurement of aqueous emulsions an impossible task with standard SEM, as the emulsion sample will boil at low pressures.

In order to image materials with high water content, such as an emulsion, other SEM techniques have been developed. One such technique is freeze-fracture cryo-SEM (cryo-SEM). As the name suggests, cryo-SEM involves the cryogenic freezing of a high water content sample in a nitrogen slurry ($T = -210\,°C$ to $-196\,°C$), which is then mounted in the cryo-SEM chamber where the sample is mechanically fractured, exposing the internal structure of the material. The fractured faces of the material can then be imaged, with the low temperature maintained by a cold stage [149, 150].

The use of cryo-SEM with Pickering emulsion samples allows the structure of the oil droplet network to be visualised along with, providing the size is suitable, the Pickering stabiliser surrounding each oil droplet [151]. This used a Philips XL30 Field Emission Scanning Electron Microscope fitted with a Gatan Alto cryo-trans system at the University of Auckland. A few drops of the emulsion were frozen in nitrogen slush. The frozen emulsion was fractured under ultra-high vacuum and then etched at $\approx -95\,°C$ for 60 s. The fractured surface was coated in platinum (10 mA, 105 s, 1 mbar argon) before being transferred to the cold stage ($\approx -170\,°C$) of the SEM. Cryo-SEM was utilised to identify the distribution of titania throughout the sample.

2.7. Size analysis of emulsions

As was mentioned in Section 1.4.1.1, the method of emulsion preparation can have an effect on the size distribution of the emulsion droplets. The method used to prepare the emulsions used throughout this work was a rotor-stator homogeniser, which routinely yields emulsion droplets larger than 1 µm [31]. The size distribution of the emulsion droplets will also change the bulk properties of the material, and as such measuring and controlling these

is an important undertaking before the bulk properties of the emulsion are evaluated.

Multiple methods can be used to measure the size of colloidal particles either as individual particles or as a population. In this work, the size measurements of emulsion samples were carried out using laser diffraction (LD). LD involves a laser being passed through the colloid sample, which results in the light from the laser being scattered at specific angles [152, 153]. The angle of scattering is inversely proportional to the particle size, resulting in small angle scattering for large particle sizes, and wide angle scattering for smaller particles. The data can then be interpreted using standard models, which will result in an inferred distribution of sizes for the emulsion.

The measurements of emulsion droplet size for this work were carried out using a Malvern Mastersizer 3000 (Malvern Instruments Ltd., Malvern, Worcestershire, UK.). This was performed using the Hydro SM attachment, which allows for samples of the emulsion material to be passed through an optical window continuously, allowing for averaging of a significant sample volume during any measurements. The sample is driven through the instrument by an impeller, the speed of which was set to $1200\,\mathrm{min}^{-1}$, which was found to be sufficient to push the emulsion through the optical window while not breaking the emulsion. Each measurement involves both a red (632.8 nm He-Ne Laser) and blue light (470 nm LED) measurement, affording size analysis coverage over a wide range ($\approx$0.01 µm to 3500 µm), with the red laser providing coverage for larger particle sizes, while the blue light covers smaller sizes.

The process of measuring the size distribution of each emulsion sample follows the standard recommended processes involved filling the instrument with Milli-Q water before aligning the instrument through the automated alignment process. Following the alignment, a background measurement was run with both the red and blue lights of the instrument. The red light measurement is run with a 20 s background measurement, while the blue light measurement is carried out with a 10 s background measurement. This is carried out to account for any scattering that occurs due to contamination of the instrument or Milli-Q water. As the emulsion droplets are expected to primarily be measured by the red laser, the red light background is measured for a longer time period.

The sample was then loaded to an obscuration percentage between 10 % and 15 %, and the size analysis was carried out. The red laser measurement uses a 25 s sample measurement time, while the blue light measurement is carried out with a 5 s sample measurement time. These measurements were carried out with four repeats, with a 2 s delay between each repeat. The data was captured on an array of detectors, and the measured light in-

tensity pattern was used to calculate the size distribution based on calculated patterns giving intensities at each angle using Mie theory [153].

There are a range of size distribution values reported throughout this work including:

- D[4,3] – A volume weighted mean particle size as shown in Equation 2.3 where D_i is the diameter of the *ith* particle.

$$\mathrm{D}[4,3] = \frac{\sum_i (D_i)^4}{\sum_i (D_i)^3} \tag{2.3}$$

- $\mathrm{D_v}(10)$ – The 10th volume percentile particle diameter.
- $\mathrm{D_v}(50)$ – The 50th volume percentile particle diameter.
- $\mathrm{D_v}(90)$ – The 90th volume percentile particle diameter.
- Uniformity – A measure of the absolute deviation from the median value.
- Span – The width of the size distribution of particle diameters, as described by Equation 2.4.

$$Span = \frac{D_v(90) - D_v(10)}{D_v(50)} \tag{2.4}$$

After each measurement the sample was ejected, and the instrument was washed with Milli-Q water, and if necessary isopropyl alcohol. Results are presented with a mean and standard deviation of a number of measurements as described in each chapter.

2.8. Rheology

The rheological techniques that were employed in this work were selected to provide information on the viscoelastic properties of the materials. All rheological measurements presented in this work were carried out on a TA Instruments Discovery Hybrid Rheometer (DHR-2) together with a range of accessories (Discovery HR-2, TA Instruments, New Castle, Delaware, USA.). The geometries that were used are described below, along with an outline of the situations in which they were applied.

2.8.1. Geometries employed

The DHR-2 functions through a selectable top geometry that both drives the geometry, and measures the resultant torques and displacement. The choice of stationary bottom geometry allows for temperature and environmental control, optical or high pressure setups. In this work (with the exception of the Couette geometry), the base stage used was a

hardened surface Peltier plate with a reported temperature control range from −40 °C to 200 °C. This Peltier plate was topped with either a flat 316 stainless steel parallel plate, or a 308 stainless steel plate with a 65 mm diameter crosshatched section (TA Instruments, Delaware, USA.).

2.8.1.1. 40 mm parallel plate

A simple geometry that can be used on a rotational rheometer is a parallel plate. As suggested by the name, the geometry is comprised of two parallel stainless steel plates. The parallel plate geometry is a simple, fast-to-use geometry. However, due to the parallel nature of this geometry, the strain across the diameter is non-uniform. This is described by Equation 2.5, in which $\dot{\gamma}_r$ is the shear rate at radius r, $\dot{\theta}_r$ is the rotational velocity at radius r, and h is the gap height.

$$\dot{\gamma}_r = \frac{\dot{\theta}_r}{h} \tag{2.5}$$

Equation 2.5 accounts for the strain dependence on the rotational velocity, which will change with the radius, increasing as the radius is increased. The differential strain field that is experienced by the sample can lead to differences in the resultant data that is measured [154].

The bottom plate was in most cases a 316 stainless steel plate mounted directly on to the Peltier plate. The top half of the geometry was a 40 mm diameter 316 stainless steel Smart-Swap™ geometry. Due to this geometry being a parallel plate it can be used at almost any gap height, making it a very useful tool. The choice of gap height is often determined by the size of the colloidal particles that are being measured. It is often recommended to set the gap height at least 10 × the diameter of the colloid being measured [103]. Given the average sizes of the emulsion droplets prepared in this work were ≈20 µm to ≈40 µm, the experiments described in this work used a gap height of 400 µm.

2.8.1.2. 40 mm hatched plate

One issue that can affect the results obtained from a smooth parallel plate (or other smooth geometry such as a cone and plate) is wall slip. This is a phenomenon that can occur in emulsions and other colloidal dispersion that involves the depletion of the discontinuous phase close to a solid boundary. This leads to a corresponding local increase of the continuous phase (in the case of the emulsions discussed in this work, the aqueous phase) at the boundary, which in turn can reduce the friction between the solid boundary

and the viscoelastic fluid, since in general the viscosity of the aqueous continuous phase will be less than that of the bulk emulsion. This lubrication between the sample and the geometry will lead to erroneous results, where the measured torque may be lower than expected for the colloid.

In order to lower the effect that wall slip can have on the measurements a roughened surface geometry may be used. There are different roughened surfaces available, from sandblasted metal, to crosshatched parallel plates. The roughened geometry used in this work was a 40 mm crosshatched 308 stainless steel Smart-Swap^{TM} parallel geometry at a gap height of 400 µm. The cross-hatching provides a surface that is covered with small square pyramids (1 mm×1 mm base, 1 mm height). The top 40 mm hatched plate is used in conjunction with a hatched base plate sitting atop a Peltier stage. The roughened surface of these plates works to increase the friction between the sample and the solid surface of the geometry, allowing more accurate measurements to be made.

2.8.1.3. 40 mm cone and plate

As was mentioned in Section 2.8.1.1, one of the issues that needs to be accounted for with a parallel plate geometry is the non-uniform strain field caused by the differences in circumferential velocity that is applied across the radius of the plate. One method that can be used to alleviate this issue is the use of a cone and plate geometry. A cone and plate geometry is a bottom parallel plate while the top geometry is a truncated cone with a very slight angle (typically 0.5° to 4° for 8 mm to 60 mm diameter cones).

The angle of the truncated cone allows the gap height to change across the radius of the geometry, accounting for the change in circumferential velocity. The relationship between the gap height and circumferential velocity leads to the strain profile across the radius being uniform [103]. For this geometry to lead to a uniform stress field it must be operated at the appropriate gap height, which is determined by the angle of the cone. This limit on the gap height can unfortunately result in the particle size of a colloidal sample being too large to reliably capture data (i.e. gap height being less than 10× the average particle size).

In this work a 40 mm 2.009° 308 stainless steel Smart-Swap^{TM} Cone geometry was used as the top half, along with a parallel Peltier Plate as the base with the gap height set at 400 µm.

2.8.1.4. Double walled Couette

The measurement of systems with very low viscosities can be challenging with parallel plate, or cone and plate geometries due to sample run off, and the small contact surface available. One method for combating this is to use a plate with a larger diameter, thus exposing more area of the sample to the applied forces and measurements. Another method involves the use of a double walled Couette geometry. This exposes the sample fluid to a greatly increased surface area of the geometry, with both the inner and outer walls of the top half of the geometry being in contact with the fluid. This allows for much greater sensitivity with materials that have a low viscosity. One trade-off with this geometry is the much greater sample volume needed to fill the gap between the top and bottom sections of the tool. In this work, the Couette geometry that was used was a double gap rotor and cup used in conjunction with a Peltier concentric cylinder temperature system. This system allows for temperature control between $-20\,°C$ to $150\,°C$, while also giving quality data from low viscosity samples.

2.8.2. Development of experimental parameters

The development of experimental parameters is somewhat of a trial and error process, where while there are some standard starting points, these may not be suitable for every material that is investigated. In this work, the experimental methods used for each rheology technique were investigated initially as each new emulsion system was prepared. The experimental parameters used in each chapter of this work are outlined below. Each set of parameters was chosen to limit degradation of the sample, while capturing as wide a range of data as possible. All rheology experiments reported in this work were run at a controlled temperature of $20\,°C$. Before each experiment the material was presheared. This preshearing was carried out in order to minimise any differences in shear history of each emulsion. A range of preshearing regimes were investigated throughout this work. It was found that the application of a preshear did result in differences between measurements, and as such a standard regime was adopted throughout (results of which are not shown).

2.8.2.1. Flow experiments

As discussed in Section 1.5.4.1, a flow experiment can provide information about the stress and viscosity response to a varied shear rate. The shear rate can be increased, or decreased as the experiment is carried out, each of which may influence the results that are obtained. In this work, all flow experiments were carried out starting with low shear

rates followed by stepping up to higher rates [131, 133].

Flow sweep experiments in Chapter 3 were carried out with the following parameters:

- Temperature: 20 °C
- Shear rate: $0.01\,s^{-1}$ to $100\,s^{-1}$
- Points per decade: 5
- Conditioning time: 10 s
- Averaging time: 20 s
- Preshear: $0.1\,rad\,s^{-1}$ for 30 s
- Equilibration time before experiment: 0 s

Flow sweep experiments in Chapter 4 were carried out with the following parameters:

- Temperature: 20 °C
- Shear rate: $0.01\,s^{-1}$ to $1000\,s^{-1}$
- Points per decade: 10
- Conditioning time: 10 s
- Averaging time: 20 s
- Preshear: $0.1\,rad\,s^{-1}$ for 30 s
- Equilibration time before experiment: 0 s

Flow experiments in Chapter 5 were carried out with the following parameters:

- Temperature: 20 °C
- Shear rate: $0.01\,s^{-1}$ to $1\,s^{-1}$
- Points per decade: 10
- Conditioning time: 10 s
- Averaging time: 20 s
- Preshear: $0.1\,rad\,s^{-1}$ for 30 s
- Equilibration time before experiment: 0 s

Models were fit to the flow sweep data and the quality of fits of the models were measured by the r^2 value. The r^2 value is calculated via Equation 2.6, in which y_i and f_i are the measured and fitted data at point i respectively, and $\bar{y}$ is the mean data value. The r^2 values presented were calculated using the software package Origin (OriginLab, Northampton, MA, USA.) during the fitting of each model to the curve.

$$r^2 = 1 - \frac{\sum_i (y_i - f_i)^2}{\sum_i (y_i - \bar{y})^2} \tag{2.6}$$

2.8.2.2. Oscillatory experiments

The use of oscillatory rheology experiments were discussed in Section 1.5.4.2. There are two main parameters that can be manipulated to extract important information about the rheological properties of a system, oscillatory strain, and oscillatory frequency. Each of these are monitored in two separate, but related, experiments. Both of these experiments can be carried out in either an increasing or decreasing manner. In this work, all oscillatory experiments were carried out in an increasing manner.

Strain sweep experiments in Chapter 3 were carried out with the following parameters:

- Temperature: 20 °C
- Angular Frequency: $1\,\mathrm{rad\,s^{-1}}$
- Strain Percentage: 0.01 % to 15 000 %
- Points Per Decade: 5
- Conditioning Time: 5 s
- Sampling Time: 10 s
- Preshear: $1\,\mathrm{rad\,s^{-1}}$ for 30 s
- Equilibration time before experiment: 0 s

Strain sweep experiments in Chapter 4 were carried out with the following parameters:

- Temperature: 20 °C
- Angular Frequency: $1\,\mathrm{rad\,s^{-1}}$
- Strain Percentage: 0.029 % to 2852.11 %
- Points Per Decade: 10
- Conditioning Time: 5 s
- Sampling Time: 10 s
- Preshear: $1\,\mathrm{rad\,s^{-1}}$ for 30 s
- Equilibration time before experiment: 0 s

Frequency sweep experiments in Chapter 4 were carried out with the following parameters (note: The strain percentage used was changed between each emulsion in order to maintain a position in the linear viscoelastic region. The values given encompass the range of values used):

- Temperature: 20 °C
- Angular Frequency: 0.1 rad s^{-1} to 250 rad s^{-1}
- Strain Percentage: 0.4 % to 1 %
- Points Per Decade: 5
- Conditioning Time: 5 s
- Sampling Time: 5 s
- Preshear: 1 rad s^{-1} for 30 s
- Equilibration time before experiment: 0 s

Strain sweep experiments in Chapter 5 were carried out with the following parameters:

- Temperature: 20 °C
- Angular Frequency: 1 rad s^{-1}
- Strain Percentage: 0.01 % to 15 000 %
- Points Per Decade: 5
- Conditioning Time: 5 s
- Sampling Time: 10 s
- Preshear: 1 rad s^{-1} for 30 s
- Equilibration time before experiment: 0 s

Frequency sweep experiments in Chapter 5 were carried out with the following parameters:

- Temperature: 20 °C
- Angular Frequency: 0.1 rad s^{-1} to 500 rad s^{-1}
- Strain Percentage: 0.25 %
- Points Per Decade: 5
- Conditioning Time: 5 s
- Sampling Time: 5 s
- Preshear: 1 rad s^{-1} for 30 s
- Equilibration time before experiment: 0 s

2.8.2.3. Creep and creep recovery experiments

Creep and creep recovery experiments can be an accurate, although time consuming, method for measuring the yield stress of a viscoelastic material [135]. A creep experiment involves monitoring the strain of the sample while a given stress is applied for a time period before releasing the stress for the recovery phase. This is repeated at increasing stresses, and changes in the strain profile are analysed in order to determine the yield stress of the material. In this work all creep experiments were carried out by increasing the applied stress in a stepwise manner.

Creep and creep recovery experiments in Chapter 3 were carried out with the following parameters:

- Temperature: 20 °C
- Preshear: $1\,\mathrm{rad\,s^{-1}}$ for 30 s
- Equilibration time before experiment: 0 s

Errors are not presented for creep experiments due to the nature of the measurements limiting the ability to average a series of measurements.

3 Comparing different approaches to measuring the Pickering emulsion yield stress

3.1. Introduction

In the work presented here a variety of methods for the extraction of a yield stress value for a Pickering emulsion system across a range of oil volume percentages are evaluated and compared. One of the key properties of Pickering emulsions is the viscoelastic behaviour [7, 155, 156]. The yield stress is the critical stress value at which the emulsion is no longer able to store the stress applied in an elastic manner. Instead it must yield, or move, to dissipate this stored and applied stress in a viscous manner, so that the emulsion ceases to behave in a solid-like manner and instead begins to flow like a liquid. While the concept of this critical stress value appears to be straightforward, experimentally obtaining the "correct" value is challenging. Many researchers have outlined methods for obtaining what they assert is the "correct" value, and there is still ongoing debate about the accuracy of different methods [124–131]. Here we consider the three main methods used to extract yield stresses.

The first method considered in this chapter involves the use of a flow curve. The flow curve is a classical method for the determination of the yield stress, in which the applied shear rate is varied logarithmically, while the shear stress is monitored. The yield stress can be extracted from this data via two methods; extrapolation of the measured stress as the applied shear rate approaches zero, or via fitting of the data with a model. Here Bingham or Herschel-Bulkley models, Eq. 1.19 and 1.20, were considered.

The second method that is considered in this chapter utilises an amplitude sweep. This involves a varied oscillatory strain that is applied at a set frequency, while the storage and

loss moduli are measured. There are a number of ways to evaluate the yield stress from this oscillatory experiment. The first that is used in this chapter involves determining the cross-over point of the storage and loss moduli as a function of oscillatory strain ($G' = G''$) [15]. Following this, the storage modulus in the linear viscoelastic region is fitted with an average, while the storage modulus is also fitted separately below the inflection point with a power law curve in the shear thinning region. The intersection of these two fittings has previously been described as a measure of the yield stress [157]. The third oscillatory method utilised to evaluate the yield stress involved plotting the shear stress as a function of shear strain, and again fitting the data below and above the inflection point of the data. The intersection of these fittings of the shear stress vs. shear strain has also previously been described as the yield stress [14, 130, 158].

The third method used to measure the yield stress is by measurement of creep. This involves the application of a constant stress for a time period while monitoring the resultant strain. The applied stress is then released and the strain is again monitored. When comparing the measurements, a sample which shows little increase in the measured strain is demonstrating unyielded behaviour, while a material which demonstrates an increased strain response demonstrates yielded behaviour. In order to quantify the yield stress using this method, the measurement is repeated at a number of applied stresses and the results are compared.

Each of these three methods will be compared using a set of Pickering emulsions in this chapter. The emulsions used to undertake this task were an oil-in-water Pickering emulsion stabilised by silica nanoparticles. This work aimed to describe the differences between each method for measuring the yield stress, and use this information to describe the emulsions yielding processes in terms of the microscopic rearrangements of oil droplets.

3.2. Experimental methods

3.2.1. Materials used

Pickering emulsions utilised in this chapter were an oil-in-water system with the oil phase comprising of a 60:40 (vol. % : vol. %) mixture of isopropyl myristate and dodecane (as described in Chapter 2). This particular mixture of oils was chosen due to the isopropyl myristate adding some degree of hydrophilicity to the discontinuous phase improving the wetting of the charged silica stabiliser. Synthetic fumed hydrophilic silica nanoparticles were used as the emulsifier in this system. The aqueous phase of the emulsion systems was

prepared from Milli-Q water, with NaCl added to yield a final electrolyte concentration of $0.03\,\mathrm{mol\,L^{-1}}$.

3.2.2. Emulsion preparation

Formation of the emulsions involved the dosage of dry silica nanoparticles into a vessel (5 wt. %). The appropriate volume of oil, and aqueous phases were then added to the vessel consecutively. Once the required volumes were added, the system was homogenised with a rotor-stator homogeniser (PowerGen 125, Fisher Scientific) at $30\,000\,\mathrm{min^{-1}}$ for 2 minutes while moving the homogeniser head throughout the sample. Once the samples were fully emulsified, samples were taken and diluted with the appropriate aqueous material to the desired oil volume fraction. Samples with the following oil volume fraction were obtained 50, 45, 40, 35, 30 and 25 vol. %.

3.2.3. Droplet analysis

Droplets were analysed for both morphology and size using microscopy and laser diffraction. Optical microscopy was carried out in dilute systems (∼2.5 vol. %), in order to reduce excessive light scattering, with a sample of the diluted system being placed into a welled slide. Optical micrograph images were captured with a 40× objective on a Zeiss Axiophot Microscope.

Confocal microscopy was carried out using a 30 vol. % emulsion system on a Leica SP5 DM6000B Scanning Confocal Microscope with a 63× oil–immersion objective. The emulsions had ≈0.0005 M Nile Blue as a charged aqueous stain, and ≈0.0005 M Nile Red as a oleophilic stain. The Nile Blue dye was excited with a 633 nm laser and the emission captured between 638 nm to 785 nm. The Nile Red dye was excited with a 514 nm laser and the emission captured between 518 nm to 627 nm.

Droplet size analysis was carried out using a Mastersizer 3000 and processed with the accompanying software package (version 3.30). Analysis of the droplet size distribution of various batches of this emulsion are shown in Table 3.1.

While the optical microscopy methods used in Fig. 3.2 show the bulk structure of the emulsion droplets, it is not possible, at this magnification, to directly visualise the location of the 100 nm to 500 nm silica aggregates present in the Pickering emulsion system. In order to better determine the location of the silica in these Pickering emulsion systems, cryo-SEM images of the interfacial structures in the emulsions were obtained. Cryo-SEM was utilised to identify the distribution of silica throughout the sample. Cryo-SEM images

presented in this chapter were captured by Dr. Catherine Whitby, utilising a 30 vol. % emulsion stabilised by 2.5 wt. % silica.

3.2.4. Rheological measurements

Emulsion samples were left at rest overnight to develop a network structure before rheological analysis was carried out. Rheological measurements were carried out at 20 °C with both a 40 mm parallel plate geometry, and a 40 mm hatched plate geometry, each with a gap height of 400 µm on a DHR-2 rheometer. Emulsion samples were loaded on to the rheometer with a disposable Pasteur pipette in a careful manner to minimise the shear effect from the pipette. Preparing the material for analysis was carried out by pre-shearing for 30 seconds at 0.1 rad s^{-1}, with no equilibration time before the experiment was carried out. The pre-shear was carried out on these materials in order to apply a uniform deformation to each sample before any measurements are taken. Three experiments were run with each of the three yield stress methods on each loaded emulsion sample: a strain sweep monitoring stress, G′, and G″, a flow curve monitoring stress and viscosity, and a creep test showing the effect of constant stresses on the sample.

Initially, a hatched plate geometry was used for the emulsions at each oil volume percentage in order to remove any effect that wall slip may have. A parallel plate geometry was utilised for comparison. It was found that at oil volume percentages of 35 vol. % and below there was a difference in the data captured between the parallel and hatched plate geometries, similar to changes that have been attributed to wall slip by previous workers [159]. In comparison, at oil volume percentages of 40 vol. % and greater the differences between the results obtained for each geometry reduced significantly. Due to this, at oil volume percentages of 35 vol. % and below the hatched plate geometry was used, while at oil volume percentages of 40 vol. % and above the parallel plate geometry was employed due to its ease of use.

3.2.4.1. Flow curve

Flow curve experiments were performed with an increasing shear rate from 0.01 s^{-1} to 100 s^{-1}, again with 5 data points per decade, with 20 s of averaging per point measured after a 10 s conditioning step. Higher shear rates were attempted with these emulsion systems (100 s^{-1} to 1000 s^{-1}). However, these high shear rates resulted in obvious physical degradation of the emulsions structure, something previously reported by others with Pickering emulsions [54]. Figure 3.1 shows the emulsion system both before and after shear at

$100\,s^{-1}$ and $1000\,s^{-1}$.

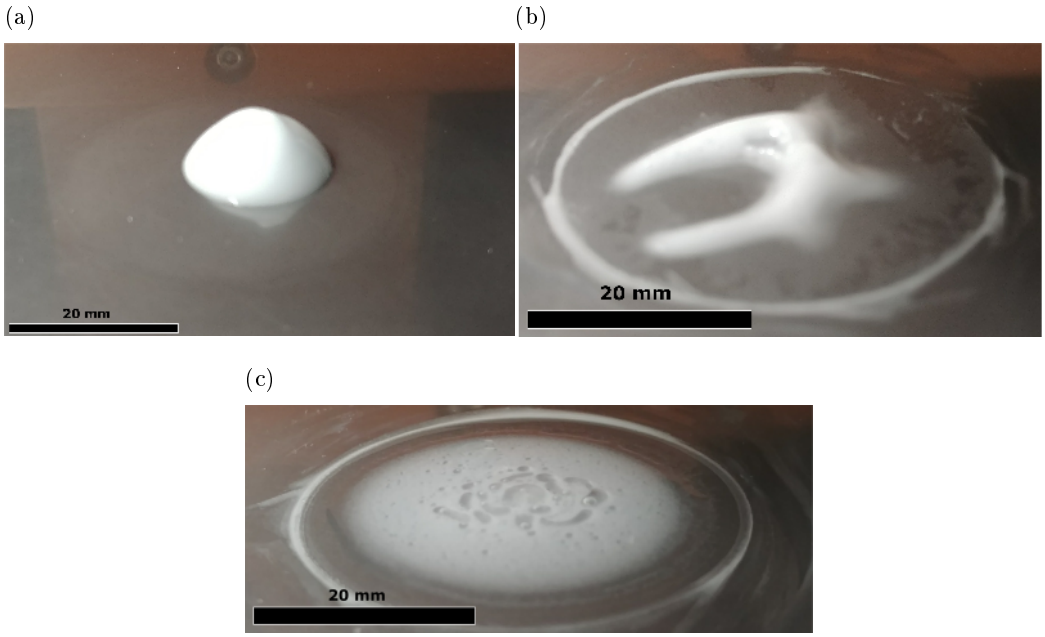

Fig. 3.1 Example images of a high oil volume percentage emulsion before and after shear has been applied. a) Emulsion sample before any shear has been applied. b) Emulsion sample after a maximum shear rate of $100\,s^{-1}$ has been applied showing a stable sample. c) Emulsion sample after a maximum shear rate of $1000\,s^{-1}$ has been applied showing the damage to the emulsion system, as shown via the colour change and splitting of the emulsion system.

3.2.4.2. Strain sweep

Strain sweep measurements were all performed across the strain range of 0.01 % to 15 000 %, at a constant frequency of $1\,rad\,s^{-1}$, with 5 data points measured per decade with 10 s averaging time after a 5 s condition step per data point. The strain vs. stress, G′ and G″ curves were evaluated for the material. The range of strains chosen here allowed for full coverage of the areas of interest with each emulsion measured, covering both the elastic state of the emulsions at low strain percentages, and the viscous nature of the systems at high strain percentage. The error values reported in the tabulated data were calculated as the spread between the average calculated value, and the minimum or maximum value for the given data.

Data from multiple measurements for both the flow and oscillatory rheology were taken and averaged to give an accurate representation of the systems investigated. The points defined by the symbols in each graph are the mean value for these measurements, while the range of data obtained is shown by the shaded areas for each oil volume percentage. Errors reported for the tabulated data are the difference between the average calculated

value and the minimum/maximum value for each shear rate.

3.2.4.3. Creep and creep relaxation

The creep experiment was performed after the flow curve and strain sweep methods due to the need for some prior knowledge of the approximate range of the yield stress, so that the range of values used for the creep measurement encompassed the yield stress value. Creep measurements were carried out with a range of applied stresses, with sample replacement between each measurement. The stresses were applied for a minimum of 180 s, with the resultant displacement of the sample being measured as the stress was applied. Then, the sample was left to relax for a minimum of 180 s with the displacement of the sample being measured. Errors are not presented for creep experiments due to the nature of the measurements limiting the ability to average measurements.

3.3. Results

3.3.1. Emulsion microstructure

While experimental methods are most often concerned with the bulk physical properties of many emulsion based products, it is important to recognise that these properties are implicitly a function of the microstructure of the emulsion systems [114]. It can then be seen that for meaningful repeatable measurements of the yielding and flow of emulsion systems to be made, the microstructures must be controlled with both droplet size, and any network formation due to flocculation between the oil droplets and the silica particles remaining constant.

As Fig. 3.2 shows, this emulsion system is comprised of spherical droplets with an average diameter of approximately 20 µm as determined by optical microscopy. The droplets demonstrate a degree of flocculation, likely due to attractive interactions (covered in more detail later in Chapter 4). Table 3.1 shows the mean droplet diameter is 24.3 ± 3.0 µm, with a span of 1.36 ± 0.01 when measured by light scattering.

While Pickering emulsion systems can demonstrate remarkable stability, some Pickering emulsion systems can be vulnerable to the effects of coalescence over time, especially with the daily mixing that these systems were exposed to [52, 90, 160]. This coalescence will result in an increase in the droplet size, and will ultimately change the interactions between the droplets, which in turn will result in a different overall network structure forming. The size of the emulsion droplets was measured over a period of two weeks to evaluate the

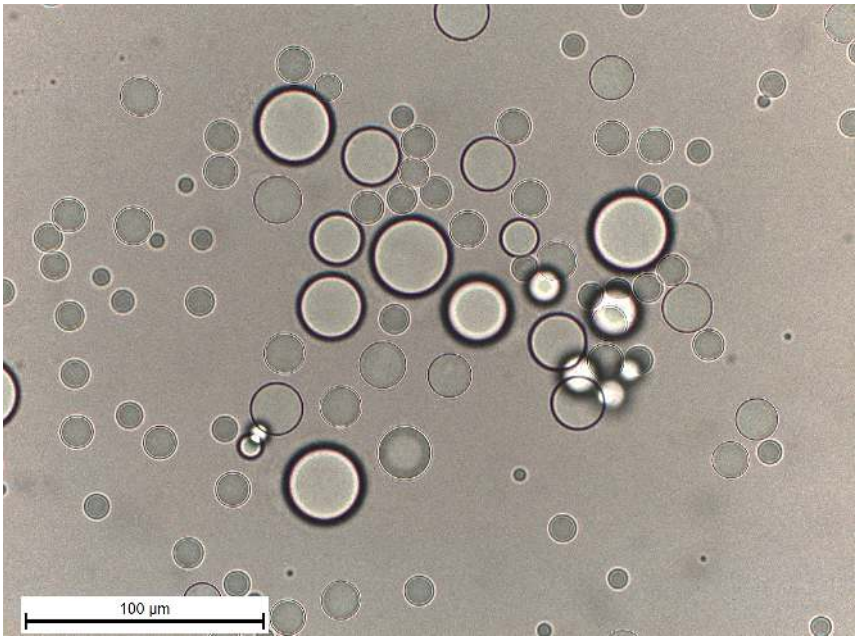

Fig. 3.2 Optical micrograph of a ≈2.5 vol. % Pickering emulsion system. The image shows that droplet morphology is spherical, with no misshapen droplets.

Table 3.1. Droplet size analysis of a number of batches of oil-in-water Pickering emulsions stabilised by 5 wt. % silica showing the similarity of emulsion sizes across multiple preparations.

Batch	D [4,3] µm	D_v (10) µm	D_v (50) µm	D_v (90) µm	Uniformity	Span
1	23.9	10.8	20.8	40.1	0.459	1.408
2	26.2	12.0	22.5	42.6	0.463	1.361
3	28.9	15.0	26.6	46.2	0.367	1.175
4	21.1	9.45	18.1	35.3	0.471	1.427
5	21.4	9.50	18.3	35.8	0.478	1.441

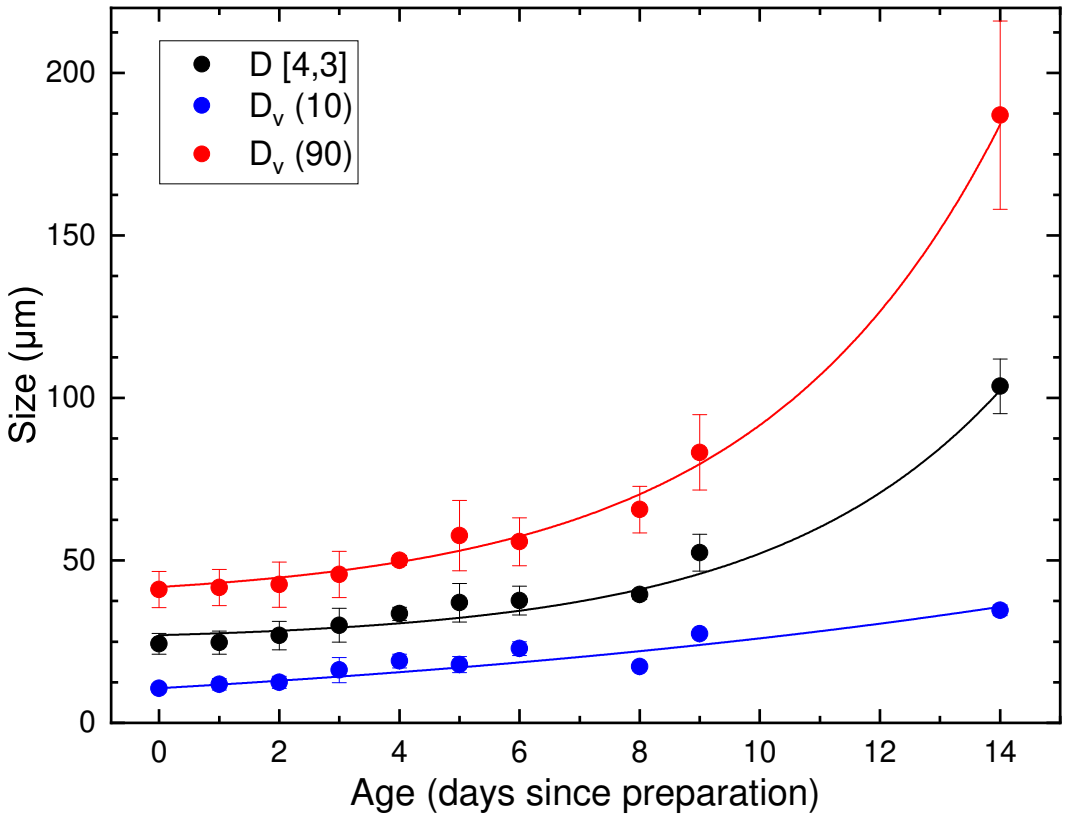

Fig. 3.3 Changes in the size of oil-in-water Pickering emulsion droplets stabilised by 5 wt. % silica over the course of two weeks from the time of preparation. Lines are placed to guide the eye to the trend in the data. Samples used for rheological analysis were used one or two days after preparation.

rate at which coalescence occurs in this system. Figure 3.3 shows both this change in size, and an increase in the variation of the oil droplets as they age for up to two weeks with mixing each time a sample was taken. Due to these changes in the droplet sizes, rheological measurements were all made on emulsions within two days of preparation.

The micrographs obtained from the confocal microscopy used to image these emulsions are demonstrated in Fig. 3.4. The micrograph shows four oil droplets surrounded by an aqueous phase that is filled with silica nanoparticles. In addition to the presence of silica in the aqueous phase, there appear to be shells of silica forming around the oil droplets, consistent with these being Pickering emulsions that are stabilised by solid nanoparticles.

Two cryo-SEM images are displayed in Fig. 3.5a and 3.5b showing the structure of these silica stabilised Pickering emulsions at two different magnifications. These figures highlight the distribution of oil, water, and silica throughout the emulsion system. The labels shown in Fig. 3.5a indicate that the oil droplets are the discontinuous phase distributed in an continuous aqueous phase which in turn has a network of silica nanoparticles throughout. In addition to the silica network that is present, it can also be seen that each oil droplet

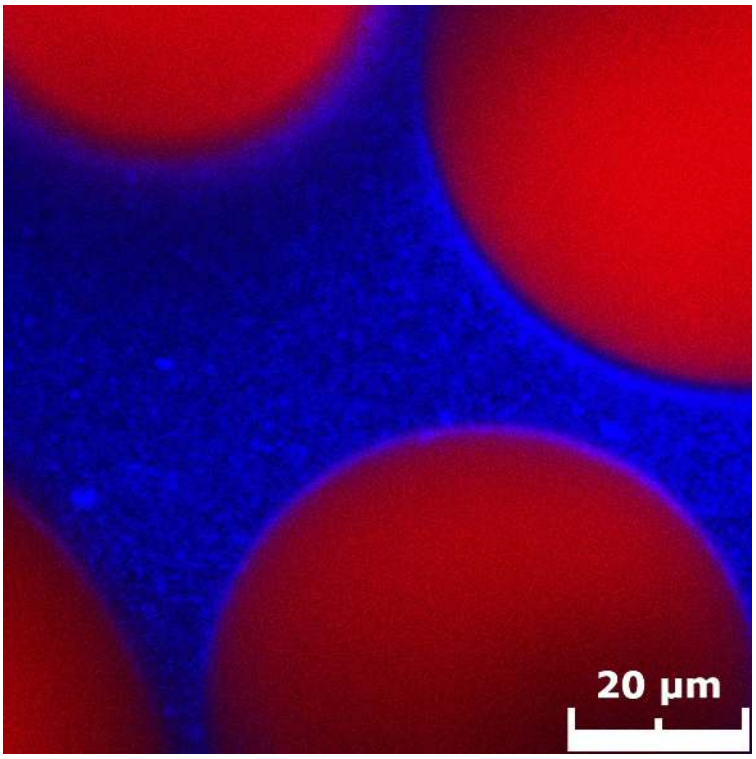

Fig. 3.4 Confocal microscopy of 30 vol. % oil-in-water Pickering emulsion stabilised by 5 wt. % silica, showing the structural features, and the distribution of materials. Red colouration is the result of the oleophilic dye added to the oil. Blue colouration is due to the charged dye added to the aqueous phase to stain the silica nanoparticles.

has a coating of nanoparticles, as expected for a Pickering emulsion. Fig. 3.5b shows a similar sample of emulsion at a higher magnification level, allowing a clearer view of the multi-layered silica coating of each oil droplet. These cryo-SEM images demonstrate the three dimensional network that forms. This network is comprised of the coated oil droplets, excess silica aggregates, and is distributed throughout the aqueous continuous phase.

The network structure between the oil droplets is demonstrated to some degree in both Figs. 3.4 and 3.5. In contrast to this, Fig. 3.2 does not show an overall network structure forming between the droplets. This is due to the dilute nature of the sample used for optical microscopy. The bulk emulsions, which have oil volume percentages that are between 10 and 20 times greater, will have droplets which are located in close proximity. It has been demonstrated previously that increasing electrolyte concentrations will lead to a decrease in the electrostatic repulsion between suspended silica particles [8, 24]. This can result in an attractive interaction between the silica particles, giving a system where the emulsion droplets will be within close proximity of each other [23] (observed in Figs. 3.4 and 3.5). Due to these interactions, the droplets will form a network mesh throughout the bulk sample, the strength of which is accounted for by both the van der Waals and electrostatic repulsion components of the DLVO theory. It has been demonstrated previously that the network structure of a system will affect the rheology of the materials [161–163]. The network structure that is formed between the oil droplets is built with the excess silica aggregates that are present in the aqueous phase. This excess of the solid stabiliser is known to provide an increase in the elastic strength of Pickering emulsions [90]. This chapter will demonstrate the effect that this network of particles will have on the rheology of these emulsion systems.

3.3.2. Emulsion viscous flow curves

The first approach to determining the yield stress of the emulsions involved the measuring their viscous flow behaviour. The flow behaviours measured here were both the viscosity and the stress response to an increasing shear rate. Both of these responses are presented and discussed below.

The origin of the viscosity of a particular material arises from the intermolecular or, in the case of colloidal systems, the interparticle interactions. The interactions between the particles or molecules in a system will add a level of friction as a shear is applied to the fluid. This is observed physically as the viscosity. As the shear stress is changed, some systems (non-Newtonian fluids) will show a change in the measured viscosity. Figure 3.6 shows

(a)

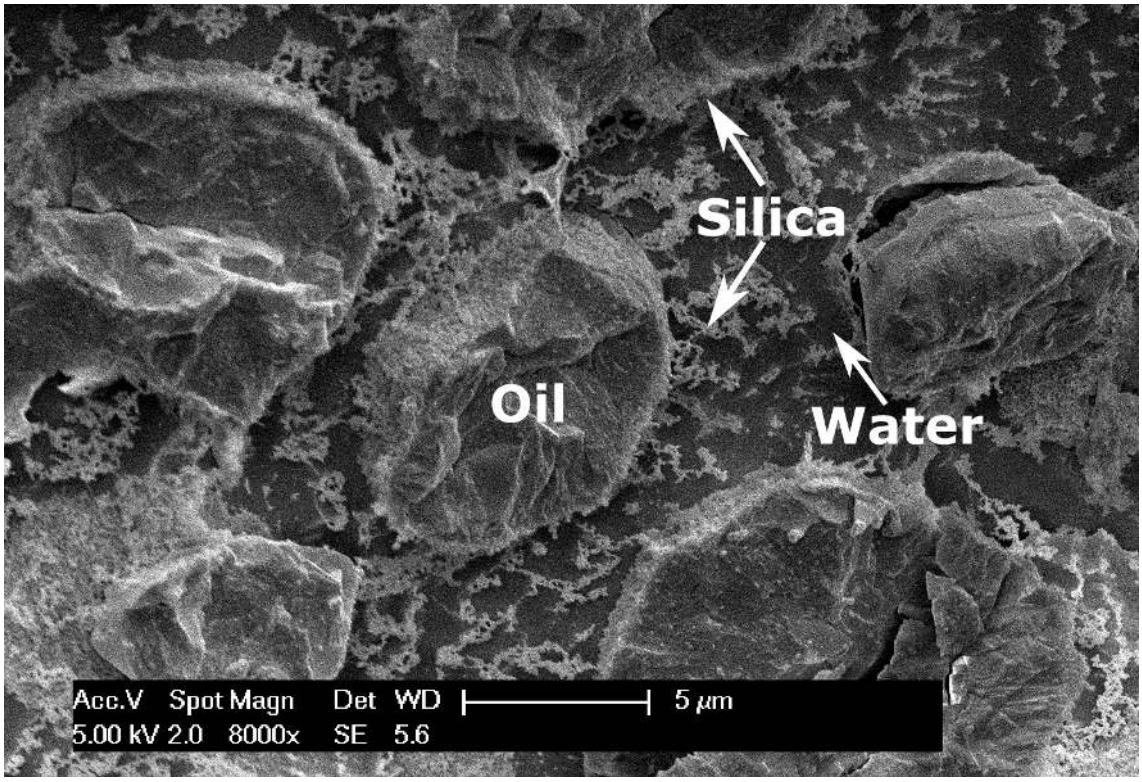

(b)

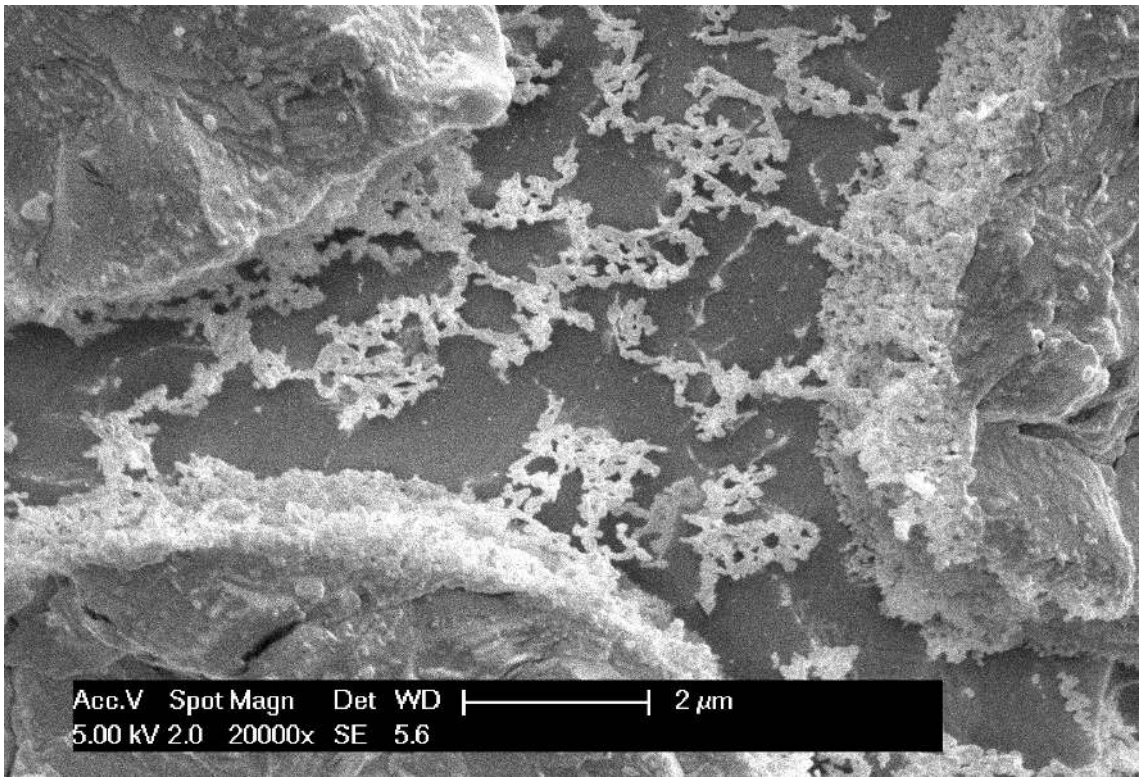

Fig. 3.5 Cryo-SEM image of a 30 vol. % Pickering emulsion stabilised by 2.5 wt. % silica. (a) Micrograph demonstrating the oil droplets dispersed throughout an aqueous phase containing a network of suspended silica nanoparticles. Labels have been added to identify each component. (b) Higher magnification image demonstrating three oil droplets and the interfaces between them. This image demonstrates the silica shell that surrounds each oil droplet, while also demonstrating the network of silica nano-particles between oil droplets. Cryo-SEM images presented here were obtained by Dr. Catherine Whitby at the University of Auckland.

the changes in viscosity for an emulsion system with a range of oil volume percentages (while maintaining a fixed droplet size), as the applied shear rate is increased. This figure demonstrates that as the shear rate is increased, the viscosity of each emulsion decreases, consistent with these emulsions being shear–thinning fluids. This shear–thinning fits well within the accepted behaviour of emulsion systems at the volume fractions investigated here [97]. This behaviour is understood to arise from the networks of droplets that make up the system being disrupted as increasing shear stresses are applied. The rearrangement of these networks alters the interparticle interactions supporting the system, and therefore reduces the viscosity of the emulsion.

A further feature that is notable in Fig. 3.6 is the affect that oil volume percentage has on the viscosity of the system at each applied shear rate. Increasing the oil volume percentage from 25 vol. % to 50 vol. % increases the viscosity by over two orders of magnitude — a significant difference for such similar systems. These changes can be explained through the density of the network present in the continuous phase of these systems. At the higher volume percentage samples, a larger volume of the system is taken up by oil droplets, and as such there will be an increase in the friction experienced in the material as shear stresses are applied to it. When a lower volume percentage sample is examined, a network will still be formed between the droplets in the sample. This will still add a level of friction inside the sample. However, there are less "network building" elements present in the sample which will result in the overall viscosity being lower.

As discussed in Section 2.8.2.1, there are models which permit predictions of the viscosity of an emulsion as a function of volume percentage based on the viscosities of the component materials. The models used for these systems are the Einstein (Equation 1.16), Batchelor (Equation 1.17), and Kreiger-Dougherty models (Equation 1.18), each restated below.

$$\eta_r = \eta_c(1 + 2.5\phi) \tag{1.16}$$

$$\eta_r = \eta_c(1 + 2.5\phi + 6.2\phi^2) \tag{1.17}$$

$$\eta_r = \eta_c \left(1 - \frac{\phi}{\phi_p}\right)^{-2.5\phi_p} \tag{1.18}$$

In each of these models η_r is the relative viscosity of the dispersion, η_c is the viscosity of the continuous phase, ϕ is the oil volume percentage of the dispersion (the discontinuous phase volume percentage), and ϕ_p is the maximum packing fraction for poly-disperse hard

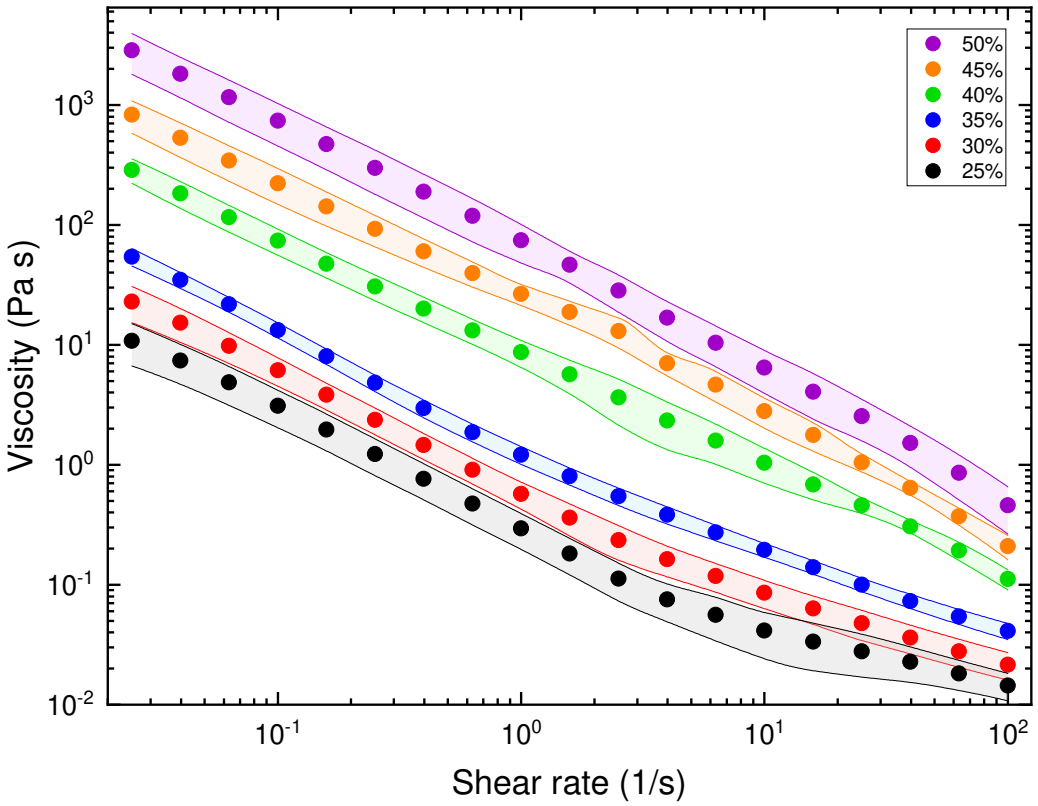

Fig. 3.6 Viscosity response to an increasing shear rate of oil-in-water Pickering emulsions stabilised by between 2.5 wt. % and 5 wt. % silica. The oil volume percentage of each of the emulsions are presented in the legend. Shaded areas indicate the variation in multiple measurements of each emulsion system.

Table 3.2. Relative viscosity of each emulsion oil volume percentage calculated via the three models, as well a comparison to the low shear measured viscosity of each oil-in-water Pickering emulsion stabilised by between 2.5 wt. % and 5 wt. % silica.

Oil volume percentage (vol. %)	Einstein model viscosity (Pa s)	Batchelor model viscosity (Pa s)	Krieger-Dougherty model viscosity (Pa s)	Measured viscosity (Pa s)
25	1.4×10^{-3}	1.8×10^{-3}	2.0×10^{-3}	11 ± 4
30	1.5×10^{-3}	2.1×10^{-3}	2.5×10^{-3}	23 ± 9
35	1.6×10^{-3}	2.3×10^{-3}	3.2×10^{-3}	54 ± 10
40	1.7×10^{-3}	2.6×10^{-3}	4.3×10^{-3}	290 ± 80
45	1.8×10^{-3}	3.0×10^{-3}	6.2×10^{-3}	830 ± 280
50	1.9×10^{-3}	3.4×10^{-3}	1.0×10^{-2}	2900 ± 1200

spheres ($\phi_p = 0.64$). The values calculated for each volume percentage with each model are shown in Table 3.2 and compared with experimental results. In all cases it is observed that the measured low shear viscosity for each emulsion is substantially greater than the viscosities predicted by each model. This difference is not unexpected, as each model does not include any parameters to describe the non-zero interactions between the oil droplets in the emulsions [115–121, 164]. It can also be seen that the measured viscosity has a much higher dependence on oil volume percentage than any of the models. This higher dependence can be explained due to the increased interactions between the emulsion droplets and aqueous silica network at higher oil volume percentages. The increases in oil volume percentage will decrease the volume of aqueous phase separating the oil droplets, increasing the network strength.

The measurement of the stress response of a material to a change in shear rate is a routine and well used tool for a rheologist to employ when trying to understand a given material. One of the key metrics that can be extracted from the shear rate dependence of the stress is the yield stress. As noted in Section 2.8.2.1, the yield stress is an often debated concept. In this work the term will be used to describe the minimum force that is required to commence flow of a material [97, 124–129]. The results from the stress measurements carried out for this work are provided in Fig. 3.7. This indicates that, for these materials, while the oil volume percentage is increased, the stress required to maintain a given shear rate increases in a predicable manner. Figure 3.7 shows that high oil volume percentage samples ($\geq$40 vol. %) demonstrate a relatively constant stress response with shear rate across the range of shear rates accessible to the emulsion system.

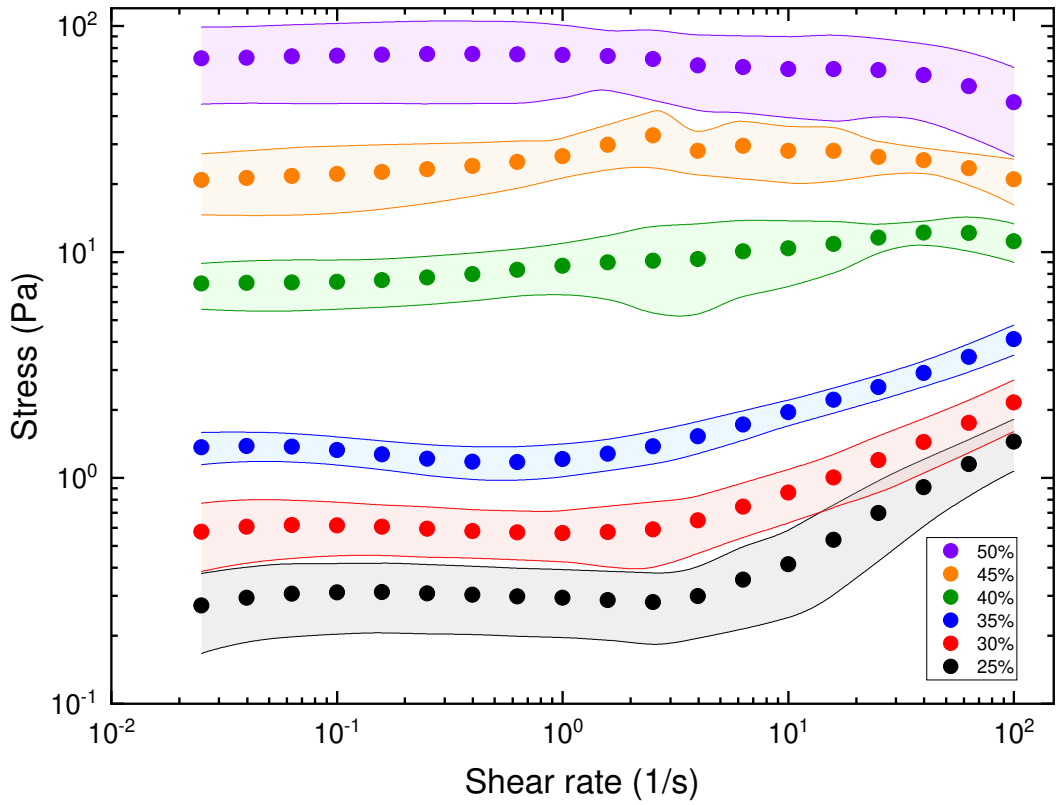

Fig. 3.7 Dependence of stress on an applied shear rate for oil-in-water Pickering emulsion stabilised by between 2.5 wt. % and 5 wt. % silica across a range of oil volume percentages (as indicated in the figure legend). Shaded areas indicate the variation in multiple measurements of these emulsion systems.

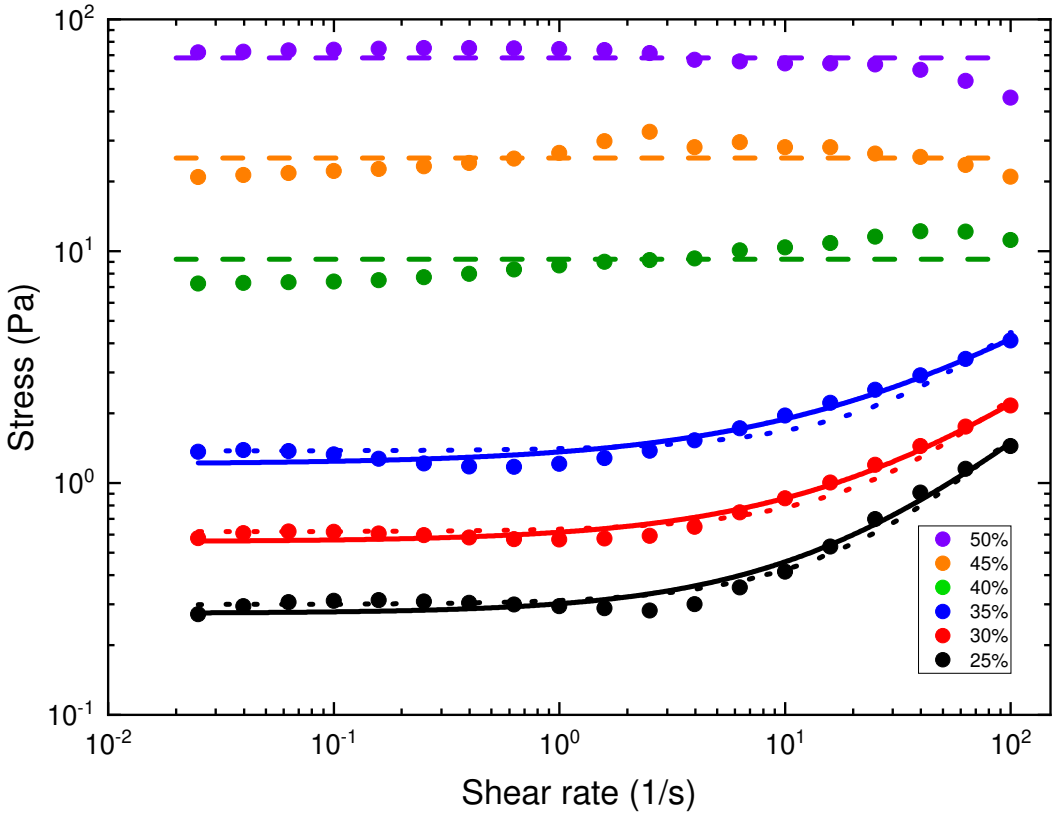

Fig. 3.8 Fittings of the stress dependence on an applied shear rate for oil-in-water Pickering emulsion stabilised by between 2.5 wt. % and 5 wt. % silica across a range of oil volume percentages (as indicated in the figure legend). Determination of the yield stress was carried out in different ways for each oil volume percentage. Samples with 40 vol. % or greater involved the fitting of an average to find the stress (dashed lines). Samples with 35 vol. % or lower were fitted with the Herschel-Bulkley (solid lines), and Bingham models (dotted lines). Averages were also fitted to the low shear rate plateaus of 25 to 35 vol. % samples (not shown).

Due to the linear response observed at ≥40 vol. % the only fitting that was carried out on these three emulsions was averaging, which afforded yield stress values of the materials. These shear responses have been seen previously in high volume percentage emulsions, and have been described as being due to inhomogeneous flow [130]. Lower oil volume percentage emulsions (≤35 vol. %) demonstrate an interesting non-linear response to the increasing shear rate applied to the materials, with an asymptotic–like plateau at low shear rates. The plateau at low shear rates was fitted again with an average, which allows an approximation of the yield stress of the emulsions. Fitting of the power law component of these curves was carried out with both the Herschel-Bulkley and Bingham models, and the results are shown in Fig. 3.8 [101, 102].

The r^2 value values for the Herschel-Bulkley curves to the data was found to be high, with r^2 values between 0.98 to 0.99. The fit that this data had to the Bingham model

resulted in r^2 values within the range of 0.94 to 0.98. It is important to note that the stress response of these emulsion systems will likely change at higher shear rates. However, as acquisition of the yield stress is the target of this work, higher shear rates were not investigated. Yield stress values extracted from these stress plots are provided in Table 3.3.

Interestingly, although perhaps unsurprisingly, the yield stresses extracted via each method are similar at each oil volume percentage. The errors presented on each measurement, for the most part, cover the range of data presented by each method. As each of the flow curves presented here were carried out with an increasing shear rate, the yield stress values extracted here are ascribed to being static yield stresses; the static yield stress being the minimum stress that is required to make a material begin to flow from a static state.

Comparisons between the data seen in Table 3.3 shows that each of the methods employed to extract a yield stress number give very similar results. It is expected that both the Herschel-Bulkley and Bingham fits will be closely related to each other, as the Herschel-Bulkley equation is simply a modified Bingham fit, with a power value of n acting on the shear rate. Both the Bingham and Herschel-Bulkley equations are shown in Equation 1.19 and 1.20 respectively.

$$\tau = \tau_0 + k\dot{\gamma} \tag{1.19}$$

$$\tau = \tau_0 + k\dot{\gamma}^n \tag{1.20}$$

In each of these equations τ_0 is the characteristic yield stress of the material, τ is the shear stress, k is a consistency function, and n is a flow index. The flow index is a value that can be used to demonstrate the shear response of a material. When the value of the flow index is greater than 1 the fluid is a shear thickening material, while when the value is less than 1 the material will demonstrate a shear thinning behaviour. If the value of the flow index, and the yield stress value, are $n = 1$ and $\tau_0 = 0$ the model will reduce to describing a Newtonian fluid. For each of the three data sets to which a Herschel-Bulkley model was fitted the value of the flow index was $n = 0.63$, $n = 0.73$, and $n = 0.82$ for the 25, 30 and 35 vol. % emulsions respectively, all of which are less than $n = 1$, indicating that each sample demonstrates shear thinning behaviour. This is consistent with the viscosity data reported in Section 3.3.2.

Table 3.3. Yield stress values for a range of oil-in-water Pickering emulsions stabilised by between 2.5 wt. % and 5 wt. % silica at a number of oil volume percentages as measured via fittings of the stress response to an increase in the applied shear rate.

Oil volume percentage (vol. %)	Average low shear stress (Pa)	Herschel-Bulkley fitting of stress (Pa)	Bingham fitting of stress (Pa)
25	0.3 ± 0.1	0.3 ± 0.1	0.3 ± 0.1
30	0.6 ± 0.1	0.6 ± 0.2	0.6 ± 0.1
35	1.3 ± 0.2	1.2 ± 0.2	1.4 ± 0.2
40	9 ± 2	6 ± 2	8 ± 3
45	25 ± 6	–	–
50	70 ± 30	–	–

3.3.3. Oscillatory measurements

Previous measurements carried out on the emulsion samples reported in this chapter have all induced flow in the materials by shearing the samples in a single direction. An alternative approach used to extract the yield stress is the use of oscillatory rheology measurements. The measurements in this section investigate the elastic properties of the emulsions by applying an oscillatory strain or stress to the samples. In the case of these measurements, the applied strain was controlled, and the stress response was measured. As was noted in Section 2.8.2.2, the stress and applied strain can be used to calculate a value for the storage (G′), and loss (G″) moduli via Equations 1.24 and 1.26,

$$G' = \frac{\sigma_0}{\gamma_0} cos\ \delta \tag{1.24}$$

$$G'' = \frac{\tau_{(t)}}{\gamma_{(t)}} sin\ \delta \tag{1.26}$$

in which $\tau_{(t)}$ and $\gamma_{(t)}$ are both the stress and strain components, while δ is the phase change between the applied strain and measured stress response.

Figure 3.9 shows the changes in elastic potential of these systems as the oil volume percentage of the emulsions were increased. As the oil volume percentage is increased, the values for both G' and G'' increase substantially. This is to be expected as the network structure inside the emulsions becomes more densely interconnected. Across all of the measured oil volume percentages there is a region at low strain percentages where the value of

G' is independent of strain. This region is observed across many colloidal systems, and has previously been explained as being the region in which the energy applied to the materials through the strain is largely stored elastically, rather than dissipated viscously [165]. As the oil volume percentage is increased from 25 to 50 vol. % in the present study, the value of G' in the linear viscoelastic region increases by over two orders of magnitude from ≈2 Pa to ≈600 Pa, demonstrating an increase in the elasticity of the materials. Another feature of the plots shown in Fig. 3.9 is the rate at which the G' of the linear viscoelastic region increases as the oil volume percentage is increased. The data presented at lower volume percentages (≤35 vol. %) shows only a small difference between each emulsion measured, when compared to the range of data seen at higher volume percentages (≥40 vol. %). This effect was also seen to some degree earlier in Fig. 3.7, and is interpreted here as being due to the volume of network building components present in each emulsion sample. At lower oil volume percent there will be a lower number of oil droplets present per unit volume of continuous phase, which will lead to an overall weaker network being formed. Once a critical number of droplets is reached, the network that is present in these emulsion samples will become sufficiently wide ranging to significantly increase both the yield stress and the elasticity.

Another distinguishing feature of these plots is the peak that is seen in the G'' data for each oil volume percentage. This is a peak that is often seen in viscoelastic fluids. The origin of this peak is due to a decrease in the structural relaxation time at high strain percentages [166–169]. It has been posited previously that fitting the shear thinning behaviour seen after this peak in the G'' will result in a power law where the G'' exponent (n) is "always about one half of the exponent associated with $G'(m)$" (Equation 3.1, in which G' or G'' are the storage and loss moduli respectively, α is a scale factor, γ is the shear strain percentage, and ν is the power slope of the curve) [166].

$$(G'/G'') = \alpha\gamma^{\nu} \tag{3.1}$$

This assertion was tested against these emulsions, and was found not to be consistent across the full range of oil volume percentages measured here. However this is not unexpected, as the emulsion system used here has an attractive interaction between the emulsion droplets. The exponents extracted for each G' and G'' fitting, displayed in Table 3.4 , shows variation in the slopes of G' and G'' across the volume percentages measured, while the ratio of n/m also varies significantly. At low oil volume percentages (25 vol. % and 30 vol. %) the slope of both G' and G'' were low, demonstrating the limited struc-

ture in these low droplet density systems. The ratio of $^{n}/_{\mathrm{m}}$ at these low volume percentage samples is slightly higher than that posited by previous researchers [166–169].

At higher oil volume percentages ($\geq$35 vol. %) the slope of both G' and G'' increased to larger power values, with 50 vol. % having a power for G'' more than twice as large as that of the 25 vol. % sample. The power value of G' also increased by around 15 % as the oil volume percentage increased from 25 vol. % to 50 vol. %. Changes in the slope values result in the ratio of $^{n}/_{m}$ changing from ≈ 1.3 at 50 vol. % to ≈ 2.3 at 25 vol. %. This change is not unexpected, as the network structures that were formed between the emulsion droplets present in the higher volume percentage samples will alter yielding profile of these materials. At low volume percentages, once the sample has begun to yield, the separation of oil droplets will be substantial, which will result in significant shear thinning. This is demonstrated in the data as an increased ratio between the power coefficients, $^{n}/_{m}$, for the slopes of G' and G''. The absolute slopes of these low volume percentage are also lower, due to there being less structure in the samples to break down.

When the yielding processes of the higher volume percentage samples are considered, the slopes of both G' and G'' are greater, with the larger change occurring in the G'' slope value, with an increase from $\gamma^{-0.43}$ to $\gamma^{-0.91}$ when comparing the 25 vol. % and 50 vol. % samples — an indication that the yielding process involves the disruption of a more substantial network.

As the yielding process begins the material transitions through a network disruption process, where the overall network of the emulsion begins to break down into smaller flocs of droplets, before transitioning through a cage–breaking process where the oil droplets are separated from their nearest neighbours. It is expected that these processes would normally be seen as two separate peaks in G'', (as they appear to be to some degree in the 40 vol. % data, Fig. 3.9) [12, 13, 142]. However it is possible that the two peaks have merged into a single broader peak in the data.

There are multiple methods which can be employed to extract a yield stress from these oscillatory measurements. The first method is to find the point at which the plots of G' and G'' cross-over ($G' = G''$) [15]. At strain percentages larger than this point the viscous dissipation component (G'') will become larger than the elastic dissipation (G'). As this transition from elastic dissipation to viscous dissipation occurs, the system can be considered to have yielded. The second method that can be used to gather a yield stress involves the fitting of two line segments to the G' curve. The first line segment is an average of the linear viscoelastic region, or the region where there is little change in the G'

(a)

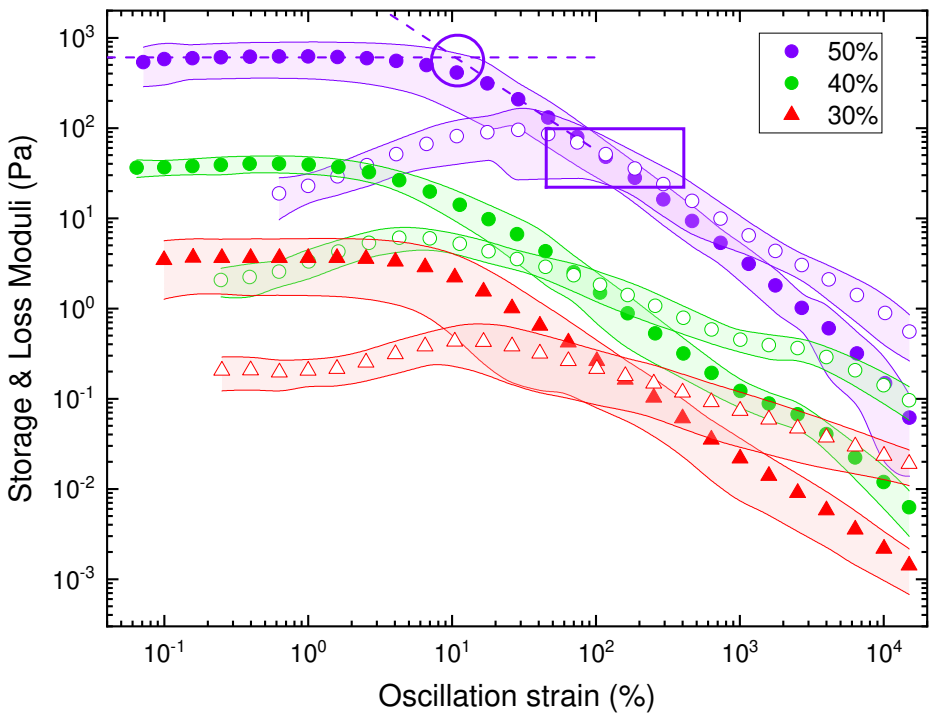

(b)

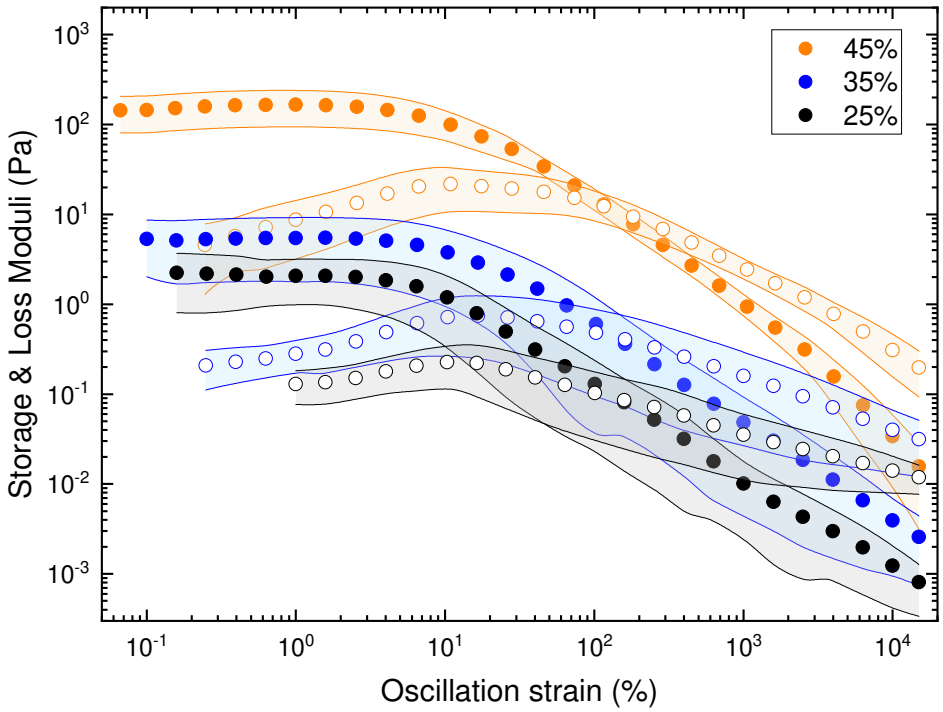

Fig. 3.9 Response of the elastic storage modulus (filled symbols) and the viscous loss modulus (unfilled symbols) of oil-in-water Pickering emulsions stabilised by between 2.5 wt. % and 5 wt. % silica across a range of oil volume percentages to changes in the applied oscillatory strain at a constant oscillation frequency ($1\,\mathrm{rad\,s^{-1}}$). (a) and (b) are for data from multiple vol. % samples which have been separated for clarity. For the 50 vol. % system a rectangle highlights the area where the cross-over between the storage and loss moduli, while the dashed lines show the fittings added to the storage moduli, with the circle showing the cross-over of the two fits. Shaded areas indicate the variation in multiple measurements of these emulsion systems.

Table 3.4. Power values for the slope of G' and G'' in the shear thinning region of Fig. 3.9, and the ratio of these two values. The power values for G' are denoted as m, while the power values for G'' are denoted as n.

50 vol. %	$G' \propto \gamma^{-1.19}$ $G'' \propto \gamma^{-0.91}$	$n/m = 1.31$
45 vol. %	$G' \propto \gamma^{-1.14}$ $G'' \propto \gamma^{-0.86}$	$n/m = 1.33$
40 vol. %	$G' \propto \gamma^{-1.15}$ $G'' \propto \gamma^{-0.58}$	$n/m = 2.00$
35 vol. %	$G' \propto \gamma^{-1.07}$ $G'' \propto \gamma^{-0.56}$	$n/m = 1.92$
30 vol. %	$G' \propto \gamma^{-1.03}$ $G'' \propto \gamma^{-0.48}$	$n/m = 2.15$
25 vol. %	$G' \propto \gamma^{-1.01}$ $G'' \propto \gamma^{-0.43}$	$n/\mathrm{m} = 2.34$

value as the strain percentage is increased, with the second fitting being a power law fit to the section of G' past the linear viscoelastic region. The intersection point of each of these fits corresponds with the inflection point for the G' curve, and together with the coefficient of the power law used, is another descriptor of the yield stress. The final method used to obtain a yield stress value from oscillatory measurements used in this chapter arises from an analysis of the shear stress vs. shear strain data. As with the previous method, extracting the yield stress from the data involves the fitting of curves. Two curves are fitted to this plot: a power law component at low strain, and then either an average, or second power law, at higher shear strain percentages. Again, the cross-over point of these two curves indicates the inflection point in the data, which can be taken to be the yield stress for each sample, while the values of the power laws used are also useful information.

The values of the yield stress extracted from the shear strain vs. G' and G'' are shown in Table 3.5. A cursory analysis of the average yield stress values collected from the two methods used on this plot demonstrates a difference between each extraction method. The average yield stress values obtained from the G' and G'' cross over are approximately twice those of values obtained from the fitting of G' across all oil volume percentage emulsions measured. While the average values obtained from the G' and G'' cross over are larger than those from the fitting of G', the range of errors obtained with the cross over of G' and G'' are also significantly larger. This results in the range of values from the cross over of G' and G'' and the values from the fitting of G' overlapping when the errors are taken

Table 3.5. Yield strain and yield stress results for a range of oil-in-water Pickering emulsions stabilised by between 2.5 wt. % and 5 wt. % silica at a number of oil volume percentages as measured via fittings of the elastic storage and viscous loss moduli responses to an increase in the oscillatory strain.

Oil volume percentage (vol. %)	Cross over of G' and G'' as a strain percentage (%)	Cross over of G' and G'' as a yield stress (Pa)	Intersection of fittings as a strain percentage (%)	Intersection of fittings as a yield stress (Pa)
25	150 ± 60	0.2 ± 0.1	5 ± 3	0.10 ± 0.07
30	140 ± 40	0.4 ± 0.3	7 ± 4	0.20 ± 0.15
35	140 ± 80	0.8 ± 0.8	10 ± 8	0.4 ± 0.3
40	80 ± 30	2.0 ± 1.5	4 ± 6	1.0 ± 0.7
45	125 ± 30	20 ± 6	8 ± 5	9 ± 3
50	100 ± 15	80 ± 40	11 ± 3	45 ± 40

into account. The significant errors that are present in the cross over of G' and G'' limit the viability of this method for the emulsion system investigated in this work.

The final oscillatory method that is used to extract a yield stress is the stress vs. strain plot, as is seen in Fig. 3.10. As with the previous oscillatory data, it is possible to extract a yield stress from the intersection of two power law fittings to the curves. This region is highlighted in a single curve in Fig. 3.10 by the purple circle superimposed on the 50 vol. %. The value for the yield stress is then taken as the stress value at this intersection point, and the values extracted for each oil volume percentage measured are shown in Table 3.6. These values, as with the previous sets, all show a slow increase at low oil volume percentages, with a greater spread between the data at higher oil percentages. There are also some interesting changes in the shape of the curves as the oil volume percentage changes. At high volume percentages (45 and 50 vol. %) the shape of the curve is readily interpreted, and can be fitted with two power law functions. When the oil volume percentage drops to 40 vol. % a secondary plateau emerges at high strain percentages. This secondary plateau is likely due to a non-standard yielding process occurring. It is proposed here that this second yielding process is due to the attractive nature of these Pickering emulsion samples, and this will be investigated further in Chapter 4. When the curves for the lower volume percentage samples (25 vol. %, 30 vol. % and 35 vol. %) are inspected this secondary yielding phenomena is not observed as a peak. However, there is an increase in the stress as the strain is increased, indicating that another yielding event may take place at a higher strain percentage.

The errors obtained for the fitting of each data presented in Table 3.6 are significant. The origin of these large errors is apparent in Fig. 3.10, where fitting of the highest and lowest

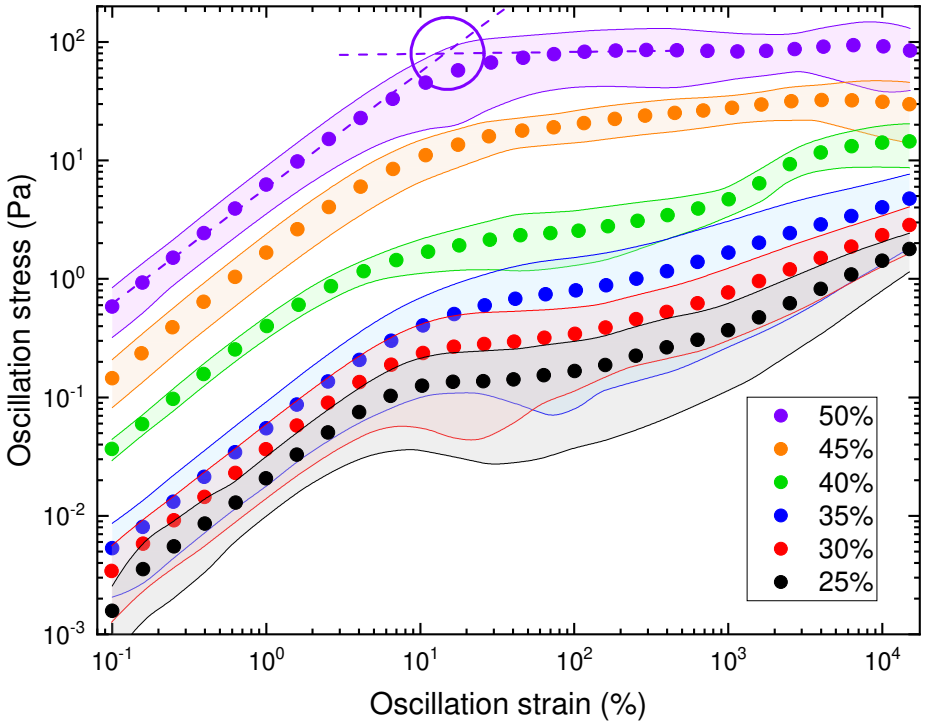

Fig. 3.10 Responses of oscillatory stress to an increasing oscillatory strain for oil-in-water Pickering emulsions stabilised by between 2.5 wt. % and 5 wt. % silica across a range of oil volume percentages. Shaded areas indicate the variation in multiple measurements of these emulsion systems. Lines are power-law fits of the behaviour well above and well below the yielding point, the intersection of which is shown by the circle (the yield stress).

Table 3.6. Yield strain and yield stress results for a range of oil-in-water Pickering emulsions stabilised by between 2.5 wt. % and 5 wt. % of silica nanoparticles at a number of oil volume percentages as measured via fittings of the oscillatory stress response to an increase in the applied oscillatory strain.

Oil volume percentage (vol. %)	Intersection of fittings of stress-strain curve (Pa)
25	0.1 ± 0.1
30	0.20 ± 0.17
35	0.4 ± 0.3
40	1.4 ± 1.0
45	15 ± 5
50	80 ± 50

data for each volume percentage results in a significant range of yield stress values. This effect is demonstrated clearly with the lower oil volume percentage emulsions, where the errors are close to the measured value. If the system is comprised of networked structures it might be expected that the rheological results would be more reproducible, and as such the errors may be lower. As the oil volume percentage is decreased the oil droplet network structure became far less populated. The limited number of oil droplets present in these emulsion systems leads to structures that may well be variable and sensitive to the shear history of the sample. Any such sensitivity would result in rheological measurements that would vary in their magnitude, thus giving rise to large errors.

The power laws that were fitted all had very similar values of the power used for each fitted section. The first increase in stress seen at each volume percentage was found to have a relationship of $\gamma^{0.99\pm0.02}$. The secondary increase seen in the samples 25 vol. %, 30 vol. %, 35 vol. % and 40 vol. % had an increased range of slopes, with an average value of $\gamma^{0.52\pm0.14}$. The similarity of the coefficients for each yielding step indicates that the microscopic rearrangements that occurred at each step were similar across the range of oil volume percentages investigated here. This is consistent with work by others that investigated multistage yielding processes in colloidal glasses, and theorised that two distinct processes occur [13]. The behaviour of these multi-step yielding processes will be further investigated in Chapter 4.

3.3.4. Creep test and creep recovery

The final method utilised to determine the yield stress of these emulsion samples was a creep test. Creep and creep recovery testing is a method for determining the yield stress of a material with great accuracy. However, that accuracy is dependent on the user having sufficient time, and sample, available to carry out repeated measurements with slight variations in the applied stress. This method was utilised with two different oil volume percentage samples after all of the previous methods had been completed, and a range of yield stress values had been extracted for each sample. The results for these two emulsions are shown below.

The first emulsion analysed with the creep test was a 40 vol. % sample. The results of this are displayed in Fig. 3.11, where it is apparent that there were two groupings of curves. These two groups of data demonstrate the difference between a sample which has yielded, and one which has not. The 9 Pa and 10 Pa curves demonstrate previously unyielded sample, which is defined in this experiment by the lack of any significant change in the strain experienced by the sample as the experiential time progresses. This lack of movement of the sample is due to the applied stress not being sufficient to disrupt the network of oil droplets throughout the material, leaving the material acting as a solid where the applied stress is dissipated in an elastic manner. The four remaining curves show a very different behaviour over time. These curves, where the applied stress is greater than 12 Pa, show a significant change in the measured strain as the experiment time progresses. This demonstrates that the emulsions yielded, or that the network of oil droplets inside the material were disrupted by the applied stress. This disruption results in a liquid-like material which flows as the stress is continually applied over the course of the experiment.

During the recovery phase of each experiment, both the yielded and unyielded samples demonstrated a subtle but notable difference in the data obtained. In Fig. 3.11 the recovery or relaxation data is denoted by the open symbols. Initially, the unyielded data demonstrated a small drop in the measured strain when the applied stress is removed. This is due the release of the elastic energy stored in the slight deformation of the material's network structure. As this energy was released, the emulsion moved back towards the original configuration of droplets within the sample. In comparison, the relaxation step seen in the yielded samples demonstrated a different response. These yielded samples showed no change in the measured strain as the applied stress was removed. This was due to there being no elastic energy stored in the droplet network of these emulsions after they have yielded. The applied stress during the creep phase was sufficiently large to break-up

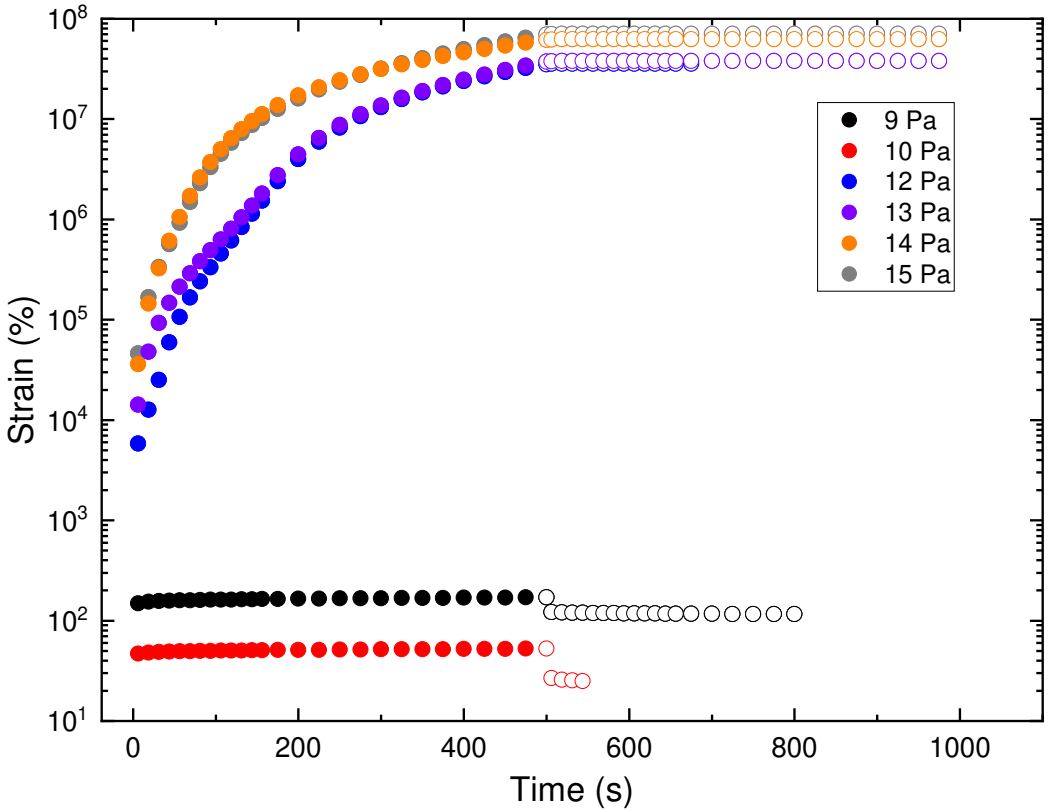

Fig. 3.11 Time dependence of strain obtained from several creep experiments run on an emulsion with an oil volume of 40%. Each set of data shown was taken with a new volume of emulsion being loaded, and with the specified stress being applied. Filled symbols indicate the time over which the stress was applied, while unfilled show the relaxation period with no applied stress.

the network of droplets in the sample, which resulted in the applied stress being dissipated through the flow of the sample. The lack of energy stored in the network meant the sample was not able to "bounce back" to its original form.

It would have been expected that the lowest applied stress would have the smallest strain deformation, while the highest applied stress would be expected to deform the largest amount with a large strain. Somewhat counter-intuitively this did not appear to be the case for this set of data (and others presented in this work), with increases in the applied stress not necessarily leading to increases in the resultant strain. However, this did not alter the measurement of the yield stress with this experiment. This scatter in the measured data was not able to be immediately repeated, an indication of possible differences in the structure of each individual loaded emulsion sample.

The determination of the yield stress is carried out via repeated measurements at different applied stresses. Once a range of measurements were compiled, the yield stress was determined by finding the split in the groupings of data. The stress at which the slope of the curves change significantly is the yield stress for the material. For example, the data shown in Fig. 3.11 shows a delineation between the 10 Pa and the 12 Pa curves, indicating that the yield stress for this sample is between these two values ((11 ± 1) Pa).

Repeating these creep experiments on a 30 vol. % emulsion affords the results that are provided in Fig. 3.12. As with the 40 vol. %, there is a notable change in strain percentage as the sample yields. Again, the samples with the lowest change in strain percentage over time were the unyielded samples (black and red markers). These two samples were again able to elastically dissipate the applied stress without significantly increasing the measured strain. When the applied stress was removed in the relaxation step, the measured strain dropped as the sample releases the energy store elastically in the droplet network. Samples with applied stresses greater than the two unyielded measurements showed a large increase in the measured strain percentage across the measurement time. This is similar to that observed for the 30 vol. % samples, where the stresses applied were sufficient to break the network structure in the emulsion, leading to the sample being unable to store the applied energy elastically, and instead dissipating the energy in a viscous manner. The yield stress value for the 30 vol. % emulsions were deduced to be between 0.9 Pa and 0.95 Pa ((0.925 ± 0.025) Pa).

There is one obvious outlier in Fig. 3.12 — the measurement with 1.1 Pa. This data set showed elastic-like behaviour at a short experimental times, followed by a rapid increase in the measured strain at $\sim$350 s, after which the sample exhibited shows viscous-like be-

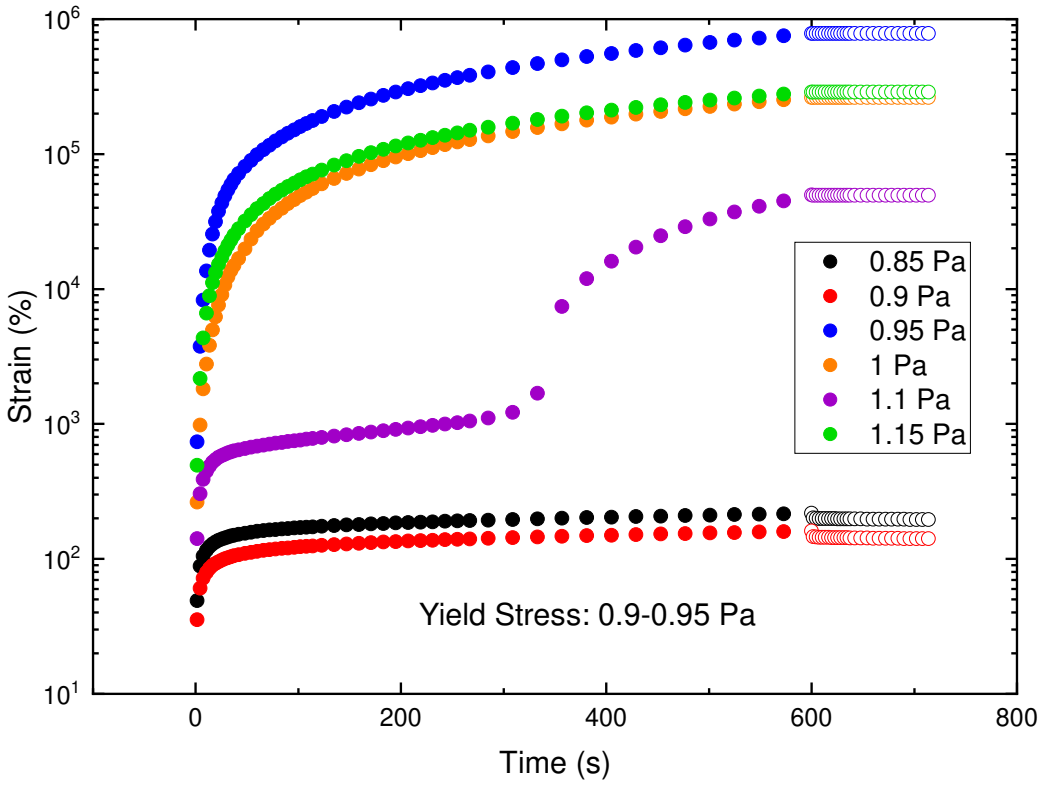

Fig. 3.12 Creep and creep recovery tests for 30 vol. % oil-in-water Pickering emulsions stabilised by 3 wt. % of silica nanoparticles. The creep is applied at the given stress (see legend) for 600 s, after which the applied stress is released for 180 s. The groupings of the data demonstrate the yield stress to be between 0.9 Pa to 0.95 Pa.

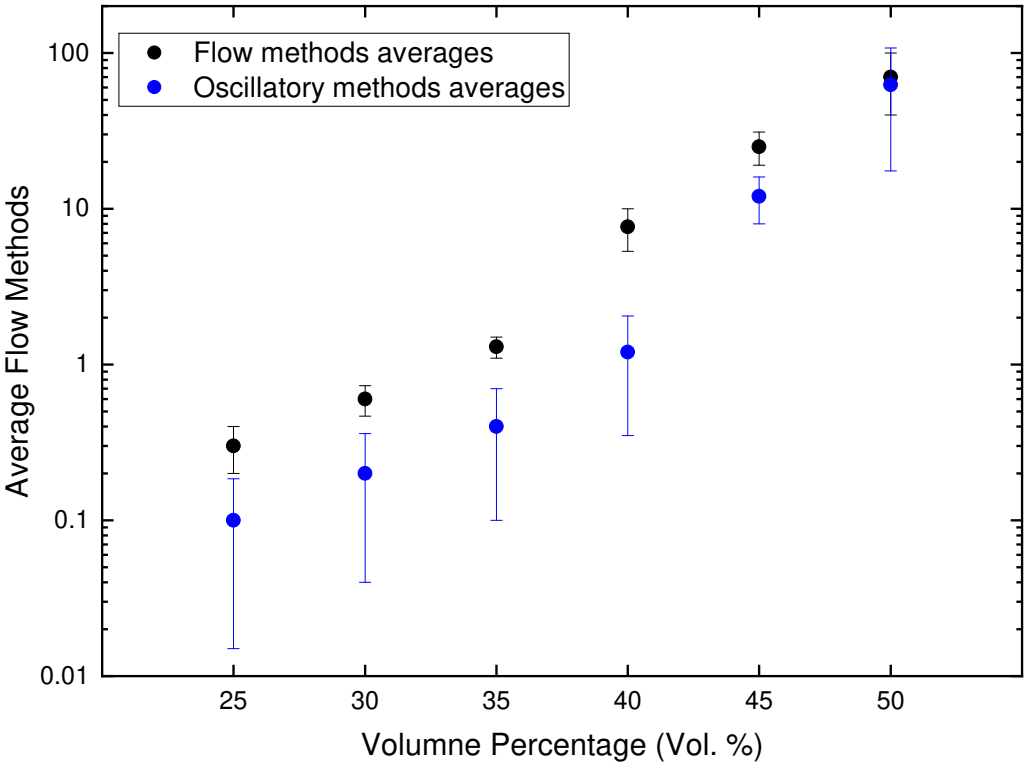

Fig. 3.13 Average values of the yield stress for oil-in-water Pickering emulsions stabilised by between 2.5 wt. % and 5 wt. % of silica nanoparticles at different oil volume percentages, measured through flow methods or oscillatory methods.

haviour. This behaviour was unexpected for this type of material, and was not immediately repeatable at this applied stress, but was also seen on other occasions (not shown here). The shape of the curve for the 1.1 Pa is similar to that seen in creep experiments analysing the fracture of steel [170] – this may suggest that there is a stress build up and fracture of the emulsion network in the present case. Further work would be required to test this hypothesis.

3.4. Comparisons of yield stress methods and conclusions

In the past, there has been significant debate in the literature about both the best method to measure a yield stress, as well as if a yield stress is even a "real" property of any material. In this work, a range of methods have been utilised to measure a number of different yield stress values. Figure 3.13 provides a summary highlighting the differences between the average values for the yield stress measured by flow methods (low shear average, Herschel-Bulkley fit, and Bingham fit) compared to the average values of obtained by oscillatory fitting methods (stress-strain curve fitting and strain sweep curve fitting).

Table 3.7. Relationship between oil volume percentage and the yield stress measured for a range of oil-in-water Pickering emulsions stabilised by between 2.5 wt. % and 5 wt. % of silica nanoparticles.

Method	Scaling of yield stress
Low shear stress average	$\approx \phi_{oil}^{12\pm2.6}$
Herschel-Bulkley fit	$\approx \phi_{oil}^{13\pm2.2}$
Bingham fit	$\approx \phi_{oil}^{11\pm2.5}$
Storage/loss moduli cross–over	$\approx \phi_{oil}^{16\pm2.9}$
Storage modulus inflection point	$\approx \phi_{oil}^{17\pm2.8}$
Stress-strain inflection point	$\approx \phi_{oil}^{18\pm0.9}$

The data in Fig. 3.13, and the data for each individual method (not shown) show a positive power law shape to the yield stress as the oil volume percentage is increased. This marked increase in the strength of the emulsion as the oil volume percentage increases is an anticipated trend that can be explained by the growing number of network elements present in the emulsion samples [171]. When the yield stresses are compared for each method, the data follows an exponential growth with an offset y-axis intercept. This demonstrates that these emulsion systems demonstrate a minimum yield stress at low volume percentages. This is due to a weakly associated network forming between the oil droplets, even at low oil volume percentages, which results in a material that is able to demonstrate elastic behaviour. For each measurement technique this relationship was fitted with Equation 3.2, in which σ_y is the measured yield stress, σ_{y0} is an offset factor (or the minimum yield stress for the given material), ϕ_{oil} is the oil volume percentage, and C is the scaling factor.

$$\sigma_y = \sigma_{y0} + \phi_{oil}^{C} \tag{3.2}$$

The resultant scaling factors for each individual method are listed in Table 3.7, and demonstrate that increasing the oil volume percentage of an emulsion has a strong affect on the measured yield stress of the material. The scaling of each method is also found to vary, indicating that as the structure of the emulsion changes, the method chosen to measure the yield stress can lead to notable differences in the reported yield stress. The fitted oscillatory methods both display a higher dependence on the oil volume percentage, with scaling values of $\approx \phi_{oil}^{17\pm2.2}$, compared to the scaling values of $\approx \phi_{oil}^{12\pm2.4}$ obtained via the viscous flow methods.

While the yield stress values obtained at each oil volume percentage are similar, there is a

Table 3.8. Yield stress values for two selected oil volume percentages as extracted from multiple different methods

Oil volume percentage	30 vol. %	40 vol. %
Low shear average of flow curve (Pa)	0.6 ± 0.1	9 ± 2
Herschel-Bulkley fit of flow curve (Pa)	0.6 ± 0.2	6 ± 2
Bingham fit of flow curve (Pa)	0.6 ± 0.1	8 ± 3
Stress-strain curve fitting (Pa)	0.20 ± 0.17	1.4 ± 1.0
Strain sweep curve cross–over fitting (Pa)	0.4 ± 0.3	2 ± 1.5
Strain sweep curve fitting (Pa)	0.20 ± 0.15	1 ± 7
Creep experiment (Pa)	0.925 ± 0.025	11 ± 1

separation in the yield stress values obtained by oscillatory or flow methods, while the yield stress values from the storage/loss moduli cross-over point is exceptionally varied. When comparing the individual methods used to extract a yield stress, the creep method gave rise to the largest interpreted yield stress at each oil volume percentage. Comparing the flow rheology and fitted oscillatory techniques, the fitted oscillatory methods are consistently lower. This is demonstrated in Table 3.8, where the yield stress values for 30 vol. % and 40 vol. % are compared for each method.

It is known that the shear history of a viscoelastic material, such as these emulsions, can have an effect on the measured properties [131]. Due to this dependence, characterising an accurate value of the yield stress is often a challenging process. Of the methods utilised here, the creep experiment can be viewed as the value with the least artifacts due to rheological shear history [14]. This is due to the step-wise nature of this measurement, where a single sample is used per stress measurement. This "new" sample for each measurement removes the need to consider the shear history of the material that may be imparted from previous applied stresses. Due to the lack of network damage that could be caused by the shear history of a material, the values obtained for the yield stress with these creep measurements are larger than that seen with any of the other measurement methods utilised.

While the values obtained from a creep measurement are not affected by network damage from the shear history, they are a cumbersome measurement, and are largely inefficient for measuring the yield stress of a large number of samples. Due to this, the yield stress of a material is often measured via a flow rheology method, where stress is plotted against shear rate. This method can be carried out with either an increasing or decreasing shear rate,

and the results of these may not always be comparable. An increasing shear rate is the preferred method where the material shows thixotropy (which Pickering emulsions often do), as the shear history will be less affected by an initial low rate of shear [131]. The yield stress that is extracted from this increasing shear experiment is known as the static yield stress. A static yield stress is thought to be the stress required to begin flow in a material, and will often be lower than the dynamic (the minimum stress required to maintain flow) yield stress [131, 133]. While this low shear rate history will have a smaller effect, it will result in some change. This is seen in the data of Table 3.8, where the values obtained via these flow curve methods are systematically lower than that of the creep experiments.

The other experiment type that was used to measure yield stresses for these emulsions systems were oscillatory measurements. As these are dynamic measurements, which require stepping through shear strains throughout the measurement, they also impart a non-zero shear history onto the sample. There were three values extracted from these oscillatory measurements, each of which defines the yield stress at a different unique point. The first, and most primitive, method utilised is the cross-over point of G' and G''. This point is known as the characteristic modulus, and is the point at which the viscous behaviour of the material becomes the dominant feature. While this point is easily definable, it does occur after a significant amount of viscous dissipation has already taken place. Due to this, defining this point as the yield stress is a flawed exercise, as the material has already begun to flow at this point. The flow that has occurred will result in the applied yield strain and stress that is reported being larger. The second method applied to the oscillatory data was the fitting of the storage modulus in order to determine the inflection point. As this inflection point is the first point at which the elastic behaviour begins to decrease, the stress at this point can be considered to be the yield stress. The yield stresses obtained from this inflection point was found to be smaller than that obtained via the flow methods. This is due to the oscillatory strain that was applied to the material being low enough to not cause significant disruption to the elastic network structure of the emulsion system. There were additionally what appear to be other inflection points in some of the data presented. These secondary inflection points are attributed to multistage yielding processes, and will be investigated in later chapters. Finally, when the oscillatory data was plotted as oscillatory stress vs. oscillatory strain, the yield stress was again extracted by determining the inflection point in the data. The values of the yield stress that were extracted from this method were found to be exceptionally varied at each volume percentage. The range of these data demonstrates the variation in the viscous dissipation

of the materials.

This chapter has reported and compared a number of methods that can be used to measure the yield stress of Pickering emulsions. The yield stress of six emulsions with varied oil volume percentages were evaluated and compared. It was demonstrated that the oil volume percentage of the emulsions, unsurprisingly, had a significant affect on the yield stresses measured. This is consistent with the formation of network structures between the oil droplets, which become greater at higher oil volume percentages.

There were multiple methods used to measure the yield stress, and the differences between each have been compared. The creep and relaxation methods demonstrated the largest yield stress at each oil volume percentage investigated. While the creep experiment allows accurate measurements, it is also the most time consuming, and can be prone to user error or sample variation over time. Flow methods that were used in this chapter were found to be similar to one another. This is due to the similarities of the fitting equations used to extract yield stresses from the data. Oscillatory experiments were demonstrated to have a number of different methods to measure the yield stress of these emulsions. Comparisons between the oscillatory methods have been made, and it has been demonstrated that there can be significant differences between the evaluated yield stresses.

The use of these different methods to determine the yield stress has shown that the chosen definition of the yield stress is an important factor that must be considered. The best definition of the yield stress is the point at which the material is no longer able to elastically store energy, and must instead flow. When considering this definition, it becomes clear that some of the methods used to gather the yield stresses presented in this chapter do not fit well with this definition. The cross-over point of the G' and G'' is one of these methods, as at this point viscous dissipation has already begun. The inflection point of the storage modulus does, however, appear to fit well with the definition of the yield stress. This has been described as the point at which the emulsion begins to drop in elastic behaviour, indicating that the material has begun to flow. Flow rheology techniques are a standard and quick method for the determination of the yield stress. Each of the methods used to fit the flow rheology data demonstrate similar resultant yield stresses, the values of which were higher than the corresponding oscillatory fits. While this is likely due to the flow induced in the system, these methods still remain a common and viable method for the determination of the yield stress in viscoelastic materials.

These emulsion systems were also imaged using a number of microscopy techniques, demonstrating the network structure formed by emulsion droplets, while also showing the

structure of the individual emulsion droplets, including the silica nanoparticle coating.

Another of the rheological properties of these emulsions that was studied was the viscosity. It was found that the low shear viscosities of the emulsions were affected by the changing oil volume percentage of these systems. This, along with microscopy images, demonstrate the network structure formed between these emulsions. In comparison, the high shear viscosities of each emulsion were similar, indicating that high shear rates break down the network into smaller component structures.

One notable feature of the data demonstrated in Fig. 3.10 was the occurrence of multi-step yielding processes breaking down network structures present in the emulsion systems. Other groups have proposed that these occur due to attractive interactions between colloidal particles[12, 13, 15, 142]. These processes will be further investigated in the next chapter through the alteration of the interactions between the oil droplets.

4 Using salt to manipulate the flow behaviour of Pickering emulsions

4.1. Introduction

In the previous chapter emulsions were prepared with a silica nanoparticle coating to investigate a range of methods for measuring the yield stress of an emulsion. The emulsions that were prepared for this were demonstrated to have attractive interactions between the oil droplets. The extent of attraction between the silica nanoparticles stabilising these emulsions was modified for the work in this chapter, resulting in emulsions with differing interactions between the oil droplets.

The work reported in this chapter demonstrates one method for modifying the interactions between Pickering emulsion droplets, ranging from attractive through to repulsive. The silica nanoparticles used to form Pickering emulsions in this study are weakly acidic when dispersed in aqueous systems, yielding negative surface charges on the silica particles. The interactions between these silica nanoparticle-coated Pickering emulsion droplets were modified through the addition of sodium chloride to the aqueous continuous phase. The resultant changes in emulsion properties caused by these modified interactions were investigated through multiple methods, including microscopy and rheology. This chapter reports on the rheology of Pickering emulsions stabilised by silica nanoparticles which have had the repulsive interactions screened through the addition of NaCl to the aqueous phase. It was anticipated that above a given NaCl concentration the surface charge will be sufficiently screened, so that the attractive van der Waals forces between these colloidal particles overcome the diminished repulsive electrostatic interactions. Emulsions with this level of salt will be referred to as being “attractive” and “high salt”, while those with a

lower salt concentration will be referred to as "repulsive" or "low salt". The results of these changes in surface charge screening were demonstrated to alter the bulk physical properties of the emulsions, while also resulting in some complex flow behaviours in a number of situations. These phenomena are discussed in this chapter, along with proposals for their physical origins. The results presented here demonstrate progress towards understanding of the microscopic processes that occur as emulsions yield, and how altering the interactions between oil droplets can influence these processes.

4.2. Experimental methods

4.2.1. Materials

The Pickering emulsions in this chapter were prepared in a similar manner to those in Chapter 3. The emulsions were prepared as oil-in-water (o/w) emulsions with the oil phase being comprised of a 60:40 (vol. % : vol. %) mixture of isopropyl myristate and dodecane. This particular mixture of oils was chosen due to the isopropyl myristate adding some slight hydrophilicity to the discontinuous phase allowing for improved wetting of the charged silica stabiliser.

In order to alter the interactions between the emulsion droplets the ionic strength of the aqueous phase was changed. This was carried out with the addition of concentrated NaCl solutions. Here it is assumed that NaCl is an ideal, inert, and indifferent electrolyte, resulting in the ionic strength being directly predictable from the concentration of NaCl in the aqueous phase of the emulsion.

Synthetic fumed hydrophilic silica nanoparticles were employed as the emulsifier in these systems, which were used after being dried in an oven at ≈150 °C for at least 12 h. This pretreatment was found to increase the stability of the resultant emulsions at high and low salt concentrations (results not included). The mass loss of the silica with temperature was investigated via thermogravimetric analysis (TGA), a technique which involves the weighing of a sample as the temperature is increased in a controlled manner. The use of TGA allows any mass loss from heating to be quantified, however it does not give a direct answer as to what the lost mass is comprised of. The TGA results for the N20 silica is demonstrated in Fig. 4.1, which shows the effect that an increased temperature has on the mass over time. A 3.7 % mass loss was observed by 100 min after the temperature had been held at 150 °C for over 90 min. This mass loss is attributed to evaporation of water. Following this there is a small increase in the mass as the experiment continues (0.9 %).

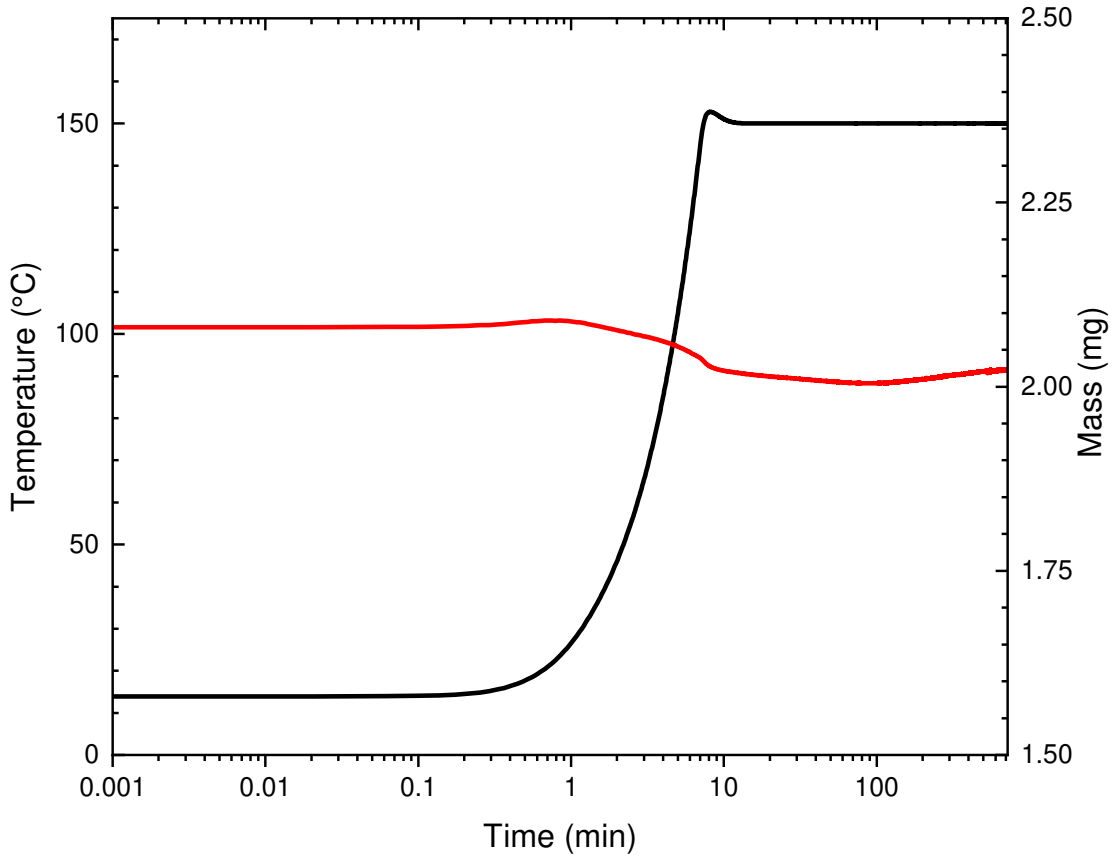

Fig. 4.1 Thermogravimetric analysis of N20 silica demonstrating the mass change (red) and temperature (black) over time as the temperature was increased at a rate of 20 °C min^{-1} up to a max temperature of 150 °C which was maintained for 12 hours.

4.2.2. Zeta potential measurements

As has been discussed in Sections 1.4.1.5 and 2.2, zeta potential is an indication of the surface charge of a particle, and therefore can be used as a measure of the interaction between the nanoparticles. The work in this chapter reports Pickering emulsions with differing interactions between the oil droplets coated with silica nanoparticles. The silica nanoparticles that were used here have a substantial surface coating of Si-OH groups (silanol) which, in aqueous systems, will deprotonate to a pH dependent extent leaving $Si\text{-}O^-$ groups (the pKa of silanol groups have been calculated to be between 8.5 ± 0.6 and 5.6 ± 0.6 dependent on the orientation of the hydrogen-bonded water [172]). While the extent of silanol deprotonation will be pH dependent, the present study has a continuous phase that is water with varied concentrations of NaCl, and as such would not be expected to change between samples. The pH reported for 4 % aqueous dispersions of these silica nanoparticles is 3.8 to 4.3, demonstrating that there is a significant amount of deprotonation in aqueous media [173]. This leaves a net negative surface charge that will lead to a repulsive interaction between the silica nanoparticles. The effect of the surface charge of these nanoparticles can be altered by screening the charges through changing the concentration of the aqueous phase electrolyte. Adding electrolyte to the aqueous phase will reduce the Debye length, and therefore the repulsive interaction between the nanoparticles. The magnitude of the effective charge of the silica nanoparticles at the slip plane can be measured by the zeta potential.

In order to quantify what effect the addition of electrolyte has on the interactions between of the silica nanoparticles a series of silica dispersions were prepared. The electrolyte concentration of these dispersions was altered from 10^{-7} M (theoretical ionic strength of Milli-Q water) through to 0.1 M NaCl. The zeta potential of these silica dispersions was then measured multiple times (Section 2.2). The average and standard deviation of between four and twelve reported values at each of the salt concentrations (each reported value is the average of three measurements with up to 100 scans) are provided in Table 4.1.

4.2.3. Emulsion preparation

As was briefly outlined in Section 2.3, the emulsions for this chapter were created by first weighing the appropriate amount of oven dried N20 silica nanoparticles into a 50 mL centrifuge tube. The silica nanoparticles were then wet initially with the aqueous phase, Milli-Q water, before the oil phase was added (a 60:40 mixture of isopropyl myristate and dodecane). The mixture was then homogenised with a Miccra D-9 high-speed homogeniser

at 39 000 min^{-1} for 2 min. The initial stock emulsion was prepared with ≈5 wt. % silica, and 30 vol. % oil.

4.2.4. Emulsion dilution

The initial stock emulsions were diluted with either Milli-Q water, or NaCl solutions (0.2 M and 3 M). These emulsions were diluted from an initial oil volume percentage of 30 vol. %, to a final oil volume percentage of 20 vol. %. The diluted emulsions had a NaCl concentration of either 10^{-4} M (repulsive, low salt), 0.066 M (intermediate, only carried out with a limited range of experiments), or 1.66 M (attractive, high salt), with each having a silica weight percentage of 3.45 wt. %.

4.2.5. Droplet analysis

The size distribution and morphology of the droplets present in the attractive and repulsive Pickering emulsions were analysed by using optical microscopy and laser diffraction techniques. Optical microscopy was carried out in dilute emulsions (≈1.25 vol. %) in order to reduce the scattering effects of multiple layers of emulsion droplets. The diluted samples were loaded onto a welled glass slide and images were captured on a Zeiss Axiophot microscope with both 10× and 40× magnification objectives in order to highlight the various structural features. Confocal microscopy was utilised to demonstrate the distribution of the materials throughout the emulsion samples. For confocal microscopy each emulsion had $\approx 9 \times 10^{-4}$ M Nile Blue added as a charged aqueous stain, and $\approx 9 \times 10^{-4}$ M Nile Red added as an oleophilic stain. The Nile Blue dye was excited with a 633 nm laser, with the emission captured between 634 nm to 781 nm. The Nile Red dye was excited with a 514 nm laser, with the emission captured between 518 nm to 627 nm. Laser diffraction was carried out using a Mastersizer 3000 (Section 2.7).

4.2.6. Rheological measurements

One of the most important properties to characterise with these emulsions is the difference in the bulk rheology. This chapter reports and interprets these differences in the bulk rheology. The rheological properties of these emulsions were measured within three days of preparation in order to maintain a consistent droplet size distribution across all measurements (see Section 3.3.1). Rheological data were collected as averages of multiple measurements (between four and eight for each method, with the exception of the medium salt emulsion which is presented as a single data set), with error bars calculated as a stan-

dard deviation. Measurements for the average data presented in this section were carried out using a 40 mm parallel plate geometry at a gap height of 400 µm on a DHR-2 rheometer. These results were also compared with data obtained using a 40 mm hatched plate geometry at a gap height of 400 µm, and a double walled couette geometry, with the results being found to be comparable across each tool (results not shown here).

4.2.6.1. Flow measurements

Flow curve experiments were performed with an increasing shear rate from $0.1\,s^{-1}$ to $1000\,s^{-1}$ with 10 data points per decade, and 20 s of averaging per point measured, after a 10 s conditioning step.

4.2.6.2. Strain sweep

Strain sweep measurements were all performed across the strain range of 0.03 % to 2852 % at a constant frequency of $1\,rad\,s^{-1}$, with 10 data points measured per decade for the high and low salt emulsions (20 per decade for the intermediate salt emulsion), and 10 s averaging time per point for the high and low salt emulsions (5 s for the intermediate salt emulsion), after a 5 s condition step per data point. The strain vs. stress, G', and G'' curves were evaluated for each material. The range of strains chosen here allowed for full coverage of the areas of interest for each emulsion measured, showing both the elastic state of the emulsions at low strain percentages, and the viscous nature of the systems at high strain percentage.

4.2.6.3. Frequency sweep

Frequency sweep measurements were performed at a strain percentage that was found to be within the linear viscoelastic region from the previous strain sweep measurements. The strain percentage used for each measurement in these experiments was 0.4 % to 1 %. The frequency range that was used for these experiments was $0.1\,rad\,s^{-1}$ to $250\,rad\,s^{-1}$, with 10 data points per decade.

4.3. Results and discussion

4.3.1. Zeta potential measurements

The data presented in Table 4.1 suggests that as the NaCl concentration is increased the zeta potential tends towards zero for these suspensions. This is consistent with changes in

Table 4.1. Zeta potential of 0.1 wt. % silica nanoparticle dispersions as the NaCl concentration is increased.

Salt concentrations (M)	Average zeta potentials (mV)
10^{-7}	-25 ± 7
10^{-4}	-29 ± 3
10^{-3}	-18 ± 1
10^{-2}	-12 ± 2
2.5×10^{-2}	-9 ± 2
5×10^{-2}	-4.5 ± 3
10^{-1}	-5 ± 2

the screening of the silica nanoparticles surface charge, through significant reductions in the Debye length from 300 nm at 10^{-7} M NaCl to 0.96 nm when the salt concentration is increased to 10^{-1} M NaCl. This shows that the Debye length was significantly larger than the diameter of the silica nanoparticles at 10^{-7} M NaCl. However, when the NaCl concentration was increased to 1×10^{-1} M the Debye length dropped significantly, demonstrating that the system is likely to display attractive interactions between the silica nanoparticles.

Previous researchers have demonstrated that many colloids with an absolute zeta potential value greater than 20 mV are moderately stable, or can be classed as "repulsive" in the nature of the interaction between particles [174]. A colloidal dispersion with a zeta potential with an absolute value less than 20 mV is deemed to be unstable, forming aggregates, or demonstrating an "attractive" interaction between particles.

Table 4.1 shows that at low NaCl concentrations (i.e. $<10^{-3}$ M) the zeta potential is greater in magnitude than 20 mV, and is therefore expected to have a repulsive interaction between the nanoparticles in the dispersion [174]. As the NaCl concentration is increased the zeta potential becomes less negative, tending towards 0 mV, indicating that at high salt concentrations the interaction between the nanoparticle dispersion will be expected to be attractive. The changes in the zeta potentials with NaCl concentration gives scope to further investigate the effects that this change in salt will have on the interactions between emulsion droplets stabilised by this silica. Throughout the work presented in this chapter emulsions are described as one of three salt levels; low salt 1×10^{-4} M NaCl, intermediate salt 0.066 M NaCl, and high salt 1.66 M, each giving rise to characteristic behaviours.

The interaction energies for a number of these silica suspensions at different salt concen-

trations were calculated using DLVO analysis. This is for silica particles alone dispersed in an aqueous continuous phase. The interactions of silica-coated oil droplets in aqueous continuous phase has not been considered here. DLVO analysis involved the calculation of both the attractive, and repulsive interactions between pairs of silica nanoparticles. The DLVO equations used in this chapter assume the two interacting bodies to be identical spherical particles. The silica particles used in this chapter are not spherical particles, but instead are fractal agglomerations of smaller spherical particles. However, for the DLVO calculations these fractal silica particles are assumed to be spherical with a radius of 125 nm. The repulsive interaction, as a function of separation, $\phi_R(D)$, were calculated by Equations 1.2 and 1.3 [23, 24, 48, 57].

$$\phi_R(D) = \frac{32\pi\varepsilon\varepsilon_0 a k_B^2 T^2 \gamma^2}{e^2 z^2} \exp(-\kappa D) \tag{1.2}$$

$$\gamma = \frac{\exp(\frac{ze\varphi_d}{2k_B T}) - 1}{\exp(\frac{ze\varphi_d}{2k_B T}) + 1} \tag{1.3}$$

In these equations ε and ε_0 are the relative dielectric constant, and the dielectric constant of a vacuum respectively, while a, k_B, T, e, and z are the particle radii, Boltzmann constant, absolute temperature, the charge of an electron, and the valence of the ions respectively. κ and D are the inverse double layer thickness and the interparticle separation respectively, and γ is described in Equation 1.3, where φ_d is the potential energy at the Stern layer (taken as the zeta potential in this work). The salt concentrations of the suspension (c) is accounted for as a component of the κ term along with R as the gas constant, and F as the Faraday constant, as described by Equation 1.4.

$$\kappa^{-1} = \sqrt{\frac{\epsilon\epsilon_0 RT}{2 \times 10^3 F^2 c}} \tag{1.4}$$

The attractive interaction as a function of distance between two spheres ($\phi_A(D)$) is described by Equation 1.5 [58].

$$\phi_A(D) = -\frac{H}{3}\left[\frac{a^2}{D(4a+D)} + \frac{a^2}{(2a+D)^2} + \frac{1}{2}\ln\left(1 - \frac{4a^2}{(2a+D)^2}\right)\right] \tag{1.5}$$

In this equation H is the Hamaker constant for the given material. The Hamaker constant used for the fumed silica nanoparticles was taken to be 6.3×10^{-21} J [57]. The repulsive and attractive components can be summed, resulting in the total interaction at a given particle separation (Equation 1.6).

$$\phi_T(D) = \phi_R(D) + \phi_A(D) \tag{1.6}$$

These calculations were carried out for silica suspensions across a range of salt concentrations, and the results are demonstrated in Fig. 4.2. These plots demonstrate the screening effect that the addition of salt is predicted to have on the repulsive interactions between the silica particles. At low salt concentrations ($<10 \times 10^{-3}$ M) the repulsive interaction is the dominant force across most separation distances with a primary peaks of $\approx 75\, k_B T$, $\approx 90\, k_B T$ and $\approx 25\, k_B T$ at a separation distances of 7.9 nm, 2.2 nm and 2.1 nm for 1×10^{-7} M, 1×10^{-4} M and 1×10^{-3} M NaCl concentrations respectively. This results in particles that are repulsive to one another. As the salt concentration is increased, the repulsive interaction between the silica particles decreases, leaving the attractive forces as the dominant feature over all interparticle distances, with no primary repulsive peak evident in the 0.1 M NaCl dispersion. There is a small primary peak of $\approx 2\, k_B T$ at a separation distance of 2.4 nm in the 1×10^{-2} M NaCl dispersion, however this is not sufficient to provide a repulsive interaction between the nanoparticles. The dominant attractive force across these high salt systems will result in the aggregation of the silica particles, and the formation of an attractive network. In both the low and high salt calculations it is calculated that there is a strong attractive interaction at small particle separation distances. This attractive interaction is demonstrated macroscopically as the sedimentation of the particles over time. Each suspension demonstrated some degree of sedimentation over time, suggesting that the particles do progressively aggregate.

It is important to note that these calculations are an incomplete view of the interactions that are between the particles in the silica suspensions. There have been assumptions made about the particle size, shape, and charge distribution, while other interacting forces such as hydration, and any strong ion pairing interactions between the sodium ions and the silica surfaces are not considered. Additionally, when these particles are used to stabilise emulsions, the particles will become fixed at the interface. This will result in changes to the interaction energy due to the partial wetting of the silica by each liquid. As such, the resultant figures are only a guide as to the interactions between these fumed silica suspensions.

4.3.2. Emulsion microstructure

Laser diffraction analysis of these emulsions shows a slight difference between the size distributions of the high and low salt emulsions. This is demonstrated in Fig. 4.3, where the

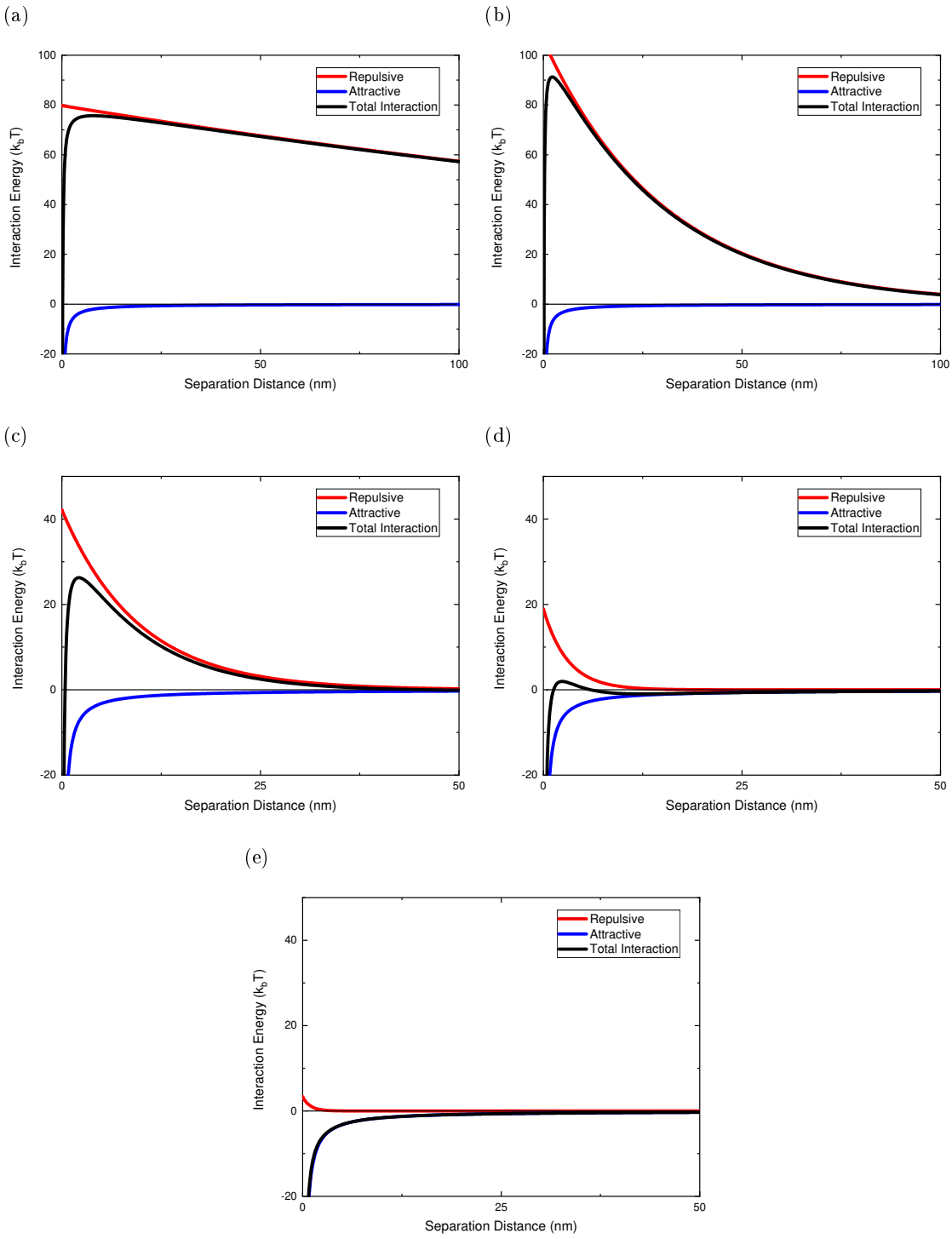

Fig. 4.2 Potential energy curves of the interaction between two spherical particles at a range of salt concentrations, each of which has a different zeta potential. (a) 10^{-7} M NaCl, 25 mV, primary peak: $\approx 75\, k_B T$ at 7.9 nm (b) 0.0001 M NaCl, 29 mV, primary peak: $\approx 90\, k_B T$ at 2.2 nm (c) 0.001 M NaCl, 18 mV, primary peak: $\approx 25\, k_B T$ at 2.1 nm (d) 0.01 M NaCl, 12 mV primary peak: $\approx 2\, k_B T$ at 2.4 nm (e) 0.1 M NaCl, 5 mV. (ε, 78.54, a, 125 nm, T, 298.15 K, A, 6.3×10^{-21} J, κ, $3.29 \times 10^{7}\,\mathrm{nm}^{-1}$).

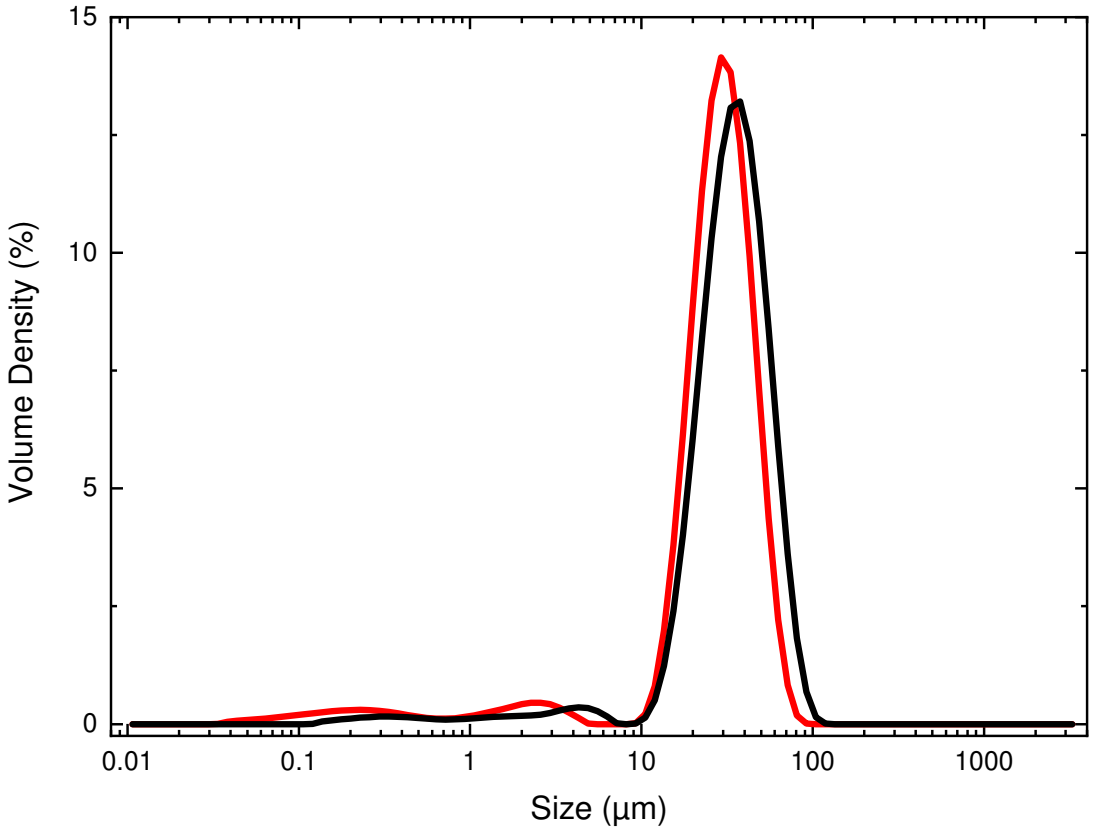

Fig. 4.3 Size distribution of 20 vol. % oil-in-water Pickering emulsions stabilised by 3.45 wt. % of silica nanoparticles at high salt (1.66 M, black, D [4,3], D_v (10), D_v (50), D_v (90): 36.3 µm, 17.9 µm, 34.3 µm and 58.9 µm, uniformity, span: 0.382, 1.196) and low salt concentration (1×10^{-4} M, red, D [4,3], D_v (10), D_v (50), D_v (90): 31.7 µm, 18.0 µm, 29.8 µm and 48.4 µm, uniformity, span: 0.373, 1.153) as measured by laser diffraction.

average size distributions of a set of attractive and repulsive emulsions are shown. Figure 4.3 shows a largely monomodal size distribution at ≈34 µm and ≈30 µm for the attractive and repulsive emulsions respectively. The numerical analysis of this data is listed in Table 4.2, and provides evidence that the size distributions of each emulsion are similar.

Light microscopy of both high, medium, and low salt emulsions show a marked difference in the bulk structure of the samples. Low magnification images of these low, medium, and high salt emulsion are displayed in Fig. 4.4. Figure 4.4 demonstrates the differences in the network structure of the three emulsion systems, with the low salt (Fig. 4.4a) showing a number of well separated oil droplets, with no significant contact between each droplet. The medium salt image (Fig. 4.4b) demonstrates a number of individual droplets (or small flocs), alongside a large network of droplets. This shows the intermediate structure of the medium salt emulsion, sharing some the of features from both the high and low salt systems. The image for the high salt emulsion (Fig. 4.4c) has a considerably larger number

Table 4.2. Droplet size analysis of high (1.66 M) and low (1×10^{-4} M) salt 20 vol. % oil-in-water Pickering emulsions stabilised by 3.45 wt. % of silica nanoparticles demonstrating the similarities between the two emulsion preparations.

Salt	D [4,3] µm	D_v (10) µm	D_v (50) µm	D_v (90) µm	Uniformity	Span
Low	31.7	18.0	29.8	48.4	0.373	1.153
High	36.3	17.9	34.3	58.9	0.382	1.196

of droplets forming groups or flocs, consistent with the attractive interaction between the oil droplets, leading to formation of a network structure.

When the groups of droplets are imaged at a higher magnification, the differences between the droplet interactions are further evident (Fig. 4.5). Figure 4.5a shows the low salt emulsion with limited contact between oil droplets. When comparing the high salt emulsion, the network structures between the oil droplets become more evident, with droplets overlapping both in and out of the focal plane of this image (Fig. 4.5b).

Confocal microscopy allows imaging of only a single focal plane through a material. This allows the core and shell of the emulsion droplets to be clearly imaged with limited interference from other focal planes. The use of fluorescent dyes demonstrates the separation of the oil, and aqueous phase, provides further evidence that an oil-in-water emulsion, stabilised with a particle shell has been formed. This is demonstrated in Fig 4.6, where the oil phase of the emulsion is coloured red, and the silica in the aqueous phase is coloured blue.

Figure 4.6a demonstrates the distribution of Nile Blue and Red in the low salt Pickering emulsion systems. The Nile Red dye is located in the spherical oil droplets, and is evenly distributed throughout these drops. In comparison the Nile Blue dye is located outside these spherical droplets, in shells surrounding each oil droplet, and in a relatively homogeneous network throughout the aqueous phase. This demonstrates that the silica present in the aqueous phase is located both at the interface between the oil and water (acting as a Pickering stabiliser, stabilising the emulsion), with the remaining silica residing in the bulk aqueous phase.

When Fig. 4.6b is considered a similar image was captured. The Nile Red is again located inside the spherical oil droplets, and is homogeneous in its distribution inside said droplets. The Nile Blue is again located in the aqueous phase, with dense shells forming around each oil droplet, and the remaining silica distributed throughout the aqueous phase. However, comparing the confocal micrographs for the low and high salt, there do appear

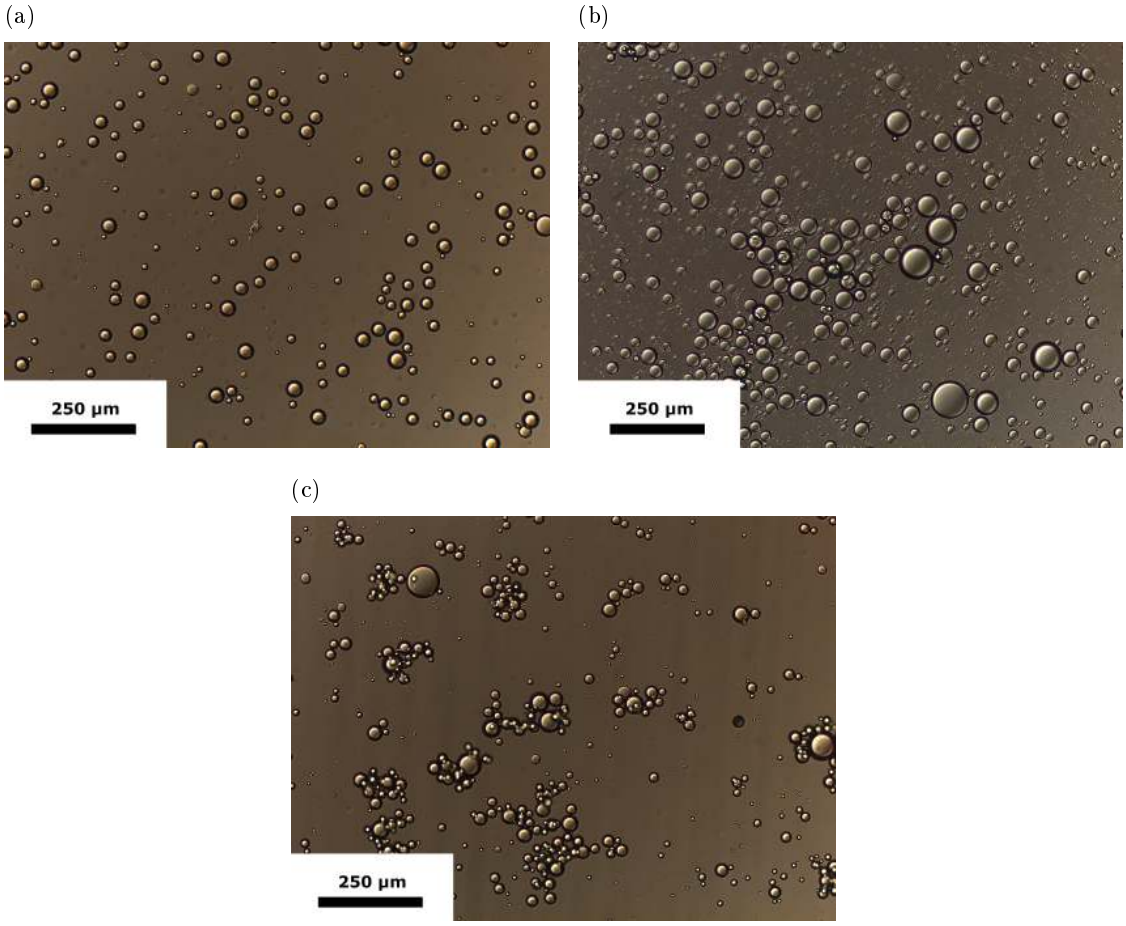

Fig. 4.4 Optical micrograph (10× objective) of ≈1.25 vol. % oil-in-water Pickering emulsions stabilised by 3.45 wt. % of silica nanoparticles demonstrating the morphology of (a) low salt (1×10^{-4} M), (b) medium salt (0.066 M), and (c) high salt (1.66 M) emulsion systems. The morphology of the droplets is spherical in all cases, while there is a noticeable difference in the network structure present.

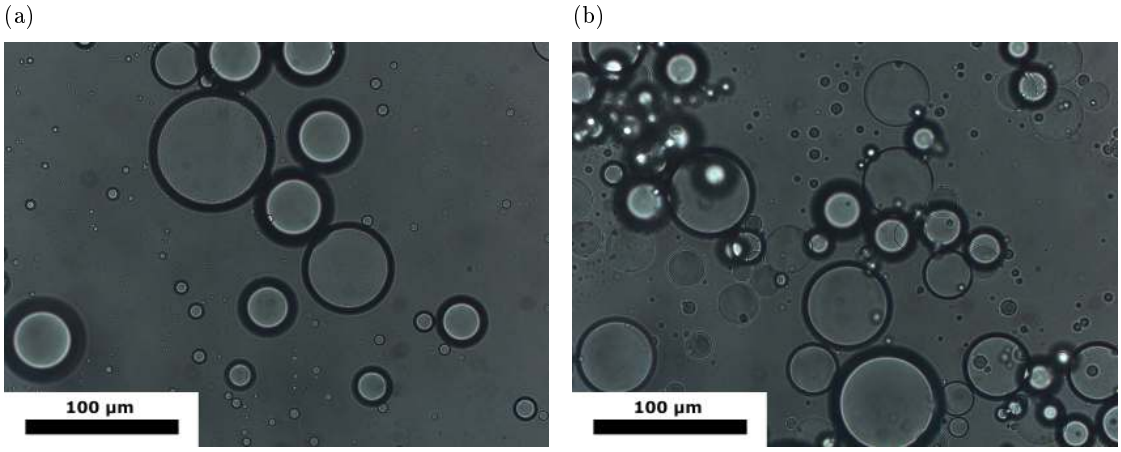

Fig. 4.5 Optical micrograph (40× objective) of ≈1.25 vol. % oil-in-water Pickering emulsions stabilised by ≈1.66 wt. % of silica nanoparticles demonstrating the morphology of both a (a) low salt (1×10^{-4} M), and (b) high salt (1.66 M) emulsion systems. The morphology of the droplets is spherical in both cases, while there is a noticeable difference in the network structure present.

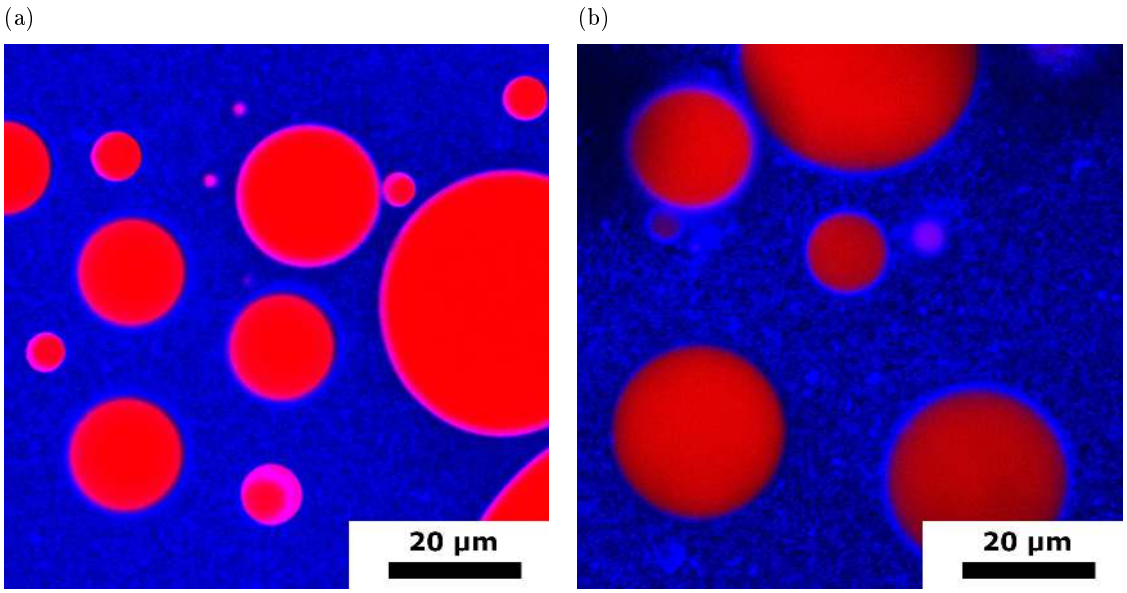

Fig. 4.6 Confocal micrograph of 20 vol. % oil-in-water Pickering emulsions stabilised by 3.45 wt. % of silica nanoparticles demonstrating the morphology and material distribution of both a (a) low salt (1×10^{-4} M) and (b) high salt (1.66 M) emulsion systems.

to be some subtle differences. The low salt image (Fig. 4.6a) appears to have a more homogeneous distribution of the silica in the aqueous phase, shown by the finer pattern of dye distributed throughout the aqueous phase. The high salt image (Fig. 4.6b) appears to have an increase in the coarseness of the silica distributed throughout the aqueous phase, consistent with silica flocs throughout that phase, an expected occurrence due to the attractive nature of the interactions between the silica particles.

4.3.3. Rheological measurements

Previous techniques used to analyse these emulsions have demonstrated that the size, and shape of the emulsion droplets are similar, however, there appears to be differences in the network structures formed between the droplets. The differences in the network structure between these emulsions was then investigated using rheological techniques.

4.3.3.1. Viscous flow rheology

Viscosity is routinely used to describe the bulk features of viscoelastic materials. As discussed in Section 1.5.4.1, viscosity is a measure of how resistant a given material is to flow. The method employed to analyse the viscosity in this work is a viscous flow curve. Such curves report the viscosity as the shear rate applied to a fluid is increased. The effect that this increase in shear rate has on the viscosity of the two emulsions is demonstrated

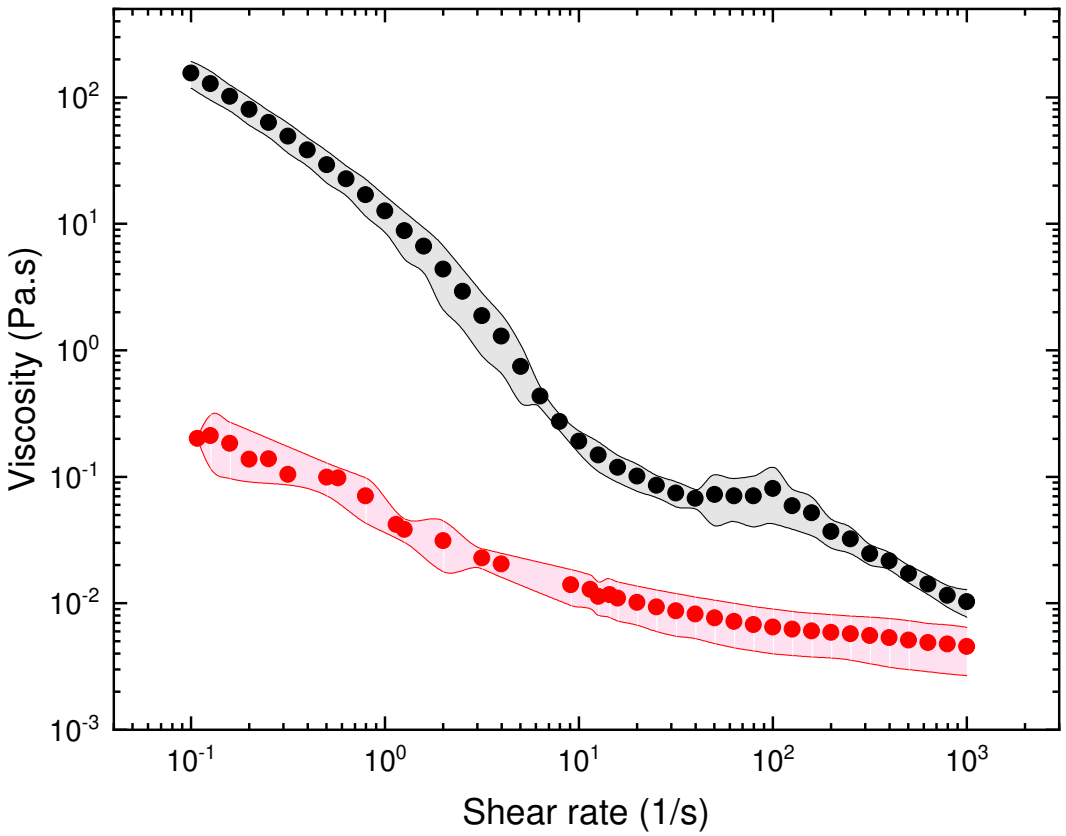

Fig. 4.7 Viscosity response to an increasing shear rate of 20 vol. % oil-in-water Pickering emulsions stabilised with 3.45 wt. % of silica nanoparticles at low (1×10^{-4} M, •) and high salt (1.66 M, •). Shaded areas indicate the variation in multiple measurements of these emulsion systems.

in Fig. 4.7. This figure shows that both the high, and low salt emulsions exhibit shear thinning behaviour, becoming less viscous as the shear rate increases. At lower shear rates ($0.1\,s^{-1}$), the viscosities of the two emulsions are substantially different, with the high salt emulsion having a viscosity that is about three orders of magnitude larger than that of the low salt emulsion. This is detailed in Table 4.3, which lists the low shear ($0.1\,s^{-1}$) viscosity of both the high and low salt emulsions, alongside calculated zero shear viscosities based on the constituents of the emulsions (Section 1.5.4.1). In addition to the two extremes of the salt concentration, the viscosity response of the medium salt emulsion was also investigated. This medium salt system was found to be similar to the low salt system, indicating that the structure that is present between the intermediate strength silica and emulsion network is similar to that for the low salt emulsions. The data from the medium salt emulsion is not displayed in Fig. 4.7 for clarity.

This difference between the low shear viscosities of the high and low salt emulsions was expected due to the difference in interactions between the emulsion droplets. The high

Table 4.3. Zero shear calculated viscosities from a selection of models and a comparison to the measured low shear ($0.1\,s^{-1}$) viscosities of the repulsive low (1×10^{-4} M) and attractive high salt (1.66 M) 20 vol. % oil-in-water 3.45 wt. % silica stabilised Pickering emulsions presented in this work.

Oil volume percentage (vol. %)	Einstein model viscosity (Pa s)	Batchelor model viscosity (Pa s)	Kreiger-Dougherty model viscosity (Pa s)	Attractive emulsion measured viscosity (Pa s)	Repulsive emulsion measured viscosity (Pa s)
20%	1.3×10^{-3}	1.6×10^{-3}	1.6×10^{-3}	150 ± 60	0.20 ± 0.17

salt emulsion is expected to have an attractive interaction between the oil droplets. This attractive interaction is anticipated to lead to an increase in the friction between the emulsion droplets, resulting in the measured low shear viscosity of the high salt emulsion being much larger than if there was no attractive interaction between the droplets. The calculated zero shear viscosities also shown in Table 4.3 demonstrate the predicted viscosities based on non-interacting hard spheres. This lack of interaction between the model particles leads to low shear viscosities that are far smaller than both the high salt and low salt emulsions.

Another feature of the data demonstrated in Fig. 4.7 is the viscosity at high shear rates ($1000\,s^{-1}$) for each emulsion. While the low shear viscosities of each emulsion differ by about three orders of magnitude, the high shear viscosities differ by only a factor of two, with the low salt emulsion having a high shear viscosity of 0.005 ± 0.003 Pa s, while the high salt emulsions high shear viscosity is 0.010 ± 0.005 Pa s. This decrease in the difference between the viscosities at high shear rates can be accounted for by the changes in the emulsion structure as the shear rate is increased. At low shear rates the emulsions have different network structures (as shown in Fig. 4.5). The extensive network structure that is present in the high salt emulsion leads to an increased viscosity. As the applied shear is increased, this network structure will begin to break down, leading to a less extensive attractive network of droplets. This weakened network will begin to resemble that present in low salt emulsions, where there are relatively few flocs of oil droplets present (as shown in Fig. 4.5). As the microscopic droplet structures become similar at high shear rates, the measured viscosities will also become similar and approach those predicted by each of the models presented.

While monitoring the viscosity of the emulsions as the shear rate was increased, the shear stress was also monitored within the same experiment. The response of the shear stress to this change in shear rate is displayed in Fig. 4.8 demonstrates the differences between the shear stress response of the high and low salt emulsions (medium salt is not shown for

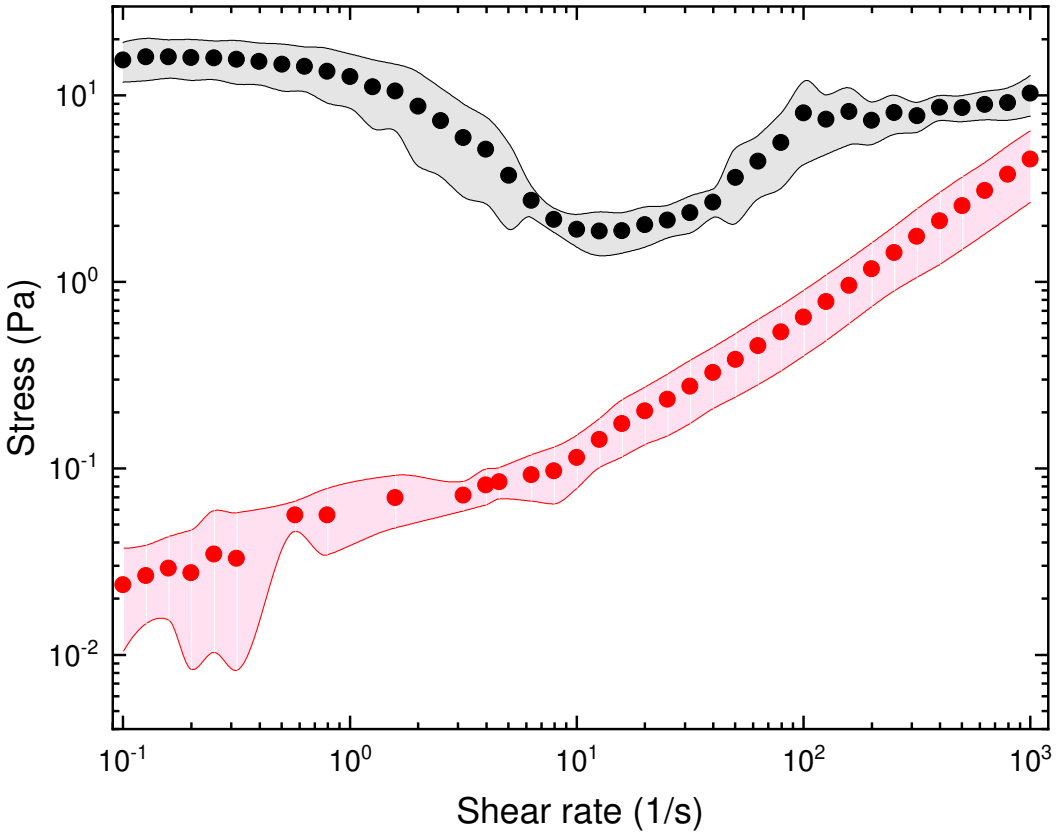

Fig. 4.8 Shear rate vs. stress for 20 vol. % oil-in-water Pickering emulsion stabilised by 3.45 wt. % silica at low (1×10^{-4} M, •) and high salt (1.66 M, •). Shaded areas indicate the variation in multiple measurements of these emulsion systems.

clarity, and was found to behave in a similar manner to that of the low salt emulsion).

It is clear from the data presented that there is a significant difference in the stress response of the high and low salt emulsions. Initially the stress response of the high salt emulsion is insensitive to an increasing shear, until there is a notable decrease in the stress at about $2\,s^{-1}$. At higher shear rates the measured stress begins to increase with the shear rate. This behaviour is indicative of anomalous flow regimes (shear banding), and has been described by other workers [133, 141, 175–182]. In these previous reports anomalous flow was described as a transition from a solid-like network structure throughout the material to smaller flocs or sheets of 2-D networks. These move within the sample, lowering the stress and viscosity measured during this transition. Once this transition has completed, the stress begins to increase with shear rate as the break-up of the flocs occurs, leaving the primary network components. Figure 4.9 demonstrates a schematic diagram depicting the multiple stage yielding that is proposed to occur within these materials with attractive network structure. Multiple stage yielding has been demonstrated in a range of materials including particle suspensions [12, 13], surfactant stabilised emulsions [142], and silica

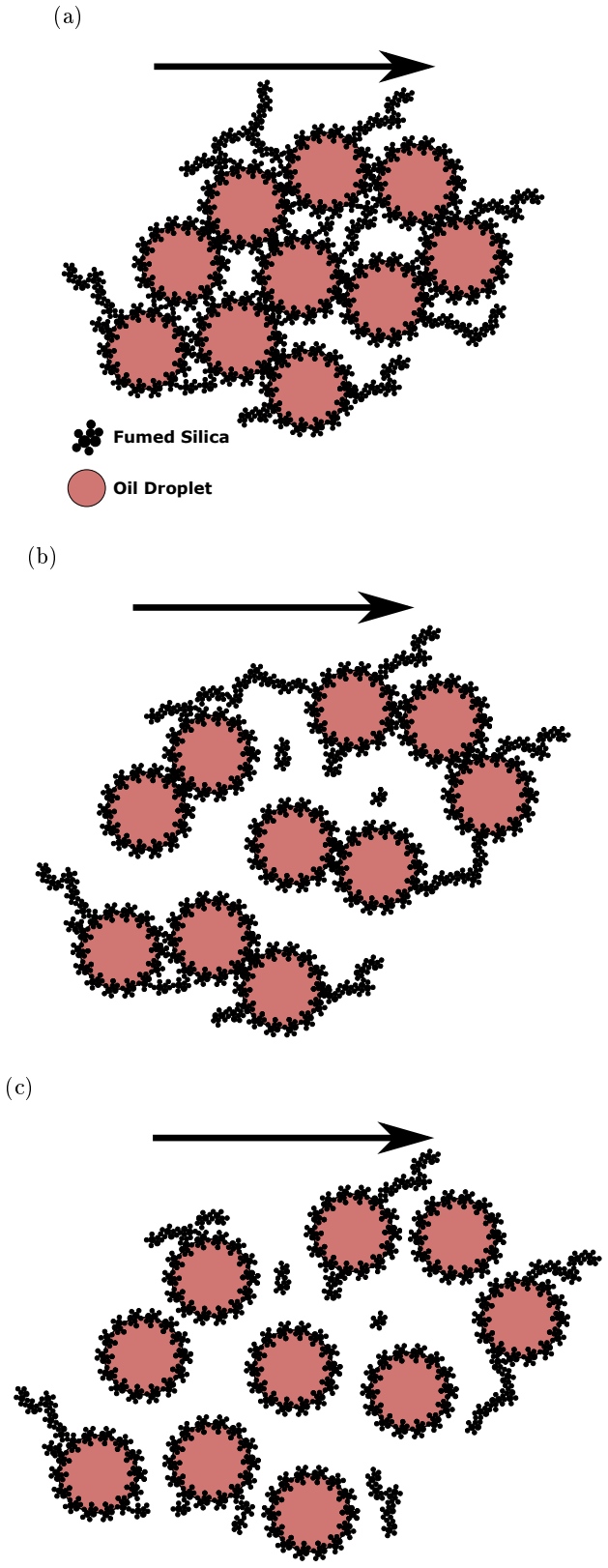

Fig. 4.9 Schematic diagram demonstrating the multi-stage yielding processes that occur in emulsions with attractive interactions between the oil droplets (red circles) and silica nanoparticles (collections of black dots). Arrows indicate the shear applied to the sample. Silica particles and oil droplets are not drawn to scale in this diagram. (a) Unyielded emulsion with a network structure formed. (b) Flocs of oil droplets demonstrating the first yielding step that attractive colloidal materials can display, with a limited network between the silica nanoparticles. (c) Fully yielded emulsion demonstrating droplets with no network structure present.

stabilised Pickering emulsions [8] when measured through oscillatory rheology. To the best of our knowledge, this is the first demonstration of this decrease in the stress response with an oil-in-water Pickering emulsion.

The stress response that is present in the high salt data appears to demonstrate this multiple stage yielding behaviour that has been seen in previous materials. The high salt emulsion displays attractive interactions between the emulsion droplets. This attractive interaction is assumed here to lead to the formation of an elastic network structure. The network of attractive emulsion droplets in turn leads to the emulsion structure behaving in a solid like manner at low applied stresses, in that it does not flow, but instead stores some of the applied energy in an elastic manner. As the stress increases, the attractive network structure begins to no longer to be able to store the applied energy, and begins to fracture into smaller flocs. This is apparent with the decrease in the measured stress. As the applied shear rate continues to rise, the measured stress begins to increase. This increase in the stress appears to fit the typical behaviour for shear thinning materials that approach Newtonian-like properties at sufficiently high shear rates. This again supports the proposition that the flocs remaining in the system are beginning to yield, breaking into smaller groups of droplets. At high shear rates, the measured stress approaches that of the low salt emulsion, suggestive of both materials being comprised of similar structures at high shear rates. This indicates that droplet network structures comprising each emulsion have been broken down into similar sized components (e.g. individual or small groups of network elements).

In comparison to this, the stress response of the medium, and low salt emulsion shows a marked increase in the measured stress, from a low value, as the shear rate is increased. This increasing stress is typical stress–shear rate behaviour of a shear thinning fluid that approaches Newtonian-like behaviour as the applied shear increases and the component emulsion droplets begin to move independently of one another. This typical behaviour can be fitted with a number of models in order to extract the yield stress parameter as shown in Fig. 4.10.

The yield stress parameter was discussed in Chapter 3, and is the force that is required to make the material begin to yield and flow. A yield stress was extracted from both the low, medium, and high salt emulsion samples. As the high salt emulsion displayed relatively linear behaviour, only an average was fitted to the data, leaving the fitting of models for the low salt emulsion. Three different methods are used to extract a yield stress from the low salt emulsion, with the low shear average, a Bingham [102] (Equation 1.19),

and a Herschel-Bulkley fit [101] (Equation 1.20).

The data in Fig. 4.10 demonstrates that both the medium and low salt emulsions show similar yield stresses for each emulsion (medium salt: 0.03 Pa when fitted with both Herschel-Bulkley and Bingham models, low salt: 0.03 ± 0.02 Pa when fitted with both a low shear average and Herschel-Bulkley model, 0.04 ± 0.02 Pa when fitted with the Bingham model). This was an unexpected result, as the medium salt emulsion was expected to show a yield stress that was between the high and low salt emulsions. The similarity demonstrates that the network formed between the groups of droplets in each of these emulsions is a relatively weak structure. Surprisingly, the medium salt remains at this yield stress over a large shear rate range, giving an indication that the yielding process for the medium salt emulsion is a more complex process when compared to the low salt system.

The high salt system however, displays an attractive network formed between the oil droplets that is extensive, and robust. This attractive network results in a high viscosity system, that demonstrates interesting stress response behaviours. The fitting of a yield stress curve to the high salt emulsion is a somewhat more challenging proposition. As is displayed in Fig. 4.10, two different averages were applied to the high salt data. The first of these was taken across the full range of the data presented, and was calculated as an average. This average of the full curve gave a yield stress of 8 ± 4 Pa. In addition to this, the stress response below $1\,s^{-1}$ was also averaged separately. This data was fitted independently of the full data due to the decrease in the stress response after this point. As the reasons for this decrease in the stress response has been proposed in this work as being due to the breakdown of the network structure of the emulsion, fitting this initial section will give a yield stress that corresponds to the full network of the material. The yield stress attributed to this section was 15 ± 6 Pa.

Comparing these values with those of the low and medium salt emulsions, the high salt emulsion shows an increased yield stress. These differences between the yield stress values of these emulsions is consistent with the proposed changes in the network structures of the emulsions. At low salt levels the network structure formed between the emulsion droplets is expected to be weak. This weakness will lead to emulsion systems that are able to yield and flow with the application of a small stress.

Optical microscopy of the medium salt emulsion demonstrated the intermediate structures present in the emulsion system (Fig. 4.4b) as evidenced by network structure present between a number of droplets, while a number of individual droplets were found to still be

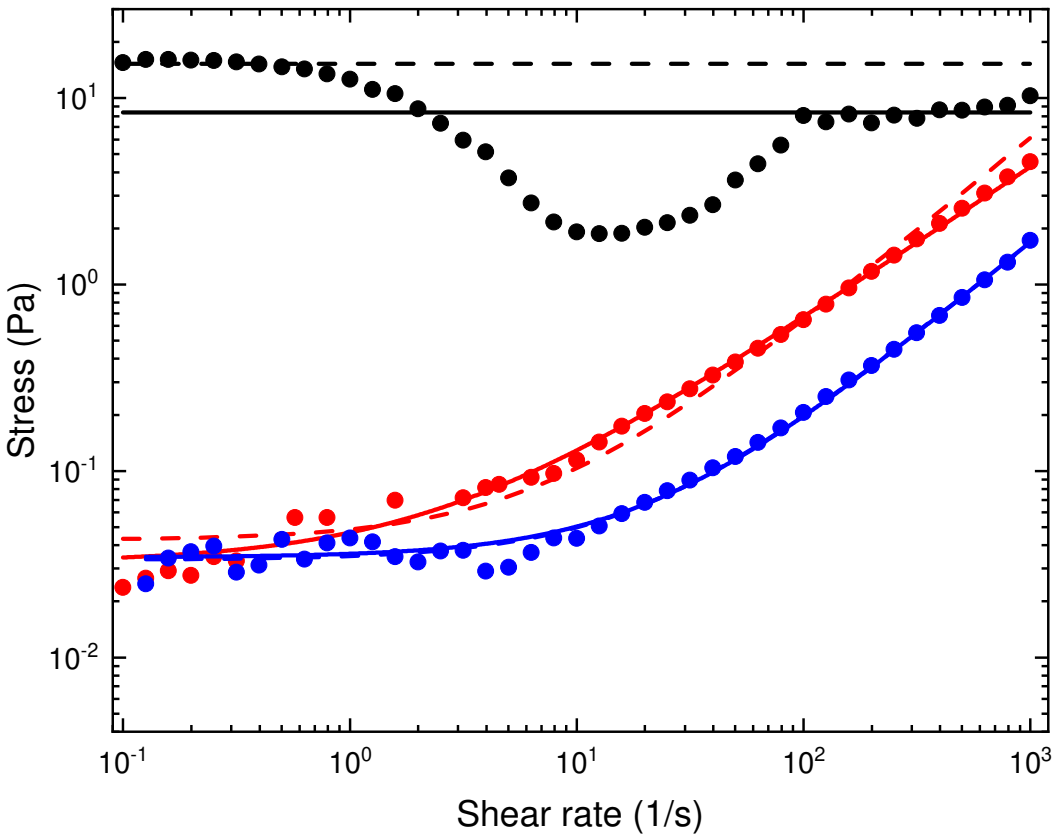

Fig. 4.10 Shear rate vs. stress for 20 vol. % oil-in-water Pickering emulsions stabilised by 3.45 wt. % silica at low salt (1×10^{-4} M, •), intermediate salt (0.066 M, •), and high salt (1.66 M, •). Lines demonstrate the fittings of these data with each of the applied models. With the high salt emulsion, the solid black line is the average over the full data range (8 ± 4 Pa), while the dashed black line is an average below a shear rate of $1\,s^{-1}$ (15 ± 6 Pa). With the medium and low salt emulsions, the solid blue and red lines are the Herschel-Bulkley model (medium salt, 0.03 Pa; low salt, 0.03 ± 0.02 Pa), while the dashed blue and red lines are the Bingham model fittings (medium salt, 0.03 Pa; low salt, 0.04 ± 0.02 Pa). The medium and low salt emulsions were also fitted with averages to the low shear plateau (not shown here) (medium salt, 0.04 Pa; low salt, 0.03 ± 0.02 Pa).

separate from the network structures. These changes point to a structure containing flocs of droplets that do not form a strong cohesive network throughout the full emulsion sample. These changes were demonstrated in the stress response for the medium salt emulsion, with the lack of a network throughout the emulsion leading to a low yield stress, while the attractive flocs result in the yielding process occurring over a larger shear rate range as the flocs break-down. Contrasting these with the high salt emulsion, the measured yield stresses are greater, indicating that there is significant network structure formed between the oil droplets. This network affords the emulsion an increase in solid–like behaviour.

4.3.3.2. Amplitude analysis

Oscillatory rheology is used in this chapter to give insight into, and demonstrate the differences between, the elastic properties of the emulsion systems. The first demonstration of the elastic properties of these emulsions was the strain sweep experiment. This experiment measured the storage and loss moduli as the oscillation strain was increased, allowing the elastic properties of the material to be investigated. The results of this experiment are shown in Fig. 4.11 and demonstrates the stark differences between the elastic properties of the high and low salt Pickering emulsions, while also demonstrating the novel intermediate behaviours in some medium salt emulsions. Again, the high salt emulsion exhibits much greater structural properties when compared to the low salt emulsion. This is best indicated by the differences in the first displayed values of the storage moduli of the linear viscoelastic region of each emulsion. The high salt emulsion has a storage modulus that is $\approx$100 Pa, compared to $\approx$0.004 Pa for the low salt emulsion. This difference is again consistent with the difference between the proposed network structures formed by the two emulsions. In addition to the differences between the two extremes, the medium salt emulsion shows elastic properties that lay between the high and low salt systems with the initial storage modulus of $\approx$0.9 Pa.

The high salt emulsion data shown in Fig. 4.11 is indicative of typical viscoelastic behaviour [183, 184]. At low strain percentages the high salt emulsion data shows a storage modulus that is insensitive to an increasing oscillation strain. This is known as the linear viscoelastic region, and demonstrates the region in which the materials properties are elastic-like [103]. As the strain is increased through this linear viscoelastic region the loss modulus of the high salt emulsion increases to a peak approaching the storage modulus. As the strain is increased further, the storage modulus begins to decrease, intersecting the also decreasing loss modulus. There are key points in this plot, each of which can be used to

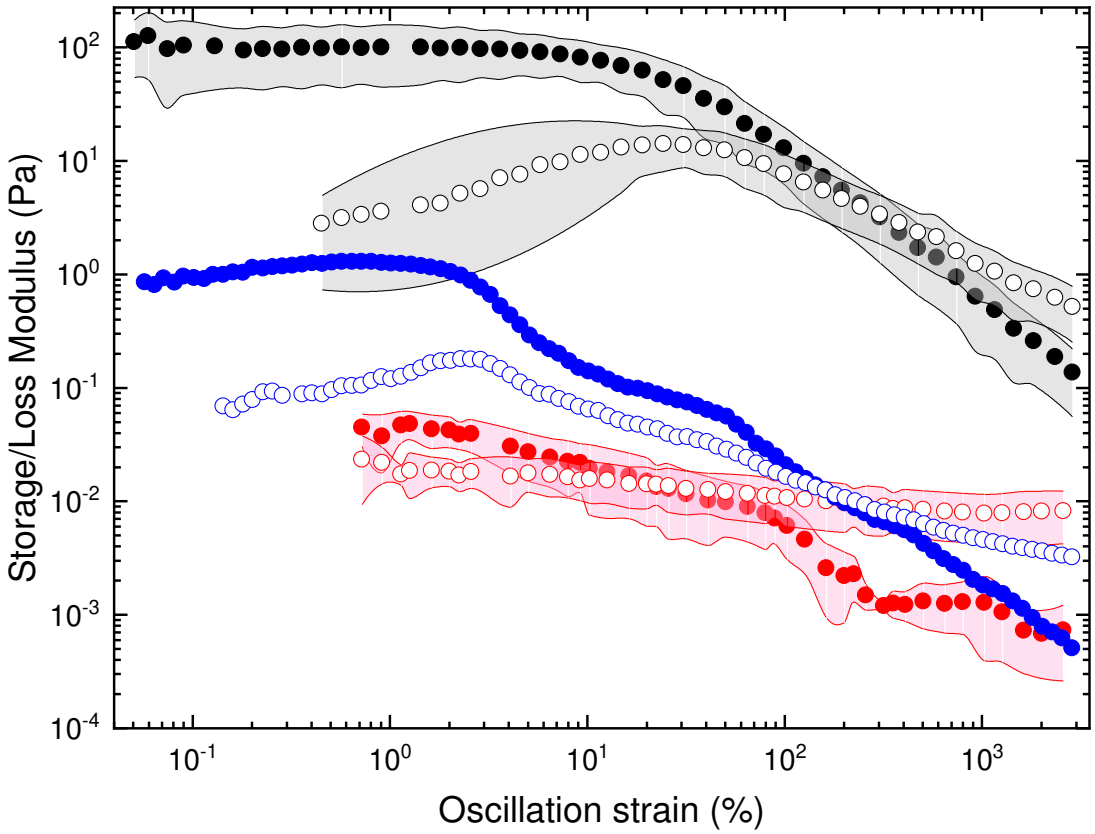

Fig. 4.11 Response of the elastic storage modulus (filled symbols) and the viscous loss modulus (unfilled symbols) of 20 vol. % oil-in-water Pickering emulsions stabilised by 3.45 wt. % silica low (1×10^{-4} M, •), medium (0.066 M, •), and high (1.66 M, •) salt to changes in the applied oscillatory strain at a constant oscillation frequency ($1\,\mathrm{rad\,s^{-1}}$). Shaded areas indicate the variation in multiple measurements of these emulsion systems.

describe properties of the material. The first key point is the end of the linear viscoelastic region, where the solid–like behaviour of the material begins to decrease. This point can be identified by fitting an average to the linear viscoelastic region, and a power law curve to the decreasing slope, as illustrated in Fig. 4.12. Following this, the intersection between the storage and loss moduli is the point at which the liquid–like behaviour of the material becomes the dominant property, and the material is able to readily flow. Each of these points can be considered to be classed as the yield stress (as discussed in Chapter 3), and the values extracted from each of these methods are demonstrated in Table 4.4, showing that the yield stresses obtained using these oscillatory methods are larger than that measured from the flow curves shown earlier (Fig. 4.10). One further notable feature of this high salt data is the broad nature of the loss modulus peak. The width of this peak is an indication that the peak may be comprised of multiple different yielding events that occur at similar strain percentages.

Some interesting behaviour is found for the medium salt emulsion. In comparison to the high salt system which demonstrates a single power law decrease in the storage modulus during the shear thinning phase, the medium salt system shows a clear deviation at about 10 % strain. This deviation indicates that multiple yielding events occur within this oil-in-water Pickering emulsion system that have attractive interactions between the emulsion droplets. In addition to being present in the storage modulus, this behaviour is found, to some extent, in the loss modulus of the medium salt system. Due to these indications of multiple yielding steps, the data was fitted to extract each of the two yield stresses present. The first yield stress was extracted as the inflection point between the linear viscoelastic region and the first decrease, while the second yield stress was taken as the inflection point between the final decrease in the storage modulus and the medium strain plateau. In addition to these two points, the cross over between the storage and loss moduli was also measured, and displayed with all of the yield stress data in Table 4.4.

When the data from the high and medium salt emulsions are compared with that for the low salt system, it is clear that there are significant differences. In comparison to the higher salt systems, which shows a linear viscoelastic region at low strain, the low salt emulsion shows no such behaviour. Instead, the low salt emulsion demonstrates storage and loss moduli which are almost equal at low strain. As the strain is increased the storage modulus decreases while the loss modulus stays relatively constant, leading to a cross-over point. The behaviour of this low salt emulsion demonstrates that this emulsion is unable to store any significant amount of energy in an elastic manner. This behaviour is not

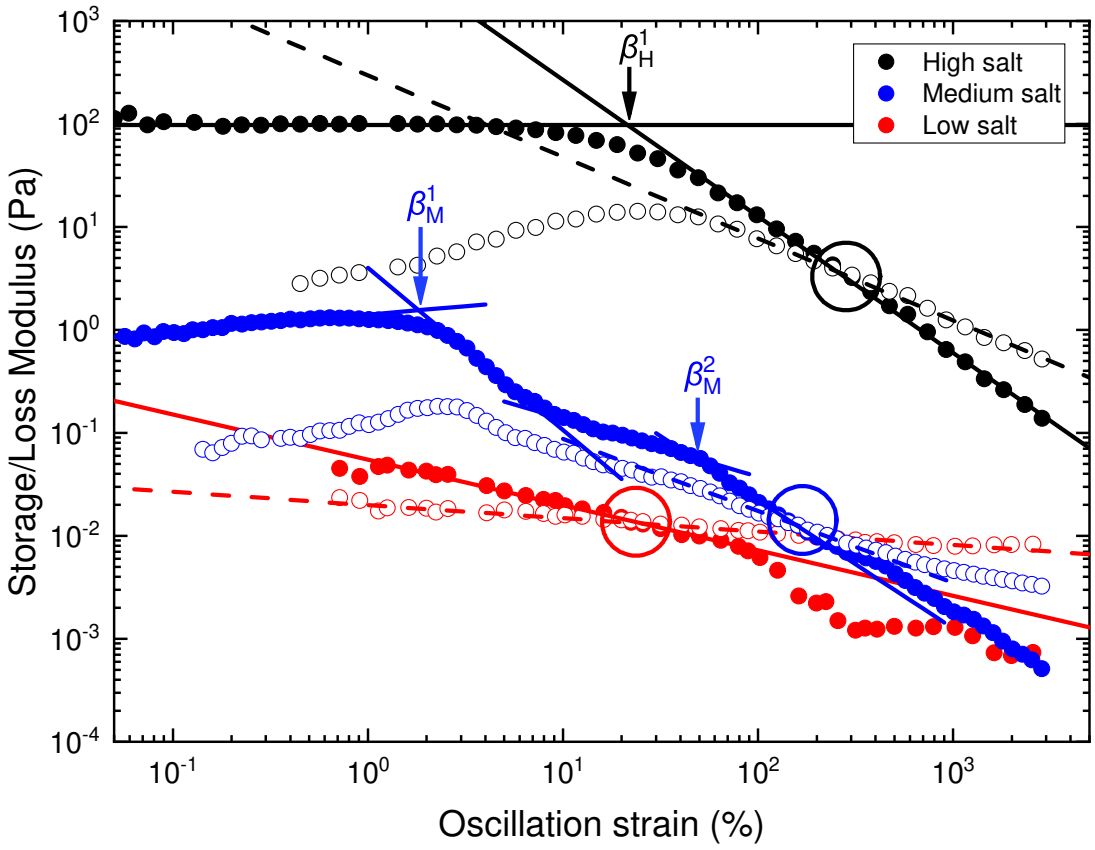

Fig. 4.12 Response of the elastic storage modulus (filled) and the viscous loss modulus (unfilled) of 20 vol. % oil-in-water Pickering emulsions stabilised by 3.45 wt. % silica at low (1×10^{-4} M, •), medium (0.066 M, •), and high (1.66 M, •) salt to changes in the applied oscillatory strain at a constant oscillation frequency ($1\,\mathrm{rad\,s^{-1}}$). Solid lines are fitted to the storage modulus, while dashed lines are fitted to the loss modulus. Circles highlight the cross-over points at which $G' = G''$, one measure of the yield strain, from which a yield stress can be found (low salt: yield strain, 20 ± 60 %; yield stress, 0.01 ± 0.01 Pa; medium salt: yield strain, 160 %; yield stress, 0.01 Pa; high salt: yield strain, 270 ± 100 %; yield stress, 14 ± 10 Pa). The inflection point of the high salt storage modulus are indicated with β^1_H (yield strain, 20 ± 20 %; yield stress, 13 ± 10 Pa), while the two inflection points of the medium salt emulsions are labeled β^1_M (yield strain, 1.8 %; yield stress, 0.02 Pa), and β^2_M (yield strain, 46.4 %; yield stress, 0.03 Pa).

unexpected, as the repulsive interactions between the emulsion particles do not enable the formation of a coherent network structure throughout the bulk material. The lack of a full network throughout the emulsion leads to a material that has significant liquid-like properties, resulting in a material that dissipates energy in a viscous manner. Due to the lack of a linear viscoelastic region, fitting of the storage modulus above and below the inflection point cannot be carried out for this data. The yield stress obtained from the cross–over point is displayed in Table 4.4, and is found to be similar to that measured with the flow curve (Fig. 4.8).

Table 4.4. Yield stress values obtained from the strain sweep measurements of high and low salt silica stabilised Pickering emulsions.

Emulsion type, X	Cross over of G' and G'' as a strain percentage (%)	Cross over of G' and G'' as a yield stress (Pa)	β_X^1 as a strain percentage (%)	β_X^1 as a yield stress (Pa)	β_X^2 as a strain percentage (%)	β_X^2 as a yield stress (Pa)
High (H)	270 ± 100	14 ± 10	20 ± 20	13 ± 10	-	-
Medium (M)	160	0.01	1.8	0.02	46.4	0.03
Low (L)	20 ± 60	0.01 ± 0.01	-	-	-	-

The power law fitting parameters that were applied to the decreases in both the storage and loss moduli can also be compared with each other, giving some more information about these emulsion systems. As was discussed in Section 3.3.3, it has been proposed that the shear thinning behaviour in the G'' will result in a power law where the G'' exponent (n) is about one half of the exponent associated with $G'(m)$ [166–169]. The coefficients of the power laws for each emulsion are shown in Table 4.5. The ratios displayed in Table 4.5 are in near agreement with this assertion for most of the data. When the high salt emulsions are considered, the n/m ratio is found to be 0.62. As the high salt emulsion has been demonstrated to have attractive interactions between the oil droplets, it is proposed here that this attractive interaction results in the slopes of the storage and loss moduli decreasing with strain at a similar rate. This is due to the breakdown of the network between the emulsion droplets requiring a higher applied strain to break the flocs.

As the medium salt emulsion demonstrated two yield events, there were two coefficients used to fit each of the shear thinning sections of the storage modulus. The first decrease in the storage modulus was fitted with a power law with a coefficient of $G' \propto \gamma^{-1.6}$, higher than that found with the high or low salt emulsions, indicating that the yielding process here was different to that occurring in the other systems. The second decrease was fitted with a power law of $G' \propto \gamma^{-1.2}$, similar to that for the high salt emulsion. This is an indication that the yielding processes that occur in this second step, and the high salt emulsion are similar.

When compared with the low salt data, which has been demonstrated to have repulsive interactions between the oil droplets, it is clear that there is a significant difference in the ratio of slopes. In the low salt emulsion, the shear–thinning behaviour of the loss modulus is very negligible (as demonstrated by the near horizontal shape to the loss modulus curve), while the storage modulus decreases with shear rate. This demonstrates the rapid break down of the weak repulsive network structures that have been found to be present in the low salt emulsion system.

While also monitoring the storage and loss moduli response to an increasing strain, the corresponding oscillatory stress was also measured for both the high, medium, and low salt emulsions. The data from this stress vs. strain experiment is displayed in Fig. 4.13. Once again there are notable difference between the data for the high, medium, and low salt emulsions.

The high salt data shows behaviour that is typical for viscoelastic materials, with a power law increase in the measured stress as the oscillation strain increases at low strain

Table 4.5. Power coefficients for the fits of the storage and loss moduli of high and low salt emulsions. Power law fittings were applied to the shear thinning section of the curves.

Salt Level	Coefficient value	Ratio
High	$G' \propto \gamma^{-1.3\pm0.3}$ $G'' \propto \gamma^{-0.8\pm0.2}$	$n/m = 0.62$
Medium	First inflection, $G' \propto \gamma^{-1.6}$	$n/m = 0.44$
	Second inflection, $G' \propto \gamma^{-1.2}$	$n/m = 0.58$
	$G'' \propto \gamma^{-0.7}$	
Low	$G' \propto \gamma^{-0.4\pm0.1}$ $G'' \propto \gamma^{-0.1\pm0.1}$	$n/m = 0.25$

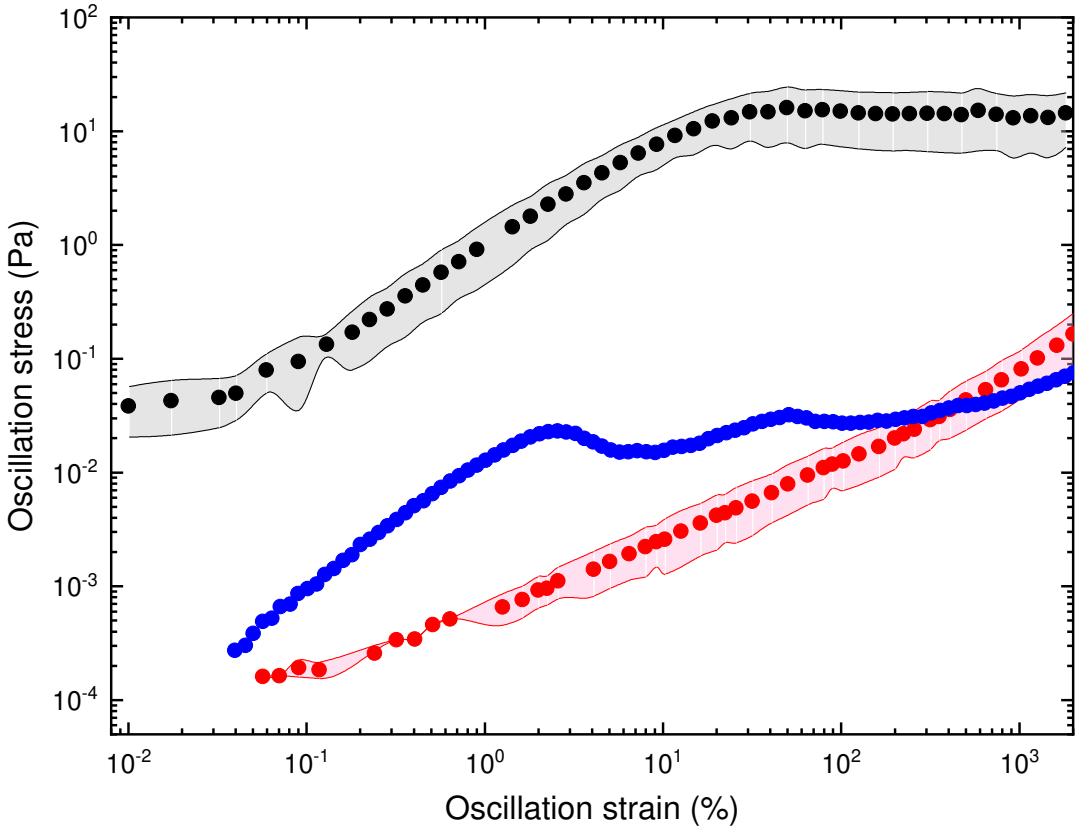

Fig. 4.13 Responses of oscillatory stress to an increasing oscillatory strain for 20 vol. % oil-in-water Pickering emulsions stabilised by 3.45 wt. % silica at high, (1.66 M, •), medium (0.066 M, •), and low salt (1×10^{-4} M, •) concentrations. Shaded areas indicate the variation in multiple measurements of these emulsion systems.

Table 4.6. Yield strain and yield stress values obtained from stress – strain measurements of high (1.66 M), medium (0.066 M), and low salt (1×10^{-4} M) 20 vol. % oil-in-water Pickering emulsions stabilised by 3.45 wt. % silica.

Salt level, X	β_X^1 as a strain percentage (%)	β_X^1 as a stress (Pa)	β_X^2 as a strain percentage (%)	β_X^2 as a stress (Pa)
High (H)	17 ± 5	15 ± 10	-	-
Medium (M)	2	0.03	50	0.03
Low (L)	-	-	-	-

percentages. An inflection point is then reached where this power law behaviour ceases, and the measured stress becomes relatively insensitive to any further increase in the applied strain percentage across the range applied. This inflection point is an important feature that can be used to describe the yield stress of the material. The inflection point of the high salt data was found by fitting a power law to the low strain section, and an average to the high strain section. The intersection of these two fits marks the yield stress and yield strain of the material. The resultant values are shown in Table 4.6. The exponent of the power law at low strain percentages was found to be $\gamma^{0.97}$. The curves which were fitted to the data are shown in Fig. 4.14.

The medium salt emulsion again shows non-standard behaviour, with one main inflection point, followed by a secondary peak. Power laws were fit to multiple sections of the curve to describe each of these inflection points as the yield stresses apparent in these intermediate strength emulsions. The inflection points, β_M^1 and β_M^2, found from these fittings are shown in Table 4.6. The exponents of the power law fitted at the low strain percentage was $\gamma^{1.1}$, while at intermediate strains before the second yield event was $\gamma^{0.46}$.

When the data for the low salt emulsion is considered the behaviour displays a substantial difference. The low salt data lacks any notable inflection point, indicating that there is no significant structural change in the emulsion as the strain percentage is increased. This is likely due to the material yielding at a very low strain, with the behaviour demonstrated here likely being the strain hardening region of the curve [185–187]. The strain hardening region of these curves will show an exponential increase in the measured stress until the material fractures, at which stage the stress will decrease rapidly. In this repulsive emulsion as the applied strain is increased the oil droplets will become increasingly interlocked. This will result in a hardening of the material at short time scales.

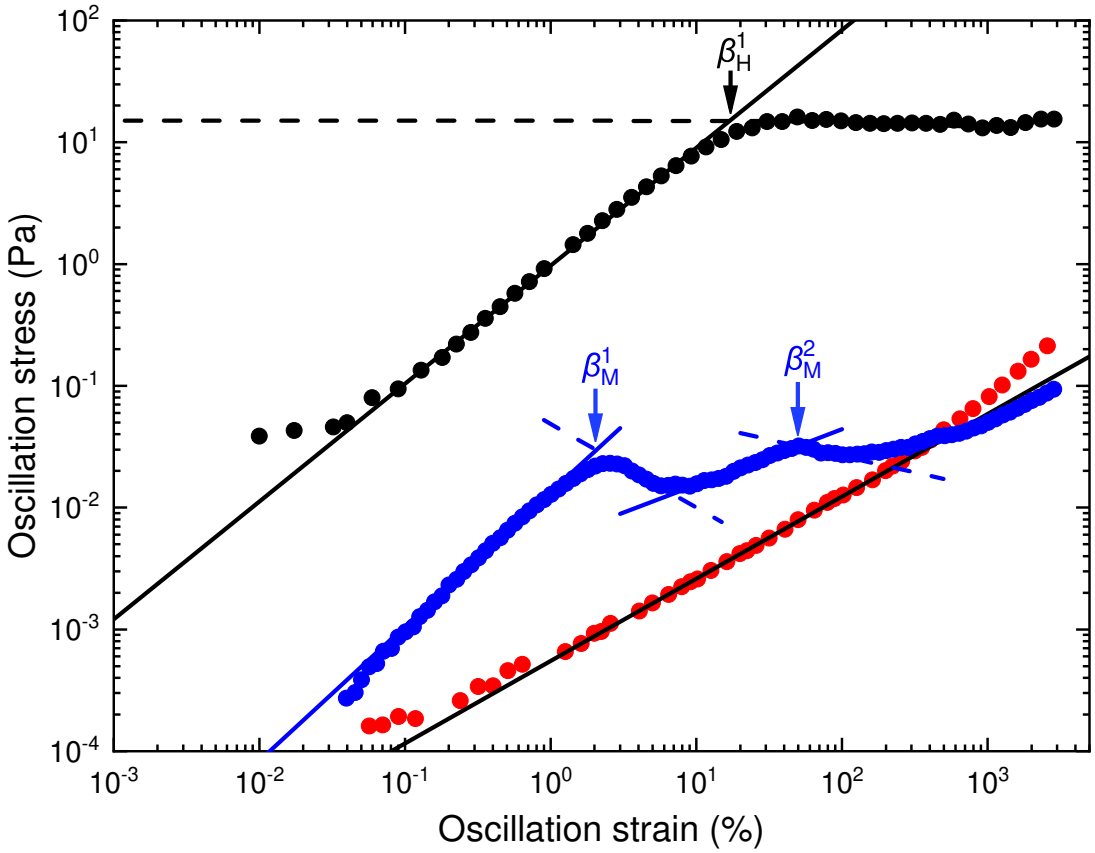

Fig. 4.14 Fitted responses of oscillatory stress to an increasing oscillatory strain for 20 vol. % oil-in-water Pickering emulsions stabilised by 3.45 wt. % silica at high (1.66 M, •), medium (0.066 M, •), and low salt (1×10^{-4} M, •) concentrations. Lines indicate the fittings that were applied to each data, with β_H^1 (15 ± 10 Pa) pointing to the inflection point in the high salt emulsion, β_M^1 (0.03 Pa) and β_M^2 (0.03 Pa) mark the two inflection points seen in the medium salt data.

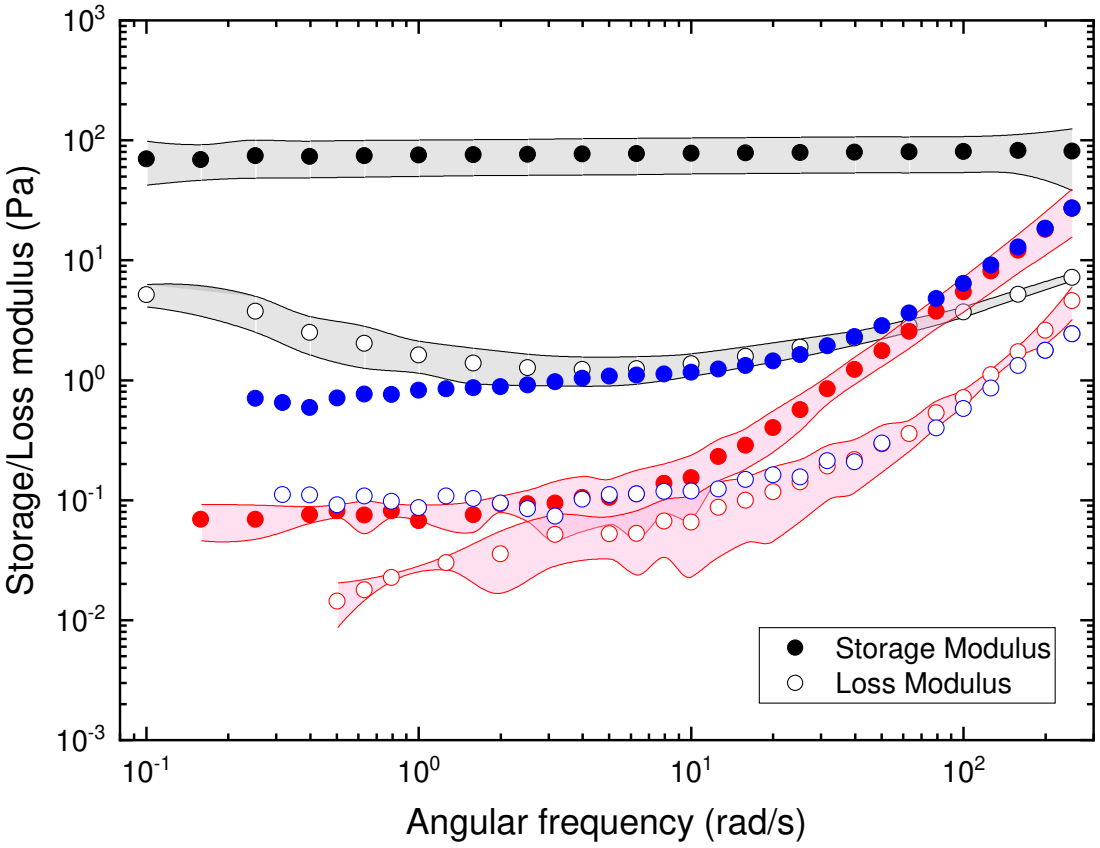

Fig. 4.15 Response of the elastic storage modulus (filled) and the viscous loss modulus (unfilled) of 20 vol. % oil-in-water Pickering emulsions stabilised by 3.45 wt. % silica at high (1.66 M, •), medium (0.066 M, •), and low salt (1×10^{-4} M, •) to an increasing oscillation frequency at a oscillatory strain of 0.4 % to 1 %. Shaded areas indicate the variation in multiple measurements of these emulsion systems.

4.3.3.3. Frequency analysis

Section 4.3.3.2 demonstrated the elastic response of these emulsions to a varied strain percentage at a set oscillatory frequency. This section probes the elastic behaviour of a varied oscillatory frequency at strain percentages between 0.4 % and 1 %. The strain percentage chosen for these measurements was selected as a value in the linear viscoelastic region of each emulsion. This allowed the elastic behaviour of the material to be probed as a function of the applied frequency. The response of the storage and loss modulus to the increasing frequency is demonstrated in Fig. 4.15.

This figure shows both the high, medium, and low salt storage and loss moduli responses to an increasing frequency, and again show a significant difference between the data measured for the low, intermediate, and high salt emulsions. When the high salt data is considered, there is a difference between the storage and loss modulus by over an order of

magnitude. This demonstrates the solid-like elastic behaviour of the high salt emulsion. The high salt emulsion also shows remarkably little change in the storage and loss moduli across the range of frequencies probed, indicating that the system is able to store the applied energy in an elastic manner within the attractive network formed between the oil droplets [188].

The medium salt emulsion data shows significant elastic behaviour at low frequencies. This is demonstrated by the storage modulus being nearly one order of magnitude larger than that of the loss modulus. Another feature of this curve is the power law increase in both the storage and loss moduli as the angular frequency of the applied oscillation increases. This feature is known as a glassy transition, that indicates that the system is no longer able to dissipate the applied energy in a viscous manner at the short time scales of the oscillations [103]. This is observed as a hardening of the material.

The low salt emulsion shows different behaviour from the high salt system. Initially, the difference in values between the storage and loss moduli is considerably smaller than those for both the high and medium salt emulsions. This indicates that the emulsion is able to store much less energy elastically when compared to the high and medium salt systems and is an expected result for this emulsion system. The low salt system has been shown to have repulsive interactions between the oil droplets which will result in any network forming when the emulsion is in a static (or close to) state being very weak. Such weak networks are unable to store significant amounts of energy elastically, and instead will dissipate the applied energy in a viscous manner through the motion of droplets. The low salt emulsion also demonstrates a glassy transition as the frequency of the applied oscillation increases, showing that the viscous dissipation process for this material occurs at longer time scales than the frequency of the applied strain.

4.4. Comparisons and discussion

Work carried out by other groups has investigated the rheological behaviour of glassy colloidal suspensions, surfactant, and Pickering stabilised emulsions, with attractive and repulsive interactions between the colloidal particles or emulsion droplets [8–10, 12, 13, 15, 130, 142]. For example, Datta et al. [142] investigated a sodium dodecyl sulphate (SDS) silicone oil in water emulsion (with a droplet radius of 250 nm). The interactions between the oil droplets were altered through changes to the SDS concentration. When the SDS concentration is below but close to that of the critical micelle concentration, (8 mM), the depletion interaction between droplets in the system is limited, and droplets display a very

weak attractive interaction. A strong attractive interaction is obtained by adding SDS to the system, increasing the concentration significantly greater than the critical micelle concentration. They found that at high droplet volume percentages (greater than the random close packing volume, >64 %) the elastic potential of both strongly and weakly attractive emulsions are similar to each other, indicating that the elastic potential was largely dominated by topological interactions . However, when the droplet volume percentage is lower than 64 %, the weakly attractive emulsions become significantly weakened when compared to their strongly attractive counterparts. Another notable feature of the rheology of these two different emulsion systems were the specific shapes of the oscillatory rheology curves. The strongly attractive emulsions demonstrate two distinct peaks in the loss modulus during the yielding process. This dual peak behaviour is not observed in the weakly attractive interactions; instead, the materials yield with a standard single peak profile. The interesting yielding behaviour demonstrated by these workers has highlighted how surfactant stabilised emulsions, comprised of relatively small droplets, can form an interconnected elastic network, which adds significantly to the bulk structure.

Pham et al. [12, 13] investigated similar behaviour with two different colloidal glasses made of hard spheres. The first was poly-methylmethacrylate spheres (with particle radii of 130 nm) suspended in *cis*-decalin, with and without short-range attractive interparticle interactions induced by adding a non-absorbing polymer (polystyrene – radius of gyration 11 nm. The second glassy material investigated was a suspension of poly-methylmethacrylate spheres stabilised by chemically grafting with poly-(12-hydroxystearic acid) in *cis*-decalin. The interactions in this colloidal suspension were also altered through the addition of a non-absorbing polymer (polystyrene), which induced attractive depletion interactions between the colloidal particles at sufficiently high concentrations. These colloidal suspensions were prepared at high particle loading (≈60 vol. %). When these materials had attractive interactions between the colloidal particles, complex multistage yielding behaviour was observed in the oscillatory rheology. These multistage yielding processes were proposed to be due to network breaking, and cage-breaking effects. The attractive interactions between the gel particles increased the strength of the materials compared to that of the repulsive gels at the same volume percentage. As the particle loading was reduced, the multi-stage yielding processes were still apparent in the systems with attractive interactions, indicating that this multi-stage yielding was due to the breaking of the attractive network formed between the particles, rather than the close packing of the particles. The multi-stage yielding was not seen in the systems with repulsive inter-

actions, instead a single yielding process was observed when the particle loading is above the random close packing percentage.

In a recent study, Katepalli et al. [8] investigated these multistage yielding events in two Pickering emulsions stabilised by silica nanoparticles with different shapes. Both spherical and fumed silica nanoparticles were used as Pickering stabilisers, with two different salt concentrations (1×10^{-4} M and 0.05 M NaCl) utilised to alter the interaction between the particle coated emulsion droplets. The fumed silica coated emulsion droplets formed at 1×10^{-4} M NaCl had an average diameter of ≈20 µm with a relative broad droplet size distribution, while those prepared at 0.05 M NaCl had droplet diameters of ≈10 µm, again with a broad size distribution. The emulsions used in this study were prepared at a relatively high droplet concentration of 50 vol. %, near to the random close packing volume of ≈64 vol. %. This resulted in many of the oil droplets in these emulsions being in close contact, aiding in the development of any network structure. The viscosity of these emulsions were measured across a relatively narrow shear rate range ($10\,s^{-1}$ to $100\,s^{-1}$), and the results demonstrated typical shear thinning behaviour with no apparent deviations from the curve. The elasticity of these emulsions was also investigated with amplitude sweep measurements, where the applied oscillatory strain was altered (0.1 % to 100 %). These results demonstrated two distinct yielding events in the strain sweep rheology of fumed silica stabilised Pickering emulsions when the salt concentration was 1×10^{-4} M. When the salt concentration was raised to 0.05 M, these two distinct yielding events appear to have merged into a single broad yield event. The oscillatory rheology of the spherical silica stabilised emulsions showed the lower strength of the emulsions when compared to those employing fumed silica. Despite this significant reduction in the strength of the emulsion, the multiple yielding events did still appear to occur, albeit in a less pronounced manner. This indicates that the multi-stage yielding process was not a product of the interlocking nature of the fumed silica coated droplets, but rather the attractive interaction between the silica particles.

The results presented in the present work have demonstrated that the formation of attractive interactions between colloidal particles, here oil-in-water emulsion droplets stabilised by silica particles, can result in the appearance of multiple yielding events in rheological measurements. Studies reported by other workers had been carried out at relatively high volume percentages (>50 vol. %), leading to significant contact between the particles or droplets present in the materials. The work presented in this chapter demonstrates that these multiple yielding events can occur at a significantly lower volume percentage

(20 vol. %) through the controlled alteration of the interaction energies between emulsion droplets. This was carried out by screening of the repulsive surface charge of the silica with the addition of NaCl to the aqueous phase altering the interactions between the drops from repulsive to attractive. Additionally, this study has utilised a wide range of rheological techniques to characterise the viscous, and elastic properties of low volume percentage silica stabilised Pickering emulsions.

This chapter has demonstrated that, through the addition of salts to a low volume percentage Pickering emulsion system, the network structure of the system can be significantly, and systematically, altered. The interactions between the silica used to coat the drops was inferred via zeta potential measurements, with the changes further indicated using DLVO calculations. The predicted changes to these interactions were visually observed by microscopy techniques, where the low salt emulsion has well dispersed, unflocculated oil droplets. In comparison, the high (attractive), and medium salt (intermediate) emulsions contained flocculated groups of droplets forming network structures throughout the emulsion. These changes in the emulsion droplet network were found to significantly alter a wide range of the rheological properties of these emulsions. The rheological properties have been compared, and some of the notable data points are summarised in Table 4.7, while the drivers behind these changes are discussed below.

The results presented in Table 4.7 compare some of the key differences between the high (attractive), medium (intermediate), and low salt (repulsive) emulsions. These differences are the result of a range of significant structural changes caused by changes in the interactions between the emulsion droplets. There are two key properties considered in this chapter, the presence of an elastic droplet network structure, and the break-up of said network.

The formation of an elastic network structure in these emulsions is a dependent on the salt concentration of the emulsion system. Data measured for low salt (1×10^{-4} M NaCl) emulsion systems were consistent with emulsion systems having repulsive interactions between the oil droplets. The repulsive interactions between the oil droplets have been demonstrated, throughout the range of rheological and microscopic techniques used in this work, to hinder the formation of an elastic network structure between the oil droplets. This presents in the low shear viscous flow rheology as significantly lower viscosities, about three orders of magnitude lower than that of the high salt emulsions. This reduced viscosity and stress response indicates that there is little structure present. When the low shear viscosity of the high salt emulsion is considered, the measured values are demonstrated

to be significantly larger than those for the low salt emulsions (≈3 orders of magnitude larger). This is ascribed to be the result of the extensive elastic network structure that is present in the high salt emulsion, and is caused by the attractive interactions between the silica particles. In addition to the low shear viscosity, the structure of the droplet network is demonstrated by the value of G' in the linear viscoelastic regime, as shown in Table 4.7. In the low salt emulsion, there is a very limited linear viscoelastic region, with a measured G' value of $0.04 \pm 0.01\,\mathrm{Pa}$. The lack of a significant linear viscoelastic region, and the low G' value, were perhaps the most convincing evidence for the lack of any significant network between the oil droplets of these low salt emulsions. As the salt concentration of the emulsion was increased, the linear viscoelastic region becomes more pronounced. This is the case for both the medium and high salt emulsion systems. The medium salt emulsion demonstrated a linear viscoelastic regime that was ≈2 orders of magnitude greater than that for the low salt system, while also being apparent across a wider range of applied strains. These differences indicate the presence of a network structure between the oil droplets, adding to the solid-like properties of the emulsion. The increase in solid-like behaviour was further demonstrated with the high salt emulsion, with G' in the linear viscoelastic region being $100 \pm 50\,\mathrm{Pa}$. This solid-like behaviour indicated by these measurements is a direct result of the proposed network structure formed between the oil droplets and silica particles present in the high and medium salt emulsions. These results have demonstrated the effect that a cohesive elastic network can have on the bulk properties of a Pickering emulsion system. This is similar to results obtained previously by other workers, and outline that alterations to the interaction energies between colloidal particles yield changes in the rheological properties of a given charged system [8, 57].

Table 4.7. Comparison of high and low salt emulsion data between key measurements for a range of 20 vol. % oil-in-water Pickering emulsions stabilised by 3.45 wt. % silica where the NaCl concentration of the aqueous phase is altered from 1×10^{-4} M (low salt, repulsive), to 0.066 M (medium salt, intermediate), and 1.66 M (high salt, attractive).

Method	High salt	Medium salt primary event (β_M^1)	Medium salt secondary event (β_M^2)	Low salt
Low shear viscosity	150 ± 60 Pa s	–	–	0.20 ± 0.17 Pa s
G' in the linear viscoelastic region	100 ± 50 Pa	1 Pa		0.04 ± 0.01 Pa
Stress linear fit	15 ± 6 Pa	0.04 Pa		0.03 ± 0.02 Pa
Bingham fit stress	–	0.03 Pa		0.04 ± 0.02 Pa
Herschel-Bulkley fit stress	–	0.03 Pa		0.03 ± 0.02 Pa
G' and G'' cross over stress	14 ± 10 Pa	0.01 Pa		0.01 ± 0.01 Pa
G' inflection point stress	13 ± 10 Pa	0.02 Pa	0.03 Pa	–
Stress vs. strain inflection point stress	15 ± 10 Pa	0.02 Pa	0.03 Pa	–
Low frequency G'	70 ± 40 Pa	0.7 Pa		0.07 ± 0.03 Pa

While a material can display significant structure at rest, the transition to flow often gives rise to more interesting measurable phenomena. This was the case with the emulsion systems measured here, and the results obtained provide insights into the break-up or disruption of the networks present in these systems. The processes involved in the yielding of colloidal systems has previously been demonstrated to be related to the types structures present in the system [12–15, 142, 189]. The structures present in the emulsions prepared in this chapter have ranged from weak repulsive materials, with limited structure, to strong elastic networks. Rheological measurements of the weak repulsive materials show very little network break-up, due to the limited network structure that is present in this system. This is demonstrated in Fig. 4.11, in which G' and G'' were measured against an increasing oscillatory strain. The data in this figure showed a relatively unchanging G'' across the applied strain range, while the G' component was only slowly decaying from an initially low value. This is a deviation from the results presented by Katepalli et al. [8], and is likely a result of the significantly lower volume percentage of the emulsions presented here. Additionally, the yield stress values for the low salt emulsion system presented in Table 4.7 were found to be very small in comparison to the high salt emulsion, indicating that the break-down of any temporary static network structure is a process that does not require a significant amount of force. As the salt level of the emulsion was increased, the network break-up processes change, and display additional features. The break-up of the network present in the medium salt emulsion occurs across two distinct events found in the oscillatory rheology, and a single break-up event in the flow rheology measurements. The break-up events measured in the oscillatory techniques were found to be due to two separate processes, a network disruption event at low strains, followed by a cage or floc breaking event at higher strain percentages [12, 13, 15, 142, 188]. Interestingly, these two separate yielding events were not visible in the flow rheology of the medium salt emulsion. This is proposed here to be a result of the similarity of the yield stress values measured for each of the two yielding events. As a result of this similarity, it is expected that the two break-up processes will not be individually distinguishable in the flow curve, instead appearing as a single yield process. Increasing the salt concentration to a high salt system further alters the break-up processes found in the rheology results. Initially, for the flow rheology of the high salt emulsion the stress demonstrated non-standard flow behaviour, as shown by the decrease in the measured stress as the shear rate was increased (Fig. 4.8). Flow behaviours such as these have been reported before, and have been described as anomalous flow [175–177]. In this work, these flow behaviours are proposed as being due to two separate break-up

processes. The initial decrease in the stress results from the break–up of the overall network structure, leaving flocs of oil droplets moving somewhat independently of one another (network breaking). This is thought to be the first stage of yielding in this material, which has been described previously by other groups [12, 13, 15, 130, 142]. As the shear rate is further increased, the stress begins to increase, an indication of the second yield event, the break-up of the flocs present in the system (cage breaking). Somewhat surprisingly, these two network break-up events are not easily distinguishable in the oscillatory rheology measurements for the high salt emulsion. Instead, a single broad break-up is present, likely the result of the overlap of the two separate events. This overlap has been demonstrated in previous works investigating emulsion systems with attractive inter-droplet interactions [8, 142].

The origin and characterisation of multiple yielding events, that have been demonstrated in the rheology of some colloidal systems, has been an area of interest for some time now [12–15, 142, 189]. This chapter has presented a unique low volume percentage colloidal system in which these multiple yielding events occur, while demonstrating a wide range of the techniques that can be used to characterise these systems. Both the bulk rheological, and the microscopic structure of these emulsion system has been shown to be systematically tunable through the addition of salt. The ability to control the properties of an emulsion through this addition provides a foundation to allow the development of products with the desired bulk properties. The next chapter will investigate a method other than the addition of salt for modifying the rheological properties of a Pickering emulsion system.

5 Using pH to manipulate the flow behaviour of Pickering emulsions

5.1. Introduction

Previous chapters in this thesis have reported Pickering emulsions that have been stabilised by silica nanoparticles, where the interactions between the nanoparticles were controlled by altering the ionic strength of the solution. In this chapter, the behaviour of another Pickering stabiliser, titanium dioxide nanoparticles (titania), is considered. These particles were chosen due to their surface chemical properties, uniform needle-like primary particle shape, and ready availability with reliable quality. The specific titania particles (Eusolex® T-2000) are ellipsoidal particles (20 nm × 100 nm) comprised of a core of titanium dioxide and a surface coating comprised of aluminium oxide, simeticone (Fig. 5.1), and "titanol" (Ti—OH) [190, 191], which afford the particles pH sensitive properties. In contrast to the work reported in Chapter 4, where salt concentration was used to alter the Debye length, leading to changes in the interaction strength between the silica particles, this affords the opportunity to modify the attractive interactions between the titania particles through changes to the surface chemistry, and hence the surface charge, by altering the pH of the suspension.

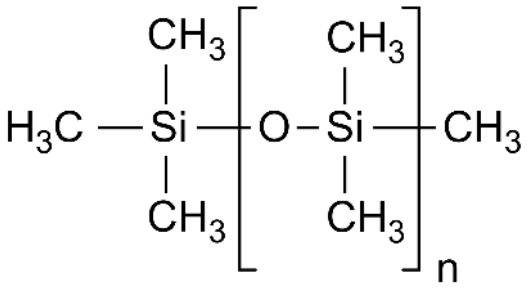

Fig. 5.1 Molecular structure of simeticone.

The Eusolex® T-2000 nanoparticles have a surface coating of aluminium oxide, simeticone, and titanol which alter the hydrophobicity of the particles, with the aluminium oxide and titanol increasing the hydrophilicity, while the simeticone contributes a degree of hydrophobicity to the material. The aluminium oxide coating on the nanoparticles is added as it increases the viability as a UV blocker for use in sun care products. One notable property of the aluminium oxide coating is the amphoteric nature. This will result in the aluminium oxide reacting with both acid or base added to the Pickering emulsions, or suspensions. These reactions will alter the pH of the material, and the products may result in the formation of charged species on the surface of the nanoparticles. The titanol surface will also demonstrate sensitivity to changes in the pH of the surrounding media, becoming protonated at low pH, and deprotonated at high pH, altering the surface charge of the nanoparticles. Simeticone is expected to be unaffected by the addition of acid or base (within reasonable limits) due to the stability of the Si-O, and Si-C bonds. The surface coating of these nanoparticles results in an apparent contact angle against water of 129° [73].

5.2. Experimental methods

5.2.1. Materials used

Pickering emulsions presented in this chapter were prepared as oil-in-water systems using a dodecane oil phase (> 99 %, Sigma Aldrich), which was passed through a neutral alumina column to remove polar impurities. Eusolex® T-2000 was used as a stabiliser in this chapter without further purification or pretreatment. This is a synthetic titanium dioxide nanoparticle that is needle-like in shape with a width of 20 nm, and length of 100 nm. These nanoparticles have a coating of aluminium oxide (8 wt. % to 11 wt. %) and simeticone (1 wt. % to 3 wt. %) (Eusolex® T-2000, Merck) [190, 191]. The aqueous phase had a low background salt level added in the form of NaCl (AR grade, Fisher Scientific) to a final concentration of 1×10^{-4} mol L^{-1}. The acid used in this chapter was 37 vol. % hydrochloric acid (AR grade, Fisher Scientific) which was diluted to the appropriate concentrations, while the base was sodium hydroxide (AR grade, Fisher Scientific), which was prepared to the appropriate concentrations.

5.2.2. Particle analysis

Before emulsions were prepared at a given pH, the relationship between pH and surface charge needed to be established. This was carried out in a series of steps. First the pH of titania suspensions were measured using a pH meter (SevenEasy pH, Mettler Toledo, Columbus, Ohio, USA) as known concentrations of acid or base were titrated against dispersions of titania nanoparticles at a range of particle concentrations. This measured pH was compared against the theoretical calculated pH in order to demonstrate the buffer capacity of the titania nanoparticles. The theoretical pH was calculated from the volumes of acid or base added to the aqueous component of the system, assuming no interactions with other species. Once the effect of pH was determined, the zeta potential of ≈0.01 wt. % and ≈0.7 wt. % dispersions of titania nanoparticles at a range of pH values were measured using a Malvern Zetasizer Nano with disposable folded capillary cells (DTS1070).

The shape of the titania nanoparticles was confirmed using both transmission electron microscopy (TEM), and scanning electron microscopy (SEM). This microscopy was carried out by drying small droplets of suspensions of the nanoparticles originally at pH 6 and pH 12 onto microscopy stubs before imaging. As the images were taken in a dry state, they are only representative of the structure of single nanoparticles. TEM and SEM imaging was carried out by Niki Minards at the Manawatu Microscopy Imaging Centre using a FEI Tecnai G2 Biotwin TEM and a FEI Quanta 200 Environmental SEM.

5.2.3. Emulsion preparation

To prepare these emulsions a 1 wt. % dispersion of titania was prepared in a 1×10^{-4} mol L^{-1} NaCl solution. This solution was further diluted with 1×10^{-4} mol L^{-1} NaCl to a final titania concentration of 0.7 wt. %. To this, a volume of dodecane was added (50 vol. %), and the solution was homogenised with a rotor-stator homogeniser (PowerGen 125, Fisher Scientific) at 30 000 min^{-1} for 2 minutes while moving the homogeniser head throughout the sample. Once the samples were fully emulsified, samples were taken and diluted with the appropriate acidic or basic solutions to the desired oil volume fraction of 30 vol. % giving two emulsions with either a calculated pH of 6 or 12.

5.2.4. Droplet analysis

Droplets were analysed for both morphology and size using optical, confocal microscopy, and dynamic laser scattering. Optical microscopy was carried out in dilute systems (∼1.5 vol. %) in order to reduce excessive scattering with the diluted sample placed in a welled slide.

Optical micrograph images were captured with a 40× objective on a Zeiss Axiophot Microscope. Confocal microscopy was carried out on undiluted samples (30 vol. %) which had two different fluorescent dyes added, one oleophilic dye (Nile Red, $\approx 9 \times 10^{-4}$ M), and another charged hydrophilic dye (Nile Blue, $\approx 9 \times 10^{-4}$ M). The two dyes were used specifically to demonstrate the oil droplet morphology and distribution (with the oleophilic dye, Nile Red), and the distribution of titania nanoparticles within the surrounding aqueous media (with the charged dye, Nile Blue). Excitation of the Nile Red dye was carried out with a 514 nm laser at 39 % power while the emission was captured between 519 nm to 671 nm for the pH 6 emulsion, and 650 nm to 787 nm for the pH 12 emulsion. Nile blue involved excitation and measurement of emission at different ranges for pH 6 and pH 12 samples. At pH 6 excitation was carried out with a 633 nm laser at 30 % power with the emission captured between 634 nm to 800 nm. At pH 12 the excitation was carried out with both a 633 nm laser at 42 % power and a 561 nm laser at 45 % power with the emission captured between 650 nm to 787 nm. These images were captured using a 63× oil-immersion objective attached to a Leica DM6000B SP5 confocal laser scanning microscope with a 3× digital zoom provided via software.

Particle size analysis of the emulsions used a Mastersizer 3000 and was processed with the accompanying software package (version 3.70). An initial measurement of each emulsion preparation was measured across a full size range of 0.01 µm to 1000 µm, followed by repeat measurements across a more limited size range of 1 µm to 1000 µm, in order to remove the large broad peak that is associated with free titania particles (individual titania particles are ellipsoidal with dimensions of 20 nm × 100 nm).

While the optical microscopy methods show the bulk structure of the emulsion droplets, it is not possible to directly visualize the location of the titania present in the Pickering emulsion system. To better determine the location of the titania in these Pickering emulsion systems, freeze-fracture cryo-scanning electron microscopy (cryo-SEM) images of the interfacial structures in the emulsions were obtained. This used a Philips XL30 Field Emission Scanning Electron Microscope fitted with a Gatan Alto cryo-trans system at the University of Auckland. A few drops of the emulsion were frozen in nitrogen slush. The frozen emulsion was fractured under ultra-high vacuum and then etched at $\approx -95\,^{\circ}$C for 60 s. The fractured surface was coated in platinum (10 mA, 105 s, 1 mbar argon) before being transferred to the cold stage ($\approx -170\,^{\circ}$C) of the SEM. Cryo-SEM (cryo-SEM) was utilised to identify the distribution of titania throughout the sample. Cryo-SEM images presented in this chapter were captured by Dr. Catherine Whitby, utilising a 30 vol. %

emulsion stabilised by 0.7 wt. % of titania at pH 6.

5.2.5. Rheological measurements

Emulsion samples were left to rest overnight to develop a standard structure before rheological analysis was carried out (as described in section 3.3.1. While this is a different emulsion, similar results are expected, and as such this standard was maintained). Rheological measurements were carried out at 20 °C and with a 40 mm parallel plate geometry at a gap height of 400 µm on a DHR-2 rheometer (TA Instruments). Emulsion samples were placed on to a rheometer plate with a disposable Pasteur pipette. Preparing the material for analysis was carried out by preshearing for 30 seconds at $0.1\,\mathrm{rad\,s^{-1}}$, with no equilibration time before the experiment was carried out. A number of experiments were run on each emulsion, a strain sweep monitoring the strain dependence of stress, G', and G'', a frequency sweep monitoring the frequency dependence of G' and G'', and a flow curve monitoring stress and viscosity.

5.2.5.1. Strain sweep

Strain sweep measurements were all performed across the strain range of 0.01 % to 15 000 % at a constant frequency of $1\,\mathrm{rad\,s^{-1}}$ with 5 data points measured per decade with 10 s averaging time per point after a 5 s condition step per data point. The strain vs. stress, G', and G'' curves were measured for the material. The range of strains chosen here allowed for full coverage of the areas of interest with each emulsion measured, showing both the elastic state of the emulsions at low strain percentages, and the viscous nature of the systems at high strain percentage.

5.2.5.2. Frequency sweep

Frequency sweep measurements were performed at a strain percentage found to be within the linear viscoelastic region from the previous strain sweep measurements. The strain percentage used for each measurement in these experiments was 0.25 %. The frequency range that was used for these experiments was $0.1\,\mathrm{rad\,s^{-1}}$ to $500\,\mathrm{rad\,s^{-1}}$ with 5 data points per decade. Each point was measured by averaging over 5 s after a 5 s conditioning step.

5.2.5.3. Flow curve

Flow curve experiments were performed with an increasing shear rate from $0.01\,\mathrm{s^{-1}}$ to $1\,\mathrm{s^{-1}}$ with 10 data points per decade with 20 s of averaging per point measured after

a 10 s conditioning step. Higher shear rates were attempted with these emulsion systems ($\leq$100 s^{-1}), however due to emulsion degradation, the shear rate range was reduced (results not included).

5.2.5.4. Creep and creep recovery

The creep experiment was performed after the flow curve and strain sweep methods due to the need for some prior knowledge of the approximate range of the yield stress. Creep measurements were carried out with a range of applied stresses, with sample replacement between each measurement. The stresses were applied for a minimum of 300 s, with the resultant displacement of the sample being measured as the stress was applied. Then, the sample was left to relax for a minimum of 60 s with the displacement of the sample being measured. Errors are not presented for creep experiments due to the nature of the measurements limiting the ability to average measurements.

5.3. Results

5.3.1. Emulsion microstructure

As pH has been used in this chapter to modify the physical properties of the emulsions, the effect that the addition of acid or base has on the overall measured pH of a titania dispersion was investigated. This was carried out via a pH titration at different particle concentrations, each of which are shown in Fig. 5.2. This figure shows the typical shape for a titration curve against a buffer, with the concentration of titania altering the width of the "buffer" region of the suspension. This demonstrates the multiple regions that may display a range of surface potentials with these nanoparticles, below a calculated pH 5, the buffer region between calculated pH 5 and pH 10, and above calculated pH 10.

Once the effect that the addition of acid or base had on the pH had been quantified, the effect that these changes in pH had on the surface potential of the titania suspensions was measured. This was carried out by measuring the zeta potential of titania suspensions prepared at a range of calculated pH values and the results of this are shown in Fig. 5.3.

Figure 5.3 shows that altering the calculated pH from 2 to 12 does have a significant effect on the surface charge of the titania particles. At calculated pH values less than 9, the value of the zeta potential is positive, and increases in magnitude as the pH is further decreased. As the pH was increased greater than 10, the zeta potential becomes negative, and continues towards more negative values with further increases in pH. This fits well

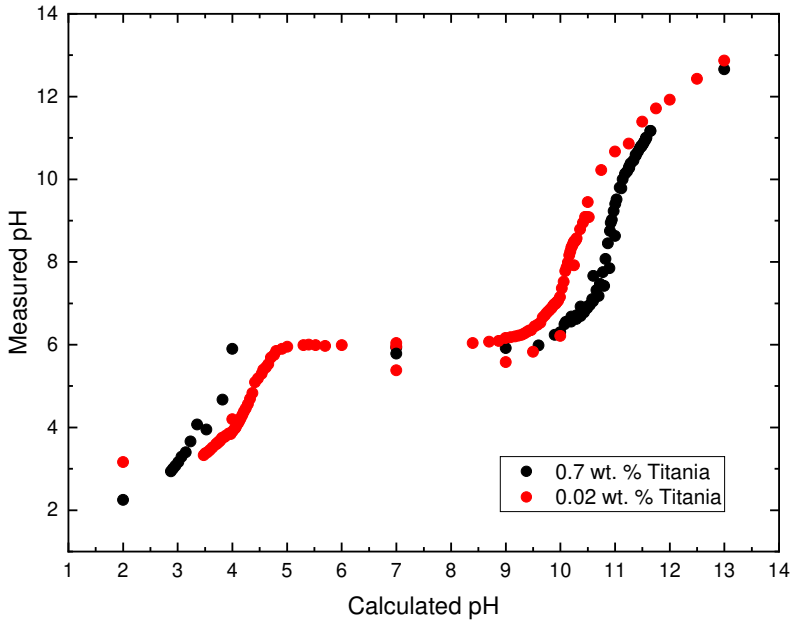

Fig. 5.2 pH sensitivity of two titania nanoparticle concentrations (0.7 wt. %, •; 0.02 wt. %, •). The measured pH is plotted against the calculated pH, which was calculated from the volumes of acid or base added to the suspensions.

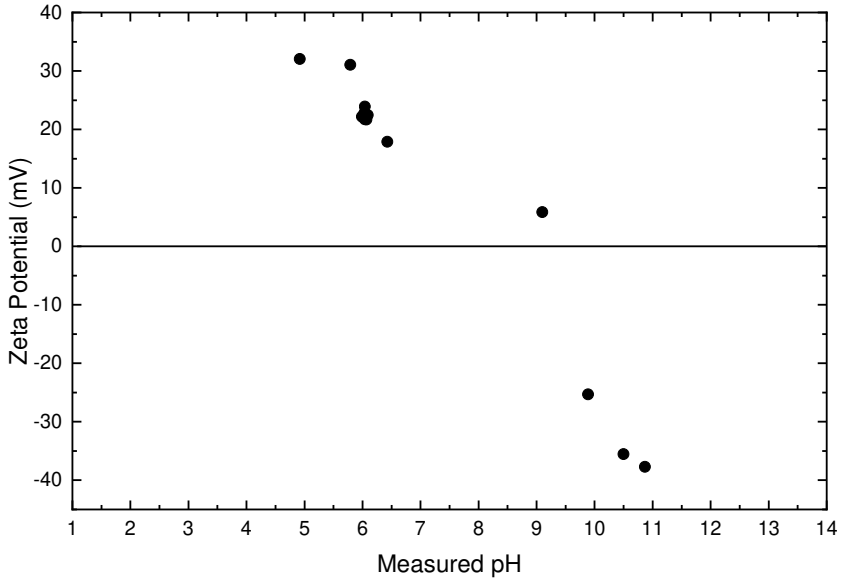

Fig. 5.3 Zeta potential measurements of 0.01 wt. % titania suspensions at a range of pH values demonstrating changes in the surface charge of the titania.

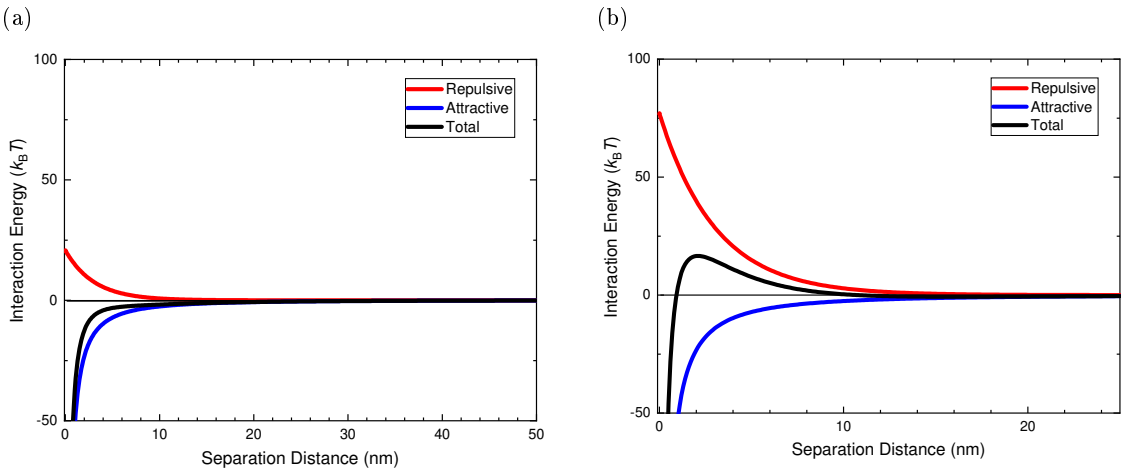

Fig. 5.4 Potential energy curves of the interaction between two spherical particles at two different pH values. The different pH causes a change in the zeta potential of the titania nanoparticles. (a) Calculations for titania suspension at pH 6. (b) Calculations for titania suspension at pH 12. ($\varepsilon = 78.54$, $a = 50\,\text{nm}$, $T = 298.15\,\text{K}$, $A = 60 \times 10^{-21}\,\text{J}$, $\kappa = 3.29 \times 10^{8}\,\text{nm}^{-1}$, $\varphi_d(\text{pH } 6) = 20\,\text{mV}$, $\varphi_d(\text{pH } 12) = -40\,\text{mV}$).

with the pH titration curve (Fig. 5.2), with the pH values of 5 and 10 being the bounds of the "buffer region", in which the measured pH is relatively insensitive to the addition of acid or base. Given these results, two measured pH levels were used to prepare emulsions throughout this work, pH 6 and pH 12.

The interaction energy profiles of the titania particles can be approximated to demonstrate the effect of pH. This was achieved via DLVO calculations, as described in Sections 1.4.1.5 and 4.3.1. The Hamaker constant that was used for the titania nanoparticles was $60 \times 10^{-21}\,\text{J}$ [192] and the two particles were assumed spherical with a radius of 50 nm in order to simplify the calculations (chosen to be between the width (20 nm) and length (100 nm) of the ellipsoidal particles). The results of these DLVO calculations for pairs of titania nanoparticles at both pH 6 and pH 12 are demonstrated in Fig. 5.4. This figure shows that at pH 6, the interaction energy is attractive across the full range of separation distances. When comparing this plot to that of the pH 12 suspension, the differences between the samples becomes evident. The calculations for the pH 12 suspension show a peak of $\approx 17\,k_B T$ at a separation distance of 2.1 nm while there is a secondary minimum at 15.7 nm of $\approx -0.7\,k_B T$. These calculations demonstrate that the pH 6 suspension will have attractive interactions between the particles, while the pH 12 has an energy barrier leading to a repulsive interaction between the particles.

The titania nanoparticles used to stabilise the emulsions in this chapter have been reported to have an ellipsoidal shape, or needle-like shape [190]. The shape of the titania

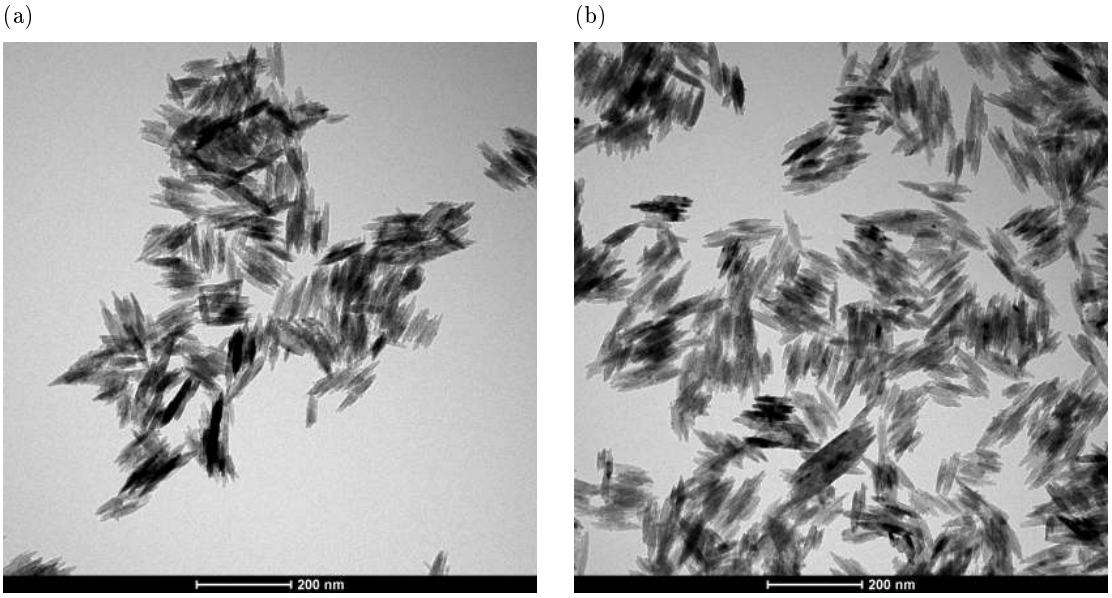

Fig. 5.5 TEM images of dried suspensions of titania nanoparticles that, in their suspended state, were (a) pH 6, and (b) pH 12. This demonstrates that there is no notable change in the size or morphology of titania particles as the pH is altered.

was investigated as a dried suspension with both TEM and SEM imaging. An example of the TEM images for both pH 6 and pH 12 suspensions are shown in Fig. 5.5. These TEM images demonstrate that the titania particles used in this work do indeed have an ellipsoidal shape. When comparing the images of the pH 6 and pH 12 suspensions there does not appear to be any significant difference between the two. This expected result is due to the requirement of dry samples for TEM imaging. This drying will likely result in aggregation of any particles, leading to results that become very similar. The TEM images also demonstrated that the size and morphology of the titania particles has not been altered by the changes in pH. SEM imaging was also carried out on these materials, which demonstrated a relatively even surface coating of titania nanoparticles on the microscopy stub at each measured pH (results not shown).

Optical micrographs of the emulsions prepared for this chapter are shown in Fig. 5.6. Both the pH 6 and pH 12 emulsion images demonstrate spherical droplets with a distribution of droplet sizes. Neither the pH 6 nor pH 12 emulsion appear to demonstrate a significant amount of flocculation between the oil droplets, likely due to the low droplet concentration of the samples.

Figure 5.7 demonstrates the shape of the distribution of titania aggregates, emulsion droplets, and flocs of droplets. Figure 5.7a demonstrates the size distribution of material present in the initial bulk emulsions prepared. From these initial bulk emulsions, the pH 6 and pH 12 emulsions were prepared by diluting the emulsion with the appropriate aqueous

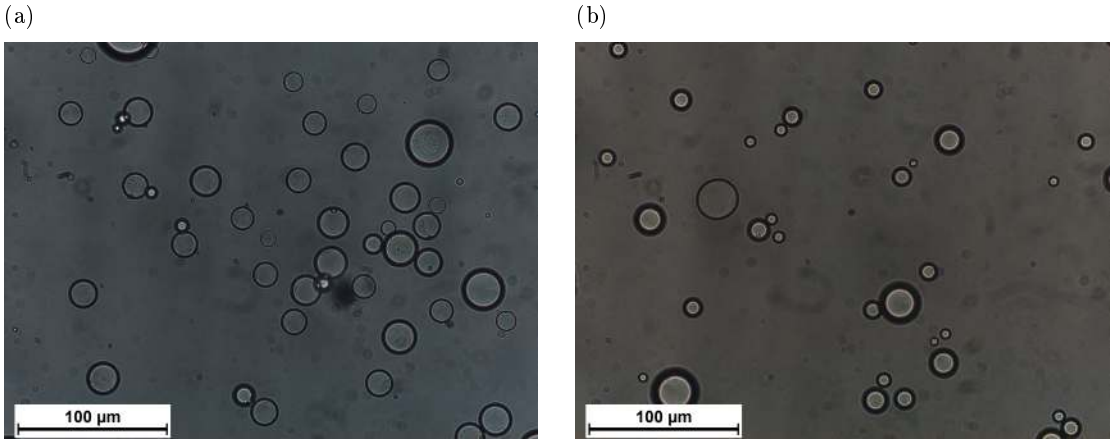

Fig. 5.6 Optical microscopy images showing the structure of ≈1.5 vol. % oil-in-water Pickering emulsions stabilised by ≈0.04 wt. % titania at both (a) pH 6 and (b) pH 12.

solutions. This was performed to ensure that each emulsion prepared had a consistent droplet size. One of the features of Fig. 5.7a is the shape of the distribution where three notable peaks in the size distribution are observed; a broad peak centred at roughly 0.1 µm, and two sharper peaks centred at about 20 µm and 100 µm. Each of these peaks can be assigned to different features present in the emulsion samples. The first broad peak at 0.1 µm is thought to be due to free titania in the sample forming aggregates rather than oil droplets given the methods used to prepare the emulsion not being expected to lead to droplets of this size [193]. The second sharper peak at 20 µm is ascribed to single droplets present in the emulsion sample, an assertion consistent with the microscopy images of Fig. 5.6. Finally, the last sharp peak at 100 µm is present to due to aggregates (or flocs) of droplets, held together by the attractive interactions between the oil droplets.

When the size distributions present in Figs. 5.7b and 5.7c are considered it shown that each of these emulsions demonstrates a slightly different distribution of particle sizes. The pH 6 emulsion demonstrated in Fig. 5.7b shows a similar distribution to that of the initial bulk emulsion, with three main peaks present in the distribution. This is expected, as the pH of this emulsion is identical to that of the initial bulk emulsion, with the only difference between the two samples being the oil volume percentage. These systems have been shown to have an attractive interaction between the titania particles, leading to the formation of flocs, which may not break down into individual droplets in the Mastersizer instrument. The distribution shown in Fig. 5.7c does not display the same pattern of peaks. The large broad peak at small sizes (0.1 µm) arises due to free titania nanoparticles in the aqueous phase, which are assumed to assemble into larger aggregates. Instead of the two sharper

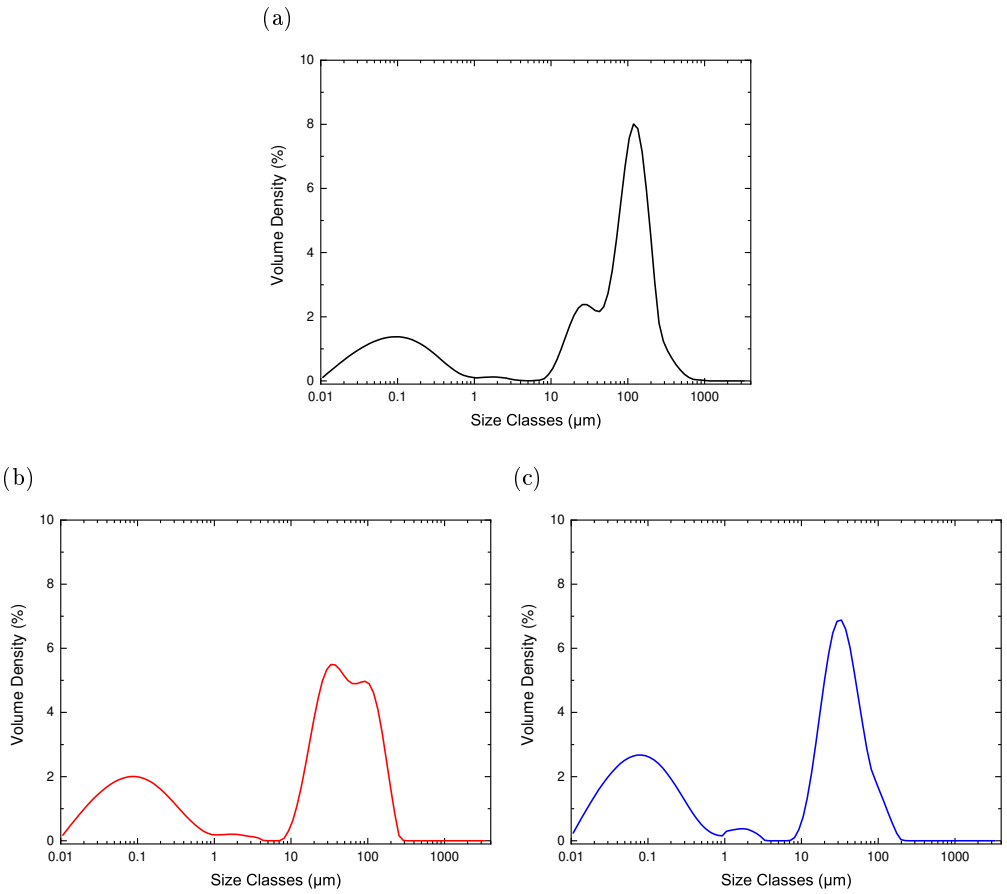

Fig. 5.7 Size distributions of oil-in-water Pickering emulsion droplets stabilised by 0.7 wt. % titania at different pH. (a) Initial bulk emulsion. (b) pH 6 emulsion. (c) pH 12 emulsion.

peaks in Figs. 5.7a and 5.7b, there is a single peak in the size distribution. This single peak at 30 µm is expected to be due to single emulsion droplets. The lack of aggregates present in this pH 12 emulsion sample is consistent with the repulsive interactions between the oil droplets. This repulsive interaction will limit the formation of network structures, and as such these are less likely to be observed in a dilute system, such as is used in the Mastersizer instrument.

Confocal microscopy allows the 'slicing' of the emulsion into almost two-dimensional slices. This allows the core and shell of the emulsion droplets to be imaged with limited interference from other z–planes (parallel to the viewing plane) that are out of the focal plane (for example the spherical tops or bottoms of each emulsion droplet). The use of fluorescent dyes highlights each phase of the emulsion. When Figs. 5.8a and 5.8b are compared, there is a difference in the distribution of the titania coating (as represented by the Nile Blue dye). In Fig. 5.8a titania is largely found to be only coating the oil droplets with a coat distributed evenly around each of the oil drops. In comparison, Fig. 5.8b shows a distribution of titania throughout the aqueous material surrounding the oil droplets with large clumps of titania forming, and an uneven coating of titania on each oil droplet. These observations are also described macroscopically with dispersion of titania in different pH solutions. At high pH (pH $>$ 10) titania was observed to aggregate within an hour, due to the poor dispersibility of the titania nanoparticles. Below pH 10, particle suspensions were stable over a longer time period, with limited aggregation occurring over the course of days. Additionally, the pH 12 emulsions were found to be more susceptible to coalescence than the pH 6 emulsions, likely a result of the incomplete particle shells demonstrated in Fig.5.8b. This resulted in the pH 12 emulsions phase separating in situations where the sample was not treated in a careful manner, i.e. phase separation occurred if the samples were shaken vigorously or for long time periods.

The location of the titania nanoparticles was further probed with cryo-SEM. Figure 5.9 shows the shell structures formed by the titania nanoparticles around each oil droplet. In addition to these shells, there are small ridges distributed throughout the water phase. These ridges are comprised of dispersed titania particles and may suggested some degree of network formation between each of the titania nanoparticle shells, although it is possible that these features are an artefact of the freezing process.

(a)

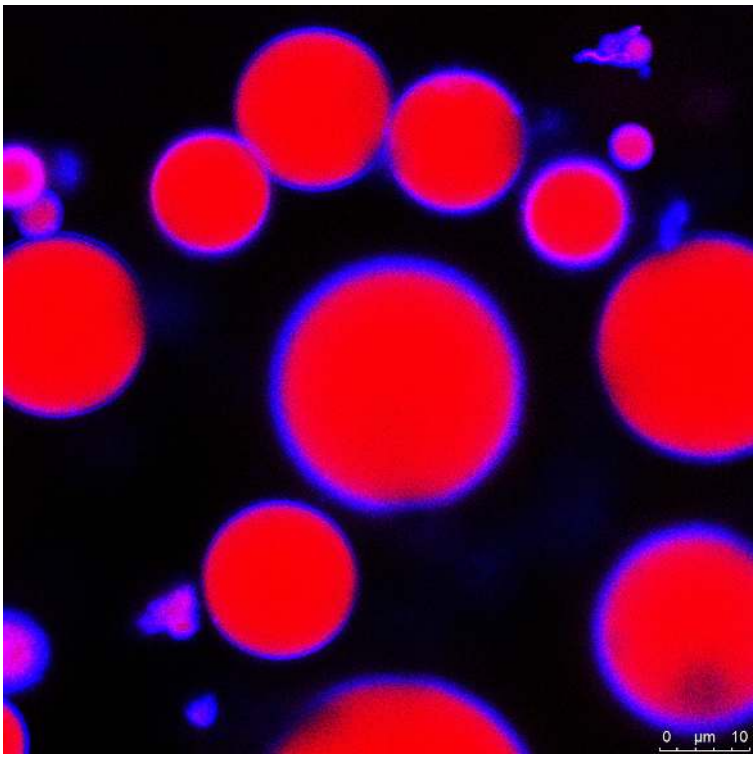

(b)

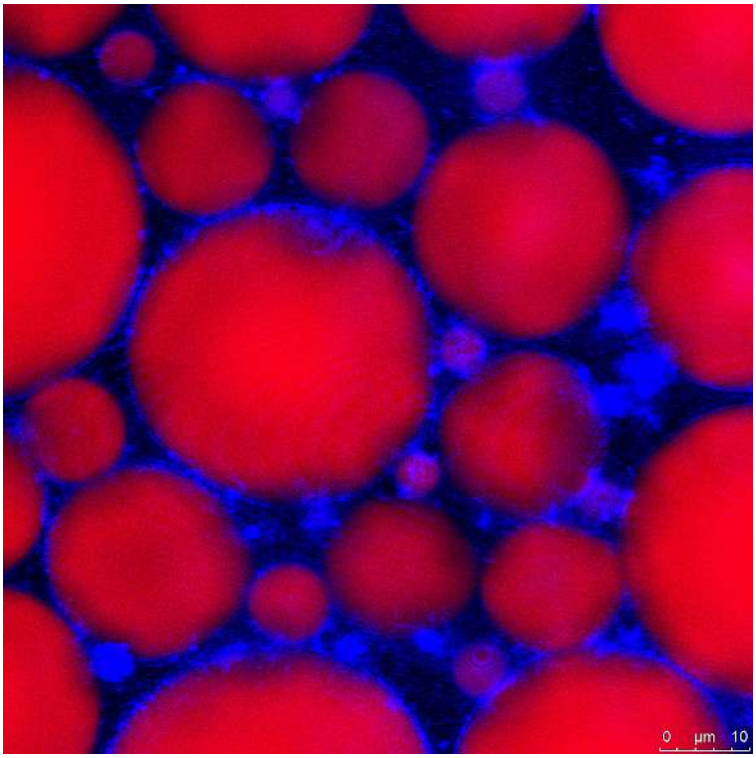

Fig. 5.8 Confocal microscopy image of 30 vol. % oil-in-water Pickering emulsions stabilised by 0.7 wt. % titania. The red colouration is representing the $\approx 9 \times 10^{-4}$ M Nile Red dye, and the blue colouration is due to the $\approx 9 \times 10^{-4}$ M Nile Blue dye. (a) pH 6. (b) pH 12.

(a)

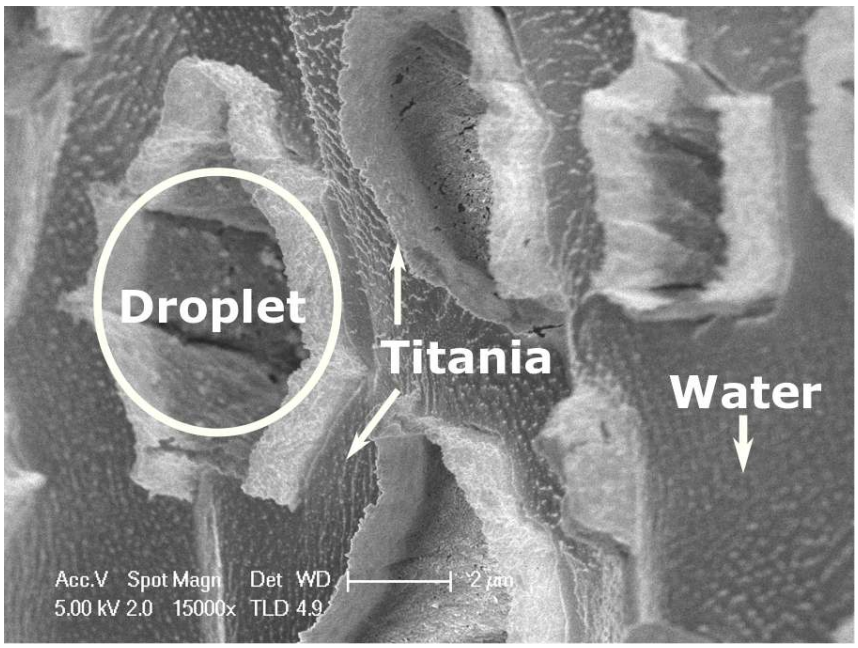

(b)

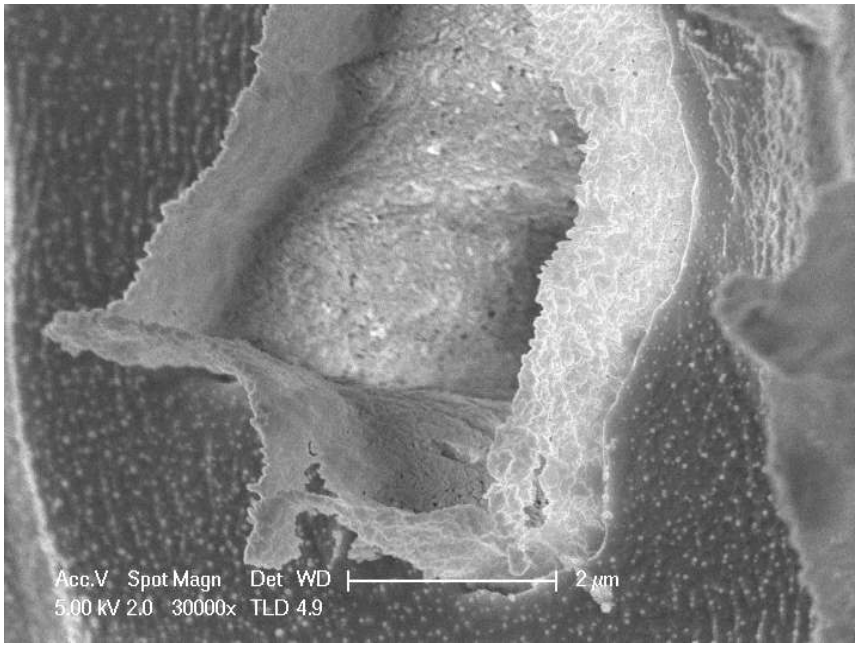

Fig. 5.9 A 30 vol. % oil-in-water Pickering emulsion stabilised by 0.7 wt. % titania at pH 6 imaged by cryo-SEM. (a) Demonstrates multiple droplet shells distributed through an aqueous phase containing titania aggregates. Labels are added to show the outline of a droplet, while also highlighting the titania forming the droplet shells and the small ridges throughout the dark grey water component. (b) Shows a single droplet shell, better demonstrating the thin shell, while also showing the ridges of titania in the aqueous phase.

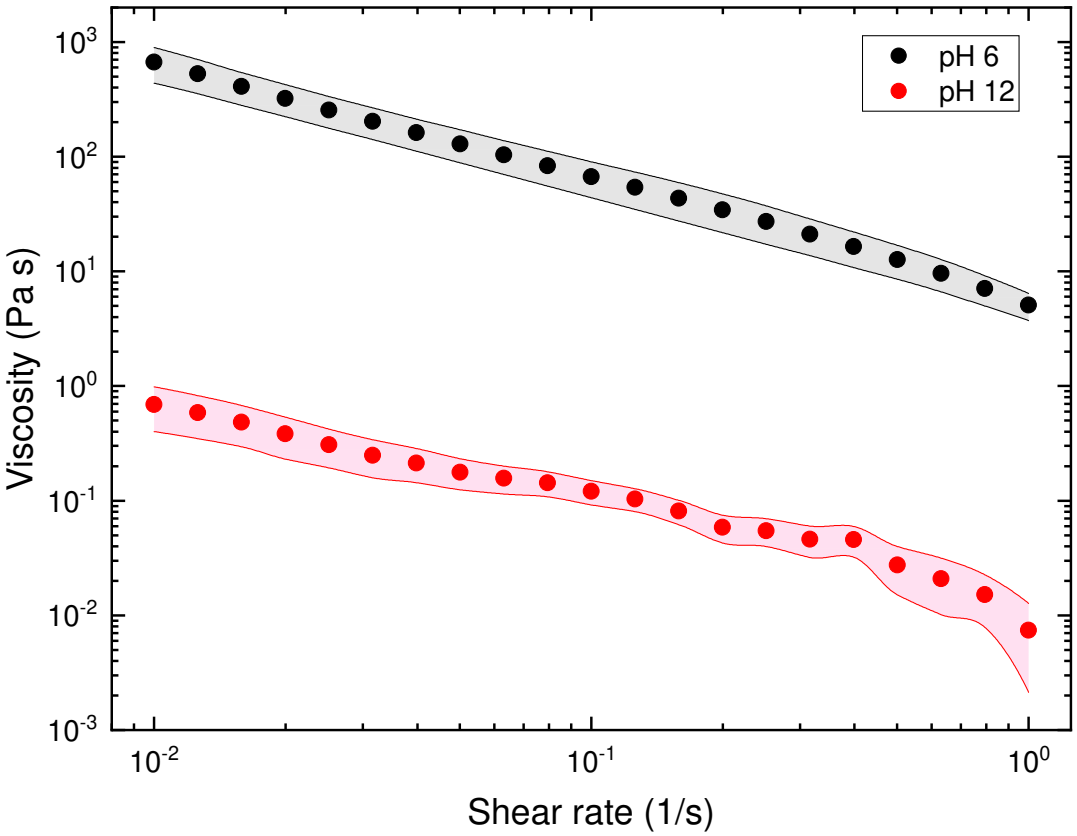

Fig. 5.10 Shear rate vs. viscosity plot for a 30 vol. % oil-in-water Pickering emulsion stabilised by 0.7 wt. % titania at pH 6 (•) or 12 (•). Shaded areas indicate the variation in multiple measurements of these emulsion systems.

5.3.2. Viscous flow rheology

As has been discussed in previous chapters, non-Newtonian fluids, such as the emulsions studied in this work, show changes in viscosity as the applied shear rate is altered. This is apparent in Fig. 5.10 where the viscosity of two titania emulsions are shown to decrease as the shear rate is increased. This decrease demonstrates the shear thinning behaviours of these emulsions. The range of shear rates investigated in this chapter are limited compared to those in previous chapters due to issues with emulsion stability at higher shear rates, where the emulsion would destabilise and phase separate at shear rates greater than $1\,s^{-1}$ (data not shown here). The ratio of the viscosities between each emulsion remains relatively constant across the range of shear rates, with the pH 6 emulsion being about three orders of magnitude larger than that of the pH 12 system.

When the low shear viscosities for each emulsion are compared it is apparent that the pH 12 emulsions are significantly less viscous, with a low shear ($1 \times 10^{-2}\,s^{-1}$) viscosity of about 0.7 Pa s compared to the nearly 700 Pa s for the pH 6 emulsion. As has been

Table 5.1. Calculated initial viscosities from a number of different models compared to the measured low shear (0.01 Pa s) viscosities of the 30 vol. % oil-in-water Pickering emulsion stabilised by 0.7 wt. % titania measured at pH 6 or 12.

Einstein model viscosity (Pa s)	Batchelor model viscosity (Pa s)	Kreiger-Dougherty model viscosity (Pa s)	pH 6 emulsion low shear viscosity (Pa s)	pH 12 emulsion low shear viscosity (Pa s)
1.5×10^{-3}	2.1×10^{-3}	2.5×10^{-3}	700 ± 200	0.7 ± 0.3

carried out in previous chapters, several models have been used to predict the low shear viscosity of an emulsion of this volume percentage. Again, these models are based around non-interacting hard spheres, and are more applicable at very low volume percentages where these assumptions are more applicable. The results of these calculations, as well as a comparison to the measured low shear viscosities for each emulsion are provided in Table 5.1.

Table 5.1 shows that the calculated values for the viscosity do not correspond well with either the pH 6 or pH 12 emulsion systems that have been evaluated here. When the viscosity of the pH 6 system is considered in comparison with the model systems, it is apparent that the measured system shows a significantly higher viscosity (by 5 orders of magnitude). This was not an unanticipated result as the pH 6 emulsion was expected to show attractive behaviour between the particle coated emulsion droplets. These attractive interactions will lead to an increase in the measured viscosity, such as is demonstrated here. With the pH 12 emulsion, it can be shown that the initial measured viscosity is higher than the models used here predict. In these experiments, this pH 12 emulsion is designed to be an emulsion with repulsive behaviour between the particle coated emulsion droplets. This repulsive interaction results in a decrease in the measured viscosity of the bulk pH 12 emulsion system when compared to the pH 6 emulsion system.

The stress response of each of the two measured emulsions is demonstrated in Fig. 5.11. When the two curves displayed in Fig. 5.11 are compared it is clear that there is a difference between the stress response of the two emulsions. Similar to the viscosity curves of Fig. 5.10, the measured stress of the pH 6 emulsion (low shear value of 6.6 Pa) is significantly greater than that of the pH 12 emulsion (low shear value of 0.007 Pa).

The shape of the stress-shear rate relationships is also of interest in gathering information about the properties of the two emulsion systems. Figure 5.11 demonstrates the relative insensitivity of the stress to changes in shear rate, with the pH 12 emulsion showing only a slight increase from 0.8×10^{-2} Pa to 2×10^{-2} Pa (with exclusion of the final few data

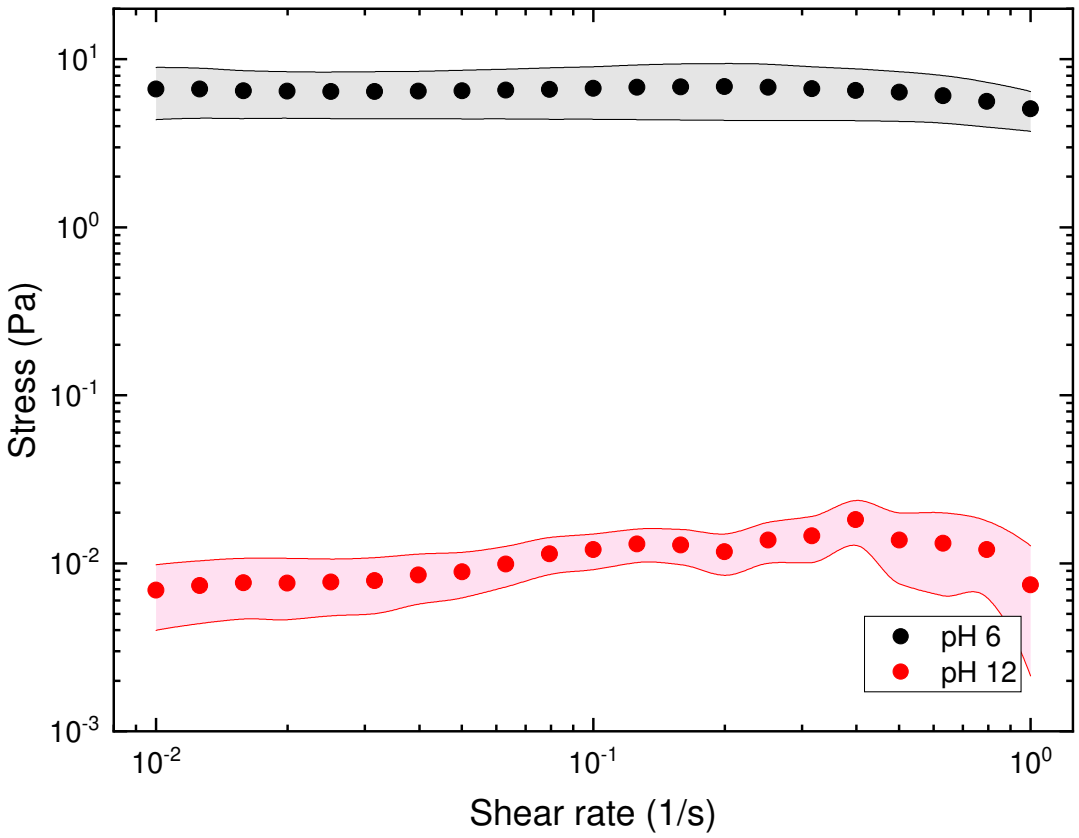

Fig. 5.11 Shear rate vs. stress for 30 vol. % oil-in-water Pickering emulsion stabilised by 0.7 wt. % titania at pH 6 (•) or 12 (•). Shaded areas indicate the variation in multiple measurements of these emulsion systems.

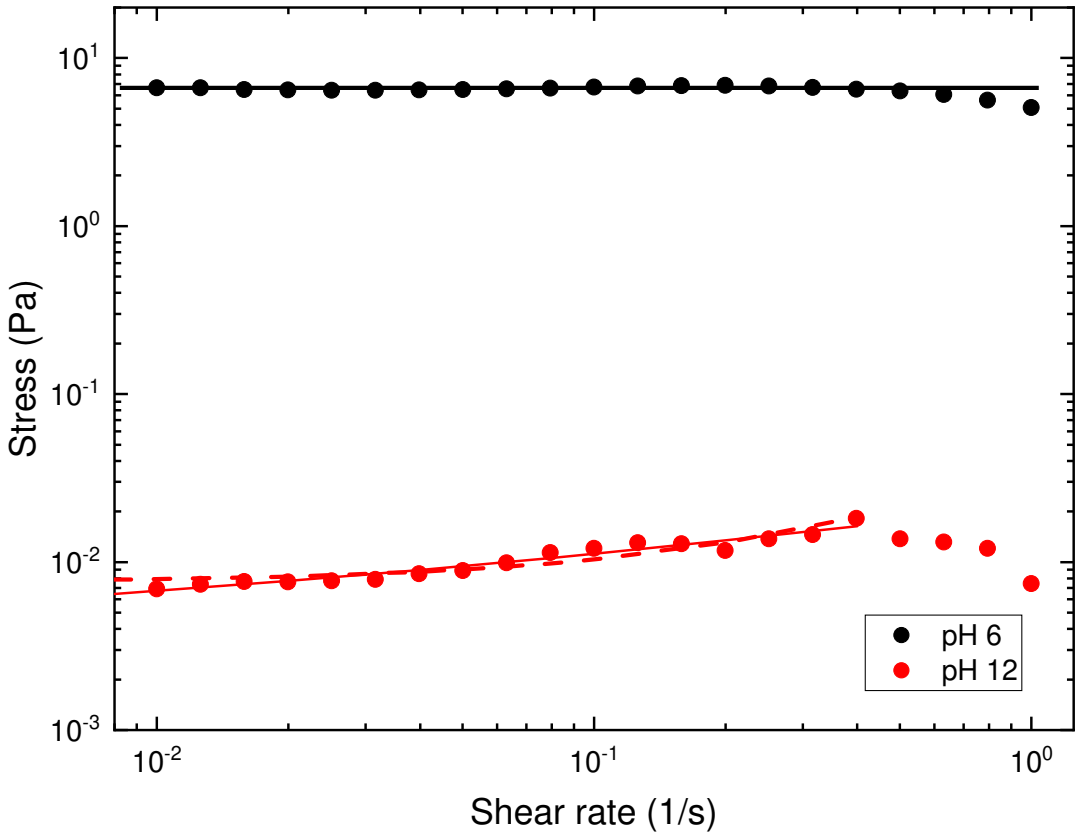

Fig. 5.12 Shear rate vs. stress for 30 vol. % oil-in-water Pickering emulsions stabilised by 0.7 wt. % titania at pH 6 (•) and pH 12 (•). Lines demonstrate the fittings of these data with each of the applied models. With the pH 6 emulsion, the solid black line is the low shear average (6 ± 2 Pa). For the pH 12 emulsion, the solid red line is the Herschel-Bulkley model (0.004 ± 0.003 Pa), while the dashed red line is the Bingham model fitting (0.008 ± 0.005 Pa). The pH 12 emulsion was also fitted with two averages (not shown here), one at low shear (0.008 ± 0.002 Pa), and one across the full applied shear range (0.008 ± 0.004 Pa).

points) in stress as the shear rate is increased, while the pH 6 emulsion stays constant at about 6 Pa to 8 Pa. Due to the lack of change in the stress of the pH 6 emulsion, the fitting of the data was limited to use of an average, while with the pH 12 emulsion, both a low shear average, and two models (Bingham and Herschel-Bulkley) were applied to extract a yield stress value.

There are large differences in the measured yield stresses for the pH 6 and pH 12 emulsions. When the pH 6 emulsion was fitted with an average the yield stress was found to be 6 ± 2 Pa. The pH 6 emulsion data was not fitted with either the Herschel-Bulkley or Bingham fits. The pH 12 emulsion was found to have a yield stress of 0.008 ± 0.002 Pa from both the average fitting, and the Bingham fit, while the fitting of the Herschel-Bulkley gave a yield stress value of 0.004 ± 0.003 Pa. The differences between the yield stresses of the

two emulsions supports the hypothesis that the change in interaction between the emulsion droplets has resulted in a substantially different network structure forming. At pH 6 the interaction between the oil droplets is expected to be attractive, and is proposed here to result in a network structure which provides the bulk strength of the emulsion. This leads to the pH 6 emulsion having a yield stress that is much greater than what may have initially been predicted. At pH 12, the emulsions are expected to have a repulsive interaction between the oil droplets. The repulsive interaction between oil droplets would not be anticipated to result in a network structure forming through the emulsion system and would lead to an emulsion with much lower bulk strength than that for the pH 6 system.

5.3.3. Oscillatory measurements

5.3.3.1. Strain analysis

As with the work reported in Chapters 3 and 4, oscillatory rheology was used to develop insight into the elastic properties of these two emulsion systems. The effect of both the amplitude and the frequency of oscillations were investigated.

Initially the effect that an increasing amplitude of oscillation had was investigated for both the pH 6 and pH 12 emulsions, and the results are displayed in Fig. 5.13. The G' and G'' for the pH 6 emulsion are significantly greater than those for the pH 12 emulsion, showing an increase in the strength of the system. This is best demonstrated by comparing the values of the storage modulus in the linear viscoelastic region where the pH 12 emulsion has an approximate value of 1.1 Pa while the pH 6 emulsion has an approximate value of 85 Pa. This difference is expected for these emulsions, as the pH 6 emulsion will have an attractive interaction between the oil droplets, leading to an increase in the strength of the emulsion system. When comparing this with the pH 12 emulsion, which has repulsive interactions between the titania-coated oil droplets, the strength of the emulsion system will be diminished.

Fitting of the curves in order to determine the yield stress of the these emulsions was again carried out in segments, with an average fitted to the linear viscoelastic region, and a power law fitted to the decreasing G' at higher strain percentages. In addition to these, a power law was also fitted to the decrease in the G'' at high strains. These fittings can then be used to extract values of the yield stress for these emulsions, through methods that have been described in Section 2.8.2.2. These fittings are shown in Fig. 5.14.

The first method used to determine the yield stress was the cross over point of the two fittings of the storage modulus of each emulsion. At the intersection of these two fittings

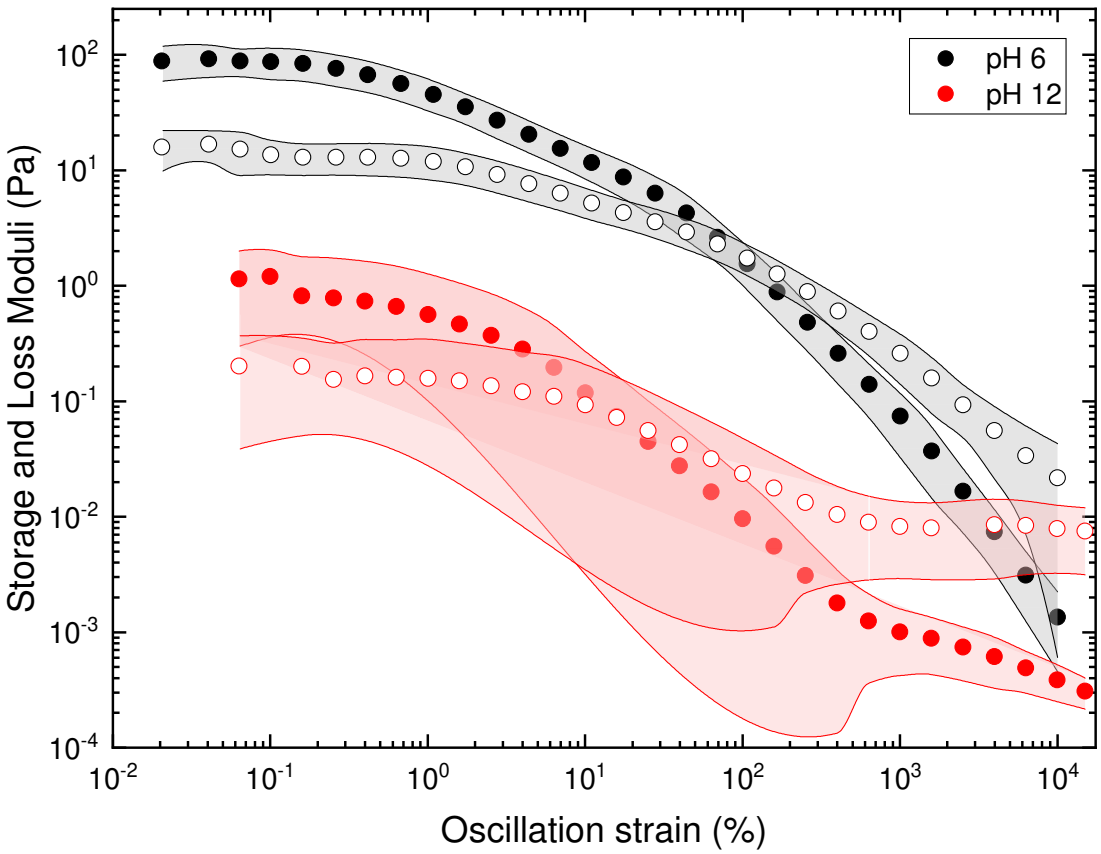

Fig. 5.13 Response of the elastic storage modulus (•) and the viscous loss modulus (○) of 30 vol. % oil-in-water Pickering emulsions stabilised by 0.7 wt. % titania at pH 6 (•) and pH 12 (•) to changes in the applied oscillatory strain at a constant oscillation frequency ($1\,\mathrm{rad\,s^{-1}}$). Shaded areas indicate the variation in multiple measurements of these emulsion systems.

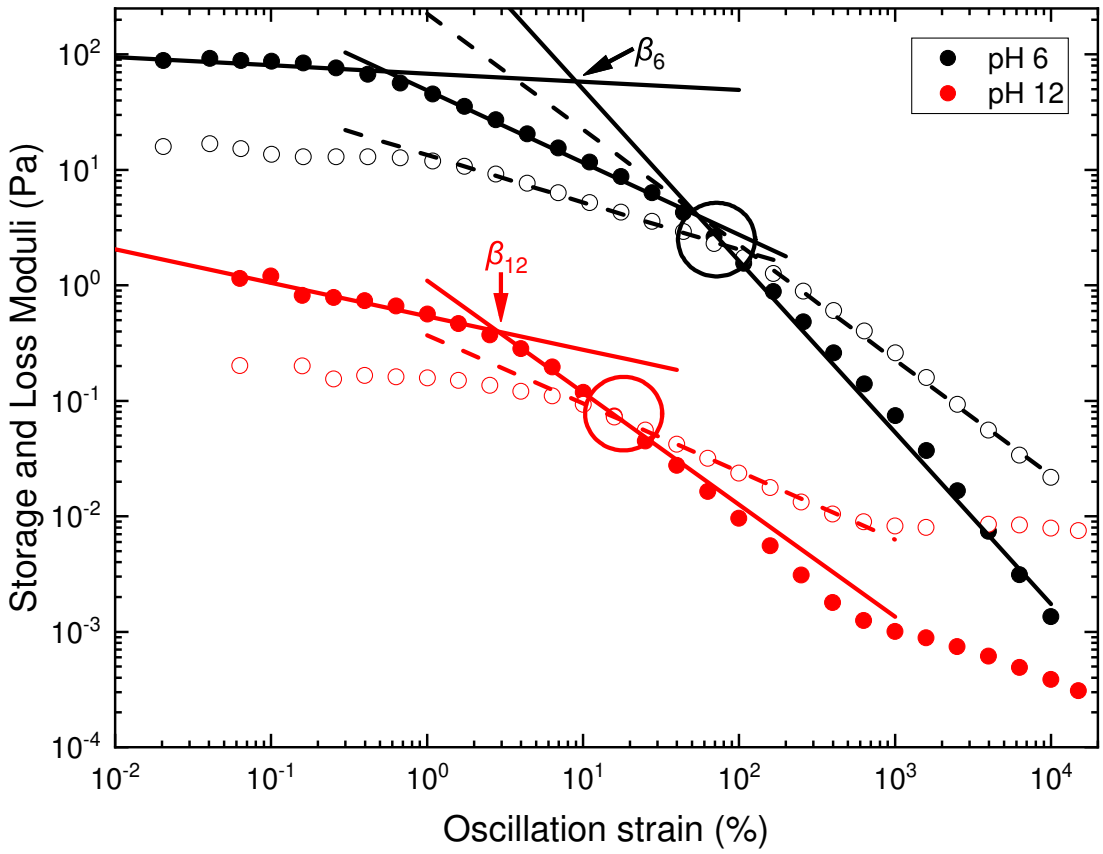

Fig. 5.14 Response of the elastic storage modulus (filled symbols) and the viscous loss modulus (unfilled symbols) of 30 vol. % oil-in-water Pickering emulsions stabilised by 0.7 wt. % titania at pH 6 (•) and pH 12 (•) to changes in the applied oscillation strain at a constant oscillation frequency ($1\,\mathrm{rad\,s^{-1}}$). The fittings of each section of these data are demonstrated by either solid (storage modulus), or dashed lines (loss modulus). The solid circles demonstrate the crossover points of the storage and loss moduli for each emulsion (pH 6: yield strain, $74 \pm 5\,\%$; yield stress, $2.26 \pm 0.01\,\mathrm{Pa}$) (pH 12: yield strain, $20 \pm 10\,\%$; yield stress, $0.04 \pm 0.02\,\mathrm{Pa}$). β_6 and β_{12} indicate the inflection points in the storage modulus at pH 6 (yield strain, $7 \pm 3\,\%$; yield stress, $1.1 \pm 0.2\,\mathrm{Pa}$) and pH 12 (yield strain, $1.8 \pm 0.6\,\%$; yield stress, $0.03 \pm 0.02\,\mathrm{Pa}$).

(marked β_X), the strain percentage was identified. This strain percentage was converted to an oscillatory stress using the data in Fig. 5.16. For the pH 6 emulsion the yield strain and yield stress were $7 \pm 3\,\%$ and $1.1 \pm 0.2\,\mathrm{Pa}$ respectively, while the values for the pH 12 emulsion were significantly smaller at $1.8 \pm 0.6\,\%$ for the yield strain, and $0.03 \pm 0.02\,\mathrm{Pa}$ for the yield stress. In addition to determining the yield stress with the fittings, the yield stress was also determined by finding the cross over point of the storage and loss modulus for each emulsion. This cross over point gives a yield strain, which is then translated into a yield stress. Both the yield strain and yield stress values from this cross-over point for the pH 6 emulsion were $74 \pm 5\,\%$ and $2.26 \pm 0.01\,\mathrm{Pa}$ respectively. In comparison, the pH 12 emulsion yield strain and yield stress values were $20 \pm 10\,\%$ and $0.04 \pm 0.02\,\mathrm{Pa}$. This has shown that the values of the yield stress obtained from each of these two methods are significantly different, with the yield stress obtained from the G' and G'' cross over being about three times larger than that of the fitting intersection method. This discrepancy is anticipated, as the choice of each point is based largely on operational differences between what is classed as the yield stress, as discussed in Chapter 3.

The pH 6 emulsion demonstrates an interesting behaviour with the changes in the storage modulus during the yielding process. The yield stresses reported in this section were measured as a fitting of the linear viscoelastic region and the slope of the storage modulus at high strain percentages. This fitting ignores the less pronounced change in the slope of the storage modulus at intermediate strain percentages. The change in slope at intermediate strain percentages demonstrates a multiple yielding process that is occurring in the pH 6 emulsion. These multiple yielding events are outlined in Fig. 5.15. As was discussed in Chapter 4, these multiple yielding events have been attributed previously to two different microscopic processes occurring in colloidal systems with attractive interactions between the particles [12, 13, 15, 130, 142]. The initial yield stress was significantly lower than that demonstrated in Fig. 5.14. This initial yield stress was ascribed to being due to the break-up of the network present in the attractive emulsion system into smaller components, such as flocs of droplets. The secondary yield event at higher strain percentages was ascribed to break-up of the flocs of droplets into individual emulsion droplets. The pH 12 emulsion does not show behaviour with multiple yielding events; instead yielding with a single change in slope of the storage modulus, until a change in behaviour at high strain percentages.

In addition to considering the storage and loss moduli response to an increase in strain, it is also possible to measure the stress response to the changes in strain percentage. The results of this for the two emulsions used here are shown in Fig. 5.16. As with previous

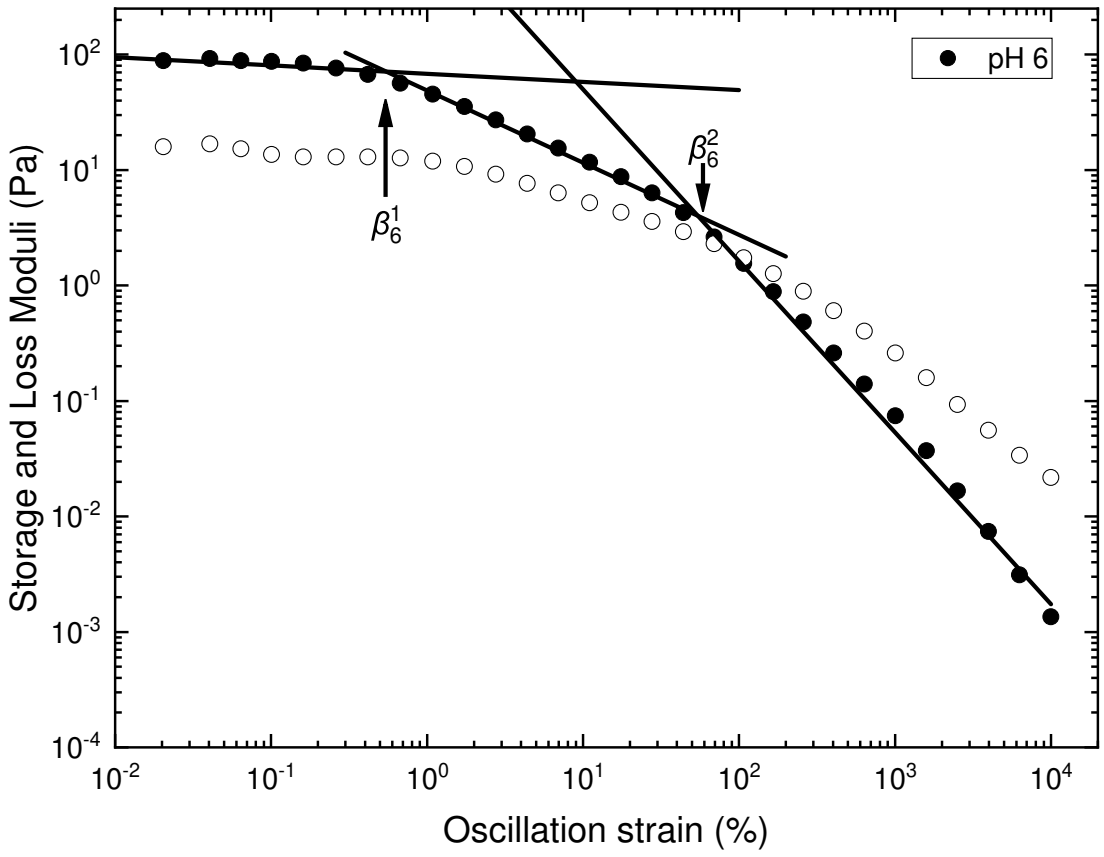

Fig. 5.15 Multiple yielding processes demonstrated in the response of the elastic storage modulus (•) and the viscous loss modulus (○) of 30 vol. % oil-in-water Pickering emulsions stabilised by 0.7 wt. % titania at pH 6 to changes in the applied oscillation strain at a constant oscillation frequency ($1\,\mathrm{rad\,s^{-1}}$). β_6^1 and β_6^2 indicate the two inflection points of the storage modulus, each of which can be taken as a separate yielding event. The first inflection point (β_6^1) occurred at a yield strain of 0.55 %, corresponding to a yield stress of 0.32 Pa, each of which were significantly lower than the second inflection point (β_6^2) values of 55 % and 2.2 Pa for the yield strain and yield stress respectively.

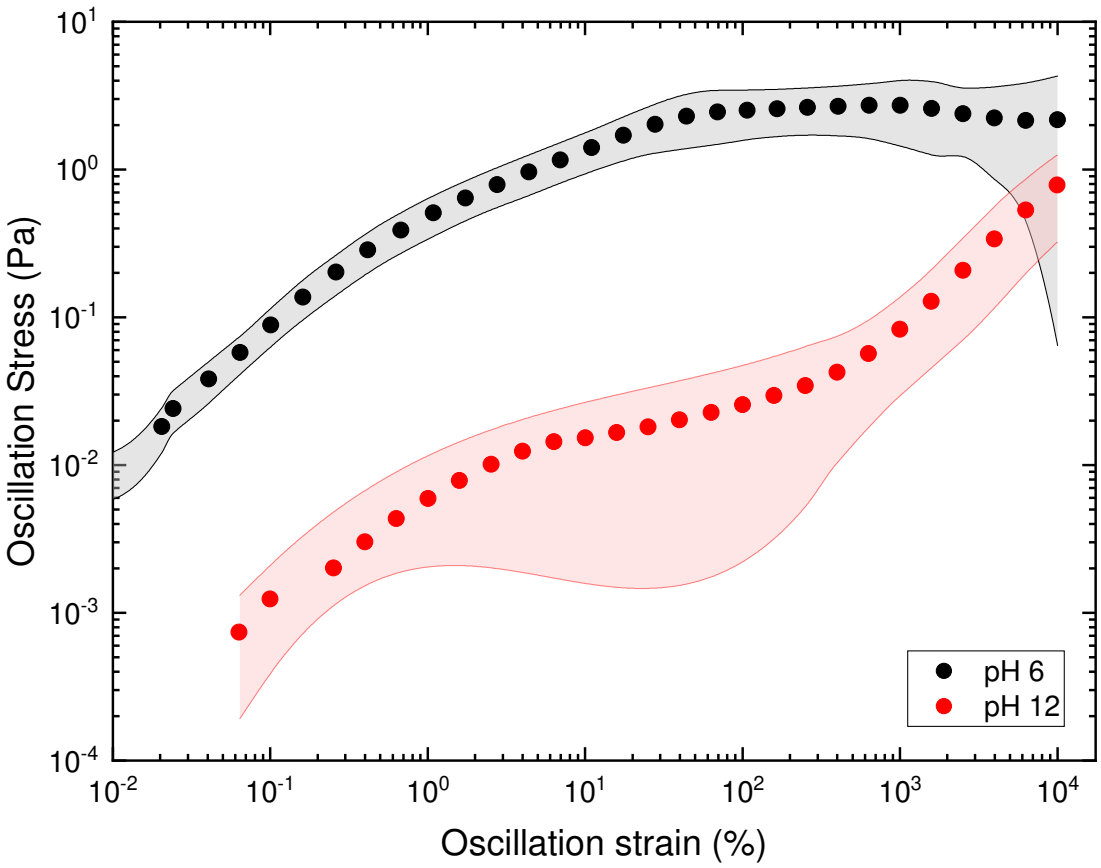

Fig. 5.16 Responses of oscillatory stress to an increasing oscillatory strain for 30 vol. % oil-in-water Pickering emulsions stabilised by 0.7 wt. % titania at pH 6 (•) and 12 (•). Shaded areas indicate the variation in multiple measurements of these emulsion systems.

data for these two emulsions, there is a significant difference in the strength of these two emulsions. Both emulsions show an increase in the measured stress at low strain rates, up to a point where the stress begins to level off in each emulsion. The stress at this inflection point is another point that can used to describe the yield stress of the emulsion. The fitting of power law curves above and below the inflection point allows a yield stress to be determined. The yield strain values were found to be 0.55 % and 55 % for the first and second inflection points respectively. Each of these yield strain values were converted to a yield stress value, giving 0.32 Pa and 2.2 Pa for the first and second inflections points respectively.

Comparing the values of the yield stress for each emulsion demonstrates a further significant difference in the strength of these two emulsions. At pH 12 the yield stress was two orders of magnitude smaller than that for the pH 6 emulsion. This difference is again attributed to being due to the differences in network structure formed within the emulsion samples. At pH 6 the emulsions has been shown to have attractive interactions between

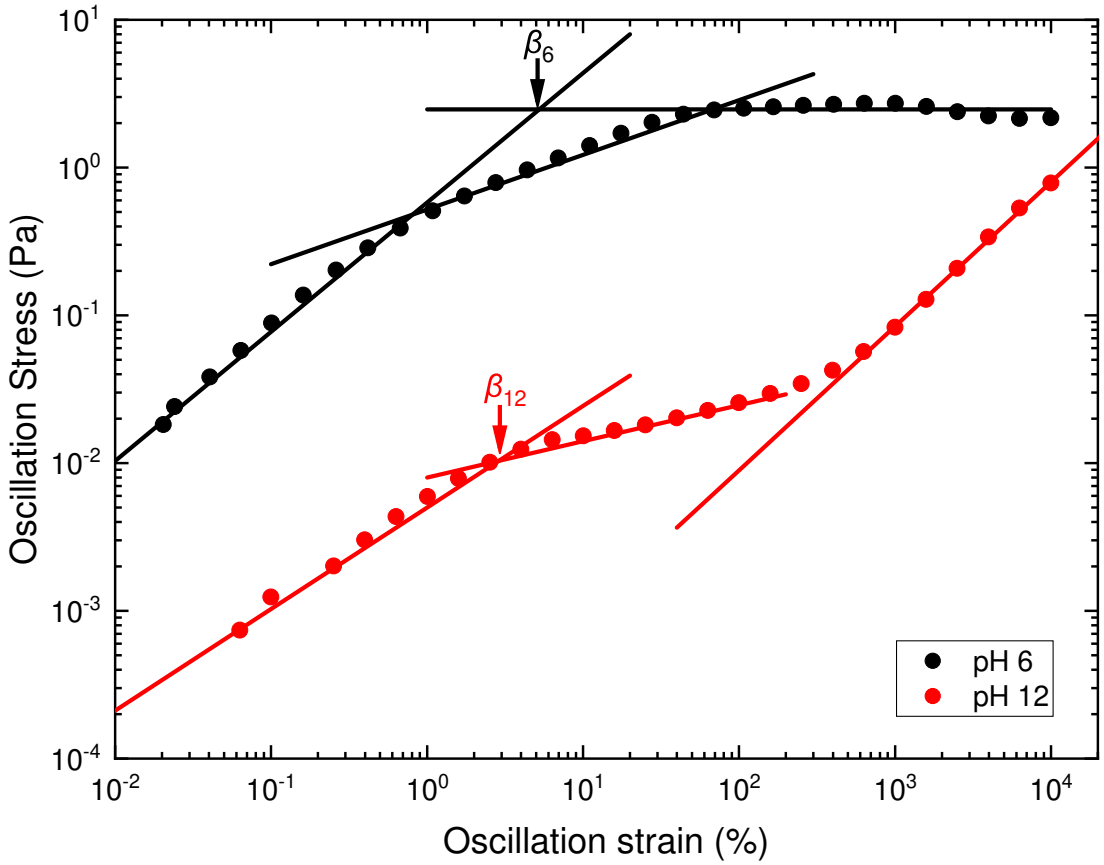

Fig. 5.17 Fitted responses of oscillatory stress to an increasing oscillatory strain for 30 vol. % oil-in-water Pickering emulsions stabilised by 0.7 wt. % titania at pH 6 (•) and 12 (•). Solid lines indicate the fittings that were applied to each data, with β_6 and β_{12} pointing to the inflection points (yield stresses) in the stress response of the pH 6 (2.25 ± 0.50 Pa) and pH 12 (0.2 ± 0.1 Pa) emulsions respectively.

the oil droplets, which is anticipated to lead to a network structure forming throughout the emulsion, increasing the measured yield stress of the emulsion. When the pH 12 emulsions are considered, the oil droplets will have repulsive interactions between each droplet. These repulsive interactions will lead to little to no network structure forming between the oil droplets. This lack of network lowers the bulk strength of the emulsion, leading to a much lower measured yield stress.

The pH 6 emulsion exhibits multiple changes in the stress response as the applied strain percentage is increased. The fittings applied, and the intersections of these fittings are demonstrated in Fig. 5.18. The yield stress values for each of the yield events were measured as 0.48 Pa for the first inflection point (β_6^1), and 2.5 Pa for the second inflection point (β_6^2). These demonstrate that the first yield event appears at lower strain than the single value measured in Fig. 5.17. This first yield event is due to the breakdown of the attractive network between the flocs of droplets, into smaller components that are able to move independent of each other. The secondary yield event demonstrated occurs at a higher stress, similar to that evident in Fig. 5.17. This second yielding event is due to the break-up of the flocs of droplets into single emulsion droplets.

5.3.3.2. Frequency analysis

In addition to altering the strain percentage applied to these two Pickering emulsions, the applied frequency of oscillation was varied. This frequency sweep analysis allows the elasticity of the emulsions to be measured and analysed. The results of these measurements are shown in Fig. 5.19.

Figure 5.19 shows a notable difference between the pH 6 and pH 12 emulsions. The G' and G'' for both emulsions show little sensitivity to the increase in oscillatory frequency below an angular frequency of $10\,\mathrm{rad\,s^{-1}}$. This insensitivity demonstrates the ability of each emulsion to absorb the energy from the applied oscillations. As the applied oscillation frequency is increased above $10\,\mathrm{rad\,s^{-1}}$, the pH 6 emulsion still shows very little change in the G' and G'', demonstrating the elastic strength of the attractive network structure present in that emulsion system. In contrast, the pH 12 emulsion shows a significant increase in both G' and G'' above the inflection point ($20\,\mathrm{rad\,s^{-1}}$). This increase is indicative of the emulsion no longer being able to dissipate the oscillatory deformations at such a high frequency, leading to a stiffening of the emulsion material. This stiffening is due to the lack of an elastic attractive network formed between the droplets, resulting in the droplets locking together, and becoming more solid like in their behaviour. The pH 6 emulsion does

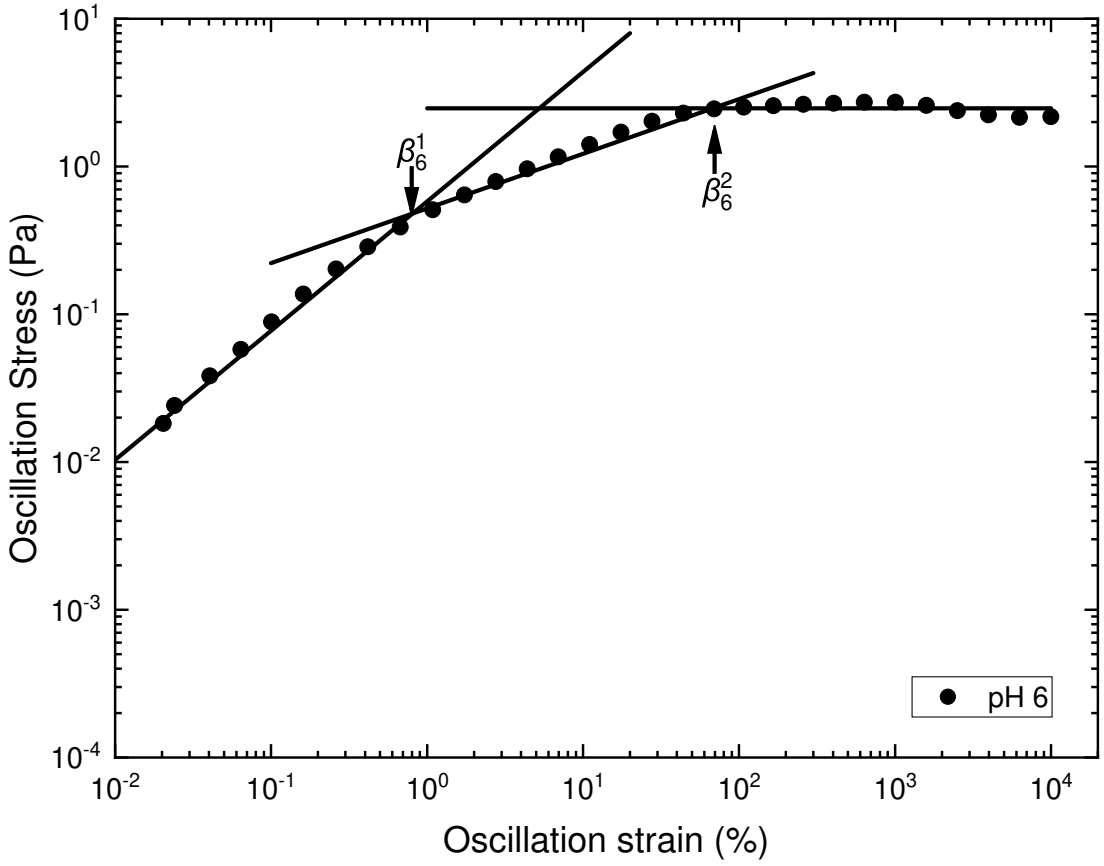

Fig. 5.18 Multiple yielding events as demonstrated in the fitted response of oscillatory stress to an increasing oscillatory strain for a 30 vol. % oil-in-water Pickering emulsion stabilised by 0.7 wt. % titania at pH 6 (•). Solid lines demonstrate the fittings applied to the data. β_6^1 and β_6^2 indicate the two inflection points of the oscillatory stress response each of which is due to a distinct yielding process. The first yield event (β_6^1) occurred at a stress of 0.48 Pa, significantly lower than the second yield event (β_6^2) which was found to be 2.5 Pa.

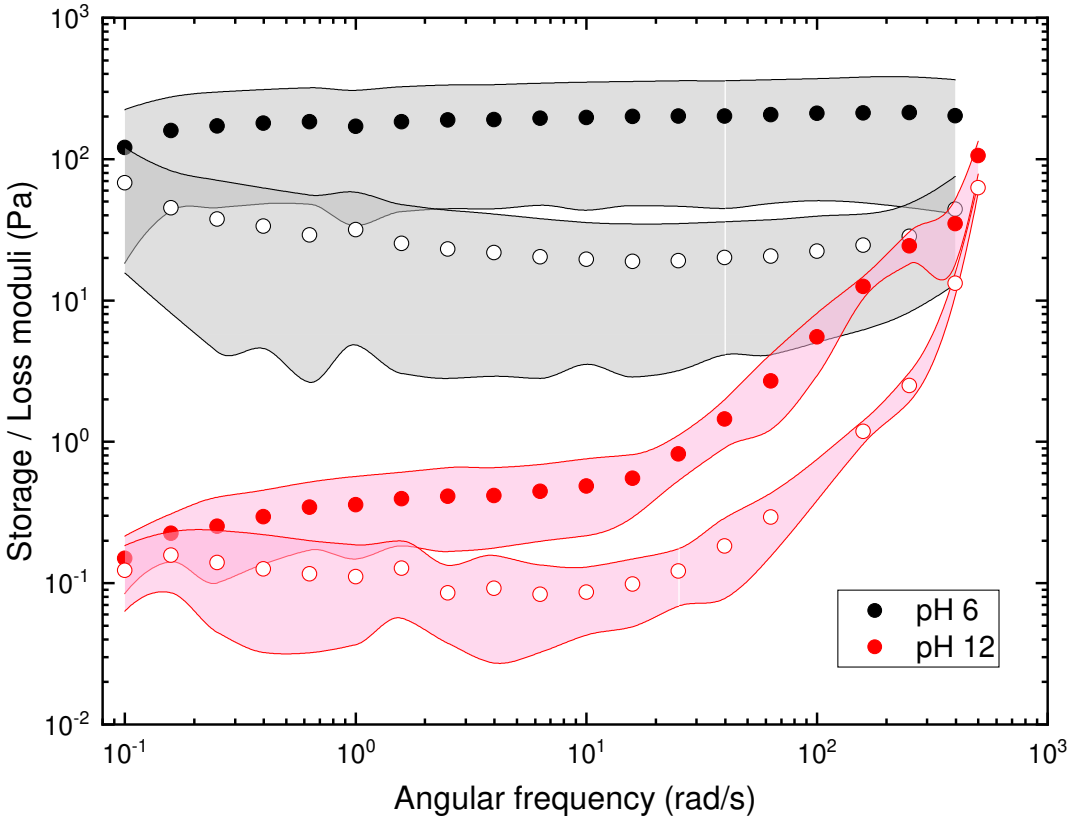

Fig. 5.19 Response of the elastic storage modulus (filled symbols) and the viscous loss modulus (unfilled symbols) of 30 vol. % oil-in-water Pickering emulsions stabilised by 0.7 wt. % titania at pH 6 (●) and pH 12 (●) to an increasing oscillation frequency at a oscillatory strain of 0.25 %. Shaded areas indicate the variation in multiple measurements of these emulsion systems.

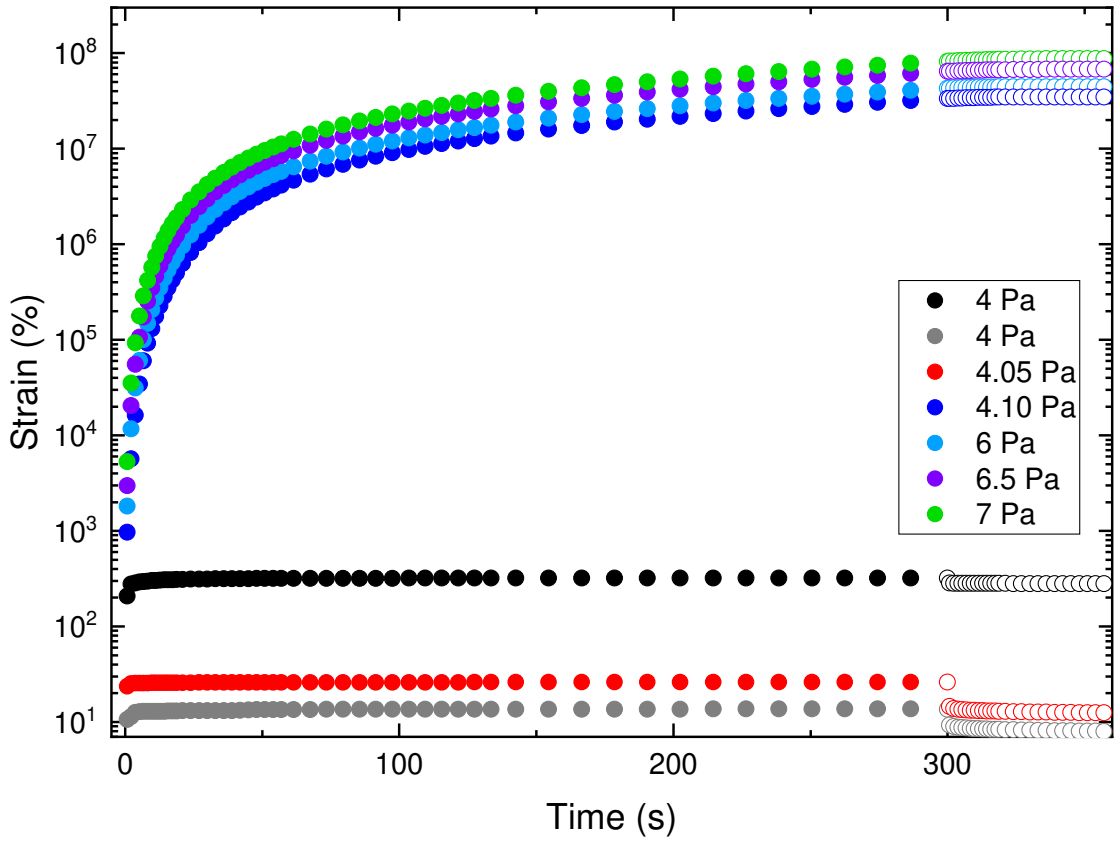

Fig. 5.20 Creep and creep recovery tests for a 30 vol. % oil-in-water Pickering emulsions stabilised by 0.7 wt. % titania at pH 6. The creep is applied at the given stress (see legend) for 300 s, after which the applied stress is released for 60 s. The groupings of the data demonstrate the yield stress to be between 4.05 Pa to 4.10 Pa.

not demonstrate this locking effect as the attractive network formed between the emulsion droplets and titania nanoparticles is able to move in an elastic manner, storing the applied energy.

5.3.4. Creep test and creep recovery

As has been described in Section 2.8.2.3, the creep and creep recovery experiments are another method that can be used to evaluate the yield stress where these are used to measure a yield stress by establishing the stress at which the strain response of the material increases dramatically over time. The results of this creep experiment for the pH 6 emulsion are demonstrated in Fig. 5.20.

As shown in Fig. 5.20 the yield stress was found to be between 4.05 Pa to 4.10 Pa. This was determined as the stress at which the two groupings of data were found to differ. When stresses are applied below the yield stress of the material, the material does not significantly move, indicating that the applied stress is absorbed elastically by the material.

As the stress applied in each experiment is increased above the yield stress, the material becomes unable to continue to store the applied stress elastically, and instead viscously dissipates the energy by flowing. The recovery phase of each measurement below the yield stress shows a small elastic bounce back as some of the elastically stored energy allows the material to return towards its original state. Above the yield stress this behaviour is not apparent; instead the material remains at the final strain, indicating that the material in these cases has yielded, and has viscously dissipated the applied stress. Interestingly, repeating the measurement at 4 Pa did not result in exactly replicated data. The origin of this discrepancy is not immediately clear, although the variations in the measured creep data throughout this thesis point towards the stochastic nature of measurements with these emulsion systems. This highlights one of the difficulties with creep measurements for the emulsion systems investigated in this work, with the range and variation in the data obtained.

Creep experiments carried out on the pH 12 emulsions are shown in Fig. 5.21. These creep experiments show multiple groupings of data, however the data does not appear to show an unambiguous yield stress. Both Fig. 5.21a and 5.21b show data that are inconsistent with each other. This is likely due to the low yield stress of this pH 12 emulsion leading to chaotic data particularly as it is likely close to the operational limits for the rheometer setup used for these measurements. This is shown at by the ringing seen in Fig. 5.21a. Ringing similar to this has been observed previously, and was attributed to "inerto-elastic ringing" which is a result of instrument inertia artefacts. Another feature of these pH 12 creep tests is the lack of a notable recovery phase in any of the measurements [194].

The use of these measurements here has once again demonstrated that the creep experiments can be a useful tool for the determination of the yield stress of the material in some cases. The yield stress that was measured for the pH 6 emulsion was found to be about 4.05 Pa to 4.10 Pa, between that of the oscillatory and flow rheology techniques. However, these creep experiments can also fail in certain situations, and do not yield results that are useful. This was shown with the pH 12 emulsion, where the creep experiments gave results that were inconsistent, likely due to the low, and variable, yield stress of the repulsive pH 12 emulsion.

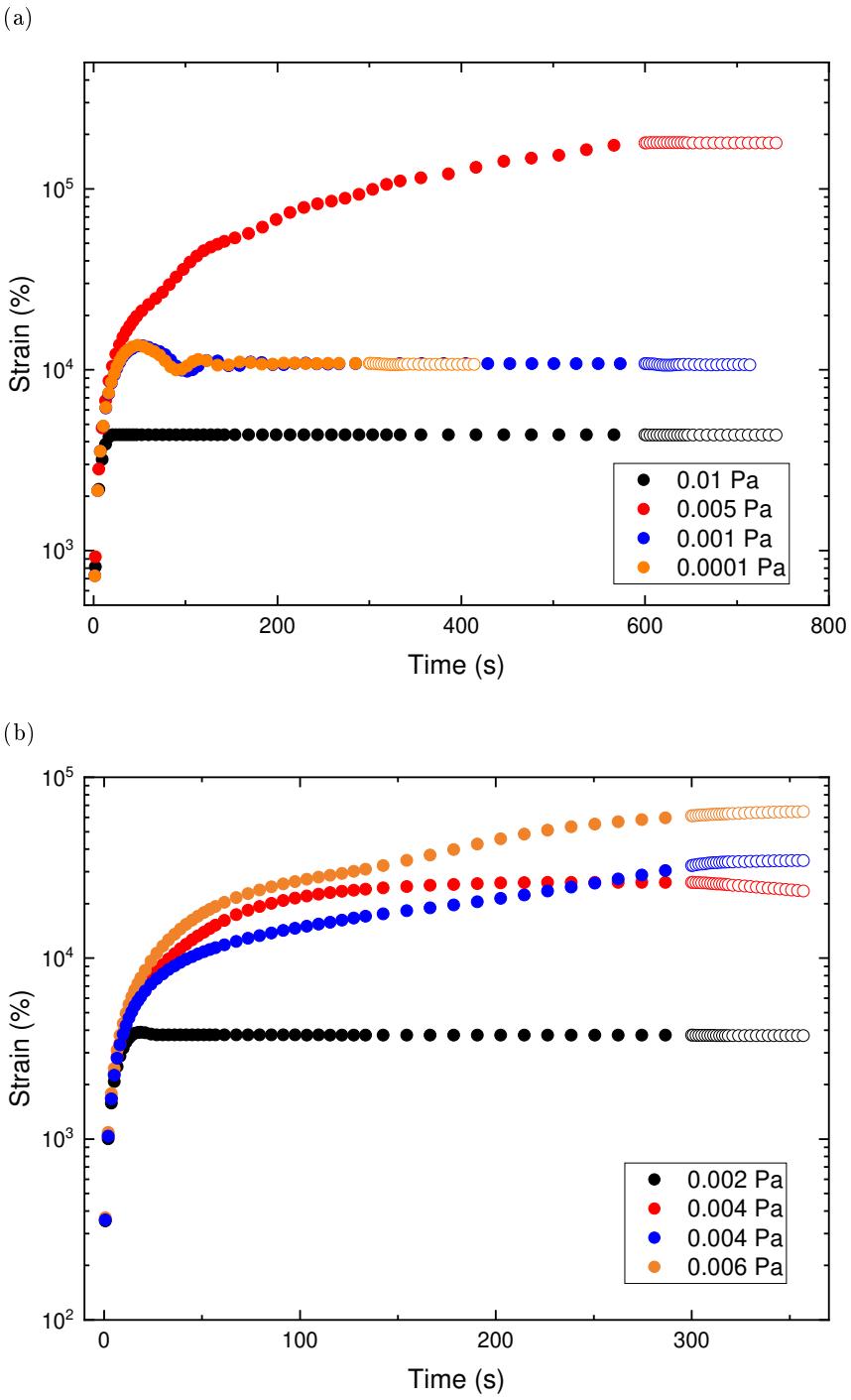

Fig. 5.21 Creep and creep recovery tests for a 30 vol. % oil-in-water Pickering emulsions stabilised by 0.7 wt. % titania at pH 12. The creep is applied at the given stress (see legend) for 300 s, after which the applied stress is released for 60 s.

5.4. Comparisons and discussion

As has been discussed in the previous chapter, altering the interactions between the particles in a colloidal material can dramatically change the bulk properties of the materials. In the previous chapter, the alteration of these interactions was carried out by adding salt to screen the surface changes of a silica stabilised Pickering emulsion. The work carried out in this chapter alters the interactions between Pickering emulsions but, in this case, the interactions were altered by pH. The use of pH to alter the properties of an emulsion is not a new area of study, with previous groups working with pH to not only alter the bulk strength of Pickering emulsions, but to also de-emulsify Pickering emulsions on demand [1, 4, 195–202]. The ability to control these emulsions with the simple addition of acid or base allows the development of products that can exhibit novel and interesting properties. This chapter has demonstrated a further method to alter the properties of an emulsion material with variations in pH.

There have been many different Pickering stabilisers used to prepare emulsions since the inception of Pickering emulsions over a century ago [66, 67, 89, 201]. The previous two chapters investigated silica nanoparticles as a Pickering stabiliser. This chapter moved on from silica nanoparticles, and utilised titanium dioxide nanoparticles. Titanium dioxide (titania) has been used, both alone, and in combination with other Pickering emulsifiers in order to stabilise emulsions [70, 72, 73, 203]. These previous works have shown that due to the hydrophobicity of different types of titania nanoparticles, that the titania can be used to stabilise Pickering emulsions. These previous works used microscopy, conductivity, and light scattering methods. While these other works have shown the ability to prepare these titania stabilised emulsions, they had not demonstrated the different rheological behaviour of these materials. This chapter has worked to fill that gap, with new understandings of how the structural properties of these materials can be altered through variations in pH.

The Pickering stabiliser used for the work in this chapter were commercially available titanium dioxide nanoparticles, Eusolex® T-2000. These nanoparticles have a surface chemistry that includes titanol groups, which allows the surface charge of the particles to be altered through the addition of acid or base to the system. This surface charging effect was investigated through a combination of pH titration and zeta potential measurements. The pH titration demonstrated the buffer-like behaviour, with the theoretical calculated pH of the suspensions matching the measured pH at low (< 5) and high pH (> 10), while there is a linear buffer region where the measured pH is insensitive to the addition of acid or

base between these two values (Fig. 5.2). This buffer region is expected to be a consequence of the surface titanium hydroxide groups reacting with the added acid or base, which will result in the surface of the nanoparticles becoming charged. The charging behaviour of these particle suspensions at different pH levels was measured by zeta potential. The zeta potential measurements demonstrated that as the measured pH increased, the zeta potential decreased from a positive initial value, and became large and negative (Fig. 5.3). This results from the deprotonation of the titanol surface groups, leaving an excess of $Ti–O^-$ surface groups, giving the surface of the nanoparticles a net negative charge. As the pH is increased past the buffer region of the nanoparticles (pH $>$ 6), the net negative charge will increase further. These changes in the surface charge with variations in pH demonstrate the ability to tune the interactions between these nanoparticles in a controllable manner and in turn alter the bulk properties of emulsions prepared with these titania nanoparticles as a Pickering emulsifier.

Another feature of the titania stabiliser used throughout this chapter is the particle shape. The titania particles used in this chapter are an ellipsoidal needle-like structure with a length of 100 nm, and a width of 20 nm, giving an aspect ratio of 5. The effect of anisotropic Pickering emulsifiers has been investigated previously by Madivala et al. [155]. In this previous work Madivala et al. sets of Pickering emulsions prepared with particle stabilisers with aspect ratios ranging from 1 to 9. They demonstrated that stable Pickering emulsions can be prepared from high aspect ratio stabilisers. They investigated the interfacial rheology of these anisotropic particles, and found that increasing the aspect ratio resulted in the formation of more elastic monolayers. This increase in elasticity was attributed to the attractive shape induced capillary interactions between the ellipsoidal nanoparticles, which leads to the formation of aggregates [204]. These previous works demonstrated the ability to form stable Pickering emulsions with the use of anisotropic particles, and provide some understanding of the forces behind the formation of aggregates at the droplet interfaces.

Titania stabilised oil-in-water Pickering emulsions prepared at pH 6 and pH 12 have been compared throughout this chapter, and some key differences have been highlighted.

The emulsion prepared at a pH 6 has been demonstrated through the measurement of zeta potentials and the subsequent DLVO calculation to display an attractive interaction between the titania nanoparticles. This attractive interaction is best demonstrated through the laser diffraction results presented in Fig. 5.7b, where the droplet size distribution is multi-modal (with peaks centred at about 30 µm and 100 µm, an indication of flocculation of

the droplets. Confocal microscopy demonstrated oil droplets coated with full particle shells, however there did not appear to be an excess of titania nanoparticles in the continuous phase of this system (Fig. 5.8a).

The attractive interactions between the titania particles of the pH 6 emulsion influenced the rheological properties of the emulsion system. The influence of this attractive interaction was demonstrated in the viscous flow rheology, where the low shear viscosity was $700 \pm 200\,\mathrm{Pa\,s}$, significantly greater than that of the components of this emulsion system (the viscosity of water is $\approx 8.9 \times 10^{-4}\,\mathrm{Pa\,s}$, and dodecane is $\approx 13 \times 10^{-4}\,\mathrm{Pa\,s}$). This demonstrates that the attractive interactions between the emulsion droplets has contributed significantly to the structure of the emulsion system through the formation of a network structure.

The elasticity of this network was demonstrated through oscillatory rheology. The strain dependence of G' and G'' for the pH 6 emulsion, shown in Fig. 5.13, demonstrates significant elastic structure, as seen by the magnitude of the G' in the linear viscoelastic region. The formation of an elastic network within an emulsion system with attractive interactions between the droplets is not a new phenomenon, and the data presented here shows similar traits to those seen previously [8, 12, 13, 90, 142, 171]. As discussed in Chapter 4, work by Katepalli et. al. [8], investigated how the use of fumed or spherical silica as Pickering stabilisers effected the rheology of attractive, or repulsive emulsion systems. They demonstrated that the shape of the particles used had a significant effect on the magnitude of G' and G'', and the response over the range of strains applied. This was seen with a fumed silica particle affording the emulsion a much greater elasticity when compared to the data presented using spherical silica particles when both systems display net attractive interactions between the particles. Katepalli attributed this difference to the interlocking nature of the fumed silica nanoparticles, which results in the formation of an elastic network between the emulsion droplets, and through the excess silica in the continuous phase. This elastic network is not apparent to the same extent when the spherical silica is considered, resulting in lower measured rheological parameters. Katepalli attributed this lowered elasticity to the lack of any volume-filling network formed between the spherical silica particles.

The results reported by Katepalli [8] demonstrate the significant differences that particle shape can have on the rheology of a Pickering emulsion system, and bears similarities to the results presented in this chapter. The titania particles used to stabilise the emulsions presented in this chapter are not spherical however, they are a uniform, smooth ellipsoidal

particle, as shown in Fig. 5.5. Despite these differences in particle shape, the rheological properties of the titania stabilised emulsions and the spherical silica stabilised emulsions presented by Katepalli were found be similar, an indication of similarities between the droplet network structure in each system. The network formed in the pH 6 emulsion is expected to be comprised only of droplet-droplet interactions, rather than the elastic network of particles and droplets that are often seen in other Pickering emulsions (e.g. Chapters 3 and 4). Oscillatory rheology measurements of the pH 6 titania emulsions uncovered similar results to that of Katepalli, with a limited viscoelastic region in response to an increasing strain, before the emulsion yields through what appears to be a two-step process. These multi-stage yielding processes have been discussed in Chapter 4, and are the result of two distinct microscopic processes, a network breaking, and a cage breaking event, as outlined in Fig. 5.22. The two yielding processes were demonstrated experimentally by each of the inflection points in the curve and have a yield stress corresponding with each. The initial inflection point is the result of the break–down of the network into flocs of attractive droplets. The second inflection point was a result of the break–down of the flocs present in the system, into individual oil droplets that are able to move independently of each other [12, 13, 15].

The pH 6 emulsion demonstrated an elastic network structure across the range of other rheological measurements carried out in this chapter. This included the response of the shear stress to an increasing shear rate (Fig. 5.11). With this, the stress response was found to be linear, with little change in the measured stress across the range of applied shear rates. This was attributed to the emulsion not fully yielding at the shear rates applied. The data were not fitted with the Herschel-Bulkley or Bingham models due to the linear shear stress response; instead an average was used and a yield stress of $6 \pm 2\,\mathrm{Pa}$ was extracted. This is yet another demonstration of the strength of the network formed between the emulsion droplets in this system.

When the pH 12 emulsion was considered, it is clear that there are significant differences in the structure when compared to the pH 6 emulsion. These differences are expected due to the zeta potential and DLVO calculations demonstrating a repulsive interaction between the titania particles. This repulsive interaction was found to alter the droplet size distribution measured by laser diffraction (Fig. 5.7c), with a monomodal distribution centred at approximately $30\,\mu\mathrm{m}$. Confocal microscopy of the pH 12 emulsion provided an interesting insight into the distribution of titania particles surrounding the oil droplets. In comparison to the complete shells of titania seen in the pH 6 system (Fig. 5.8a), the

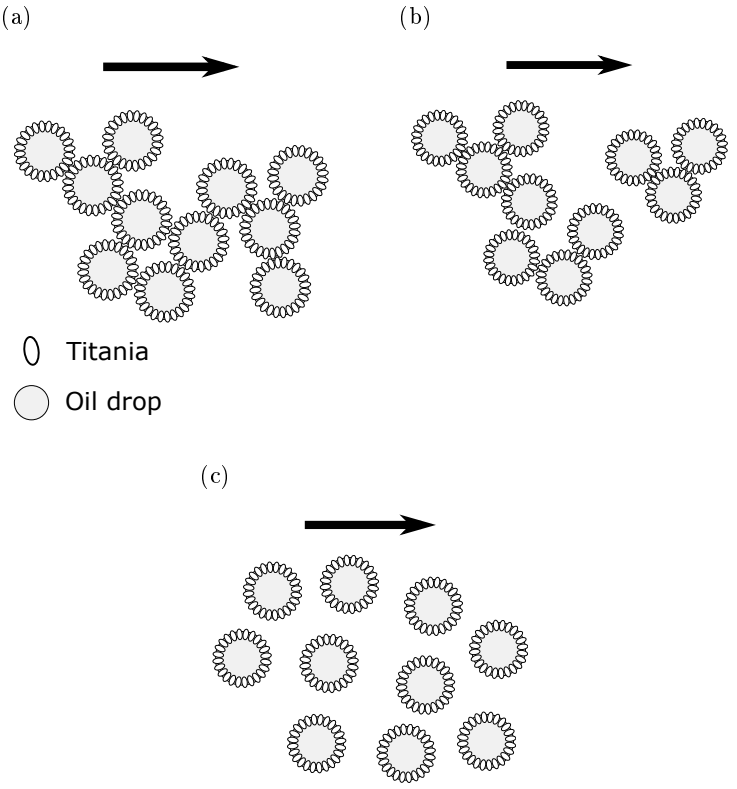

Fig. 5.22 Schematic diagram demonstrating the multi-stage yielding process that occurs in an attractive Pickering emulsion stabilised by titania nanoparticles. Arrows indicate the shear applied to the sample. Titania particles and oil droplets are not drawn to scale in this diagram. The orientation of the particles at the interface presented is a schematic, the actual orientation is unknown. (a) Unyielded emulsion with a network structure formed between the droplets, with no excess titania shown in the continuous phase. (b) Flocs of oil droplets demonstrating the first yielding step that attractive colloidal materials can display, with flocs of droplets breaking away from the full network. (c) Fully yielded emulsion demonstrating droplets with no floc structures present.

particle shells in the pH 12 emulsion appeared incomplete although sufficient to impart stability against coalescence in quiescent emulsions (Fig. 5.8b), with aggregates of titania remaining in the continuous phase. This incomplete shell appears to have resulted in the emulsion becoming less stable when exposed to high shear, resulting in the range of shear rates applied being limited [54].

The rheology of the pH 12 emulsion demonstrated the limited strength of any network that forms between the droplets. This was first shown by the low shear viscosity of the system ($0.7 \pm 0.3\,\mathrm{Pa\,s}$), roughly three orders of magnitude lower than that of the pH 6 system (Fig. 5.10). This demonstrates that there is limited friction between the emulsion droplets, allowing the system to flow with relative ease. It is important to note however that this value is still greater than the viscosities of the component liquids by about three orders of magnitude. The shear stress response was also evident from the flow rheology (Fig. 5.11), and was shown to increase slightly across the range of shear rates applied, until there was a slight dip at the upper limits of the applied shear. The decrease in the stress in the pH 12 response at high shear rate is likely due to unstable flow, leading to shear banding or phase separation [205, 206]. The shear stress response was fitted with three different models to extract yield stress values, an average at low shear rates ($0.008 \pm 0.002\,\mathrm{Pa}$), a Bingham curve ($0.008 \pm 0.005\,\mathrm{Pa}$), and a Herschel-Bulkley curve ($0.004 \pm 0.003\,\mathrm{Pa}$). Each of these demonstrates the limited force required to initiate flow in this emulsion with repulsive interactions between the oil droplets, further indicating the lack of significant particle structure present in the continuous phase of the system.

Oscillatory rheology of the pH 12 emulsion further demonstrated the limited structure present in the system. The response of G' and G'' to an increasing strain demonstrated data that was approximately three orders of magnitude lower than that of the pH 6 emulsion (Fig. 5.13). In addition to the lower magnitude, the shape profile of G' and G'' was also found to be significantly different. The pH 12 emulsion demonstrated a limited linear viscoelastic region, before a single yield event occurs as the system transitions into a viscous regime. The yield stress values obtained from the oscillatory rheology were larger than those measured via the flow methods, with the yield stress from the inflection point at $0.03 \pm 0.02\,\mathrm{Pa}$, and the crossover point at $0.04 \pm 0.02\,\mathrm{Pa}$. The frequency response of G' and G'' for the pH 12 emulsion did display some interesting features. At low frequencies the G' and G'' values were found to be similar, an indication that the system is almost fluid-like at this point. As the applied oscillatory frequency was increased, the material began to demonstrate viscoelastic behaviour, with the G' being larger than the G''. At

high frequencies both G' and G'' increase, demonstrating what could be considered strain-hardening behaviour. This behaviour has been observed previously, and was thought to be due to a transition to a glassy state; with the material becoming unable to viscously dissipate the applied strain at the measurement frequency [103]. This glassy state transition results in the materials becoming more solid–like [103].

This chapter has reported the development of a new tuneable Pickering emulsion system, and has investigated the structure and rheology of these systems. In contrast to the work reported in Chapters 3 and 4, the stabiliser used to form these emulsions does not appear to have formed a volume-filling network throughout the continuous phase of the emulsions. The tuning of the interactions between the nanoparticle stabilisers used here resulted in some interesting changes to the particle distribution surrounding the oil droplets, which altered the shear stability of the emulsion system. In addition to altering this distribution, the tuning of the interactions between the particles has been demonstrated to dramatically affect the rheological properties of the emulsion systems, with the attractive emulsion (pH 6) demonstrating significantly more elastic structure when compared to the repulsive system (pH 12). The ability to control the properties of these emulsions, and create systems with altered stabilities is something that may be very useful for future developments. The next chapter will compare the results presented here with the other chapters in this work, while also drawing some overall conclusions about the progress made, before finally providing some future direction based on the research presented.

6 Summary and conclusions

6.1. Introduction

The work in this thesis has centred on developing an understanding of the rearrangement processes under shear that occur in Pickering emulsions with attractive or repulsive inter-droplet interactions. This chapter will summarise how this has been carried out though a selection of emulsions prepared with a range of interparticle properties, and the specific techniques used to understand their properties. Additionally, comparisons are made with work carried out by previous workers, demonstrating the similarities and differences between the emulsions presented here, and those previously studied. Finally, areas in this research that could be expanded upon, as well as possible avenues of investigation that may yield interesting results in future studies are outlined.

This work started with developing an understanding of the multiple methods used for measuring and classifying the "yield stress" of Pickering emulsions (Chapter 3). This work was based on an approach taken in a previous study of surfactant stabilised emulsions [131]. The results for Pickering emulsions obtained in the present work demonstrated yield stress values which varied significantly with the range of methods utilised (approx. 0.5 to 1 order of magnitude difference between the measured values at different oil volume percentages). This is similar to the results obtained by Dinkgreve et al., where they investigated surfactant stabilised emulsions, and found that the method used significantly altered the yield stresses measured (approx. 0.5 order of magnitude difference between the measured values across the range of oil volume percentages presented), demonstrating that care must be taken when making comparisons between the yield stress properties of emulsion systems [131].

Over the course of the present investigation multi-stage yielding features became apparent in the amplitude sweep rheological data for these silica stabilised emulsions across a range of oil volume percentages, an indication of structural rearrangements in the emulsion systems. The multi-stage yielding features were investigated by preparing emulsions with

tuneable interactions between the Pickering stabilisers, ranging from repulsive to attractive interactions (Chapter 4). This was carried out by varying the NaCl concentrations of the aqueous phase of an o/w emulsion system stabilised by fumed silica particles, in order to alter the Debye length of the material, in turn selectively creating attractive or repulsive interactions between the emulsion droplets. These changes in interactions were utilised to understand the multi-stage yielding that has been observed in concentrated surfactant stabilised emulsions previously [142]. The work carried out here aimed to identify and develop a greater understanding of the microscopic rearrangement processes that occur during these multi-stage yielding processes, while demonstrating the ability to control the bulk physical properties of silica stabilised Pickering emulsions [54, 68, 89, 160, 207, 208].

Following this, a second o/w emulsion system was prepared and the rheological properties were investigated (Chapter 5). The bulk rheological properties of this emulsion system were also varied, this time by varying the pH of the aqueous phase, leading to changes in the surface charge of the Pickering stabiliser. Alterations to the surface charge of the stabiliser allowed for the interactions between the particles ranging from attractive to repulsive. These variations were found to demonstrate multi-stage yielding properties, which were shown throughout a number of rheological measurements. This second emulsion was stabilised by a smooth needle-like titania nanoparticle. The work presented in this thesis is thought to be the first investigation into the rheological properties of attractive and repulsive Pickering emulsions stabilised by titania nanoparticles. As such, this presents an important step forward in the understanding of both titania stabilised system, and Pickering emulsions with tunable properties.

This chapter outlines some of the main comparisons, both within the work carried out here, as well as with previously published results. General conclusions on the work carried out in this thesis are presented, before finally some future directions are proposed for further development of tuneable Pickering emulsions, with discussions of areas of research that will aid in fully understanding the yielding processes that have been shown in this, and previous works.

6.2. Comparisons

The questions that influenced the experiments conducted in Chapter 3 revolved around how to best define, and measure, the yield stress of Pickering emulsions. This required a range of rheological experiments be carried out on a number of silica stabilised Pickering emulsions with varied volume percentages of the dispersed phase. The resulting data

showed a strong dependence between oil volume percentage and the key data measured, such as the yield stresses, viscosities, and elasticities. This increase in rheological properties with the oil volume percentage is similar to that seen in a range of other rheology studies on materials including polymer blends, gels, food additives, and concentrated emulsions [209–213]. The dependence of the yield stress on oil volume percentage was fitted with Equation 3.2, which demonstrated a power law relationship of $\sigma_y \approx \sigma_{y0} + \phi_{oil}^{12\pm2.4}$ when measured by viscous flow methods, and $\sigma_y \approx \sigma_{y0} + \phi_{oil}^{17\pm2.2}$ when measured with oscillatory methods. Both the oil droplets and the excess silica particles (silica particles located in the continuous phase not at the oil-water interface) contribute to the structure in the emulsion, resulting in changes to the rheological properties. As the oil volume percentage in the emulsion increases, the concentration of the excess silica in the aqueous phases also increases (as a consequence of the emulsion dilution), making it difficult to separate the effect of each. The increase in oil volume percentage and excess silica leads to the formation of network structures throughout the emulsion system (as shown by microscopy), adding significantly to strength of these low volume percentage emulsions. The effects of weight percentage of particle suspensions, and the oil volume percentage of emulsion systems had been previously investigated by Dinkgreve et al. [131]. These workers demonstrated a relationship of $\sigma_y \sim (wt.\ \%)^{1.18}$ between weight percentage of a particle suspension and the yield stress of the system. The relationship between oil volume percentage and the yield stress was $\sigma_y \sim (\phi_{oil} - 64.5\%)^2$, where 64.5% is the random close packing percentage. Studies reported by Buscall et al. [214, 215] investigated the effect of volume percentage on strongly-flocculated suspensions of fractal-like nanoparticles. In this investigation they demonstrated a relationship between both compressive and shear yield stresses, and volume percentage of the suspensions. They found that the shear yield stress scaled according to $\sigma_y \sim \phi^3 a^{-2}$, with a being the particle radius. It was suggested that this scaling behaviour occurs as a result of the fractal aggregates that form the network structures throughout the material. The relationships these researchers established are significantly less dependent on volume fraction when compared to those presented in this work, indicating significant interactions between the particle-coated Pickering emulsion droplets and the excess particle network present in the systems prepared for this thesis.

Previous works by Ganley and van Duijneveldt [90] demonstrated that the oil droplets in Pickering emulsion systems can either interact with a nanoparticle network, or disrupt the nanoparticle network as a non-interacting filler. This effect was demonstrated by a scaled storage modulus increasing with oil droplet concentration when droplets are interacting

with the network. Conversely, when the filler droplets do not interact with the particle network the scaled storage modulus is shown to decrease with oil droplet concentration. In the work presented here the linear viscoelastic region storage modulus is found to increase with droplet concentration (Fig. 3.9), indicating that the droplets are interacting with the network structure that is comprised of the excess silica particles in the emulsion system (similar to what is proposed in Fig. 4.9).

Another notable difference between the data presented by Dinkgreve et al. [131] and the work here is the volume percentages of emulsion systems investigated. The emulsion systems investigated by Dinkgreve et al. were highly concentrated, with oil volume percentages ranging from 66 to 78 vol. %, greater than those investigated in this work (25 to 50 vol. %). The emulsions investigated by Dinkgreve et al. were all above the random close packing percentage of ≈64.5 vol. %, leading to close contact, and deformation of the emulsion droplets. In comparison, the emulsions presented in this work had volume percentages lower than the random close packing percentage, indicating that the emulsion droplets will not necessarily be in close contact or forced to deform due to packing. Despite the more dilute nature of the systems in this work, aggregation of both emulsion droplets and the nanoparticle network were shown through a number of microscopy techniques. Aggregation of components has been demonstrated to contribute to the significant elasticity of some Pickering emulsions systems well below the random close packing volume [216]. This was found to be the case throughout the present work as shown through the rheological properties of the systems investigated, with significant increases in the measured properties as both the oil volume percentage and particle concentration were increased.

Five different methods (viscous flow curve, storage/loss moduli cross–over, inflection point in the storage modulus, inflection point in the stress-strain curve, and creep/creep recovery) were utilised to measure the yield stress of the emulsions studied in this work, with each method resulting in slightly different average values. Figure 3.13 shows the resultant values of the yield stress measured by each method. This demonstrated that the two creep experiments both established the highest values for the yield stresses measured. This is in contrast with the data reported by Dinkgreve et al., where the creep experiments gave one of the lower yield stress values [131]. They found that the Herschel-Bulkley fitting of the flow curves resulted in the lowest yield stress values. This was not the case with the results obtained in this thesis, where each of the flow curve fitting methods gave significantly higher yield stress results when compared to the oscillatory methods. This was an unexpected result as the yield stresses measured (the static yield stress) is the minimum stress required

to initiate flow in a material, as opposed to the dynamic yield stress which is the stress at which the material transitions from having liquid-like to solid-like properties [132, 133]. There is often a difference in the measured value between the static and dynamic yield stress due to the method with which each value is obtained. Measurements of a dynamic yield stress for these materials may have resulted in a lower stress values; however, these measurements were not carried out in this work.

Fitting of stress-strain curves and the storage moduli of the strain sweep resulted in lower yield stress values than the other methods utilised. This was due to these intersection points being the point at which the emulsions begin to display liquid-like behaviour. Finally, the crossover of the storage and loss modulus gave yield stress values that bridged between the two extremes. While the yield stress values from this were not as large as those obtained from the flow curve measurements, the values are not considered here to be an accurate measure of the yield stress. This is due to the significant viscous dissipation that is underway at the point of crossover, indicating that the materials have already begun yielding. This viscous dissipation is thought to arise from the network structure between the emulsion droplets being stretched, and fracturing, leading to the separation of emulsion droplets from the bulk network structure. As the strain applied to the material increases, the network structure continues to break-down, until the system is completely yielded.

During the measurement of the yield stresses across the range of oil volume percentages, some interesting multi-stage yielding features were found in the rheological results. A broad peak observed in the loss modulus of Fig. 3.9 at certain volume percentages was taken as evidence of multi-stage yielding. These multi-stage yielding features demonstrated in the rheology of silica-stabilised emulsions was further investigated. This was carried out by altering the interaction energies between the silica nanoparticles stabilising the emulsions. The interaction energies were systematically varied through alterations of the Debye length, achieved by the addition of salt which screens the surface charges present on the nanoparticles. Similar screening effects have been noted with silica previously where the stability of silica suspensions was studied (i.e. not Pickering emulsion systems) [24, 57]. One of these previous results investigated the surprising stability of suspensions of silica nanoparticles, and noted that this stability was likely due to the hydration forces that are not considered in the classical DLVO theories. Chen et al. [57] noted that the addition of salt (or a decrease in the pH) to an aqueous suspension of silica nanoparticles results in a decrease in the repulsive interactions between the particles. This was also found to be the case in the present work with Pickering emulsion systems. In addition to calculating the

interaction energies between nanoparticles, Chen et al. [57] found that the addition of salt significantly increased the elasticity of the silica suspensions as measured with a frequency sweep measurement. The increase in the elasticity was also demonstrated in the present work with silica stabilised Pickering emulsions in Chapter 4, where the attractive (high salt, 1.66 M) emulsions were found to be far more elastic and viscous than the repulsive (low salt, 1×10^{-4} M) emulsions.

These attractive and repulsive emulsions were prepared with the goal of further investigating the multi-stage yielding processes previously reported in emulsion (and more broadly, colloid) systems [8, 12, 13, 142]. Multi-stage yielding was seen in the intermediate salt emulsion presented in this work, but were not apparent in the high salt system. Interestingly however, the high salt system had a very broad single peak in the loss modulus. This is interpreted here to be due to the yielding events occurring at very similar yield stresses, and as such, overlapping in the resultant data. Multi-stage yielding behaviour similar to this has been seen previously in two sets of Pickering emulsion systems [8]. In this previous work, a single broad yielding event was seen in the oscillatory rheology of a fumed silica stabilised 50 vol. % oil-in-water Pickering emulsion in 50 mM NaCl. Katepalli et al. [8] also reported the oscillatory rheology profile of a spherical silica stabilised 50 vol. % oil-in-water Pickering emulsion in 50 mM NaCl to demonstrate two yielding events. The systems investigated by Katepalli et al. were prepared at a higher volume percentage than those prepared in this work, and demonstrated an increased elasticity. This increase in elasticity compared to the emulsions presented in the present work is expected to be due to the increase in the oil droplet concentration, increasing the contact between emulsion droplets. In addition to these Pickering emulsions, which were prepared at oil volume percentages below the random close packing percentage, concentrated surfactant stabilised emulsions have also demonstrated multi-stage yielding behaviour [142]. Datta et al. reported that surfactant stabilised emulsion systems with attractive interactions can demonstrate multi-stage yielding processes when the oil volume percentage is above the random close packing percentage. These peaks are attributed to two different yielding processes that occur; a network breaking, and then floc breaking events. Overlap of the two yielding events was also proposed to occur in certain cases in the data presented by Datta et al. [142] where, as the oil volume percentage was decreased, the yield events moved to closer strain percentages, eventually presenting as a single peak.

As the study of the rheological properties of attractive and repulsive titania stabilised Pickering emulsions in the present work is thought to be the first investigation into the

rheology of titania stabilised emulsions, comparisons to previous or similar results cannot be made. Instead of this, comparisons are made to previous colloid and emulsion systems that have the interactions between the particles or droplets altered. Previous investigations have demonstrated that changes in pH can significantly alter the mechanical properties of an emulsion [49, 69, 208, 217–222]. A number of these studies have demonstrated differences in the rheological properties of these pH altered systems [49, 217, 218]. These studies found that as the pH is altered, the surface charge of the emulsion stabiliser (or gel particles) is also changed. As the surface charges of these systems tend to zero, the interactions between the particles in the systems become attractive, leading to systems that display an increase in solid-like behaviour. These effects were demonstrated in the titania stabilised emulsions shown throughout this work.

In addition to making the obvious comparisons with pH altered colloidal systems, comparisons to ionic strength altered systems were made. As has been discussed throughout this work, Katepalli et al. have demonstrated the effect that changes in salt concentration have on two separate emulsion system, one stabilised by fumed silica, and one by spherical silica nanoparticles [8]. A comparison has been made between the spherical silica results presented by Katepalli et al. and the titania stabilised emulsions prepared here. While the titania and spherical silica nanoparticles are different in terms of overall shape (titania is a needle-like ellipsoid, while the silica is spherical), these are smooth, regular particles, leading to particle networks which are proposed to not have the interlocking capability of fractal-like fumed silica particles. In comparison, the fumed silica nanoparticles used both in Chapters 3 and 4, as well as by Katepalli et al. have an irregular, fractal-like shape, which are proposed to result in an interlocked network forming between the particles. These differences in the particle morphology have in both the work by Katepalli et al., and the work presented here appeared to result in significant differences in the rheological properties of the prepared emulsions, demonstrating that the effect of particle shape and roughness could be an interesting area to investigate further. Katepalli et al. found the fumed silica particle coated emulsions to have a G' value of the linear viscoelastic region that was approximately an order of magnitude larger than that of the spherical silica stabilised emulsion. In addition to the difference in magnitude of the results, the shape of the G' and G'' responses also differed, with the spherical silica yielding at much lower strains, through a clear multi-stage yielding process. The fumed silica demonstrated an elastic structure over a wide strain range, before yielding with a broad single peak in the G'' response. These differences were attributed to the excess fumed silica particles forming

a volume filling network throughout the continuous phase of the emulsion, a feature that was not determined to happen with the spherical silica.

Similar comparisons can be made between the silica stabilised, and titania stabilised emulsions demonstrated throughout the work presented here. The fumed silica nanoparticles used in Chapters 3 and 4 have been shown to develop extensive particle networks throughout the continuous phase when the interactions between the particles are attractive with confocal microscopy, and cryo-SEM. In comparison, the titania stabilised emulsions reported in Chapter 5 did not demonstrate a particle network throughout the continuous phase when the interaction between the nanoparticles was attractive. It is proposed that these differences in the network structure in the continuous phase result in alterations to the rheological properties of the emulsions. One demonstration of this is the values of G' in the linear viscoelastic region for each emulsion. Both the attractive silica stabilised emulsions (20 vol. %) reported in Chapter 4, and the higher volume percentage titania stabilised emulsion (30 vol. %) reported in Chapter 5 were found to have a G' value in the region of 100 Pa. As the volume percentage of the titania stabilised emulsion was greater than that of the silica stabilised system, it would be expected that the G' value would increase accordingly. Due to the differences in network structure present in the continuous phase, this increase has not occurred. Instead, the titania stabilised emulsion is found to be weaker when compared to the silica stabilised system (yield stresses of approximately 14 Pa for the attractive silica stabilised system, compared to $\leq$2 Pa for the attractive titania stabilised system).

Comparing the response of G' and G'' to variations in applied frequency for the attractive silica and titania emulsion systems gave an interesting insight into their elastic behaviour. The attractive silica-stabilised emulsion studied in Chapter 4 showed a difference in G' and G'' of up to two orders of magnitude as the frequency of the oscillations was varied (Fig. 4.15). This demonstrated the significant elastic strength of this system, a likely result of the network formed between the emulsion droplets and silica in the continuous phase. The attractive titania-stabilised emulsion system investigated in Chapter 5 demonstrated a different response of G' and G'' to variations in the applied oscillation frequency (Fig. 5.19). While G' was still larger than G'' across the full range of frequencies investigated, the magnitude of this difference was reduced, with G' up to one order of magnitude greater than G''. This indicates that the attractive titania-stabilised emulsion system is still elastic, but the strength of this elasticity is reduced. This reduced elasticity of the titania-stabilised system is proposed to be due to the lack of an interacting network between the oil droplets

and any excess stabiliser in the aqueous phase.

6.3. Conclusions

This work has investigated a range of properties and effects that are shown in a number of Pickering emulsion systems. This started with investigations into methods for the measurement of the yield stress of Pickering emulsion materials. From this investigation, it was demonstrated that the chosen definition of the yield stress can alter the yield stress values obtained. The fitting of the inflection point from the linear viscoelastic region and shear-thinning region of the oscillatory rheology methods fit well with the yield stress definition of being the point at which a material begins to flow in a viscous manner. As the linear viscoelastic region is the region in which the material behaves in a solid-like manner before viscous dissipation occurs, the inflection point at the end of this region aligns well with the yield stress definition.

The flow curve methods that were used to measure the yield stress gave consistently high yield stresses in Chapter 3, compared to those reported by others for near-comparable systems [131]. While these methods are a fast, and commonly used method to measure the yield stress of a material, they do require extrapolation in order to quantify a yield stress from the material [223]. The creep and creep recovery experiments have demonstrated to be a useful, albeit cumbersome tool, largely due to the time required to carry out the measurements.

The ability to significantly alter the bulk rheology properties of an emulsion by either altering the Debye length through the addition of salt (Chapter 4), or by altering the surface charge of the Pickering emulsifiers (Chapter 5) was demonstrated in this work. It was shown through DLVO calculations that the interaction energies between the nanoparticles coating the Pickering emulsion droplets can be altered in a predictable manner. These alterations lead to significant changes in the elasticity of these emulsions. The effect of particle shape on the strength of the resultant emulsions has also been demonstrated through comparisons between Chapters 4 and 5, with the fractal-like fumed silica particles leading to the development of extensive elastic networks throughout the emulsion systems. This work adds to the sets of controllable colloids that have been previously demonstrated. The control of emulsion materials such as these open up the opportunity to develop products or procedures that require specific properties into the future.

6.4. Future work

The measurement of the yield stress of Pickering emulsions was demonstrated through a number of methods in this work, with the choice of method affecting the resultant value. This outlined the fact that different definitions of the yield stress alter the choice of the most appropriate method to measure the yield stress. The yield stresses that were measured with the flow curve experiments in this work were a static yield stress. The static yield stress is defined as the minimum stress required before flow begins from a static state. This differs from the dynamic yield stress, which is the stress at which the material will cease to flow. If a material is thixotropic, the static yield stress will often differ from the dynamic yield stress. In order to compare these two yield stresses, it is common to measure a flow curve with both an increasing and decreasing applied shear. In this work, the shear was applied in an increasing manner, and not in the reverse. Repeating these experiments with the measurement of the dynamic yield stress may add extra information to the understanding of these emulsion materials.

One of the centre points of this work has been the demonstrations of the ability to control the bulk rheological properties of Pickering emulsions, through control of the aqueous continuous phase. The ability to control the flow and structural properties of an emulsion system on demand in a predictable manner is a vital tool that may find further use in a range of commercial or industrial processes, such as cosmetic and food manufacture, or oil recovery. One current limiting factor for this however is the range of emulsion stabilising materials that demonstrate these novel and useful properties. Currently, these changes in the properties of these systems are seen throughout the previous and the present work to be specific cases, with specific oils, Pickering stabilisers, and aqueous phases. These specific cases are an important starting point for future research into other (Pickering) emulsion materials with a range of oils, stabilisers, and aqueous phases, such as food-safe ingredients, or heavy oils.

It has been demonstrated in this work that the nanoparticles used to stabilise Pickering emulsions can have a large effect on the bulk properties of the systems. As was mentioned in the comparisons presented in this chapter, understanding the effect of particle shape and surface roughness is an area that could be further developed. It is hypothesised here that an increase in the surface roughness of the nanoparticles would lead to an increase in the interactions between neighboring particles, and therefore lead to larger changes in the bulk rheological properties measured. Modification of nanoparticles to increase the steric

interactions between the particles could be carried out in a number of ways, including chemical modification or etching of the surfaces, mechanical grinding of microscale particles, or through heating processes similar to that used in the preparation of fumed silica. Characterisation of the surface roughness of nanoparticles can be achieved through the use of electron microscopy techniques. The effect of this roughness would be best understood in a simple colloidal dispersion, with the nanoparticles dispersed through a liquid phase, with the viscous and elastic properties of such a material providing insight into the interactions between the nanoparticles, before investigating the use in Pickering emulsions.

In addition to understanding the effect of the shape and surface roughness of the Pickering stabilisers, the effect of particle loading on network formation and emulsion structure, is an area that could be explored with rheological methods. The particle loading of the Pickering emulsions prepared for Chapter 3 was altered (from 2.5 wt. % to 5 wt. %) as a consequence of dilution of the emulsions, and the rheological properties of the systems were demonstrated to change. Indications of the expected trend in the rheological data were seen, with the elasticity decreasing as the particle loading was lowered. However, the oil volume percentage was also decreased, so the relative contribution of each component to the overall is not able to be quantified. Future work could quantify the contribution to the bulk rheological properties of nanoparticle suspensions, separating the effect which the particle concentrations have on the physical properties.

Finally, the microscopic imaging of the multiple yielding events shown in both Chapters 4 and 5 would provide insight into the structural rearrangements occurring during these yielding events. These yielding events are attributed to two different specific yielding events that are proposed to occur in colloidal materials with attractive interactions between the particles. Other groups have described this in the past, specifically for colloidal glasses and surfactant stabilised emulsions [12–15, 142, 167]. Despite this interest, and thoughtful descriptions of what may be occurring in these materials, to the best of the author's knowledge, no successful imaging of these two yielding processes has occurred. The main limitations in imaging these interactions revolved around the speed at which the emulsion droplets are moving at strains close to the yielding events. The speed of these droplets, coupled with the current standard camera frame rates available has made the imaging of these emulsions complex. Future improvements in camera technologies, imaging techniques, or experimental methods may allow the accurate measurement of these yielding events, and may finally lead to a definitive understanding of the yielding processes occurring in these complex soft materials.

Bibliography

[1] Demetriades, K.; Coupland, J. N.; McClements, D. J. *J. Food Sci.* **1997**, *62*, 342–347; doi:10.1111/j.1365-2621.1997.tb03997.x.

[2] Dickinson, E.; Parkinson, E. L. *Int. Dairy J.* **2004**, *14*, 635–645; doi:10.1016/j.idairyj.2003.12.005.

[3] Liu, F.; Tang, C.-H. *J. Agric. Food Chem.* **2013**, *61*, 8888–8898; doi:10.1021/jf401859y.

[4] Gautier, F.; Destribats, M.; Perrier-Cornet, R.; Dechézelles, J.-F.; Giermanska, J.; Héroguez, V.; Ravaine, S.; Leal-Calderon, F.; Schmitt, V. *Phys. Chem. Chem. Phys.* **2007**, *9*, 6455–6462; doi:10.1039/B710226G.

[5] Li, Z.; Ming, T.; Wang, J.; Ngai, T. *Angew. Chem.* **2009**, *121*, 8642–8645; doi:10.1002/anie.200902103.

[6] Li, C.; Li, Y.; Sun, P.; Yang, C. *Colloids Surf. A* **2013**, *431*, 142–149; doi:10.1016/j.colsurfa.2013.04.025.

[7] Song, X.; Pei, Y.; Qiao, M.; Ma, F.; Ren, H.; Zhao, Q. *Food Hydrocoll.* **2015**, *45*, 256–263; doi:10.1016/j.foodhyd.2014.12.007.

[8] Katepalli, H.; John, V. T.; Tripathi, A.; Bose, A. *J. Colloid Interface Sci.* **2017**, *485*, 11–17; doi:10.1016/j.petrol.2017.12.091.

[9] Pandey, A.; Derakhshandeh, M.; Kedzior, S. A.; Pilapil, B.; Shomrat, N.; Segal-Peretz, T.; Bryant, S. L.; Trifkovic, M. *J. Colloid Interface Sci.* **2018**, *532*, 808–818; doi:10.1016/j.jcis.2018.08.044.

[10] Griffith, C.; Daigle, H. *J. Colloid Interface Sci.* **2018**, *509*, 132–139; doi:10.1016/j.jcis.2017.08.100.

[11] Binks, B. P. *Modern Aspects of Emulsion Science*; The Royal Society of Chemistry, **1998**; doi:10.1039/9781847551474.

[12] Pham, K. N.; Petekidis, G.; Vlassopoulos, D.; Egelhaaf, S. U.; Pusey, P. N.; Poon, W. C. K. *EPL* **2006**, *75*, 624; doi:10.1209/epl/i2006-10156-y.

[13] Pham, K. N.; Petekidis, G.; Vlassopoulos, D.; Egelhaaf, S. U.; Poon, W. C. K.; Pusey, P. N. *J. Rheol* **2008**, *52*, 649–676; doi:10.1122/1.2838255.

[14] Christopoulou, C.; Petekidis, G.; Erwin, B.; Cloitre, M.; Vlassopoulos, D. *Philos. Trans. Royal Soc. A Engineering Sciences* **2009**, *367*, 5051–5071; doi:10.1098/rsta.2009.0166.

[15] Renou, F.; Stellbrink, J.; Petekidis, G. *J. Rheol* **2010**, *54*, 1219–1242; doi:10.1122/1.3483610.

[16] Cosgrove, T. *Colloid science: Principles, methods and applications*; John Wiley & Sons, **2010**; doi:10.1002/9781444305395.

[17] Birdi, K. S. *Surface and Colloid Chemistry: Principles and applications*; CRC press, **2009**; doi:10.1201/b10154.

[18] Graham, T. *Philos. Trans. Royal Soc.* **1861**, *151*, 183–224; doi:10.1098/rstl.1861.0011.

[19] Freestone, I.; Meeks, N.; Sax, M.; Higgitt, C. *Gold Bull.* **2007**, *40*, 270–277; doi:10.1007/bf03215599.

[20] Faraday, M. *Phil. Trans. R. Soc. London* **1857**, *147*, 145–181.

[21] Verwey, E. J. W. *J. Phys. Chem.* **1947**, *51*, 631–636; doi:10.1021/j150453a001.

[22] Derjaguin, B. V.; Landau, L. *Acta Physicochim: USSR* **1941**, *14*, 633–662.

[23] Yotsumoto, H.; Yoon, R.-H. *J. Colloid Interface Sci.* **1993**, *157*, 426–433; doi:10.1006/jcis.1993.1205.

[24] Yotsumoto, H.; Yoon, R.-H. *J. Colloid Interface Sci.* **1993**, *157*, 434–441; doi:10.1006/jcis.1993.1206.

[25] Gupta, A.; Eral, H. B.; Hatton, T. A.; Doyle, P. S. *Soft Matter* **2016**, *12*, 2826–2841; doi:10.1039/C5SM02958A.

[26] Kyrides, L. P.; *Insecticide*; **1941**; US Patent 2,267,204.

[27] Bragg, J. R.; *Oil recovery method using an emulsion*; **1999**; US Patent 5,855,243.

[28] Iacoviello, J. G.; Daniels, W. E.; *Vinyl acetate copolymer emulsions for paint*; **1980**; US Patent 4,219,454.

[29] Patel, A. D.; Bell, R. J.; Young, S.; Tehrani, A.; *Double emulsion based drilling fluids*; **2004**; US Patent 6,793,025.

[30] McClements, D. J. *Food emulsions: principles, practices, and techniques*; CRC press, **2015**; doi:10.1201/b18868.

[31] Urban, K.; Wagner, G.; Schaffner, D.; Röglin, D.; Ulrich, J. *Chemical Engineering & Technology: Industrial Chemistry-Plant Equipment-Process Engineering-Biotechnology* **2006**, *29*, 24–31; doi:10.1002/ceat.200500304.

[32] Pal, R. *Chem. Eng. J.* **1997**, *67*, 37–44; doi:10.1016/S1385-8947(97)00011-9.

[33] Marie, P.; Perrier-Cornet, J. M.; Gervais, P. *J. Food Eng.* **2002**, *53*, 43–51; doi:10.1016/S0260-8774(01)00138-8.

[34] Gaikwad, S. G.; Pandit, A. B. *Ultrasonics Sonochemistry* **2008**, *15*, 554–563; doi:10.1016/j.ultsonch.2007.06.011.

[35] Walstra, P. *Chem. Eng. Sci.* **1993**, *48*, 333–349; doi:10.1016/0009-2509(93)80021-H.

[36] Bibette, J.; Morse, D. C.; Witten, T. A.; Weitz, D. A. *Phys. Rev. Lett.* **1992**, *69*, 2439; doi:10.1103/PhysRevLett.69.2439.

[37] Binks, B. P.; Lumsdon, S. O. *Phys. Chem. Chem. Phys.* **1999**, *1*, 3007–3016; doi:10.1039/A902209K.

[38] Binks, B. P.; Lumsdon, S. O. *Langmuir* **2000**, *16*, 2539–2547; doi:10.1021/la991081j.

[39] Nguyen, B. T.; Nicolai, T.; Benyahia, L. *Langmuir* **2013**, *29*, 10658–10664; doi:10.1021/la402131e.

[40] Binks, B. P.; Tyowua, A. T. *Soft Matter* **2016**, *12*, 876–887; doi:10.1039/C5SM02438B.

[41] Yaqoob Khan, A.; Talegaonkar, S.; Iqbal, Z.; Jalees Ahmed, F.; Krishan Khar, R. *Curr. Drug Deliv.* **2006**, *3*, 429–443; doi:10.2174/156720106778559056.

[42] Florence, A. T.; Whitehill, D. *J. Colloid Interface Sci.* **1981**, *79*, 243–256; doi:10.1016/0021-9797(81)90066-7.

[43] Jahaniaval, F.; Kakuda, Y.; Abraham, V. *J. Am. Oil Chem. Soc.* **2003**, *80*, 25–31; doi:10.1007/s11746-003-0645-9.

[44] Tyowua, A. T.; Yiase, S. G.; Binks, B. P. *J. Colloid Interface Sci.* **2017**, *488*, 127–134; doi:10.1016/j.jcis.2016.10.089.

[45] Choi, C.-H.; Kim, J.; Nam, J.-O.; Kang, S.-M.; Jeong, S.-G.; Lee, C.-S. *ChemPhysChem* **2014**, *15*, 21–29; doi:10.1002/cphc.201300821.

[46] Bibette, J.; Roux, D.; Nallet, F. *Phys. Rev. Lett.* **1990**, *65*, 2470; doi:10.1103/PhysRevLett.65.2470.

[47] Bibette, J.; Roux, D.; Pouligny, B. *Journal de Physique II* **1992**, *2*, 401–424; doi:10.1051/jp2:1992141.

[48] Yoon, R.-H.; Ravishankar, S. A. *J. Colloid Interface Sci.* **1994**, *166*, 215–224; doi:10.1006/jcis.1994.1287.

[49] Dickinson, E. *Colloids Surf. B* **2010**, *81*, 130–140; doi:10.1016/j.colsurfb.2010.06.033.

[50] Dickinson, E.; Golding, M.; Povey, M. J. *J. Colloid Interface Sci.* **1997**, *185*, 515–529; doi:10.1006/jcis.1996.4605.

[51] Robins, M. M. *Curr. Opin. Colloid Interface Sci.* **2000**, *5*, 265–272; doi:10.1016/S1359-0294(00)00065-0.

[52] Arditty, S.; Whitby, C. P.; Binks, B. P.; Schmitt, V.; Leal-Calderon, F. *Eur. Phys. J. E* **2003**, *11*, 273–281; doi:10.1140/epje/i2003-10060-4.

[53] Tcholakova, S.; Denkov, N. D.; Ivanov, I. B.; Campbell, B. *Adv. Colloid Interface Sci.* **2006**, *123*, 259–293; doi:10.1016/j.cis.2006.05.021.

[54] Whitby, C. P.; Fischer, F. E.; Fornasiero, D.; Ralston, J. *J. Colloid Interface Sci.* **2011**, *361*, 170–177; doi:10.1016/j.jcis.2011.05.046.

[55] Voorhees, P. W. *J. Stat. Phys.* **1985**, *38*, 231–252; doi:10.1007/BF01017860.

[56] Taylor, P. *Adv. Colloid Interface Sci.* **1998**, *75*, 107–163; doi:10.1016/S0001-8686(98)00035-9.

[57] Chen, S.; Øye, G.; Sjöblom, J. *J. Disper. Sci. Technol.* **2007**, *28*, 845–853; doi:10.1080/01932690701345844.

[58] Stenhammar, J.; Linse, P.; Wennerström, H.; Karlström, G. *J. Phys. Chem. B* **2010**, *114*, 13372–13380; doi:10.1021/jp105754t.

[59] Borwankar, R. P.; Lobo, L. A.; Wasan, D. T. *Colloids and Surfaces* **1992**, *69*, 135–146; doi:10.1016/0166-6622(92)80224-P.

[60] Dickinson, E.; Golding, M. *Colloids Surf. A* **1998**, *144*, 167–177; doi:10.1016/S0927-7757(98)00573-1.

[61] Chanamai, R.; McClements, D. J. *J. Colloid Interface Sci.* **2000**, *225*, 214–218; doi:10.1006/jcis.2000.6766.

[62] Chanamai, R.; McClements, D. J. *Colloids Surf. A* **2000**, *172*, 79–86; doi:10.1016/S0927-7757(00)00551-3.

[63] Fredrick, E.; Walstra, P.; Dewettinck, K. *Adv. Colloid Interface Sci.* **2010**, *153*, 30–42; doi:10.1016/j.cis.2009.10.003.

[64] He, Y.; Wu, F.; Sun, X.; Li, R.; Guo, Y.; Li, C.; Zhang, L.; Xing, F.; Wang, W.; Gao, J. *ACS Applied Materials & Interfaces* **2013**, *5*, 4843–4855; doi:10.1021/am400582n.

[65] Ivanov, I. B.; Danov, K. D.; Kralchevsky, P. A. *Colloids Surf. A* **1999**, *152*, 161–182; doi:10.1016/S0927-7757(98)00620-7.

[66] Ramsden, W.; Gotch, F. **1903**; doi:10.1098/rspl. 1903.0034.

[67] Pickering, S. U. *Journal of the Chemical Society, Transactions* **1907**, *91*, 2001–2021; doi:10.1039/CT9079102001.

[68] Binks, B. P.; Whitby, C. P. *Langmuir* **2004**, *20*, 1130–1137; doi:10.1021/la0303557.

[69] Binks, B. P.; Whitby, C. P. *Colloids Surf. A* **2005**, *253*, 105–115; doi:10.1016/j.colsurfa.2004.10.116.

[70] Whitby, C. P.; Fornasiero, D.; Ralston, J. *J. Colloid Interface Sci.* **2010**, *342*, 205–209; doi:10.1016/j.jcis.2009.10.068.

[71] Dookhith, M.; Linares, H.; *Titanium dioxide stabilized oil in water pesticidal emulsion*; **1992**; US Patent 5,096,711.

[72] Menner, A.; Ikem, V.; Salgueiro, M.; Shaffer, M. S.; Bismarck, A. *ChemComm* **2007**, 4274–4276; doi:10.1039/B708935J.

[73] Stiller, S.; Gers-Barlag, H.; Lergenmueller, M.; Pflücker, F.; Schulz, J.; Wittern, K. P.; Daniels, R. *Colloids Surf. A* **2004**, *232*, 261–267; doi:10.1016/j.colsurfa.2003.11.003.

[74] Zhou, J.; Qiao, X.; Binks, B. P.; Sun, K.; Bai, M.; Li, Y.; Liu, Y. *Langmuir* **2011**, *27*, 3308–3316; doi:10.1021/la1036844.

[75] Chen, W.; Liu, X.; Liu, Y.; Kim, H.-I. *Mater. Lett.* **2010**, *64*, 2589–2592; doi:10.1016/j.matlet.2010.08.052.

[76] Chen, W.; Liu, X.; Liu, Y.; Bang, Y.; Kim, H.-I. *J. Ind. Eng. Chem.* **2011**, *17*, 455–460; doi:10.1016/j.jiec.2010.10.027.

[77] Huo, J.; Marcello, M.; Garai, A.; Bradshaw, D. *Adv. Mater.* **2013**, *25*, 2717–2722; doi:10.1002/adma.201204913.

[78] Yang, Y.; Fang, Z.; Chen, X.; Zhang, W.; Xie, Y.; Chen, Y.; Liu, Z.; Yuan, W. *Front. Pharmacol.* **2017**, *8*, 287; doi:10.3389/fphar.2017.00287.

[79] Thompson, K. L.; Giakoumatos, E. C.; Ata, S.; Webber, G. B.; Armes, S. P.; Wanless, E. J. *Langmuir* **2012**, *28*, 16501–16511; doi:10.1021/la3025765.

[80] Levine, S.; Bowen, B. D.; Partridge, S. J. *Colloids and surfaces* **1989**, *38*, 325–343; doi:10.1016/0166-6622(89)80271-9.

[81] French, D. J.; Brown, A. T.; Schofield, A. B.; Fowler, J.; Taylor, P.; Clegg, P. S. *Sci. Rep.* **2016**, *6*, 31401; doi:10.1038/srep31401.

[82] French, D. J.; Ph.D. thesis; University of Edinburgh; **2016**.

[83] Schulman, J. H.; Leja, J. *J. Chem. Soc. Faraday Trans.* **1954**, *50*, 598–605; doi:10.1039/TF9545000598.

[84] Bachinger, A.; Kickelbick, G. *Monatshefte für Chemie-Chemical Monthly* **2010**, *141*, 685–690; doi:10.1007/s00706-010-0273-9.

[85] Binks, B. P. *Curr. Opin. Colloid Interface Sci.* **2002**, *7*, 21–41; doi:10.1016/S1359-0294(02)00008-0.

[86] Dong, L.; Johnson, D. T. *J. Disper. Sci. Technol.* **2005**, *25*, 575–583; doi:10.1081/DIS-200027307.

[87] Vignati, E.; Piazza, R.; Lockhart, T. P. *Langmuir* **2003**, *19*, 6650–6656; doi:10.1021/la034264l.

[88] Morse, A. J.; Tan, S.-Y.; Giakoumatos, E. C.; Webber, G. B.; Armes, S. P.; Ata, S.; Wanless, E. J. *Soft Matter* **2014**, *10*, 5669–5681; doi:10.1039/C4SM00801D.

[89] Chevalier, Y.; Bolzinger, M.-A. *Colloids Surf. A* **2013**, *439*, 23–34; doi:10.1016/j.colsurfa.2013.02.054.

[90] Ganley, W. J.; van Duijneveldt, J. S. *Langmuir* **2017**, *33*, 1679–1686; doi:10.1021/acs.langmuir.6b04161.

[91] Dickinson, E.; Chen, J. *J. Disper. Sci. Technol.* **1999**, *20*, 197–213; doi:10.1080/01932699908943787.

[92] Hunter, R. J. *Zeta potential in colloid science: principles and applications*; Academic press, **2013**; Vol. 2; doi:10.1016/C2013-0-07389-6.

[93] Ishikawa, Y.; Katoh, Y.; Ohshima, H. *Colloids Surf. B* **2005**, *42*, 53–58; doi:10.1016/j.colsurfb.2005.01.006.

[94] McClements, D. J. *Curr. Opin. Colloid Interface Sci.* **2002**, *7*, 451–455; doi:10.1016/S1359-0294(02)00075-4.

[95] Groves, M. J.; Freshwater, D. C. *J. Pharm. Sci.* **1968**, *57*, 1273–1291; doi:10.1002/jps.2600570802.

[96] Barth, H. G.; Flippen, R. B. *Anal. Chem.* **1995**, *67*, 257–272; doi:10.1021/ac00108a013.

[97] Barnes, H. A. *Colloids Surf. A* **1994**, *91*, 89–95; doi:10.1016/0927-7757(93)02719-U.

[98] Chen, J.; Dickinson, E. *Colloids Surf. B* **1999**, *12*, 373–381; doi:10.1016/S0927-7765(98)00091-5.

[99] Fischer, E. K. *J. Colloid. Sci.* **1948**, *3*, 73–73; doi:10.1016/0095-8522(48)90057-9.

[100] Hagen, G. *Ann. Phys. (Berl.)* **1839**, *122*, 423–442; doi:10.1002/andp.18391220304.

[101] Herschel, W. H.; Bulkley, R. *Colloid. Polym. Sci.* **1926**, *39*, 291–300; doi:10.1007/BF01432034.

[102] Bingham, E. C. *An investigation of the laws of plastic flow*; Govt. Print. Off., **1917**; Vol. 13.

[103] Mezger, T. G. *The Rheology Handbook: For users of rotational and oscillatory rheometers*, 3rd ed.; Vincentz Network, **2011**.

[104] Barnes, H. A.; Hutton, J. F.; Walters, K. *An introduction to rheology*; Elsevier, **1989**.

[105] Philippoff, W.; Gaskins, F. H. *Trans. Soc. Rheol.* **1958**, *2*, 263–284; doi:10.1122/1.548832.

[106] Chevalier, J.; Ayela, F. *Rev. Sci. Instrum.* **2008**, *79*, 076102; doi:10.1063/1.2940219.

[107] Gupta, S.; Wang, W. S.; Vanapalli, S. A. *Biomicrofluidics* **2016**, *10*, 043402; doi:10.1063/1.4955123.

[108] Läuger, J.; Stettin, H. *Rheol. Acta* **2010**, *49*, 909–930; doi:10.1007/s00397-010-0450-0.

[109] Brummer, R. *Rheology Essentials of Cosmetic and Food Emulsions*; Springer Science & Business Media, **2006**; doi:10.1007/3-540-29087-7.

[110] Murray, B. S. *Curr. Opin. Colloid Interface Sci.* **2002**, *7*, 426–431; doi:10.1016/S1359-0294(02)00077-8.

[111] Liggieri, L.; Miller, R. *Interfacial rheology*; CRC Press, **2009**.

[112] Bender, J.; Wagner, N. J. *J. Rheol* **1996**, *40*, 899–916; doi:10.1122/1.550767.

[113] Barry, B. W. *Rheol. Acta* **1971**, *10*, 96–105; doi:10.1007/BF01972485.

[114] Pal, R. *AIChE J.* **1996**, *42*, 3181–3190; doi:10.1002/aic.690421119.

[115] Einstein, A. *Ann. Phys. (Berl.)* **1906**, *324*, 289–306; doi:10.1002/andp.19063240204.

[116] Einstein, A. *Ann. Phys. (Berl.)* **1911**, *339*, 591–592; doi:10.1002/andp.19113390313.

[117] Batchelor, G. K. *J. Fluid Mech.* **1972**, *52*, 245–268; doi:10.1017/S0022112072001399.

[118] Batchelor, G. K. *J. Fluid Mech.* **1976**, *74*, 1–29; doi:10.1017/S0022112076001663.

[119] Batchelor, G. K. *J. Fluid Mech.* **1977**, *83*, 97–117; doi:10.1017/S0022112077001062.

[120] Krieger, I. M.; Dougherty, T. J. *Trans. Soc. Rheol.* **1959**, *3*, 137–152; doi:10.1122/1.548848.

[121] Krieger, I. M. *Adv. Colloid Interface Sci.* **1972**, *3*, 111–136; doi:10.1016/0001-8686(72)80001-0.

[122] Brown, R. *The Philosophical Magazine* **1828**, *4*, 161–173; doi:10.1080/14786442808674769.

[123] Baranau, V.; Tallarek, U. *Soft Matter* **2014**, *10*, 3826–3841; doi:10.1039/C3SM52959B.

[124] Barnes, H. A. *Appl. Rheol.* **2007**, *17*, 43110–44250.

[125] Barnes, H. A. *J. Non-Newton Fluid Mech.* **1999**, *81*, 133–178; doi:10.1016/S0377-0257(98)00094-9.

[126] Barnes, H. A.; Walters, K. *Rheol. Acta* **1985**, *24*, 323–326; doi:10.1007/BF01333960.

[127] Astarita, G. *J. Rheol* **1990**, *34*, 275–277; doi:10.1122/1.550142.

[128] Evans, I. D. *J. Rheol* **1992**, *36*, 1313–1318; doi:10.1122/1.550262.

[129] Hartnett, J. P.; Hu, R. Y. Z. *J. Rheol* **1989**, *33*, 671–679; doi:10.1122/1.550006.

[130] Mason, T. G.; Bibette, J.; Weitz, D. A. *J. Colloid Interface Sci.* **1996**, *179*, 439–448; doi:10.1006/jcis.1996.0235.

[131] Dinkgreve, M.; Paredes, J.; Denn, M. M.; Bonn, D. *J. Non-Newton Fluid Mech.* **2016**, *238*, 233–241; doi:10.1016/j.jnnfm.2016.11.001.

[132] Cheng, D. C. *Rheologica Acta* **1986**, *25*, 542–554; doi:10.1007/BF01774406.

[133] Fall, A.; Paredes, J.; Bonn, D. *Phys. Rev. Lett.* **2010**, *105*, 225502; doi:10.1103/PhysRevLett.105.225502.

[134] Goodwin, J. W.; Hughes, R. W. *Rheology for chemists: an introduction*; Royal Society of Chemistry, **2008**; doi:10.1039/9781847551832.

[135] Struble, L. J.; Schultz, M. A. *Cement Concrete Res.* **1993**, *23*, 1369–1379; doi:10.1016/0008-8846(93)90074-J.

[136] Lequeux, F. *Curr. Opin. Colloid Interface Sci.* **1998**, *3*, 408–411; doi:10.1016/S1359-0294(98)80057-5.

[137] Dickinson, E. *Curr. Opin. Colloid Interface Sci.* **1998**, *3*, 633–638; doi:10.1016/S1359-0294(98)80092-7.

[138] Mason, T. G. *Curr. Opin. Colloid Interface Sci.* **1999**, *4*, 231–238; doi:10.1016/S1359-0294(99)00035-7.

[139] Derkach, S. R. *Adv. Colloid Interface Sci.* **2009**, *151*, 1–23; doi:10.1016/j.cis.2009.07.001.

[140] Pal, R. *Curr. Opin. Colloid Interface Sci.* **2011**, *16*, 41–60; doi:10.1016/j.cocis.2010.10.001.

[141] Bécu, L.; Manneville, S.; Colin, A. *Phys. Rev. Lett.* **2006**, *96*, 138302; doi:10.1103/PhysRevLett.96.138302.

[142] Datta, S. S.; Gerrard, D. D.; Rhodes, T. S.; Mason, T. G.; Weitz, D. A. *Phys. Rev. E* **2011**, *84*, 041404; doi:10.1103/PhysRevE.84.041404.

[143] Swan, J. W.; Furst, E. M. *Journal of colloid and interface science* **2012**, *388*, 92–94; doi:10.1016/j.jcis.2012.08.026.

[144] McNeil, S. E. *Characterization of nanoparticles intended for drug delivery*; Springer, **2011**; Vol. 697; doi:10.1007/978-1-60327-198-1.

[145] Prasad, V.; Semwogerere, D.; Weeks, E. R. *J. Phys. Condens. Matter* **2007**, *19*, 113102; doi:10.1088/0953-8984/19/11/113102.

[146] Greenspan, P.; Mayer, E. P.; Fowler, S. D. *J. Cell Biol.* **1985**, *100*, 965–973; doi:10.1083/jcb.100.3.965.

[147] Douhal, A. *J. Phys. Chem.* **1994**, *98*, 13131–13137; doi:10.1021/j100101a007.

[148] Egerton, R. F.; et al. *Physical principles of electron microscopy*; Springer, **2005**; doi:10.1007/978-3-319-39877-8.

[149] Mikula, R. J.; Munoz, V. A. *Colloids Surf. A* **2000**, *174*, 23–36; doi:10.1016/S0927-7757(00)00518-5.

[150] Cameron, N. R.; Sherrington, D. C.; Albiston, L.; Gregory, D. P. *Colloid. Polym. Sci.* **1996**, *274*, 592–595; doi:10.1007/BF00655236.

[151] Lee, D.; Weitz, D. A. *Adv. Mater.* **2008**, *20*, 3498–3503; doi:10.1002/adma.200800918.

[152] Roland, I.; Piel, G.; Delattre, L.; Evrard, B. *Int. J. Pharm.* **2003**, *263*, 85–94; doi:10.1016/S0378-5173(03)00364-8.

[153] *Particle Size Analysis Laser Diffraction Methods*; ISO 13320:2009; International Organization for Standardization Geneva; **2009**.

[154] Song, H. Y.; Salehiyan, R.; Li, X.; Lee, S. H.; Hyun, K. *Korea-Aust. Rheol. J. Journal* **2017**, *29*, 281–294; doi:10.1007/s13367-017-0028-9.

[155] Madivala, B.; Vandebril, S.; Fransaer, J.; Vermant, J. *Soft Matter* **2009**, *5*, 1717–1727; doi:10.1039/B816680C.

[156] Tzoumaki, M. V.; Moschakis, T.; Kiosseoglou, V.; Biliaderis, C. G. *Food Hydrocoll.* **2011**, *25*, 1521–1529; doi:10.1016/j.foodhyd.2011.02.008.

[157] Rouyer, F.; Cohen-Addad, S.; Höhler, R. *Colloids Surf. A* **2005**, *263*, 111–116; doi:10.1016/j.colsurfa.2005.01.025.

[158] Cyriac, F.; Lugt, P. M.; Bosman, R. *Tribol. T.* **2015**, *58*, 1021–1030; doi:10.1080/10402004.2015.1035414.

[159] Sánchez, M.; Valencia, C.; Franco, J. M.; Gallegos, C. *J. Colloid Interface Sci.* **2001**, *241*, 226–232; doi:10.1006/jcis.2001.7732.

[160] Juárez, J. A.; Whitby, C. P. *J. Colloid Interface Sci.* **2012**, *368*, 319–325; doi:10.1016/j.jcis.2011.11.029.

[161] Liang, B.; Shi, Y.; Hartel, R. W. *J. Am. Oil Chem. Soc.* **2008**, *85*, 397–404; doi:10.1007/s11746-008-1213-2.

[162] Stein, D. J.; Spera, F. J. *J. Volcanol. Geotherm. Res.* **1992**, *49*, 157–174; doi:10.1016/0377-0273(92)90011-2.

[163] Chen, K.; Chen, M.; Feng, Y.; Yu, G.; Zhang, L.; Li, J. *Colloids Surf. A* **2017**, *524*, 8–16; doi:10.1016/j.colsurfa.2017.02.088.

[164] Pabst, W. *Ceram.-Silikaty* **2004**, *48*, 6–13.

[165] Chawla, K. K.; Meyers, M. *Mechanical behavior of materials*; Prentice Hall Upper Saddle River, **1999**.

[166] Miyazaki, K.; Wyss, H. M.; Weitz, D. A.; Reichman, D. R. *EPL* **2006**, *75*, 915; doi:10.1209/epl/i2006-10203-9.

[167] Carrier, V.; Petekidis, G. *J. Rheol* **2009**, *53*, 245–273; doi:10.1122/1.3045803.

[168] Derec, C.; Ducouret, G.; Ajdari, A.; Lequeux, F. *Phys. Rev. E* **2003**, *67*, 061403; doi:10.1103/PhysRevE.67.061403.

[169] Sollich, P. *Phys. Rev. E* **1998**, *58*, 738; doi:10.1103/PhysRevE.58.738.

[170] Brnic, J.; Turkalj, G.; Canadija, M.; Lanc, D. *Mater. Sci. Eng. A.* **2009**, *499*, 23–27; doi:10.1016/j.msea.2007.08.102.

[171] Koumakis, N.; Petekidis, G. *Soft Matter* **2011**, *7*, 2456–2470; doi:10.1039/C0SM00957A.

[172] Sulpizi, M.; Gaigeot, M.-P.; Sprik, M. *J. Chem. Theory Comput.* **2012**, *8*, 1037–1047; doi:10.1021/ct2007154.

[173] Wacker Chemie AG; *HDK® N20 Pyrogenic Silica Technical Data Sheet*; **2018**; Version 1.14.

[174] Hanaor, D.; Michelazzi, M.; Leonelli, C.; Sorrell, C. C. *J. Eur. Ceram. Soc.* **2012**, *32*, 235–244; doi:10.1016/j.jeurceramsoc.2011.08.015.

[175] Binks, B. P.; Clint, J. H.; Whitby, C. P. *Langmuir* **2005**, *21*, 5307–5316; doi:10.1021/la050255w.

[176] Britton, M. M.; Callaghan, P. T. *Phys. Rev. Lett.* **1997**, *78*, 4930; doi:10.1103/PhysRevLett.78.4930.

[177] Cates, M. E.; McLeish, T. C. B.; Marrucci, G. *EPL* **1993**, *21*, 451; doi:10.1209/0295-5075/21/4/012.

[178] Coussot, P.; Tocquer, L.; Lanos, C.; Ovarlez, G. *J. Non-Newton Fluid Mech.* **2009**, *158*, 85–90; doi:10.1016/j.jnnfm.2008.08.003.

[179] Mewis, J.; Wagner, N. J. *Adv. Colloid Interface Sci.* **2009**, *147*, 214–227; doi:10.1016/j.cis.2008.09.005.

[180] Kuchin, N. B., I. V.and Uriev *Colloid J.* **2013**, *75*, 543–556; doi:10.1134/S1061933X13050050.

[181] Ovarlez, G.; Rodts, S.; Chateau, X.; Coussot, P. *Rheol. Acta* **2009**, *48*, 831–844; doi:10.1007/s00397-008-0344-6.

[182] Fall, A.; Bertrand, F.; Ovarlez, G.; Bonn, D. *Phys. Rev. Lett.* **2009**, *103*, 178301; doi:10.1103/PhysRevLett.103.178301.

[183] Sein, A.; Verheij, J. A.; Agterof, W. G. M. *J. Colloid Interface Sci.* **2002**, *249*, 412–422; doi:10.1006/jcis.2002.8287.

[184] Hyun, K.; Kim, S. H.; Ahn, K. H.; Lee, S. J. *J. Non-Newton Fluid Mech.* **2002**, *107*, 51–65; doi:10.1016/S0377-0257(02)00141-6.

[185] Bot, A.; van Amerongen, I. A.; Groot, R. D.; Hoekstra, N. L.; Agterof, W. G. *Polym. Gels Networks* **1996**, *4*, 189–227; doi:10.1016/0966-7822(96)00011-1.

[186] Zhang, J.; Daubert, C. R.; Foegeding, E. A. *J. Food Eng.* **2007**, *80*, 157–165; doi:doi.org/10.1016/j.jfoodeng.2006.04.057.

[187] Groot, R. D.; Bot, A.; Agterof, W. G. M. *J. Chem. Phys.* **1996**, *104*, 9202–9219; doi:10.1063/1.471611.

[188] Trappe, V.; Weitz, D. A. *Phys. Rev. Lett.* **2000**, *85*, 449; doi:10.1103/PhysRevLett.85.449.

[189] Ahuja, A.; Peifer, T.; Yang, C. C.; Ahmad, O.; Gamonpilas, C. *Rheol. Acta* **2018**; doi:10.1007/s00397-018-1106-8.

[190] Smijs, T. G.; Pavel, S. *Nanotechnol. Sci. Appl.* **2011**, *4*, 95; doi:10.2147/NSA.S19419.

[191] The European Union Scientific Committee on Cosmetic Products and Non-Food Products Intended for Consumers *Opinion of the Scientific Committee on Cosmetic Products and Non-Food Products Intended for Consumers*; The European Commission, **2000**.

[192] Faure, B.; Salazar-Alvarez, G.; Ahniyaz, A.; Villaluenga, I.; Berriozabal, G.; De Miguel, Y. R.; Bergström, L. *Sci. Technol. Adv. Mater.* **2013**, *14*, 023001; doi:10.1088/1468-6996/14/2/023001.

[193] Hebishy, E.; Ph.D. thesis; **2013**.

[194] Ewoldt, R. H.; Johnston, M. T.; Caretta, L. M. In *Complex fluids in biological systems*; Springer, **2015**; pp 207–241; doi:10.1007/978-1-4939-2065-5.

[195] Badawy, A. M. E.; Luxton, T. P.; Silva, R. G.; Scheckel, K. G.; Suidan, M. T.; Tolaymat, T. M. *Environ. Sci. Technol.* **2010**, *44*, 1260–1266; doi:10.1021/es902240k.

[196] Tombácz, E.; Szekeres, M. *Applied Clay Science* **2004**, *27*, 75–94; doi:10.1016/j.clay.2004.01.001.

[197] Fujii, S.; Read, E. S.; Binks, B. P.; Armes, S. P. *Adv. Mater.* **2005**, *17*, 1014–1018; doi:10.1002/adma.200401641.

[198] Chenglin, Y.; Yiqun, Y.; Ye, Z.; Na, L.; Xiaoya, L.; Jing, L.; Ming, J. *Langmuir* **2012**, *28*, 9211–9222; doi:10.1021/la301605a.

[199] Haase, M. F.; Grigoriev, D.; Moehwald, H.; Tiersch, B.; Shchukin, D. G. *J. Phys. Chem. C* **2010**, *114*, 17304–17310; doi:10.1021/jp104052s.

[200] Haase, M. F.; Grigoriev, D.; Moehwald, H.; Tiersch, B.; Shchukin, D. G. *Langmuir* **2010**, *27*, 74–82; doi:10.1021/la1027724.

[201] Tang, J.; Quinlan, P. J.; Tam, K. C. *Soft Matter* **2015**, *11*, 3512–3529; doi:10.1039/C5SM00247H.

[202] Yang, F.; Niu, Q.; Lan, Q.; Sun, D. *J. Colloid Interface Sci.* **2007**, *306*, 285–295; doi:doi.org/10.1016/j.jcis.2006.10.062.

[203] Chen, T.; Colver, P. J.; Bon, S. A. F. *Adv. Mater.* **2007**, *19*, 2286–2289; doi:10.1002/adma.200602447.

[204] Madivala, B.; Fransaer, J.; Vermant, J. *Langmuir* **2009**, *25*, 2718–2728; doi:10.1021/la803554u.

[205] Berret, J.-F. *Langmuir* **1997**, *13*, 2227–2234; doi:10.1021/la961078p.

[206] Spenley, N. A.; Cates, M. E.; McLeish, T. C. B. *Phys. Rev. Lett.* **1993**, *71*, 939; doi:10.1103/PhysRevLett.71.939.

[207] Frelichowska, J.; Bolzinger, M.-A.; Chevalier, Y. *Colloids Surf. A* **2009**, *343*, 70–74; doi:10.1016/j.colsurfa.2009.01.031.

[208] Arab, D.; Kantzas, A.; Bryant, S. L. *J. Petrol. Sci. Eng.* **2018**, *163*, 217–242; doi:10.1016/j.petrol.2017.12.091.

[209] Poslinski, A. J.; Ryan, M. E.; Gupta, R. K.; Seshadri, S. G.; Frechette, F. J. *J. Rheol* **1988**, *32*, 751–771; doi:10.1122/1.549991.

[210] Metzner, A. B. *J. Rheol* **1985**, *29*, 739–775; doi:10.1122/1.549808.

[211] Clark, A. H.; Gidley, M. J.; Richardson, R. K.; Ross-Murphy, S. B. *Macromolecules* **1989**, *22*, 346–351; doi:10.1021/ma00191a063.

[212] Gómez-Díaz, D.; Navaza, J. M. *J. Food Eng.* **2003**, *56*, 387–392; doi:10.1016/S0260-8774(02)00211-X.

[213] Pal, R. *Colloid. Polym. Sci.* **1999**, *277*, 583–588; doi:10.1007/s003960050429.

[214] Buscall, R.; Mills, P.; Stewart, R.; Sutton, D.; White, L.; Yates, G. *Journal of Non-Newtonian Fluid Mechanics* **1987**, *24*, 183–202; doi:10.1016/0377-0257(87)85009-7.

[215] Buscall, R.; Mills, P. D.; Goodwin, J. W.; Lawson, D. *Journal of the Chemical Society, Faraday Transactions 1: Physical Chemistry in Condensed Phases* **1988**, *84*, 4249–4260; doi:10.1039/F19888404249.

[216] Arditty, S.; Schmitt, V.; Giermanska-Kahn, J.; Leal-Calderon, F. *Journal of Colloid and Interface Science* **2004**, *275*, 659–664; doi:10.1016/j.jcis.2004.03.001.

[217] Dickinson, E. *Colloids Surf. A* **2006**, *288*, 3–11; doi:10.1016/j.colsurfa.2006.01.012.

[218] Dickinson, E. *Trends Food Sci. Technol.* **2015**, *43*, 178–188; doi:10.1016/j.tifs.2015.02.006.

[219] Mercado, R. A.; Salager, J. L.; Sadtler, V.; Marchal, P.; Choplin, L. *Colloids Surf. A* **2014**, *458*, 63–68; doi:10.1016/j.colsurfa.2014.03.109.

[220] Binks, B. P.; Rodrigues, J. A.; Frith, W. J. *Langmuir* **2007**, *23*, 3626–3636; doi:10.1021/la0634600.

[221] Pichot, R.; Ph.D. thesis; University of Birmingham; **2012**.

[222] Lan, Q.; Liu, C.; Yang, F.; Liu, S.; Xu, J.; Sun, D. *J. Colloid Interface Sci.* **2007**, *310*, 260–269; doi:10.1016/j.jcis.2007.01.081.

[223] Stokes, J. R.; Telford, J. H. *J. Non-Newton Fluid Mech.* **2004**, *124*, 137–146; doi:10.1016/j.jnnfm.2004.09.001.